ASPECTS OF MHD WAVE PROPAGATION IN SOLAR ATMOSPHERIC STRUCTURES

Cheryl Ann Mundie

A Thesis Submitted for the Degree of PhD
at the
University of St Andrews

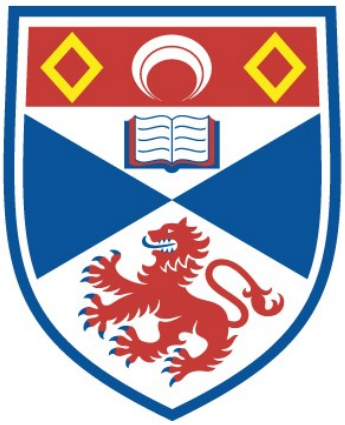

1998

Aspects of MHD Wave Propagation in Solar Atmospheric Structures

Cheryl Ann Mundie

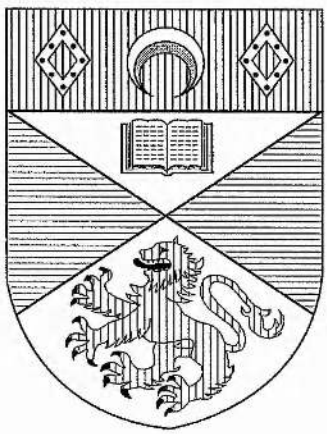

Thesis submitted for the degree of Doctor of Philosophy
of the University of St. Andrews

4 September 1998

Abstract

The theme of this thesis is ideal linear MHD wave propagation in structured media, using models relevant to structures in the solar atmosphere.

We derive dispersion relations governing the ideal linear MHD modes for stationary states which are discretely structured in velocity and other plasma properties, in a direction transverse to the magnetic field, with field-aligned steady flow; the discrete structures considered are the single interface, uniform slab and uniform cylinder. This represents an extension of earlier models for the static case (Edwin 1984), by the inclusion of structured flows. The basic effects of flow are described, drawing on a discussion of the dispersion relations.

The dispersion relations for the case of incompressible surface modes are examined in detail. We identify the qualitative effects of flow, including the onset of instability, by tracing the evolution of stable solutions and their propagation windows, as the relative flow is increased. Our analysis is presented in terms of a general formulation applicable to all three geometries (interface, slab and cylinder), revealing the combined role of dispersion and the ratio of densities in the two media.

We go on to consider the relevance of the incompressible approximation to compressible surface modes, with particular reference to the static case of a single interface one side of which is field-free. We present and investigate analytical solutions for several special cases. The properties of the solutions obtained are compared with those for the equivalent incompressible case.

Finally, we turn to the topic of global oscillations of quiescent prominences. A uniform slab model (Joarder 1993) yields, under conditions appropriate to the prominence-coronal inhomogeneity with the magnetic field threading the prominence being line-tied in the photosphere, modes which are analogous to the oscillations of a uniform string loaded with a point mass, and a formula approximating the period is given. We investigate the robustness of this formula for various plasma density profiles, assessing the applicability of the results from the uniform slab calculation to more realistic density profiles of the prominence-coronal inhomogeneity.

Declarations

I, Cheryl Ann Mundie, hereby certify that this thesis, which is approximately 50,000 words in length, has been written by me, that it is the record of work carried out by me and that it has not been submitted in any previous application for a higher degree.

Date: 4 Sept 98 Signature of candidate:

I was admitted as a research student in October 1993 and as a candidate for the degree of Ph.D. in October 1994; the higher study for which this is a record was carried out in the University of St. Andrews between 1993 and 1998.

Date: 4 Sept 98 Signature of candidate:

I hereby certify that the candidate has fulfilled the conditions of the Resolution and Regulations appropriate to the Degree of Ph.D. in the University of St. Andrews and that the candidate is qualified to submit this thesis in application to that degree.

Date: 4 Sept. 1998 Signature of supervisor: .....

In submitting this thesis to the University of St. Andrews I understand that I am giving permission for it to be made available for use in accordance with the regulations of the University Library for the time being in force, subject to any copyright vested in the work not being affected thereby. I also understand that the title and abstract will be published, and that a copy of the work may be made and supplied to any *bona fide* library or research worker.

Date: 4 Sept 98 Signature of candidate: ..

To,

Mam, Dad,

Kam, Tracy ...

. . . and Biscuit Mix, Bolshy Sparrows,
Doppler Ducks and Monkey Puzzles!

and other *Fine*Things

Acknowledgements

At the risk of sounding Very Corny Indeed, there are lots of people I would like to thank for helping me to Get To Where I Am Today.

Thanks to my supervisor Professor Bernard Roberts for giving me the freedom to go off on my various tangents, for bearing my somewhat extended period of study, and for refusing to let me throw the towel in. Thanks to Professor Eric Priest for stimulating my interest in MHD in the first place.

Thanks to my family and friends (and Sheltie-land!) for always being there, and for putting up with all my indecision and my never knowing quite when this would end.

Thanks to Mam and Dad for all their support, Wise Words and Top Tips. Thanks to my sisters Kam and Tracy for their endless supply of "cheeries" (and Sheltie Times!) and faith that I would finally get through this. Thanks to Jack ("Chack") for opening my eyes, always believing in me, sharing good times and seeing me through bad times. Thanks to Vaila ("Thing"), for lots of "Funs" in Edinburgh, St A and Sheltie-land.

Thanks to everyone in The Department that has supported me and made my time here enjoyable, particularly Gordon, David, Daniel, Ineke, Katie, Erwin, Luca, Clare and Robert. Thanks to Anita, Steve, Angel, Lowrie, Andy, Anthony and Dot. Thanks to various flatmates for putting up with me: Kath, Darren A(n unpronounceable surname), Pasi, The "Struans" (Danny, Sonja, Paul, Leigh, Maxine, Kevin), Elinor, Betty and Dave. Thanks to all my tutorial students for being fun and challenging to teach.

Finally, thanks to everyone that has ever come to one of my parties, and drunk the punch(!)

"The chief aim of all investigations of the external world should be to discover the rational order and harmony which has been imposed on it by God and which He revealed to us in the the language of mathematics."

Johannes Kepler (1571-1630)

Contents

Chapter 1

Introduction

1.1 Overview of subject area

The Sun is more than a bright ball in the sky providing the energy fuelling life on Earth. It has long been an object of fascination, justified by the array of interesting phenomena it displays and complex structures of which it is composed. Turbulent motions of the convection zone transport to the surface layers the heat generated in the fusion reactor core and the magnetic field generated in the solar dynamo; this magnetic field emerges from the downdrafts between convection cells, and ranges from the large, cool, dark sunspots dotting the active regions to the intense magnetic flux tubes which occur in the rest of the photosphere (the visible surface). The magnetic field then spreads out into the atmosphere, where it tangles up (like a ball of wool the cat has been at), forming coronal loops, holes and plumes which surround the Sun like a wispy halo only visible to the naked eye during a solar eclipse. Jet-like spicules exist in the chromosphere, and prominences hang eerily in the corona, like clouds tethered by the magnetic field, before erupting explosively; solar flares and coronal mass ejections dramatically spew matter and energy far out into space, sometimes reaching the Earth in the solar wind. New features and puzzles are regularly revealed in observations from ground and space (e.g. SOHO, YOHKOH, TRACE).

A detailed description of the Sun may be found in Priest (1982, 1995). We note three main things: the Sun is highly structured, very dynamic, and the magnetic field plays a central role. This provokes the study of waves in structured plasmas.

1.2 Introduction to MHD theory

1.2.1 MHD equations

The Sun is composed of magnetised plasma. We may study the Sun on a macroscopic scale using magnetohydrodynamics (MHD) (e.g. Cowling 1957, 1976, Priest 1982). This is a well known and commonly used theory, which combines fluid dynamics with Maxwell's equations to describe how an electrically conducting fluid (such as the solar plasma) interacts globally with a magnetic field. These equations, in which the plasma is treated as a continuum, may also be derived from the Boltzmann equations for electrons and protons (e.g. Boyd and Sanderson 1969). The MHD approach is generally suited to large scale (both spatial and temporal) phenomena. For most solar applications we may treat the plasma as a single fluid and make the assumption that all characteristic speeds of phenomena under study are non-relativistic, so that the displacement current in Ampere's Law may be neglected and the simple form of Ohm's Law may be used. We consider an inertial reference frame and neglect viscous forces, and use SI units.

With this in mind, the governing equations of solar MHD are as follows:

continuity

$$\frac{\partial \rho}{\partial t} + \nabla \cdot (\rho \mathbf{v}) = 0 \tag{1.1}$$

motion

$$\rho \frac{D\mathbf{v}}{Dt} = -\nabla p + \mathbf{j} \times \mathbf{B} + \rho \mathbf{g} \tag{1.2}$$

heat equation

$$\frac{Dp}{Dt} - \frac{\gamma p}{\rho} \frac{D\rho}{Dt} = -(\gamma - 1)\mathcal{L} \tag{1.3}$$

ideal gas law

$$p = \frac{k_B}{m} \rho T \tag{1.4}$$

solenoidal constraint

$$\nabla \cdot \mathbf{B} = 0 \tag{1.5}$$

where

$$\frac{D}{Dt} = \frac{\partial}{\partial t} + \mathbf{v} \cdot \nabla \tag{1.6}$$

is the time derivative following the motion. The above equations determine $\mathbf{B}$ the magnetic field, $\mathbf{v}$ the plasma velocity, ρ the plasma density, p the plasma pressure and T the temperature, where $\mathbf{g}$ is the acceleration due to gravity, k_B is Boltzman's constant, m is the mean particle mass, γ is the ratio of specific heats (taken to be 5/3 in most solar applications), and $\mathcal{L}$ is the energy loss function.

The electric field $\mathbf{E}$ and the current $\mathbf{j}$ are then given by:

Ampere's law

$$\nabla \times \mathbf{B} = \mu \mathbf{j} \tag{1.7}$$

Faraday's law of induction

$$\nabla \times \mathbf{E} = -\frac{\partial \mathbf{B}}{\partial t} \tag{1.8}$$

Ohm's law

$$\mathbf{j} = \sigma \left(\mathbf{E} + \mathbf{v} \times \mathbf{B} \right) \tag{1.9}$$

where μ is the magnetic permeability and σ is the electrical conductivity.

The induction equation

We may eliminate $\mathbf{E}$ and $\mathbf{j}$ from the last three equations to yield the general induction equation

$$\frac{\partial \mathbf{B}}{\partial t} = \nabla \times \left(\mathbf{v} \times \mathbf{B} \right) - \nabla \times \left(\eta \nabla \times \mathbf{B} \right) \tag{1.10}$$

where $\eta = 1/(\sigma\mu)$ is the magnetic diffusivity. For many purposes η may be taken to be uniform, leading to

$$\frac{\partial \mathbf{B}}{\partial t} = \nabla \times \left(\mathbf{v} \times \mathbf{B} \right) + \eta \nabla^2 \mathbf{B} \tag{1.11}$$

Equation (1.11) is known as the induction equation and it describes how $\mathbf{B}$ evolves with time in the presence of a flow.

Consider the physical significance of the terms on the right-handside of equation (1.11). The second term shows how the magnetic field diffuses away with time, converting magnetic energy into heat, in such a way as to smooth out any magnetic field gradients. In

the limit of a perfectly conducting fluid ($\sigma \to \infty$, i.e. $\eta \to 0$) there is no diffusion and the magnetic field gets carried around with the flow by advection, as if it were frozen to the plasma (the first term). Generally both processes contribute: the magnetic field partly gets transported by the flow and partly slips or diffuses through the plasma.

Which of the processes of advection and diffusion is dominant is determined by the magnetic Reynolds number given by

$$R_m = \frac{\tau_{diff}}{\tau_{motion}} = \frac{LV}{\eta} \tag{1.12}$$

where τ_{diff} and τ_{motion} are the respective timescales on which the magnetic field changes due to diffusion and advection acting alone; L and V are characteristic lengths and flow speeds in the medium being considered. Since the solar plasma is energetically dominated by large lengthscale features and moderate speed flows, diffusion is slow and in most cases the magnetic field may be treated as though it is frozen to the plasma. Diffusion only becomes important where there are small length scales, where it may lead to *reconnection* of fieldlines, resulting in topological changes in the fieldline structure.

The Lorentz force

From the equation of motion we see that in addition to the plasma pressure gradient and gravity, there is a magnetic force which may cause a plasma element to move. This is the Lorentz force; it may be decomposed as follows:

$$\mathbf{j} \times \mathbf{B} = (\mathbf{B} \cdot \nabla) \frac{\mathbf{B}}{\mu} - \nabla \left(\frac{B^2}{2\mu} \right) \tag{1.13}$$

The first term on the right may be thought of as a magnetic tension of amount B^2/μ along the field lines, which has a resultant effect only if the field lines are curved. The second term involves the gradient of a magnetic pressure, of amount $B^2/2\mu$, which adds to the plasma pressure gradient so that the net effect is to move plasma from regions of high to those of low total pressure.

MHD equations summary

In what follows we will mainly consider frozen-in plasmas (so that effectively $\eta = 0$ in the induction equation (1.11)) with adiabatic changes of state ($\mathcal{L} = 0$ in the heat equation

(1.3)). The main MHD equations we will use are continuity, heat (now called adiabatic), induction and motion, which with these assumptions may respectively be written as

$$\frac{D\rho}{Dt} = -\rho\nabla\cdot\mathbf{v} \tag{1.14}$$

$$\frac{Dp}{Dt} = -\frac{\gamma p}{\rho}(\rho\nabla\cdot\mathbf{v}) \tag{1.15}$$

$$\frac{D\mathbf{B}}{Dt} = -\mathbf{B}(\nabla\cdot\mathbf{v}) + (\mathbf{B}\cdot\nabla)\mathbf{v} \tag{1.16}$$

$$\rho\frac{D\mathbf{v}}{Dt} = -\nabla\left(p + \frac{B^2}{2\mu}\right) + (\mathbf{B}\cdot\nabla)\frac{\mathbf{B}}{\mu} + \rho\mathbf{g} \tag{1.17}$$

together with

$$\nabla\cdot\mathbf{B} = 0 \tag{1.18}$$

The MHD equations given here are used to describe a large variety of phenomena, provided it is a situation in which an MHD approach is valid. Although MHD is essentially an approximation, valid under certain conditions that are applicable for many solar and astrophysical applications, the equations are nevertheless complicated, exhibiting coupling, nonlinearities, three dimensional vectors, and derivatives with respect to both space and time. This makes it difficult to consider the MHD equations in complete generality. We therefore make simplifications, depending on our application, such as the neglect of certain derivatives, dissipative effects or nonlinearities, resulting in a reduced system of equations (often one dimensional or two dimensional), which is easier to extract information from. While a more general treatment may be more realistic, this is at the expense of tractability and ease of interpretation. In order to understand a particular phenomenon it is therefore essential to first of all consider a simple model, from which we may hope to deduce the fundamental effects, providing a guide to a more general treatment.

1.2.2 MHD equilibria and stationary states

Where there is negligible flow ($\mathbf{v} = 0$) and no variation with time ($\partial/\partial t = 0$), the ideal MHD equations (1.14)–(1.16) are trivially satisfied, while the equation of motion (1.17) reduces to a force balance

$$0 = -\nabla p + \mathbf{j}\times\mathbf{B} + \rho\mathbf{g} \tag{1.19}$$

between the pressure gradient, the Lorentz force and the gravitational force. Equation (1.19) largely governs this equilibrium state, although we additionally use equations (1.7),

(1.18), (1.4) and an energy equation in order to determine the equilibrium configuration. Equation (1.19) possesses several classes of solutions, and may describe complicated equilibrium structures for sunspots, prominences, coronal loops and other solar structures.

Comparing the first and third terms on the right-handside of equation (1.19), and using (1.4), we obtain a lengthscale of

$$\Lambda_0 = \frac{k_B T}{mg}; \tag{1.20}$$

Λ_0 is the (pressure) scale height. For example, Λ_0 is about 125 km in the photosphere, 500 km in the upper chromosphere, and 50,000 km in the corona. Gravity may be neglected wherever Λ_0 is large compared to other characteristic lengthscales for vertical variation.

The relative importance of the gas pressure p and magnetic pressure B^2/μ is determined by the *plasma beta*, defined by their ratio in equilibrium:

$$\beta = \frac{2\mu p}{B^2}. \tag{1.21}$$

In cases where $\beta \ll 1$, magnetic effects dominate and equation (1.19) further reduces to $\mathbf{j} \times \mathbf{B} = 0$; the magnetic field is said to be *force-free*. In the sub-class $\mathbf{j} = 0$, the magnetic field is *potential*. The solar corona is generally assumed to be force-free ($\beta \ll 1$) at large scales.

Even the reduced forms of (1.19) may exhibit quite complicated solutions. We may also consider stationary states, for which $\partial/\partial t = 0$ but the plasma has a steady flow $\mathbf{v} \neq 0$. This leads to an extra term in (1.19), and equations (1.14)–(1.16) are no longer trivially satisfied (see Section A.2.1 in the Appendix).

1.2.3 MHD waves and stability

The Sun is a highly dynamic medium, hence we must ask: given an equilibrium or stationary state, what happens when you perturb it? The forces at play in the equation of motion will either act to increase the perturbation (instability), or attempt to return to equilibrium (stability), which may lead to the propagation of waves.

In the investigation of this, a standard mathematical approach is followed. Consider an equilibrium configuration or stationary state of the form:

$$\rho = \rho_0(\mathbf{r}), \quad p = p_0(\mathbf{r}), \quad T = T_0(\mathbf{r}), \quad \mathbf{B} = \mathbf{B}_0(\mathbf{r}), \quad \mathbf{v} = \mathbf{v}_0(\mathbf{r}) \tag{1.22}$$

and perturb it slightly to yield

$$\left.\begin{array}{c} \rho = \rho_0(\mathbf{r}) + \rho_1(\mathbf{r},t), \qquad p = p_0(\mathbf{r}) + p_1(\mathbf{r},t), \qquad T = T_0(\mathbf{r}) + T_1(\mathbf{r},t), \\ \mathbf{B} = \mathbf{B}_0(\mathbf{r}) + \mathbf{B}_1(\mathbf{r},t), \qquad \mathbf{v} = \mathbf{v}_0(\mathbf{r}) + \mathbf{v}_1(\mathbf{r},t) \end{array}\right\} \tag{1.23}$$

where the subscript 1 denotes arbitrary perturbations in the given quantity, about the state (1.22). Investigate the evolution of this disturbance by substituting the perturbed state (1.23) into the ideal MHD equations (1.14)–(1.17), subject to (1.18).

Fourier analyse the perturbation quantities ψ in time, by considering a time dependence of the form

$$\psi \propto e^{i\omega t} \tag{1.24}$$

where (the real part of) ω is the angular frequency of the disturbance. The MHD equations governing the perturbed state are then solved, subject to suitable boundary conditions where appropriate, with the aim of determining ω.

Solutions with ω real, i.e. $\omega^2 > 0$, correspond to stable *waves*, which oscillate in time without growth of amplitude. Solutions with ω pure imaginary, i.e. $\omega^2 < 0$, yield decaying solutions where $\mathrm{imag}(\omega) > 0$, and growing, or *unstable* solutions where $\mathrm{imag}(\omega) < 0$. It is also possible for ω to be complex, which corresponds to a damped oscillation when $\mathrm{imag}(\omega) > 0$, that is one whose amplitude decays in time, and an overstable oscillation when $\mathrm{imag}(\omega) < 0$, that is one whose amplitude grows in time; the latter case is also *unstable*.

As a first approximation, it is customary to consider small *linear* disturbances, for which we may reduce the MHD equations by neglecting products of perturbation quantities; this process is termed *linearisation*, and removes nonlinear terms in the MHD equations. If such terms were retained, nonlinear MHD disturbances could be considered, the theory of which is beyond our scope, as are non-ideal effects; see Cramer (1995).

We will consider linear MHD theory only. The Appendix we derive the linearised forms of the ideal MHD equations, for arbitrary linear perturbations in space and time about an arbitrary stationary state; the general linearised equations are (A.18)–(A.21), with the unperturbed and perturbed states given by (1.22) and (1.23) respectively. Then the governing equations for all the situations we consider may be derived from equations

(A.18)–(A.21), which we restate here for convenience:

$$\frac{\partial \rho_1}{\partial t} = -\rho_1 (\nabla \cdot \mathbf{v}_0) - \rho_0 (\nabla \cdot \mathbf{v}_1) - (\mathbf{v}_0 \cdot \nabla) \rho_1 - (\mathbf{v}_1 \cdot \nabla) \rho_0 \tag{1.25}$$

$$\frac{\partial p_1}{\partial t} = -c_s^2 \rho_1 (\nabla \cdot \mathbf{v}_0) - c_s^2 \rho_0 (\nabla \cdot \mathbf{v}_1) - (\mathbf{v}_0 \cdot \nabla) p_1 - (\mathbf{v}_1 \cdot \nabla) p_0 \tag{1.26}$$

$$\frac{\partial \mathbf{B}_1}{\partial t} = -\mathbf{B}_1 (\nabla \cdot \mathbf{v}_0) - \mathbf{B}_0 (\nabla \cdot \mathbf{v}_1) - (\mathbf{v}_0 \cdot \nabla) \mathbf{B}_1 - (\mathbf{v}_1 \cdot \nabla) \mathbf{B}_0 + (\mathbf{B}_1 \cdot \nabla) \mathbf{v}_0 + (\mathbf{B}_0 \cdot \nabla) \mathbf{v}_1 \tag{1.27}$$

$$\rho_0 \frac{\partial \mathbf{v}_1}{\partial t} = -\nabla p_T + (\mathbf{B}_0 \cdot \nabla) \frac{\mathbf{B}_1}{\mu} + (\mathbf{B}_1 \cdot \nabla) \frac{\mathbf{B}_0}{\mu} + \rho_1 \mathbf{g} - \rho_0 (\mathbf{v}_0 \cdot \nabla) \mathbf{v}_1 - \rho_0 (\mathbf{v}_1 \cdot \nabla) \mathbf{v}_0 - \rho_1 (\mathbf{v}_0 \cdot \nabla) \mathbf{v}_0. \tag{1.28}$$

Here we have introduced the total pressure perturbation p_T given by

$$p_T = p_1 + \frac{\mathbf{B}_0 \cdot \mathbf{B}_1}{\mu}, \tag{1.29}$$

and $c_s(\mathbf{r}) = (\gamma p_0(\mathbf{r})/\rho_0(\mathbf{r}))^{1/2}$ denotes the sound speed of the (unperturbed) medium. Equations (1.25)–(1.28) are the *linearised ideal MHD equations in their most general form*, and apply, together with (1.18), to the most general case (1.23) of small perturbations about a stationary state, in any orthogonal coordinate system.

MHD waves in an infinite, unstructured medium

The simplest unperturbed state we may consider is a static uniform medium of infinite extent, in the absence of gravity. Adopting a Cartesian coordinate system, we take the magnetic field to lie along one of the axes, say the z-axis. Then the equilibrium state is given by

$$\rho = \rho_0, \quad p = p_0, \quad T = T_0, \quad \mathbf{B} = \mathbf{B}_0 = B_0 \hat{\mathbf{z}}, \quad \mathbf{v} = 0. \tag{1.30}$$

Consider the perturbed state:

$$\rho = \rho_0 + \rho_1, \quad p = p_0 + p_1, \quad T = T_0 + T_1, \quad \mathbf{B} = \mathbf{B}_0 + \mathbf{B}_1, \quad \mathbf{v} = \mathbf{v}_1. \tag{1.31}$$

where $\mathbf{B}_1 = (B_x, B_y, B_z)$ and $\mathbf{v}_1 = (v_x, v_y, v_z)$.

Then the linearised ideal MHD equations (1.25)–(1.28) have constant coefficients, and we may Fourier analyse all perturbation quantities ψ in both space and time, writing

$$\psi(\mathbf{r}, t) = \hat{\psi}\, e^{i(\omega t - qx - ly - kz)} \tag{1.32}$$

where $\hat{\psi}$ is a constant.

This leads to the well known algebraic *dispersion relation*

$$(k^2 {v_A}^2 - \omega^2)\left(\omega^4 - ({c_s}^2 + {v_A}^2)\omega^2\kappa^2 + {c_s}^2 {v_A}^2 k^2 \kappa^2\right) = 0 \tag{1.33}$$

governing linear disturbances about the uniform static equilibrium (1.30). In equation (1.33), k is the wavenumber in the positive magnetic field direction and $\kappa = (q^2+l^2+k^2)^{1/2}$ is the total wavenumber, this being the magnitude of the propagation vector (q, l, k). The sound speed c_s and Alfvén speed v_A in the uniform medium are given by

$${c_s}^2 = \frac{\gamma p_0}{\rho_0}, \qquad {v_A}^2 = \frac{{B_0}^2}{\mu\rho_0}. \tag{1.34}$$

We also define the tube (or cusp) speed c_T, given by

$${c_T}^2 = \frac{{c_s}^2 {v_A}^2}{{c_s}^2 + {v_A}^2}. \tag{1.35}$$

Equation (1.33) yields three solutions for ω^2, all of which are positive. We therefore obtain three types of MHD waves: the *Alfvén mode* is given by the vanishing of the first factor on the left-handside of (1.33); the *slow magnetoacoustic mode* and the *fast magnetoacoustic mode* respectively correspond to the smaller and larger root for ω^2 in the second factor on the left-handside of (1.33). For propagating waves, we consider the *phase speed* ω/κ, which is the speed at which a wavefront travels in the direction of propagation (q, l, k). These three mode types have quite different properties, each being governed by different interactions of the restoring forces in the equation of motion, for which we draw on the discussion of Roberts (1985).

The Alfvén mode is incompressible ($\nabla\cdot\mathbf{v}_1 = 0$), involving no changes in density or pressure ($p_T = p_1 = \rho_1 = 0$), with velocity and magnetic field perturbation both transverse to the magnetic field ($v_z = B_z = 0$). The Alfvén mode is driven entirely by the perturbed magnetic tension force, and satisfies the one-dimensional wave equation

$$\frac{\partial^2\psi}{\partial t^2} = {v_A}^2 \frac{\partial^2\psi}{\partial z^2} \tag{1.36}$$

where ψ may be any one of v_x, v_y, B_x or B_y. The Alfvén mode is analogous to transverse waves on an elastic string, with propagation speed $v_A = (\mathcal{T}/\rho_0)^{1/2}$ where $\mathcal{T} = {B_0}^2/\mu$ is the magnitude of the magnetic tension along the fieldlines.

The dispersion relation for the Alfvén mode (given by the factor on the left-handside of (1.33)), may be written in terms of the phase speed ω/κ as

$$\left(\frac{\omega}{\kappa}\right)^2 = {v_A}^2 \cos^2\phi \tag{1.37}$$

where ϕ is the angle between the propagation vector (q, l, k) and the unperturbed magnetic field $\mathbf{B}_0 = B_0\hat{\mathbf{z}}$, with $\cos\phi = k/\kappa$. Equation (1.37) shows that the Alfvén mode is unable to propagate across the magnetic field ($k = 0$ when $\phi = \pi/2$), and propagates with its greatest phase speed v_A along the magnetic field ($\kappa = |k|$ when $\phi = 0$). This anisotropy is a reflection of the preferred direction associated with the unperturbed magnetic field. The variation of phase speed ω/κ with propagation angle θ of the Alfvén mode is shown in Chapter 2, Figure 2.1 (see the plot with $M = 0$).

The magnetoacoustic modes are compressible disturbances ($\nabla\cdot\mathbf{v}_1 \neq 0$), being governed by both perturbed pressure forces and the perturbed magnetic tension, and may involve a combination of transverse and longitudinal motions. For the fast mode, the perturbed gas and magnetic pressures act in phase with each other, so as to increase the phase speed; for the slow mode, the perturbed gas and magnetic pressures act out of phase with each other, so as to decrease the phase speed. The perturbed gas pressure is isotropic, while the perturbed magnetic pressure is greatest for propagation across the magnetic field, vanishing for $\phi = 0$, while the perturbed magnetic tension vanishes when $\phi = \pi/2$.

This results in the fast mode being able to propagate in all directions; it is at its fastest for perpendicular propagation across the unperturbed magnetic field ($\phi = \pi/2$), in which case $\omega/\kappa = ({c_s}^2 + {v_A}^2)^{1/2}$. In the absence of a magnetic field, the fast mode propagates isotropically at the sound speed c_s, becoming an ordinary sound wave. The slow mode, on the other hand, is highly anisotropic and, like the Alfvén mode, it cannot propagate across the unperturbed magnetic field. As $\phi \to \pi/2$, the slow mode is given by $\omega^2 \approx \kappa^2 {c_T}^2 \cos^2\phi = k^2 {c_T}^2$. For propagation along the unperturbed magnetic field ($\phi = 0$), the respective phase speeds of the fast and slow magnetoacoustic modes are the greater and lesser of the sound and Alfvén speeds. The variation of phase speed ω/κ with propagation angle ϕ of the fast and slow magnetoacoustic modes is illustrated in Chapter 2, Figure 2.2 (see the plot with $M = 0$).

The magnetoacoustic dispersion relation (given by the second factor on the left-handside

of (1.33)), may be rewritten (Roberts 1981a) as

$$q^2 + l^2 + m^2 = 0 \tag{1.38}$$

where

$$m^2 = \frac{(k^2 {v_A}^2 - \omega^2)(\omega^2 - k^2 {c_s}^2)}{({c_s}^2 + {v_A}^2)(\omega^2 - k^2 {c_T}^2)}. \tag{1.39}$$

With q and l real (so that disturbances are finite at $x = y = \pm\infty$), we have $m^2 < 0$ from (1.38). Then (Roberts 1981a) the slow mode has phase speed ω/κ in the range $0 \leq \omega/\kappa \leq \min(c_s, v_A)$, while for the fast mode $\max(c_s, v_A) \leq \omega/\kappa \leq ({c_s}^2 + {v_A}^2)^{1/2}$.

1.3 Thesis orientation and outline

We have considered ideal linear MHD waves in an infinite, static, unstructured medium. This case gives an insight into the basic physical properties of the three types of MHD waves, and is generally applicable in situations where the physical properties of the medium are structured with a characteristic lengthscale which is large compared to the wavelength, which in turn requires that the scale height is also relatively large so that gravity may be neglected. In such cases the wave modes are well described by those of an infinite uniform medium.

However, the Sun is a highly inhomogeneous medium, which provokes the investigation of MHD waves in structured plasmas. In the investigation of wave motion in structured plasmas, the first aim is to identify the basic physics. Therefore, while quite complicated "realistic" models may exist for the equilibrium or stationary state configuration of a given solar structure, such as a sunspot or a prominence, in studying the types of waves it may support we consider simple models, which retain the most important features of the problem and have the advantage of analytical tractability.

We concentrate on large-scale plasma structuring due to magnetic effects, and neglect effects of stratification due to gravity. From the above discussion it is clear that the magnetic field introduces a preferred direction. This leads to anisotropy, particularly in the Alfvén mode and the slow magnetoacoustic mode. Therefore, a consideration of MHD waves in a medium structured in a direction *transverse* to the magnetic field may lead to

quite different results from the case of structuring which is *longitudinal* to the magnetic field. On this basis, our discussion of structuring may be divided into two parts.

1.3.1 Transverse structuring

The case of *transverse* structuring has wide applicability in solar, magnetospheric and other astrophysical contexts, and as such it has been an area of extensive research, as summarised in recent reviews (Roberts 1985, 1990, 1991b, 1992, Edwin 1991, 1992). For example, in sunspots, photospheric flux tubes, coronal loops, coronal holes, chromospheric fibrils, spicules and solar wind streamers, structuring appears to be in the form of magnetic flux tubes having different properties to their surroundings. While in reality the adjacent plasmas are connected by a continuously varying boundary layer, this layer may be considered to be narrow compared to the scale width of each medium and to the wavelength of the various wave modes. In such cases, when modelling the types of waves the inhomogeneity can support, the boundary layer may be modelled as a discontinuity in the physical properties, hence forming an interface between the media to either side, each of which may be treated as uniform.

We consider three types of *discretely structured media* (see Figure 2.3, and Roberts 1981a,b, Edwin and Roberts 1983): the *single interface* across which one or more of the unperturbed plasma variables is discontinuous; the *uniform slab* and the *uniform cylinder*, which both represent a finite-width region embedded within a uniform environment, but in cartesian and cylindrical geometry respectively. The possible applications of the single interface include the lower penumbral magnetic field in sunspots and the boundary of the magnetopause, while those of the slab or flux tube include photospheric intense tubes, sunspots and coronal loops.

In such models, the usual procedure is to treat each region separately as a uniform medium, Fourier-analysing in all dimensions but the direction of structuring; the spatial dependence in the direction of structuring is determined by the solution of an ordinary differential equation. Application of suitable boundary conditions across the interface and at large distances from it leads to a dispersion relation, from which the frequency ω is obtained. Here we consider the field-aligned phase velocity ω/k, which gives the speed of propagation along the interface, slab or cylinder.

The finite-width slab and cylinder each provide a waveguide or duct within which trapped modes may exist, with minimal disturbance outside the waveguide. Ducted modes may be classified geometrically as *kink* or *sausage*, according to whether or not the centre of the duct is displaced. Ducts may support *body modes*, waves that are internal to a structure and which are classified as fast or slow. Fast and slow body waves represent modifications to the fast and slow magnetoacoustic modes in an infinite uniform medium, but are quantized into a discrete spectrum due to the finite-width, $2a$, say, of the slab or tube. This transverse lengthscale of the duct renders the modes *dispersive*, so that ω/k depends on ka, with modes of different wavelengths along the duct being affected by this transverse lengthscale to different extents. The degree of dispersion of a ducted body mode is related to the isotropy of its counterpart in an infinite uniform medium, with the fast body modes being the more dispersive. In addition to body modes, there exist ducted *surface modes*. These modes arise *because of* the presence of the inhomogeneity, rather than being modified by it, and are evanescent to either side of the interface. Surface modes may also be classified as fast or slow, although they have no analogue in an infinite uniform medium. Ducted surface modes are dispersive, while a single interface may support nondispersive surface modes.

The properties of surface and body modes of discretely structured static equilibria have been investigated in detail by Edwin (1984), who found a rich spectrum of solutions, depending on the relative ordering of the sound and Alfvén speeds within each medium. It is also found that the properties of body modes in *continuously* structured duct models for coronal loops are similar to those of their discretely structured counterparts (Edwin and Roberts 1988, Nakariakov and Roberts 1995b), suggesting that models based on discrete structures may be usefully applied in determining the basic physics of the modes. However, continuous structuring may lead to new effects. For example, the replacement of the interface by a continuous boundary layer allows the phenomenon of *resonant absorption* (Goedbloed 1979, Rae and Roberts 1981, Goossens 1991, Goossens and Ruderman 1996), whereby the field-aligned phase velocity ω/k of the given mode matches the local Alfvén speed v_A or tube speed c_T (both of which vary transversely), leading to fieldline resonance due to the presence of singularities in the ordinary differential equation governing the transverse structure of the perturbations. Continuous structuring may also lead to

phase-mixing of Alfvén waves (Heyvaerts and Priest 1983), whereby oscillations of neighbouring fieldlines go rapidly out of phase, leading to the generation of small lengthscales. Both phase-mixing and resonant absorption can lead to heating of the plasma in the presence of dissipation, and as such may play a part in coronal heating, along with current sheet formation and reconnection, shocks and turbulence (see the reviews by Narain and Ulmschneider 1990, Hollweg 1990).

It is known (e.g. Schmieder 1997, Solanki 1997) that structured flows exist in the solar atmosphere, for example in downdrafts at the boundaries of supergranular cells, sunspots, flows within prominences and spicules, and in the solar wind. Recent space observations by SOHO have detected structured flows in the solar atmosphere (Fleck 1997), and the structure of the solar wind in the inner heliosphere has been observed with ULYSSES (Feldman, Philips, Barraclough and Hammond 1996).

It is therefore appropriate to include velocity structuring in the above models for the single interface, uniform slab and uniform cylinder, and to determine the implications for the wave modes. It is convenient to consider steady flows which are aligned with the magnetic field. We consider the aligned case for two further reasons: firstly, the flow and magnetic field both introduce preferred directions, with the most marked effects expected for the parallel case; secondly, the flows observed in the solar atmosphere and solar wind generally follow magnetic structures (Schmieder 1997). Hence the case of field-aligned flow in discretely structured media provides a good starting point for the examination of the effects of structured flows on waves in solar atmospheric structures.

It is well known that relative flows may lead to the Kelvin-Helmholtz instability (Chandrasekhar 1961, Gerwin 1968). However, due to the stabilising effect of the magnetic field, smaller relative flows may support stable modes, which are modifications to those existing in the absence of flow.

Most studies incorporating velocity structuring concentrate on either the stability properties, or the effects on stable modes of relative flows which are much smaller than the stability threshold. In a complete treatment it is necessary to connect these two phenomena, by tracing the development of a given mode from the static case up to the onset of instability. Such a treatment is made highly complicated by the compressibility of the plasma, and different parameter regimes must be considered separately. However, for

surface modes, the analysis simplifies considerably on use of the incompressible approximation, in which $c_s \to \infty$ and the modes are characterised by the Alfvén speeds in each medium.

In Chapter 2, we discuss some basic effects of flow, and derive the dispersion relations governing surface and body modes in media which are discretely structured in velocity and other plasma properties; the discrete structures considered are the single interface, the uniform slab and the uniform cylinder, sketched in Figure 2.3. The general properties of the dispersion relations are discussed for stable modes.

In Chapter 3, we consider the effects of field-aligned steady flows on incompressible surface modes of the single interface, uniform slab and uniform cylinder. We approach the problem from a general interest point of view, with the aim of uncovering the full structure of the dispersion relation, without restriction to parameter values typical of specific applications. We consider in detail the qualitative effects of flow, including the onset of instability, by tracing the development of stable solutions as the relative flow is increased. This is discussed in terms of the corresponding evolution of the propagation windows in which stable solutions for ω/k may lie. Our analysis is presented in terms of a general formulation simultaneously applicable to all three geometries, revealing the combined role of dispersion and the ratio of densities in the two media.

In Chapter 4, we consider the relevance of the incompressible approximation to compressible surface modes, with particular reference to the static case of a single interface, one side of which is field-free. We present analytical solutions for several special cases. The properties of the solutions obtained are compared with those of the equivalent incompressible case.

1.3.2 Longitudinal structuring

In our above discussion we neglected stratification due to gravity. However, we note that stratification is important in the photosphere and solar interior, and is indeed a vital ingredient in the fruitful field of helioseismology (Deubner and Gough 1984, Christensen-Dalsgaard, Gough and Toomre 1985, Leibacher, Noyes, Toomre and Ulrich 1985, Antia and Chitre 1996), which allows us to delve deep beneath the solar surface, and determine the underlying structure through considering the effects of stratification on (acoustic) p-modes

and (gravity) g-modes in the solar interior. Stratification leads to *longitudinal* structuring in vertical magnetic fields, in addition to the transverse structuring in sunspots and other photospheric magnetic flux tubes, although in the latter case an analytical treatment is possible through use of the *thin tube equations* (Roberts and Webb 1978). The inclusion of gravitational stratification modifies the results from the uniform slab and cylinder models, and a given mode may have a cutoff frequency less than which it cannot propagate upwards (e.g. Roberts 1988).

Another example of a solar plasma which is structured along the direction of the magnetic field is a quiescent prominence suspended in a coronal arcade. Prominences are vertical sheet-like structures which are very much cooler and more dense than their surroundings, and therefore represent a large-scale inhomogeneity in the solar atmosphere. They are threaded by a magnetic field which is predominantly horizontal through the prominence, passes through the tenuous corona and is anchored in the dense photosphere. Being very stable structures for long periods of time (but ultimately given to eruption) they have also been observed to oscillate. Detailed observations and theoretical modelling of the modes of oscillation of a prominence may ultimately yield seismic information about their structure and physics. Some progress has already been made in this area, which is the topic of Chapter 5 in this thesis.

While highly complex models of prominence equilibria and stationary states have been developed, from the point of view of investigating the nature of the oscillation modes it is advantageous to consider simple models. Indeed, this is another area in which uniform slab configurations find application, although in this case the magnetic field is not taken to be parallel to the interfaces. Under conditions appropriate to the prominence-coronal inhomogeneity, it is found that there exist modes which are analogous to the oscillation modes of a stretched elastic string of non-uniform density, and have periods τ given approximately by the formula

$$\tau = \frac{2\pi}{c_p}(al)^{1/2} \tag{1.40}$$

where c_p is the propagation speed characterising the mode, $2a$ is the width of the prominence sheet whose threading magnetic field is anchored at a distance l to either side of the prominence sheet. Such oscillations are termed *string modes* (Roberts 1991a, Joarder and

Roberts 1993b). Formula (1.40) is also obtained from drawing the analogy of a uniform string loaded with a point mass, and in fact yields periods consistent with observations. Numerical studies, adopting more complex equilibrium configurations, also yield results in agreement with (1.40). This suggests that, as for the case of ducted modes in coronal loops described above, the basic physics of the modes is contained within the uniform slab model.

In Chapter 5 we discuss the observations and theory of oscillations in quiescent prominences. We then investigate the applicability of the results from the uniform slab calculation to more realistic profiles of the prominence-corona inhomogeneity, considering the robustness of the formula (1.40) as a description of the period of the string mode for various density profiles.

Finally, in Chapter 6 we summarise the main results of this thesis and present suggestions for further work.

Chapter 2

MHD wave propagation in transversely structured media

2.1 Introduction

In this chapter we derive and discuss the dispersion relations governing linear MHD modes in media which are discretely structured in velocity and other plasma properties; the discrete structures considered are the single interface, the uniform slab and the uniform cylinder, each with unperturbed magnetic field and steady flow oriented parallel both to each other and to the interface, and so transverse to the direction of structuring. We consider the field-aligned phase velocity ω/k, which gives the propagation speed along the interface or duct. This may be considered as an extension of similar work done for the static case (Roberts 1981a,b, Edwin and Roberts 1982, 1983, Edwin 1984), here with the inclusion of discretely structured field-aligned steady flows.

We first consider some basic effects of flows, to be drawn on in our later analysis and discussion of the dispersion relations.

2.1.1 Basic flow effects

MHD waves in an unstructured medium with steady flows

In our investigation of the qualitative effects of steady flows on MHD wave propagation, we begin by considering the unstructured case. This is an essential starting point for

understanding modes in plasmas structured by magnetism, giving the basic modes and their propagation characteristics, and is also an essential starting point for understanding modes in plasmas structured by flows, showing how the basic properties of these modes are affected by the presence of steady flows.

We can predict some influences of flow by consideration of the well known *Doppler effect* in physics, so-called because because it was first proposed by the Austrian physicist Johann Christian Doppler in 1842. This is the phenomenon whereby the perceived frequency of a sound wave is altered when the observer is in relative motion with the source of the sound wave. A common example of this phenomenon is the lowering in pitch of a fire engine siren as it passes at speed, carrying firefighters on a mission to tackle a blaze. The effect is a perceived one, depending on where you are standing, i.e. on your frame of reference. The firefighters on board notice no change of pitch, and neither do the occupants of the ambulance following hot on the tail of the fire engine: since they are travelling at the same speed as the source, they observe the source frequency. However, the stationary observer waiting to cross the road perceives a higher frequency as the fire engine approaches, and a lower frequency as it speeds away. This difference in frequencies is related to the speed at which the fire engine is moving relative to the observer's frame of reference: the faster the relative motion, the more marked the effect.

The Doppler effect applies to any form of wave propagation, and the frequency changes can occur due to movement of the source, the receiver or the medium which supports the wave. We now turn our attention to the propagation of MHD waves in the presence of steady flows, where the Doppler effect is due to the movement of the medium with respect to a given frame of reference.

In Chapter 1 we gave the dispersion relation for MHD modes in a static unstructured medium, which we restate here:

$$(k^2 {v_A}^2 - \omega^2)\left(\omega^4 - ({c_s}^2 + {v_A}^2)\omega^2\kappa^2 + {c_s}^2 {v_A}^2 k^2 \kappa^2\right) = 0; \tag{2.1}$$

k is the wavenumber in the positive magnetic field direction and κ is the total wavenumber, this being the magnitude of the propagation vector. Note that $\kappa > 0$ while k may have either sign. In the presence of a field-aligned steady flow U we obtain (see Section 2.2.1)

a dispersion relation of identical form,

$$(k^2 {v_A}^2 - \Omega^2)\left(\Omega^4 - ({c_s}^2 + {v_A}^2)\Omega^2\kappa^2 + {c_s}^2 {v_A}^2 k^2 \kappa^2\right) = 0, \tag{2.2}$$

but now the frequency ω is replaced by a Doppler shifted frequency

$$\Omega \equiv \omega - kU; \tag{2.3}$$

note that $U > 0$ for a flow in the positive magnetic field direction, and $U < 0$ for an oppositely directed flow. In each of dispersion relations (2.1) and (2.2), the first factor corresponds to the Alfvén mode while the second factor yields the fast and slow magnetoacoustic modes. The similarity between these two dispersion relations indicates that the presence of a field-aligned steady flow causes the frequency of a given mode to be Doppler shifted from its static value. The frequency, in the static reference frame, is *increased* for propagation *with* the flow ($kU > 0$) and *decreased* for propagation *against* the flow ($kU < 0$), in the same way as a fire engine siren is heard at a higher pitch when the engine and the sound wave are both moving towards the observer.

For MHD wave propagation we usually examine the properties of the *phase speed* ω/κ as a function of the propagation vector. In general, if the phase speed varies with the magnitude κ of the propagation vector then the mode is *dispersive* while a dependence on the direction of the propagation vector means that the mode is *anisotropic.*

For the unstructured case of a uniform medium all three modes are non-dispersive but anisotropic. A convenient representation of the dispersion relation (2.2) is by means of a phase diagram: a polar plot in the (R, ϕ) plane, where the radius R (> 0) is the phase speed ω/κ for a given propagation angle ϕ to the positive magnetic field direction. In this way we may display the anisotropic dependence of the phase speed on the propagation direction for each mode.

Figures 2.1 and 2.2 contain illustrative phase diagrams for the Alfvén mode and the magnetoacoustic modes respectively, for various values of the ratio $M = U/v_A$ of the flow speed U to the Alfvén speed v_A. These Figures will be referred to throughout our discussion in this section. The Alfvén mode and the slow magnetoacoustic mode are strongly anisotropic, propagating fastest along the magnetic field ($\cos^2\phi = 1$), and not at all across it ($\cos\phi = 0$). The fast magnetoacoustic mode is almost isotropic for the

static case, and propagates fastest across the magnetic field. For all mode types, the flow introduces additional anisotropy, and there exist critical flows in the description of the topological properties of the phase diagram, as we will discuss.

Consider the dispersion relation (2.1) for the static case, rewritten as a polynomial in the phase speed ω/κ:

$$\left(v_A{}^2\cos^2\phi - \frac{\omega^2}{\kappa^2}\right)\left(\frac{\omega^4}{\kappa^4} - (c_s{}^2 + v_A{}^2)\frac{\omega^2}{\kappa^2} + c_s{}^2 v_A{}^2\cos^2\phi\right) = 0 \tag{2.4}$$

where

$$\cos\phi = \frac{k}{\kappa} \tag{2.5}$$

and ϕ is the angle between the propagation direction $\hat{\kappa}$ and the magnetic field direction $\hat{\mathbf{B}}_0$. We obtain three solutions for the square of the phase speed, corresponding to the three basic MHD modes:

$$\frac{\omega^2}{\kappa^2} = {c_{phs}}^2 \equiv \begin{cases} v_A{}^2\cos^2\phi, & \text{Alfven} \\ \frac{1}{2}(c_s{}^2 + v_A{}^2) + \frac{1}{2}\left\{(c_s{}^2 + v_A{}^2)^2 - 4c_s{}^2 v_A{}^2\cos^2\phi\right\}^{1/2}, & \text{fast} \\ \frac{1}{2}(c_s{}^2 + v_A{}^2) - \frac{1}{2}\left\{(c_s{}^2 + v_A{}^2)^2 - 4c_s{}^2 v_A{}^2\cos^2\phi\right\}^{1/2}. & \text{slow} \end{cases} \tag{2.6}$$

Note that for each mode, (2.6) gives two possible (symmetric) solutions for ω/κ. Strictly, in each case we must choose the root which satisfies

$$\frac{\omega}{\kappa} > 0, \tag{2.7}$$

although for the static case both roots give the same value of $|\omega/\kappa|$, due to symmetry. We denote this positive root c_{phs}, with expressions for ${c_{phs}}^2$ for each mode type given in (2.6).

Also of interest is the field-aligned phase velocity, ω/k, given by

$$\frac{\omega}{k} = \frac{1}{\cos\phi}\frac{\omega}{\kappa}. \tag{2.8}$$

where by (2.7) we have

$$\frac{\omega}{k}\begin{cases} > 0 \quad \text{when} \quad \cos\phi > 0, & \textit{i.e.} \text{ for propagation } \textit{with } \mathbf{B}_0 \\ < 0 \quad \text{when} \quad \cos\phi < 0, & \textit{i.e.} \text{ for propagation } \textit{against } \mathbf{B}_0 \end{cases} \tag{2.9}$$

so that the direction of propagation is defined by the sign of the field-aligned phase velocity ω/k. In the case of *parallel propagation*, that is for propagation parallel to the magnetic

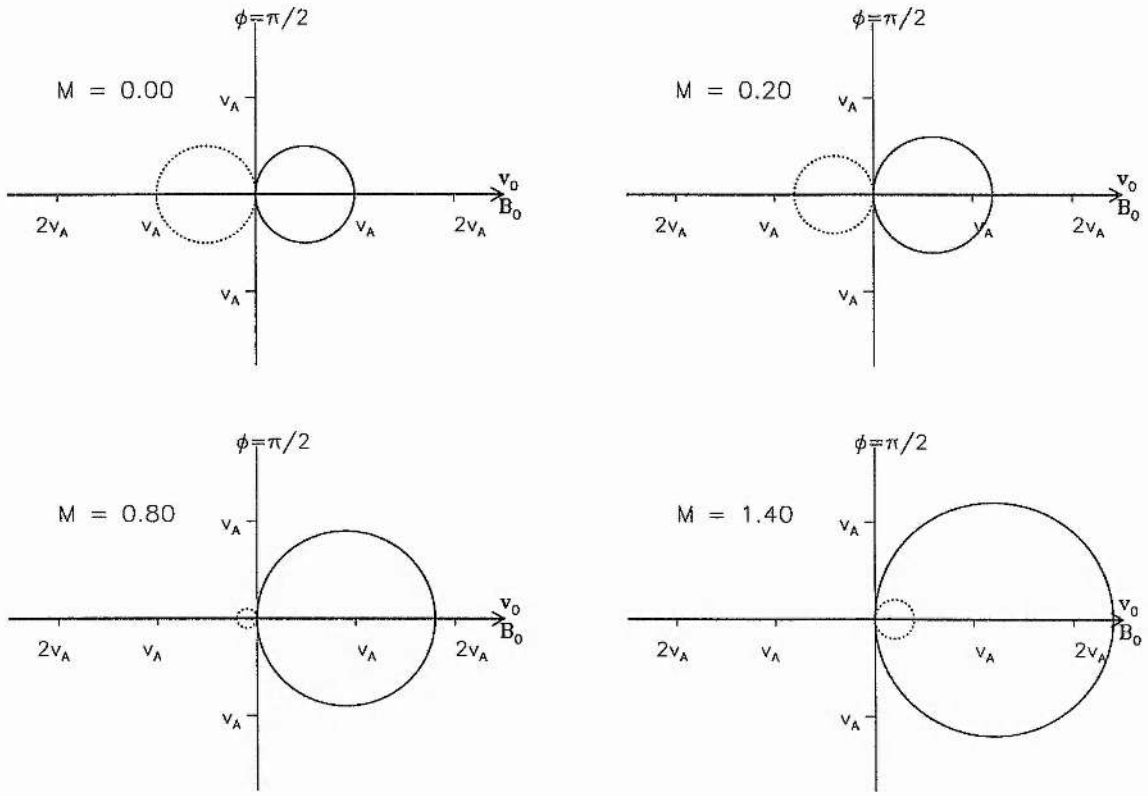

Figure 2.1: The polar phase diagram for Alfvén modes in an unstructured medium with steady field-aligned flows, where the radius $R(>0)$ is the phase speed ω/κ for a given propagation angle ϕ relative to $\mathbf{B}_0$ and $\mathbf{v}_0 = U\hat{\mathbf{B}}_0$. The solid and dotted curves correspond to the plus and minus sign respectively in solution (2.21) for the Alfvén mode; see also (2.2). We show diagrams for different ratios $M = U/v_A$ of the flow speed U to the Alfvén speed v_A, the values of M are shown on each plot. These plots may be compared with those of Figure 2.2, showing the polar phase diagrams for the fast and slow magnetoacoustic modes, on the same scale (for $c_{max} = \max(c_s, v_A) = v_A$) and for the same flow values. The static case is given by $M = 0$.

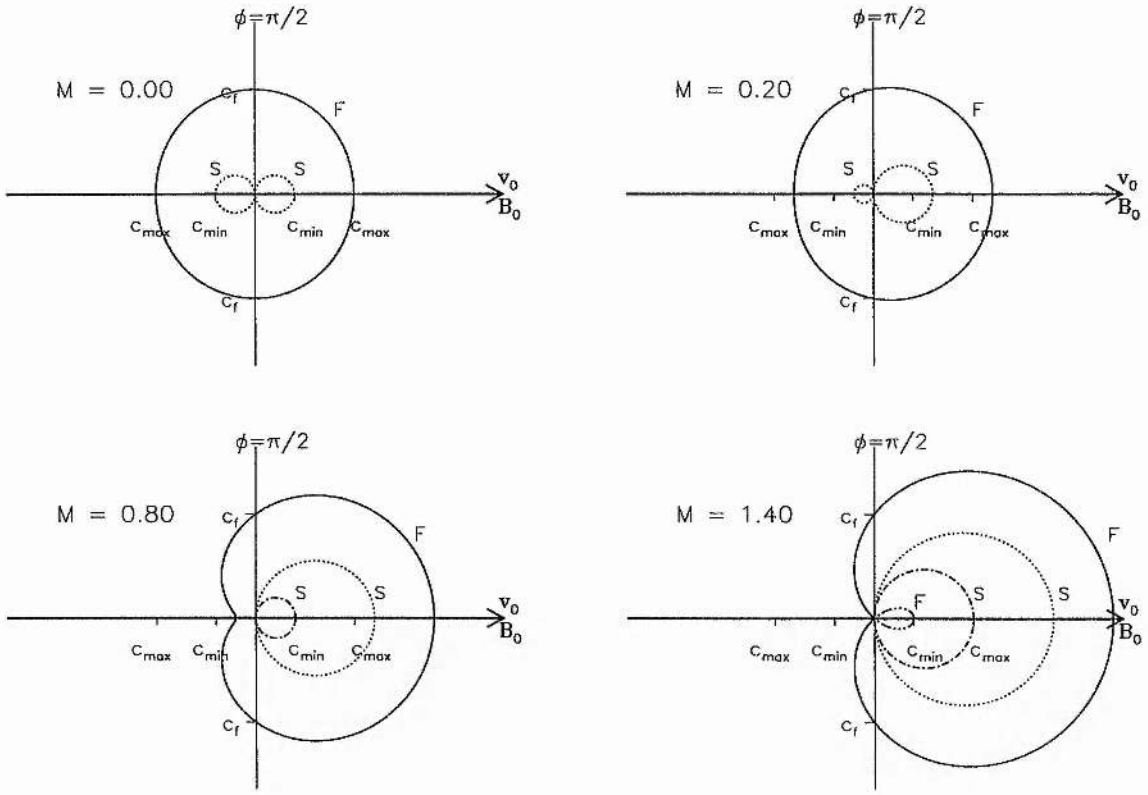

Figure 2.2: The polar phase diagram for the fast (labelled "F") and slow (labelled "S") magnetoacoustic modes in an unstructured medium with steady field-aligned flows, where $c_{min} = \min(c_s, v_A)$, $c_{max} = \max(c_s, v_A)$, $c_f = (c_s{}^2 + v_A{}^2)^{1/2}$ and the radius $R(> 0)$ is the phase speed ω/κ for a given propagation angle ϕ relative to $\mathbf{B_0}$ and $\mathbf{v_0}$. The solid and dot-dot-dot-dashed curves respectively correspond to the fast mode solutions given by the plus and minus sign in (2.12), while the dotted and dot-dashed curves respectively correspond to the slow mode solutions given by the plus and minus sign in (2.12); see also (2.6) and (2.2). With $c_{min} = c_s$, $c_{max} = v_A$ and $c_{min}/c_{max} = 0.4$, we show diagrams for different ratios $M = U/v_A$ of the flow speed U to the Alfvén speed v_A, the values of M are shown on each plot. These plots may be compared with those of Figure 2.1, showing the polar phase diagrams for the Alfvén mode, on the same scale (for $c_{max} = \max(c_s, v_A) = v_A$) and for the same flow values. The static case is given by $M = 0$.

field $\mathbf{B_0}$, we have $\cos\phi = \pm 1$ and the phase speed is given by the magnitude of the field-aligned phase velocity, that is $\omega/\kappa = |\omega/k|$.

For the static case the phase speed for a given mode and propagation angle ϕ is $\omega/\kappa = c_{phs}$, giving a field-aligned phase velocity

$$\frac{\omega}{k} = \frac{c_{phs}}{\cos\phi} \tag{2.10}$$

Noting that for each mode type c_{phs} (> 0) is symmetric in $\cos\phi$, it is clear that for the static case a mode which propagates in a given direction (*with* $\mathbf{B_0}$, say) with phase speed $\omega/\kappa = c_{phs}$, may also propagate in the opposite direction (*against* $\mathbf{B_0}$) at the *same phase speed.* This can be seen from the symmetry of the phase diagrams for the static case, given by $M = 0$ in Figures 2.1 and 2.2.

In the presence of field-aligned steady flows, since equation (2.1) is now satisfied by the Doppler shifted frequency $\Omega \equiv \omega - kU$ rather than ω, we may immediately write the solutions as

$$\frac{\Omega^2}{\kappa^2} = {c_{phs}}^2 \tag{2.11}$$

where ${c_{phs}}^2$ is the square of the phase speed of the given mode for the static case, or in the rest frame of the moving plasma, and is given by the appropriate from in (2.6). Then the phase speed ω/κ in the chosen reference frame (relative to which the plasma is moving) may take either of the forms:

$$\frac{\omega}{\kappa} = U\cos\phi \pm c_{phs} \tag{2.12}$$

with corresponding field-aligned phase velocity ω/k satisfying

$$\frac{\omega}{k} = U \pm \frac{c_{phs}}{\cos\phi}. \tag{2.13}$$

Again for each mode we obtain two possible solutions for any given propagation angle ϕ, with these solutions corresponding respectively to the plus and minus sign in (2.12) and (2.13).

Note that in the presence of flow, the two possible solutions obtained for a given value of ϕ are no longer symmetric, therefore we must take care in choosing a solution; that is, one which satisfies (2.7), or equivalently, (2.9). In the static case ($U = 0$), the correct solution in (2.12) or (2.13) is given by the plus sign, for any angle ϕ and all three mode

types. In the presence of flows, however, the choice of solution depends on the value of c_{phs} relative to $U\cos\phi$, i.e. the value of the given mode's phase speed in the absence of flow, relative to the component of the flow in the given direction of propagation. Clearly, if $|U\cos\phi| < c_{phs}$ then for any value of ϕ the plus sign remains the correct choice, since the solution given by the minus sign violates the constraints (2.7) and (2.9).

For example, let us take the flow to be in the positive magnetic field direction, i.e. $U \geq 0$, so that propagation with the magnetic field corresponds also to propagation with the flow, given by $\omega/k > 0$ and $\cos\phi > 0$. For a given mode and propagation angle ϕ, suppose that the flow satisfies

$$|U\cos\phi| < c_{phs}. \tag{2.14}$$

Then for this mode and propagation angle, the correct solution is given by the plus sign in either (2.12) or (2.13), this being applicable to propagation in either direction relative to the flow. That is, the solutions we choose from (2.13) are

$$\frac{\omega}{k} = U + \frac{c_{phs}}{\cos\phi} > 0, \qquad with \quad \mathbf{B}_0, \mathbf{v}_0 \tag{2.15}$$

$$\frac{\omega}{k} = U + \frac{c_{phs}}{\cos\phi} < 0, \qquad against \quad \mathbf{B}_0, \mathbf{v}_0 \tag{2.16}$$

with c_{phs} (> 0) given by the function of $\cos\phi$ in (2.6) appropriate to the given mode.

Note that the above contains the static case, in which we obtain two solutions at the same phase speed $\omega/\kappa = c_{phs}$ but in opposite directions, with $\omega/k = \pm c_{phs}/|\cos\phi|$. For all three modes we find that with $U \neq 0$, the solution propagating with the flow ($U\cos\phi > 0$) does so at a higher phase speed than for the static case, while the phase speed of the solution propagating in the opposite direction ($U\cos\phi < 0$) is reduced. Hence, phase speeds are Doppler shifted in a similar way to frequencies, resulting in asymmetric phase diagrams for $M > 0$ in Figures 2.1 and 2.2.

When the flow satisfies

$$|U\cos\phi| = c_{phs} \tag{2.17}$$

the phase speed of the solution propagating against the flow is reduced to zero. Then it is essentially a standing wave in the fluid.

Now consider

$$|U\cos\phi| > c_{phs} \tag{2.18}$$

so that the magnitude of the flow exceeds that of the field-aligned phase velocity in the direction of propagation. Here, we are no longer restricted to the plus sign solution in (2.12) or (2.13), and the solutions satisfying (2.7) and (2.9) are given by

$$\frac{\omega}{k} = U + \frac{c_{phs}}{\cos\phi} > 0, \qquad with \quad \mathbf{B_0}, \mathbf{v_0} \tag{2.19}$$

$$\frac{\omega}{k} = U - \frac{c_{phs}}{\cos\phi} > 0, \qquad with \quad \mathbf{B_0}, \mathbf{v_0}. \tag{2.20}$$

Note that both solutions are *with* the flow, so that there is *no propagation against the flow* for the given mode and value of $|U\cos\phi|$. Indeed, the solution given by the minus sign in (2.20) effectively corresponds to replacing $\cos\phi$ by $-\cos\phi$ in the earlier solution (2.16) for propagation against the flow. It therefore represents a mode which formerly (when inequality (2.14) was satisfied) propagated against the flow at an angle ϕ but now propagates in the opposite direction, i.e. with the flow, at an angle $\phi - \pi$: there has been a *"reversal"* in propagation direction. We may consider this mode to have been "swept forward" by the flow (we use quotes since the reversal of propagation direction is for the chosen reference frame, while in the frame of the moving fluid there is no difference from the static case). As the flow is increased further, so do the phase speeds of *both* modes (in the given reference frame).

Let us draw an analogy with ducks trying to swim up or down a fast flowing river. Propagation of waves is helped if it is with the flow, just like a duck hurtles along downstream, whereas propagation is hindered if it is against the flow, just like a duck makes heavy weather of it upstream. The upstream solution becomes a standing wave if $|U\cos\phi| = c_{phs}$, and here we may think of a duck swimming at such a speed that it maintains its position in the river, most likely near a person stood at the riverbank with an ample supply of bread. If $|U\cos\phi| > c_{phs}$ then both solutions for ω/k have the same sign, and therefore yield waves propagating in the same direction. Then the mode (like the duck!) is totally swept along by the flow and has no choice but to go downstream, since the speed at which it ordinarily (i.e. in the absence of flow) moves in a given direction is exceeded by the component of the flow in that direction. If, however, the river is flowing quite slowly, so that the duck can swim much faster than the river is flowing, then the duck is not severely affected by the flow and can swim fairly easily in any direction, although slightly better downstream than upstream. By analogy, for MHD modes if the flow is weak then the

situation is not very much different from the static case, other than a slight shift in phase speed.

Of course, while in the absence of flow a duck can swim equally fast in all directions, the three MHD waves each have different isotropy properties in a static medium, which leads to different conditions for reversal of propagation direction

For the Alfvén mode, $c_{phs} = v_A \cos\phi$ for $\cos\phi > 0$ while $c_{phs} = -v_A \cos\phi$ for $\cos\phi < 0$, and for this mode it is convenient to write the general expressions (2.12) and (2.13) as

$$\frac{\omega}{\kappa} = (U \pm v_A)\cos\phi, \qquad \frac{\omega}{k} = U \pm v_A \tag{2.21}$$

where for $\cos\phi < 0$ the plus (minus) sign in (2.12) and (2.13) corresponds to the minus (plus) sign in (2.21). Then for the Alfvén mode, the two solutions for any value of $U\cos\phi$ are given by the plus and minus sign respectively in (2.21), and the critical flow speed given by (2.17) is independent of propagation angle. Wherever $U < v_A$ (corresponding to $M < 1$ in Figure 2.1) we obtain oppositely propagating Alfvén waves: the wave propagating with the flow (given by the plus sign if $U > 0$) does so with a field aligned phase velocity of magnitude greater than v_A; while that of the oppositely propagating wave is reduced, so that it becomes stationary (in the given reference frame) when $|U| = v_A$, then reverses propagation direction when $|U| > v_A$ ($M > 1$ in Figure 2.1).

Hence, when the magnitude of the flow speed exceeds the Alfvén speed, the Alfvén mode cannot propagate (at any angle) against the flow. This is due to the strong anisotropy of the Alfvén mode, for which c_{phs} takes its greatest value (v_A) for parallel propagation, which is also the direction in which the flow has its greatest effect, vanishing for perpendicular propagation. This is similarly the case for the slow magnetoacoustic mode, which cannot propagate (at any angle) against the flow when $|U| > \min(c_s, v_A)$ (i.e. $M > 0.4$ in Figure 2.2). The fast mode, however, is almost isotropic in a static medium, and reversal only occurs for propagation vectors within some cone about the flow direction, for $|U| > \max(c_s, v_A)$ ($M > 1$ in Figure 2.2), by analogy with a duck swimming at an angle to the flow in order to improve its progress upstream.

These analogies allow us to identify some of the basic effects of flows on the stable modes of propagation. Any flow relative to the observer introduces a shift in the perceived propagation speeds, the magnitude of this shift being determined by the observer's frame

of reference. Just like if you are sitting on board or travelling at the same speed as the fire engine you notice no change in pitch, we can eliminate the Doppler shift if we choose a reference frame which is moving with the flow. Then we recover the static case, obtaining an identical phase diagram with the phase speed now being given by Ω/κ rather than ω/κ. However, just like a duck may not notice any difficulty swimming upstream in the absence of landmarks against which to measure progress, the shift in propagation speed for MHD modes only becomes important in structured flows.

Kelvin-Helmholtz instability

It is well known that the presence of structured flows may lead to the Kelvin-Helmholtz instability (Chandrasekhar 1961, Gerwin 1968).

The classical Kelvin-Helmholtz instability arises when an inviscid, incompressible fluid flows at a speed U over a heavier fluid a rest. With gravity directed perpendicular to the interface, let the suffices 0 and e denote the lower and upper fluids respectively, with $\rho_0 > \rho_e$ so that in the absence of relative flows the interface is Rayleigh-Taylor stable. Take disturbances directed along the interface with wavenumber k. Define $\alpha_0 = \rho_0/(\rho_0 + \rho_e)$, $\alpha_e = \rho_e/(\rho_0 + \rho_e)$.

Where gravity alone is included, the interface is unstable for any flow speed U, and affects modes with sufficiently short wavelengths, that is for (Chandrasekhar 1961)

$$k > k_{min} = \frac{g(\alpha_0 - \alpha_e)}{\alpha_0 \alpha_e U^2}, \tag{2.22}$$

as found by Helmholtz.

The presence of surface tension may suppress the instability: the condition for the instability to be suppressed by surface tension $\mathcal{T}$ is (Chandrasekhar 1961)

$$U^2 < \frac{g}{\alpha_0 \alpha_e} \left\{ \frac{\alpha_0 - \alpha_e}{k} + \frac{k\mathcal{T}}{g(\rho_0 + \rho_e)} \right\}, \tag{2.23}$$

the right-handside of which has a minimum at the critical wavenumber k^* satisfying $k^{*2} = (\rho_0 - \rho_e)g/\mathcal{T}$, for which (2.23) reduces to the result due to Kelvin,

$$U^2 < \frac{2}{\alpha_0 \alpha_e} \sqrt{\frac{\mathcal{T} g(\alpha_0 - \alpha_e)}{\rho_0 + \rho_e}}. \tag{2.24}$$

Note that the instability is suppressed only if *both* effects are present.

The Kelvin-Helmholtz instability may also be stabilised by magnetic fields, the effect of which depends on their orientation relative to the flow direction, which we take to be parallel. Neglecting gravity and surface tension in the above model, and considering a magnetic field of strength B_0 and B_e in regions 0 and e respectively, the condition for suppression of the Kelvin-Helmholtz instability is (Chandrasekhar 1961, Gerwin 1968)

$$U^2 \leq \frac{({B_0}^2 + {B_e}^2)}{\mu\rho_0\rho_e}\,(\rho_0 + \rho_e)\,. \tag{2.25}$$

The stabilising effect of the magnetic field is due to the magnetic tension, which enables the existence of stable surface waves in the presence of structured flows. Such surface waves represent modifications to those existing in a static medium, and become *overstable oscillations* for sufficiently large relative flows, due to the Kelvin-Helmholtz instability.

It is our interest to investigate the stable modes existing in the presence of relative flows, as modifications to those existing for the static case, and to consider the effects of dispersion and plasma inhomogeneity on the flow threshold for the occurrence of the Kelvin-Helmholtz instability in discretely structured media.

Negative energy waves

We noted above that if the magnitude of the flow exceeds the basic propagation speed then the mode will appear to reverse direction of propagation, although we can always get rid of this effect by changing the frame of reference so as to be moving with the flow. Such modes are termed *backward* waves and have been studied in a solar MHD context by Nakariakov and Roberts (1995b), Nakariakov, Roberts and Mann (1996) and Joarder, Nakariakov and Roberts (1997a). A mode that is travelling in the "wrong" direction in this way will have negative inertia in the given frame of reference, and as such are termed *negative energy waves*. Fejer (1963) discussed such waves in the context of reflection and refraction of MHD waves at an interface in relative motion: it was shown that acoustic waves transmitted across an interface into a medium moving at supersonic velocity may appear to carry a deficiency of energy with it, since the reflected wave carries more energy than the incident wave. Negative energy waves were first discussed in a solar context by Ryutova (1988).

The presence of negative energy waves can have some important implications for stability, as noted by Cairns (1979). The best known example is the Kelvin-Helmholtz instability, which is a linear instability due to the interaction between a positive energy mode and a negative energy mode. There are other less well known instabilities associated with negative energy waves. In nonideal MHD we have dissipative instabilities which occur for smaller relative flows than for the Kelvin-Helmholtz instability. For static equilibria the inclusion of dissipative terms causes disturbances to be damped, and the same is true for positive energy waves for steady flow stationary states. However, for negative energy waves, the opposite is true in that the dissipation acts to amplify the disturbance, leading to instability. The only requirement on the relative flow for this to occur is that it exceed the basic propagation speed in the given reference frame. This is a less strict criterion than for the Kelvin-Helmholtz instability. This dissipative instability has been studied in the solar MHD context by Joarder et al. (1997a). Finally, we note that a further instability associated with negative energy waves is the explosive instability. It is caused by the nonlinear interaction of three waves having a mixture of positive and negative energies (Cairns 1979).

2.2 Derivations of dispersion relations

Having presented some of the basic ideas associated with flow effects in general, we now derive the dispersion relations for the single interface, uniform slab and uniform cylinder; for the configurations, see Figure 2.3.

For the single interface case, in cartesian geometry, there is a tangential discontinuity at $x = 0$, with the stationary state given by

$$\rho,\ p,\ T,\ \mathbf{B},\ \mathbf{v} = \begin{cases} \rho_0,\ p_0,\ T_0, B_0\hat{\mathbf{z}},\ v_0\hat{\mathbf{z}}, & x < 0 \\ \rho_e,\ p_e,\ T_e, B_e\hat{\mathbf{z}},\ v_e\hat{\mathbf{z}}, & x > 0. \end{cases} \tag{2.26}$$

For the uniform slab case, there are tangential discontinuities at $x = \pm a$, with the stationary state given by

$$\rho,\ p,\ T,\ \mathbf{B},\ \mathbf{v} = \begin{cases} \rho_0,\ p_0,\ T_0, B_0\hat{\mathbf{z}},\ v_0\hat{\mathbf{z}}, & |x| < a \\ \rho_e,\ p_e,\ T_e, B_e\hat{\mathbf{z}},\ v_e\hat{\mathbf{z}}, & |x| > a. \end{cases} \tag{2.27}$$

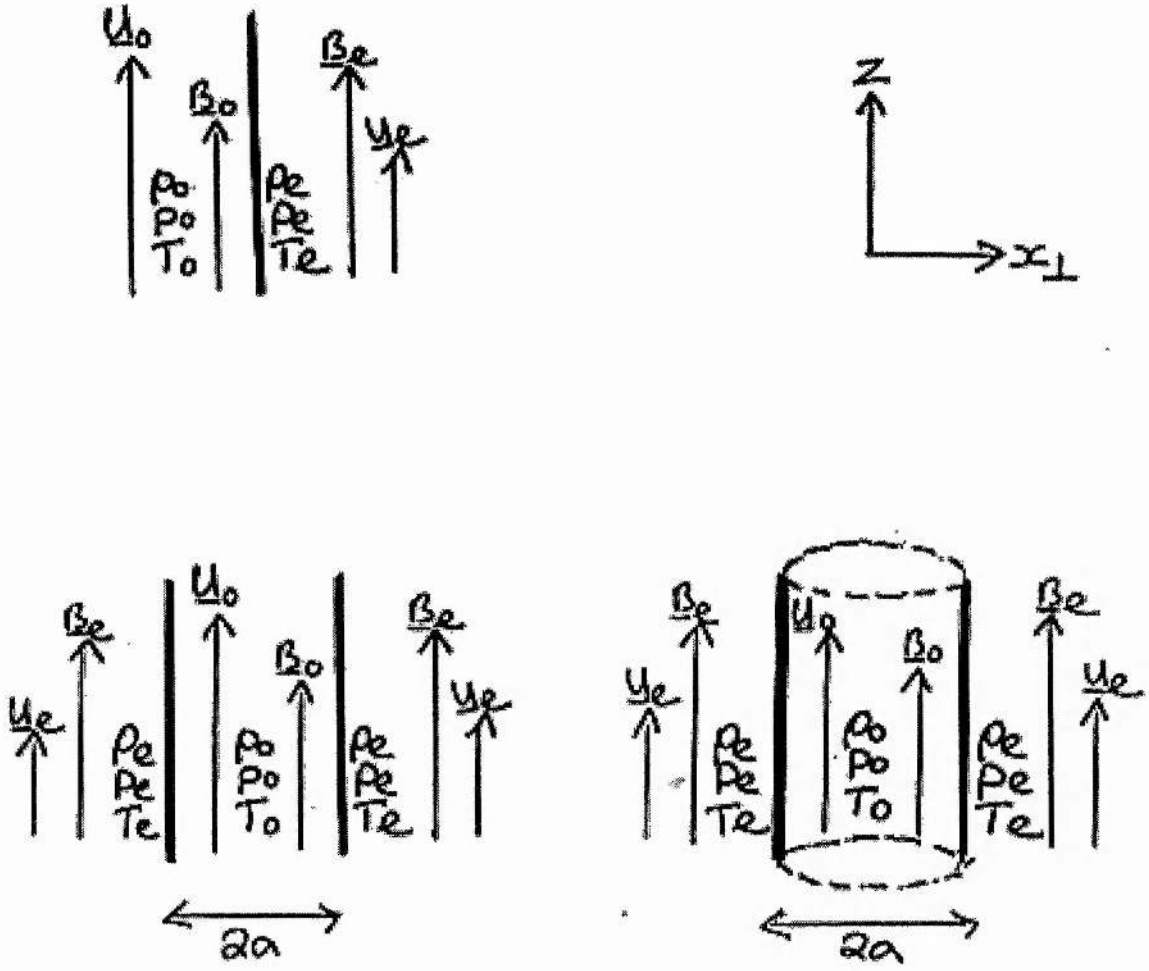

Figure 2.3: Sketches of the steady state configurations for the single interface (top left , see (2.26)), uniform slab (bottom left, see (2.27)) and uniform cylinder (bottom right, see (2.28)). Magnetic field and steady flow are parallel to the z-axis, with discrete structuring in the direction of the transverse coordinate $x_\perp$, where $x_\perp = x$ for cartesian geometry, $x_\perp = r$ in cylindrical geometry.

For the uniform cylinder case, in cylindrical geometry, there is a tangential discontinuity at $r = a$, with the stationary state by

$$\rho,\ p,\ T,\ \mathbf{B},\ \mathbf{v} = \begin{cases} \rho_0,\ p_0,\ T_0, B_0\hat{\mathbf{z}},\ v_0\hat{\mathbf{z}}, & r < a \\ \rho_e,\ p_e,\ T_e, B_e\hat{\mathbf{z}},\ v_e\hat{\mathbf{z}}, & r > a. \end{cases} \tag{2.28}$$

In each of cases (2.26)–(2.28) the stationary state equation (1.19) reduces to the pressure balance

$$p_0 + \frac{{B_0}^2}{2\mu} = p_e + \frac{{B_e}^2}{2\mu}. \tag{2.29}$$

Equation (2.29) implies that

$$\frac{\rho_e}{\rho_0} = \frac{{c_{s0}}^2 + \frac{\gamma}{2}{v_{A0}}^2}{{c_{se}}^2 + \frac{\gamma}{2}{v_{Ae}}^2} \tag{2.30}$$

where we have used ${c_{s0}}^2 = \gamma p_0/\rho_0$, ${v_{A0}}^2 = {B_0}^2/(\mu\rho_0)$, ${c_{se}}^2 = \gamma p_e/\rho_e$ and ${v_{Ae}}^2 = {B_e}^2/(\mu\rho_e)$.

2.2.1 Derivation of governing equations

For the uniform stationary state,

$$\rho = \rho_0, \quad p = p_0, \quad T = T_0, \quad \mathbf{B} = \mathbf{B}_0, \quad \mathbf{v} = \mathbf{v}_0 \tag{2.31}$$

with all parameters constant, the linearised MHD equations (1.25)–(1.28) yield

$$\left(\frac{\partial}{\partial t} + \mathbf{v}_0 \cdot \nabla\right)\rho_1 = -\rho_0\,(\nabla\cdot\mathbf{v}_1) \tag{2.32}$$

$$\left(\frac{\partial}{\partial t} + \mathbf{v}_0 \cdot \nabla\right)p_1 = -c_s^2\rho_0\,(\nabla\cdot\mathbf{v}_1) \tag{2.33}$$

$$\left(\frac{\partial}{\partial t} + \mathbf{v}_0 \cdot \nabla\right)\mathbf{B}_1 = -\mathbf{B}_0\,(\nabla\cdot\mathbf{v}_1) + (\mathbf{B}_0 \cdot \nabla)\,\mathbf{v}_1 \tag{2.34}$$

$$\rho_0\left(\frac{\partial}{\partial t} + \mathbf{v}_0 \cdot \nabla\right)\mathbf{v}_1 = -\nabla p_T + (\mathbf{B}_0 \cdot \nabla)\,\frac{\mathbf{B}_1}{\mu} \tag{2.35}$$

where

$$p_T = p_0 + \frac{\mathbf{B}_0 \cdot \mathbf{B}_1}{\mu} \tag{2.36}$$

The linearised MHD equations in the form (2.32)-(2.36) apply to any coordinate system, and the unperturbed velocity $\mathbf{v}_0$ and magnetic field $\mathbf{B}_0$ may have up to 3 components, all of which are constants. For our chosen stationary state configurations we restrict attention to the case

$$\mathbf{v}_0 = v_0\hat{\mathbf{z}}, \qquad \mathbf{B}_0 = B_0\hat{\mathbf{z}} \tag{2.37}$$

which is applicable to both cartesian and cylindrical geometry. Then given (2.37) we have, for both geometries,

$$\left.\begin{aligned} (\mathbf{v}_0 \cdot \nabla)(\alpha \mathbf{A}) &= \alpha v_0 \tfrac{\partial \mathbf{A}}{\partial z} \\ (\mathbf{v}_0 \cdot \nabla)(\nabla \alpha) &= \nabla\left((\mathbf{v}_0 \cdot \nabla)\alpha\right) \\ (\mathbf{v}_0 \cdot \nabla)[(\mathbf{B}_0 \cdot \nabla)\mathbf{A}] &= (\mathbf{B}_0 \cdot \nabla)[(\mathbf{v}_0 \cdot \nabla)\mathbf{A}] \end{aligned}\right\} \tag{2.38}$$

for any uniform scalar α and any vector $\mathbf{A}$.

Taking $(\partial/\partial t + \mathbf{v}_0 \cdot \nabla)$ of Equation (2.35), and using (2.32)-(2.35) together with (2.38), we obtain

$$\rho_0 \left[\left(\frac{\partial}{\partial t} + \mathbf{v}_0 \cdot \nabla\right)^2 - {v_A}^2 \frac{\partial^2}{\partial t^2}\right] \mathbf{v}_1 = -\nabla\left(\frac{\partial}{\partial t} + \mathbf{v}_0 \cdot \nabla\right) p_T - \rho_0 {v_A}^2 \frac{\partial \Delta}{\partial z}\hat{\mathbf{z}} \tag{2.39}$$

where

$$\left(\frac{\partial}{\partial t} + \mathbf{v}_0 \cdot \nabla\right) p_T = -\rho_0 \left[({c_s}^2 + {v_A}^2)\Delta - {v_A}^2 \Gamma\right] \tag{2.40}$$

and, given our restriction to the case (2.37), we have

$$\mathbf{v}_0 \cdot \nabla \equiv v_0 \frac{\partial}{\partial z} \tag{2.41}$$

Here we have have introduced (Lighthill 1960)

$$\Delta = \nabla \cdot \mathbf{v}_1, \qquad \Gamma = \frac{\partial v_z}{\partial z} \tag{2.42}$$

where v_z is the z-component of the perturbed velocity $\mathbf{v}_1$.

We note that the steady flow enters (2.39) only in the combination $\partial/\partial t + v_0 \partial/\partial z$. This makes it of identical form to its equivalent for the static case (see Roberts 1981a), but with

$$\frac{\partial}{\partial t} \quad \text{replaced by} \quad \left(\frac{\partial}{\partial t} + v_0 \frac{\partial}{\partial z}\right). \tag{2.43}$$

and indeed the same can be said about the linearised equations (2.32)-(2.35). Then the static case is recovered not only by setting $\mathbf{v}_0 = 0$ but also by choosing a reference frame which is moving with the flow, indicating that the basic effect of a uniform flow is to introduce a Doppler shift in frequencies, which is removed in a reference frame moving with the flow.

Equation (2.39) is applicable to uniform (discretely structured) media in both cartesian and cylindrical geometry for flows and magnetic field in the z-direction. Taking the discrete

structuring to be in a direction (the x-direction for cartesian, the r-direction for cylindrical) transverse to the magnetic field and flow we may Fourier analyse all perturbations ψ in time and in all other spatial directions: as

$$\psi = \hat{\psi}(x)e^{i(\omega t - ly - kz)} \tag{2.44}$$

for the cartesian case or

$$\psi = \hat{\psi}(r)e^{i(\omega t - n\theta - kz)} \tag{2.45}$$

for the cylindrical case. The Fourier forms of equations (2.39)-(2.42) may be combined (see Appendix) into a single ordinary differential equation in $\hat{p}_T$, the amplitude of the total pressure perturbation. Equivalent equations derived with an allowance for continuous transverse structuring (Roberts 1981a) reduce to those given below when the structuring is taken to be discrete.

For cartesian geometry we obtain (see (A.63))

$$\frac{d^2\hat{p}_T}{dx^2} - \left(m^2 + l^2\right)\hat{p}_T = 0 \tag{2.46}$$

where

$$m^2 = \frac{(k^2v_A^2 - \Omega^2)(\Omega^2 - k^2c_s^2)}{(c_s^2 + v_A^2)(\Omega^2 - k^2c_T^2)}. \tag{2.47}$$

Equation (2.46) is also satisfied by $\hat{\Delta}$. Equation (2.46) is given by Hardee (1995); the same equation is satisfied (for magnetoacoustic modes) by $\hat{v}_x$ (Nakariakov and Roberts 1995a). A similar equation is obtained for the static case by Roberts (1981a), but here we have ω replaced by $\Omega = \omega - v_0k$ in our expression for m^2. Our equations reduce to those of Roberts (1981a) for the special case of no equilibrium flow $v_0 = 0$. For an infinite uniform medium we may Fourier analyse in the x direction to recover the magnetoacoustic dispersion relation (2.1) (with ω replaced by Ω), with Alfvén modes being given here by $\hat{p}_T = 0$.

For cylindrical geometry $\hat{p}_T$ satisfies Bessel's equation (see (A.86))

$$\frac{d^2\hat{p}_T}{dr^2} + \frac{1}{r}\frac{d\hat{p}_T}{dr} - \left(m^2 + \frac{n^2}{r^2}\right)\hat{p}_T = 0 \tag{2.48}$$

where, as for the cartesian case,

$$m^2 = \frac{(k^2v_A^2 - \Omega^2)(\Omega^2 - k^2c_s^2)}{(c_s^2 + v_A^2)(\Omega^2 - k^2c_T^2)}. \tag{2.49}$$

Equation (2.48) is also satisfied by $\hat{\Delta}$, and was obtained for the static case (with ω replaced here by Ω) by Edwin and Roberts (1983), see also Roberts and Webb (1978). The case $\hat{p}_T = 0$ yields torsional Alfvén waves.

In each case the other perturbations can be expressed in terms of $\hat{p}_T$. The relevant expressions are given in the Appendix. In particular, if we denote by $\hat{v}_\perp$ the amplitude of the perturbation of transverse velocity, then for each geometry the relation between $\hat{v}_\perp$ ($=\hat{v}_x$ for cartesian, $\hat{v}_r$ for cylindrical) and $\hat{p}_T$ is (see equations (A.66) and (A.87))

$$\hat{v}_\perp = \frac{-i\Omega}{\rho_0(k^2 {v_A}^2 - \Omega^2)} \frac{d\hat{p}_T}{dx_\perp} \tag{2.50}$$

where transverse coordinate $x_\perp$ is x for cartesian, r for cylindrical.

2.2.2 General form of the dispersion relation

Equations (2.46) and (2.48) were derived under the assumption of a uniform stationary state, with magnetic field and steady flow in the z-direction. For discretely structured media, with tangential discontinuities between uniform regions of differing physical properties, equations (2.46) and (2.48) may be applied to each region separately, with the form of m^2 taken as appropriate to the physical conditions. The general solution for each region contains two arbitrary constants. The dispersion relation is found by applying boundary conditions in order to link the solutions and eliminate the arbitrary constants. We apply jump conditions at the interface, together with requirements on the physical behaviour of solutions at large distance from the inhomogeneity. For the finite-width inhomogeneities (slab and cylinder) we further consider behaviour at the axis of symmetry.

In cartesian geometry, two types of inhomogeneity are the single interface and the uniform slab, both of which have applications in the solar atmosphere and the magnetosphere. In cylindrical geometry we study the uniform cylinder, which for some applications, such as photospheric flux tubes and coronal loops, may be more appropriate than cartesian models. The steady state configurations chosen allow us to apply a general treatment, applicable to all three cases, with the solution $\hat{p}_T$ to be specified. Then for each case the dispersion relation follows immediately once a suitable form of $\hat{p}_T$ is chosen for each region.

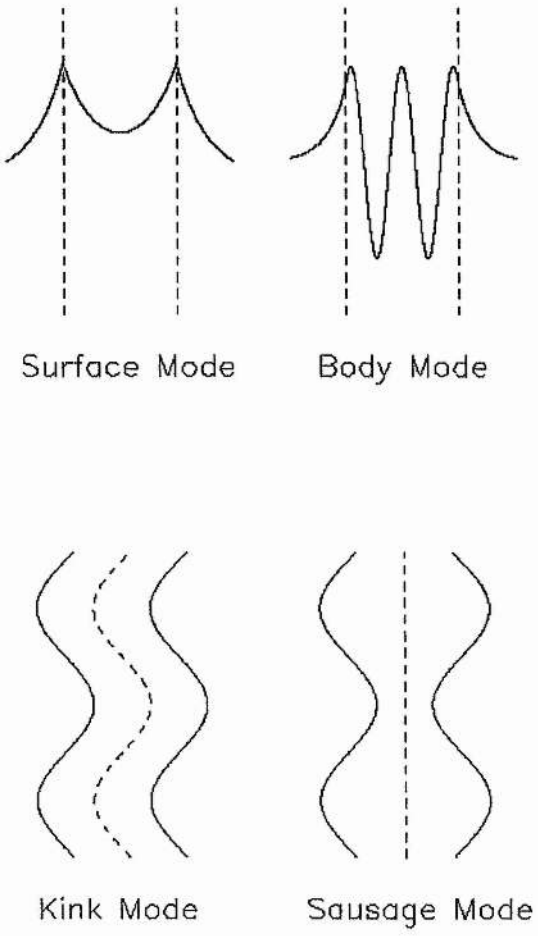

Figure 2.4: Sketches of the transverse behaviour of surface and body modes, and kink and sausage modes (after Roberts and Ulmschneider (1997), this reproduction courtesy of K. J. Mills).

In our general treatment we assume that for each region the solution for $\hat{p}_T$ contains only one arbitrary constant, the other independent solution having been eliminated. For the single interface there are two semi-infinite regions, while for both the slab and the cylinder there is additionally a central region of finite width. On physical grounds we can eliminate solutions for the semi-infinite regions which are either oscillatory or unbounded as $x_\perp \to \infty$. For the finite width regions, having eliminated solutions which are not well behaved at $x_\perp = 0$, we allow two classes of solutions: those which are oscillatory (*body modes*) and those which are evanescent (*surface modes*) away from the interface (this behaviour being for real values of ω). For each mode class, there are two independent solutions: those which are asymmetric and disturb the centre of the inhomogeneity (*kink modes*), and those which are symmetric and leave the centre undisturbed (*sausage modes*). The transverse behaviour for each mode type is illustrated in Figure 2.4. For symmetric configurations we may treat the sausage and kink solutions separately. Further, while for the uniform slab there are *two* interfaces at different values of $x_\perp$, for a symmetric configuration it is sufficient for the purposes of deriving the dispersion relation to consider only $x_\perp > 0$. The transverse behaviour for each mode type is illustrated in Figure 2.4.

These points allow us to present a general dispersion relation derivation, where the boundary conditions are applied at a single interface $x_\perp = a$ and the solution for each side of the interface contains only one arbitrary constant, the other having been eliminated by use of other boundary conditions. Then for each geometry (single interface, slab, cylinder) we will specify the appropriate solutions for each mode class (surface or body) and type (sausage or kink), where appropriate, and hence immediately obtain the dispersion relation for the given mode. This general treatment allows us to compare and contrast the different modes for the different geometries, see Section 2.3.

Boundary conditions at the interface

Consider the boundary conditions to be applied at the interface, given by $x_\perp = a$ where $x_\perp$ is the appropriate transverse coordinate (x for cartesian, r for cylindrical).

Appropriate conditions are continuity of the displaced boundary and continuity of the total pressure perturbation (see the discussion in Campos (1987)). The condition of continuity of the displaced boundary is equivalent to continuity of the transverse displacement

$\xi(\mathbf{r},t)$ at the boundary. Strictly, the boundary conditions ought to be applied across the *displaced* boundary, but for *linear* displacements the boundary conditions may be applied at the unperturbed boundary position, $x_\perp = a$ (Nakariakov and Roberts 1995a).

Now the transverse displacement ξ may be expressed in terms of the transverse velocity $v_\perp$ ($= v_x$ for cartesian case, v_r for cylindrical case) using

$$v_\perp = \frac{d\xi}{dt} = \frac{\partial \xi}{\partial t} + v_0 \frac{\partial \xi}{\partial z}. \tag{2.51}$$

Hence the transverse velocity reflects displacements due not only to the disturbance but also to the steady flow.

If both $v_\perp$ and ξ take the appropriate Fourier form (given by (A.51) for the cartesian case, and (A.79) for the cylindrical case) then this yields

$$\hat{\xi} = \frac{\hat{v}_\perp}{i\Omega} = \frac{-1}{\rho_0(k^2 {v_A}^2 - \Omega^2)} \frac{d\hat{p}_T}{dx_\perp} \tag{2.52}$$

where we have substituted for $\hat{v}_\perp$ using Equations (A.66) and (A.87). We note that for the static case the boundary condition usually quoted is continuity of the velocity $\hat{v}_\perp$, whereas here we have continuity of the displacement $\hat{\xi}$. For the static case these two conditions are equivalent, since the factor $i\omega$ is constant. However, in the presence of relative flows it is strictly the continuity of $\hat{\xi}$ that must be applied, since $\hat{v}_\perp$ is in fact discontinuous due to the discontinuity in Ω. While Mann et al. (1992) applied continuity of the velocity rather than the displacement, this error was corrected in Nakariakov et al. (1996).

Hence, in mathematical terms, for an interface at $x_\perp = a$, the boundary conditions that we apply on our solutions for $\hat{p}_T$ are

1. continuity of $\frac{1}{\varepsilon}\frac{d\hat{p}_T}{dx_\perp}$ across $x_\perp = a$
2. continuity of $\hat{p}_T$ across $x_\perp = a$

where

$$\varepsilon = \rho_0(k^2 {v_A}^2 - \Omega^2) \tag{2.53}$$

and the transverse coordinate $x_\perp$ is x for the cartesian case and r for the cylindrical case. We note that our derivation of the governing ordinary differential equation ((2.46) or (2.48)) requires that $\varepsilon \neq 0$.

General dispersion relation

Say our solutions to either side of the interface at $x_\perp$ are

$$\hat{p}_T(x_\perp) = \begin{cases} C_0 \hat{p}_{T0}(x_\perp), & x_\perp < a \\ C_e \hat{p}_{Te}(x_\perp), & x_\perp > a \end{cases} \tag{2.54}$$

where C_0, C_e are arbitrary constants and each of $\hat{p}_{T0}(x_\perp)$, $\hat{p}_{Te}(x_\perp)$ are one of a given pair of linearly independent solutions to either (2.46) or (2.48) as appropriate, the other having been eliminated on physical grounds or on the basis of symmetry (see Sections 2.2.3 and 2.2.4 below).

The boundary conditions at the interface may be represented by the matrix equation

$$\begin{pmatrix} \hat{p}_{T0} & \hat{p}_{Te} \\ \frac{1}{\varepsilon_0}\frac{d\hat{p}_{T0}}{dx_\perp} & \frac{1}{\varepsilon_e}\frac{d\hat{p}_{Te}}{dx_\perp} \end{pmatrix} \begin{pmatrix} C_0 \\ -C_e \end{pmatrix} = 0 \tag{2.55}$$

with $\hat{p}_{Ti}$, $d\hat{p}_{Ti}/dx_\perp$ evaluated at $x_\perp = a$.

For a nontrivial solution the determinant must be zero, which yields the *general dispersion relation*

$$\frac{\varepsilon_e}{\varepsilon_0} = \frac{\hat{p}_{T0}}{d\hat{p}_{T0}/dx_\perp} \frac{d\hat{p}_{Te}/dx_\perp}{\hat{p}_{Te}} \tag{2.56}$$

with all expressions being evaluated at $x_\perp = a$. Equation 2.56 is the general dispersion relation applicable to all three geometries under consideration. We determine the form appropriate to particular geometries and mode types by choosing appropriate forms for the functions $\hat{p}_{T0}(x)$ and $\hat{p}_{Te}(x)$ in our solution (2.54) for the amplitude of the total pressure perturbation, $\hat{p}_T(x)$.

2.2.3 Dispersion relations for cartesian geometry

Solutions to the ordinary differential equation

Recall that all linear perturbations may be expressed in terms of $\hat{p}_T$, where $\hat{p}_T$ satisfies the second order ordinary differential equation (2.46).

We must determine appropriate choices for $\hat{p}_{Ti}(x)$ to either side of the interface at $x = a$ for each case. We will confine discussion here to modes with $l = 0$, for which the governing equation reduces to (Nakariakov and Roberts 1995a, Mann, Marsch and

Roberts 1992)

$$\frac{d^2\hat{p}_{Ti}}{dx^2} - m_i^2\hat{p}_{Ti} = 0 \tag{2.57}$$

where

$$m_i^2 = \frac{(k^2v_{Ai}^2 - \Omega_i^2)(\Omega_i^2 - k^2c_{si}^2)}{(c_{si}^2 + v_{Ai}^2)(\Omega_i^2 - k^2c_{Ti}^2)} \tag{2.58}$$

and the subscript i indicates the region under consideration, with $i = 0$, $x < a$ and $i = e$, $x > a$. The general solution of (2.57) is

$$\hat{p}_{Ti} = C_ie^{-m_ix} + D_ie^{m_ix} \tag{2.59}$$

where C_i, D_i are arbitrary constants and m_i and ${m_i}^2$ may be complex for complex ω.

For stable solutions we have ω real, hence ${m_i}^2$ real, and the general solution may be written in terms of real variables as

$$\hat{p}_{Ti} = \begin{cases} C_i\cosh(m_ix) + D_i\sinh(m_ix), & m_i^2 > 0 \\ C_i\cos(n_ix) + D_i\sin(n_ix), & n_i^2 = -m_i^2 > 0 \end{cases} \tag{2.60}$$

where the form taken assures real variables. For stable modes, the sign of ${m_i}^2$ determines whether the solution is evanescent (${m_i}^2 > 0$) away from the interface or oscillatory (${m_i}^2 < 0$) within the given region.

The general solution of (2.57) contains two arbitrary constants. However, by physical considerations and symmetry, we may reduce the problem to consideration of only one of the two linearly independent solutions in each region. The form of solution we will use depends on the properties of and required behaviour within the given region.

We will consider separately the specific cases of the single interface and the uniform slab (double interface). For both cases we will find that by requirements at $x = 0$ and as $|x| \to \infty$ we need only consider solutions with one arbitrary constant.

Dispersion relation for single interface

Consider the case of a single interface at $x = a$, separating two unequal uniform media, each with a uniform flow and magnetic field in the z-direction. For simplicity we may take $a = 0$, so that the interface is along the z-axis. We wish to investigate modes which arise due to the presence of the interface. We therefore impose the conditions that $\hat{v}_x \to 0$ as $|x| \to \infty$ in order to give decreasing amplitudes away from the interface. In this way the

mode is confined to the vicinity of the interface, and is analogous to a wave propagating along the surface of a lake. Hence the term "surface wave".

Hence we choose solutions in the form $\hat{p}_{T0}(x) = e^{m_0 x}$, $\hat{p}_{Te}(x) = e^{-m_e x}$ where Real $(m_0) > 0$ and Real $(m_e) > 0$, so that the disturbance decays in amplitude away from the interface. Then we may write the dispersion relation as

$$\frac{\rho_e \left(k^2 v_{Ae}^2 - \Omega_e^2\right)}{\rho_0 \left(k^2 v_{A0}^2 - \Omega_0^2\right)} = -\frac{m_e}{m_0}, \tag{2.61}$$

with the density ratio ρ_e/ρ_0 given by the pressure balance condition (2.30). Dispersion relation (2.61) has appeared in the literature in various forms for the static case (Wentzel 1979, Roberts 1981a, Somasundaram and Uberoi 1982, Jain and Roberts 1991) and with flows (Parker 1964, Singh and Talwar 1994).

Dispersion relations for uniform slab

Now consider the case of a uniform slab embedded within a uniform environment. This time there are two interfaces, at $x = \pm a$. We therefore have three uniform regions, each with equilibrium flow and magnetic field in the z-direction, but we take the regions $x > a$ and $x < -a$ to have identical properties. The symmetry of this configuration means that we need consider only $x > 0$, applying boundary conditions at one interface ($x = a$) only.

Again we are primarily interested in modes which are associated with the slab itself. In order to confine the disturbance to the vicinity of the slab, we again impose $\hat{p}_T \to 0$ as $|x| \to \infty$ so that the amplitudes decrease away from the interface. We therefore choose the exponential from of the solutions for the outer regions, and for $x > a$ we have $\hat{p}_{Te}(x) = e^{-m_e(x-a)}$ with Real $(m_e) > 0$.

For the region between the interfaces our requirement is that the solution remain bounded within $|x| < a$. We obtain two classes of solutions, according to the sign of m_0^2.

The case $m_0^2 > 0$ gives evanescent behaviour away from the interface, and we may use either the exponential form or the hyperbolic form of the solutions. We choose to use the hyperbolic form so that we may consider odd and even solutions separately. We obtain $\hat{p}_{T0}(x) = \sinh(m_0 x)$ for the kink modes, giving dispersion relation

$$\frac{\rho_e \left(k^2 v_{Ae}^2 - \Omega_e^2\right)}{\rho_0 \left(k^2 v_{A0}^2 - \Omega_0^2\right)} = -\frac{m_e}{m_0} \tanh(m_0 a) \tag{2.62}$$

with the density ratio ρ_e/ρ_0 given by the pressure balance condition (2.30). For the sausage modes the appropriate solution is $\hat{p}_{T0}(x) = \cosh(m_0 x)$ giving dispersion relation

$$\frac{\rho_e\left(k^2 v_{Ae}^2 - \Omega_e^2\right)}{\rho_0\left(k^2 v_{A0}^2 - \Omega_0^2\right)} = -\frac{m_e}{m_0}\coth(m_0 a), \tag{2.63}$$

again with ρ_e/ρ_0 given by (2.30).

The case ${m_0}^2 > 0$ yields a surface mode, propagating along both interfaces and being primarily confined to the vicinity of each interface. It is analogous to the surface modes of a single interface, although modes with wavelengths large enough to notice both interfaces will have modified properties compared to those of a single interface. Modes of different wavelengths will be affected to different extents. As a result the waves become *dispersive*, with phase speeds dependent on wavelength. However, short wavelength modes will not be significantly affected by both interfaces and we therefore expect to recover the single interface in this case.

An alternative to surface modes is to have oscillatory behaviour within $|x| < a$. This corresponds to the case $m_0^2 = -n_0^2 < 0$ where we use the sine and cosine functions with argument $n_0 a > 0$. These modes are analogous to those of an infinite uniform medium, and represent their modification when the mode is affected by a lengthscale. As for the surface modes, this lengthscale introduces dispersion. However the difference between these modes and the surface modes is that they are oscillatory within the body of the slab, hence the term *body modes*, and have different phase speed ranges (see Section 2.3 below for further discussion of body modes).

We may consider two type of body modes according to their symmetry properties. For kink modes we choose $\hat{p}_{T0}(x) = \sin(n_0 x)$ giving dispersion relation

$$\frac{\rho_e\left(k^2 v_{Ae}^2 - \Omega_e^2\right)}{\rho_0\left(k^2 v_{A0}^2 - \Omega_0^2\right)} = -\frac{m_e}{n_0}\tan(n_0 a) \tag{2.64}$$

while for the sausage modes the choice $\hat{p}_{T0}(x) = \cos(n_0 x)$ yields dispersion relation

$$\frac{\rho_e\left(k^2 v_{Ae}^2 - \Omega_e^2\right)}{\rho_0\left(k^2 v_{A0}^2 - \Omega_0^2\right)} = \frac{m_e}{n_0}\cot(n_0 a). \tag{2.65}$$

In each of (2.64) and (2.65) the density ratio ρ_e/ρ_0 is given by the pressure balance condition (2.30).

Dispersion relations (2.62)-(2.65) have appeared in the literature in various forms for the static case (Roberts 1981b, Edwin and Roberts 1983, Singh and Talwar 1993) and with

flows (Satya Narayanan and Somasundaram 1985, Singh and Talwar 1994, Nakariakov and Roberts 1995a, Nakariakov, Roberts and Mann 1996, Joarder, Nakariakov and Roberts 1997b).

The above mode classification is based on the assumption that m^2 is real. For the static case, this is a valid assumption as only stable modes ($\omega^2 > 0$, that is ω real) exist (Roberts 1981a, Edwin and Roberts 1982). However, with the inclusion of flows there is a possibility that ω may be complex, leading to complex m^2 and m. Then for solutions to be bounded as $|x| \to \infty$ we require Real $(m_e) > 0$ (Singh and Talwar 1994), while we classify the modes as surface or body according to their properties in the static case.

2.2.4 Dispersion relations for cylindrical geometry

Solutions to the ordinary differential equation

Recall that all linear perturbations may be expressed in terms of $\hat{p}_T$, where $\hat{p}_T$ satisfies the second order ordinary differential equation (2.48), which to recap is

$$\frac{d^2\hat{p}_{Ti}}{dr^2} + \frac{1}{r}\frac{d\hat{p}_{Ti}}{dr} - \left(m_i^2 + \frac{n^2}{r^2}\right)\hat{p}_{Ti} = 0 \tag{2.66}$$

where ${m_i}^2$ is defined by (2.58) and the subscript i indicates the region under consideration, with $i = 0$, $r < a$ and $i = e$, $r > a$.

We must determine appropriate choices for $\hat{p}_{Ti}(r)$ to either side of the interface at $r = a$ for each case. For stable solutions we have ω real, hence ${m_i}^2$ real, and the general solution may be written in terms of real variables as (Abramowitz and Stegun 1965)

$$\hat{p}_{Ti} = \begin{cases} C_i I_n(m_i r) + D_i K_n(m_i r), & m_i^2 > 0 \\ C_i J_n(n_i r) + D_i Y_n(n_i r), & n_i^2 = -m_i^2 > 0 \end{cases} \tag{2.67}$$

where the form taken ensures real variables in the Bessel functions J_n and Y_n and the modified Bessel functions I_n and K_n (Abramowitz and Stegun 1965), and C_i, D_i are arbitrary constants. In Figure 2.5 we show these Bessel functions (for real arguments) for $n = 0$ and 1. The Bessel functions may be thought of as the cylindrical counterparts of the sine and cosine functions arising for cartesian geometry, meanwhile the modified Bessel functions relate to the exponential and hyperbolic functions. Again we see that for

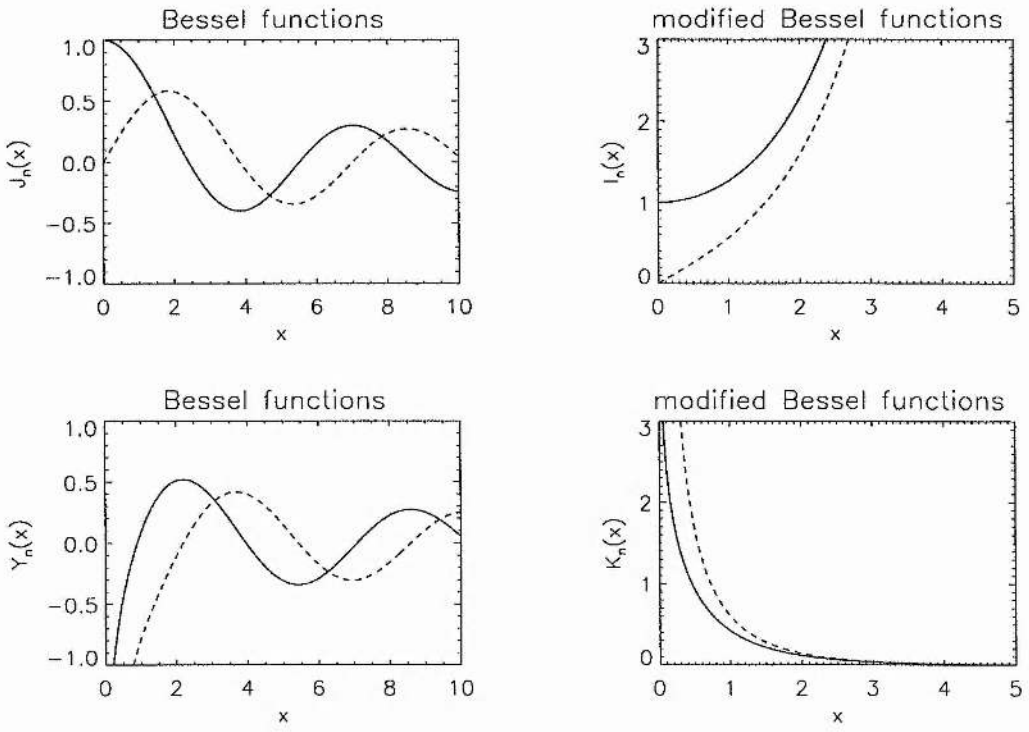

Figure 2.5: Sketches of the nth Bessel functions and modified Bessel functions (with real arguments), for $n = 0$ (solid curves) and $n = 1$ (dashed curves).

stable modes, the sign of $m_i{}^2$ determines whether the solution is evanescent ($m_i{}^2 > 0$) away from the interface or oscillatory ($m_i{}^2 < 0$) within the given region.

For the region within the cylinder, we require the solution to be bounded, particularly at $r = 0$. Hence our appropriate solution inside the cylinder, depending on the sign of m_0^2, is

$$\hat{p}_{T0}(r) = \begin{cases} I_n(m_0 r), & m_0^2 > 0 \\ J_n(n_0 r), & n_0^2 = -m_0^2 > 0 \end{cases} \tag{2.68}$$

Then if $m_0^2 > 0$ we have evanescent behaviour in $r < a$, corresponding to a surface mode. If $m_0^2 < 0$ we have oscillatory behaviour in $r < a$, corresponding to a body mode. Note that within the cylinder m^2 may be positive or negative.

The solution must also be bounded at large distances from the cylinder. In fact we require the solution to be non-oscillatory outside the cylinder so that the disturbances are principally confined to the vicinity of the cylinder (so that leaky waves (Cally 1986) are neglected). Hence, in $r > a$ we choose the solution $\hat{p}_{Te}(r) = K_n(m_e r)$, where $m_e^2 > 0$. Therefore m^2 must be positive in the environment of the cylinder.

Dispersion relations for uniform cylinder

For surface modes ($m_0^2 > 0$) the appropriate solutions are $\hat{p}_{T0} = I_n(m_0 r)$, $\hat{p}_{Te} = K_n(m_e r)$ so that the dispersion relation is

$$\frac{\rho_e \left(k^2 v_{Ae}^2 - \Omega_e^2\right)}{\rho_0 \left(k^2 v_{A0}^2 - \Omega_0^2\right)} = \frac{m_e}{m_0} \frac{I_n(m_0 a) K_n'(m_e a)}{I_n'(m_0 a) K_n(m_e a)} \tag{2.69}$$

where the density ratio ρ_e/ρ_0 given by the pressure balance condition (2.30), and $n = 0,\ 1$ denote sausage and kink modes respectively, while $n \geq 2$ corresponds to fluting modes.

For body modes ($m_0^2 = -n_0^2 < 0$) the appropriate solutions are $\hat{p}_{T0} = J_n(n_0 r)$, $\hat{p}_{Te} = K_n(m_e r)$ so that the dispersion relation is

$$\frac{\rho_e \left(k^2 v_{Ae}^2 - \Omega_e^2\right)}{\rho_0 \left(k^2 v_{A0}^2 - \Omega_0^2\right)} = \frac{m_e}{n_0} \frac{J_n(n_0 a) K_n'(m_e a)}{J_n'(n_0 a) K_n(m_e a)} \tag{2.70}$$

again with ρ_e/ρ_0 given by (2.30) and $n = 0,\ 1$ denoting sausage and kink modes respectively, while $n \geq 2$ corresponds to fluting modes.

In both dispersion relations $K_n'(m_e a) = dK_n(x)/dx$ evaluated at $x = m_e a$, similarly for the other Bessel function derivatives. Dispersion relations (2.69) and (2.70) have appeared

in the literature in various forms for the static case (Roberts and Webb 1978, Roberts and Webb 1979, Uberoi and Somasundaram 1980, Wilson 1980, Spruit 1982, Edwin and Roberts 1983, Roberts 1987) and with flows (Somasundaram and Satya Narayanan 1987, Satya Narayanan 1991).

The above mode classification is based on the assumption that m^2 is real. For the static case, this is a valid assumption as only stable modes ($\omega^2 > 0$, that is ω real) exist (Edwin and Roberts 1983). However, with the inclusion of flows there is a possibility that ω may be complex, leading to complex m^2 and m. Then for solutions to be bounded as $|x| \to \infty$ we require Re $m_e > 0$, while we classify the modes as surface or body according to their properties in the static case.

2.3 General discussion of the dispersion relations

We have obtained nine different dispersion relations: for the single interface we have one dispersion relation governing surface modes only, whereas for the slab and cylinder we have separate equations for surface and body modes, each of which have a different form for sausage and kink modes.

There is a large body of literature on the properties of these dispersion relations for the static case (Roberts and Webb 1978, 1979, Wentzel 1979, Wilson 1980, Roberts 1981a,b, Spruit 1982, Somasundaram and Uberoi 1982, Edwin and Roberts 1982, 1983, Abdelatif 1988, Miles and Roberts 1989, Evans and Roberts 1990, Jain and Roberts 1991) while the investigation of the effects of field-aligned steady flows on these modes (Satya Narayanan and Somasundaram 1985, Roberts 1987, Satya Narayanan 1991, Mann et al. 1992, Singh and Talwar 1994, Nakariakov and Roberts 1995a, Nakariakov et al. 1996, Joarder et al. 1997b) is a developing subject.

The usual approach to studying each of the above dispersion relations is to solve for the field-aligned phase velocity

$$c_p \equiv \frac{\omega}{k} \tag{2.71}$$

as a function of the vertical dimensionless wavenumber ka, which is a measure of the vertical wavelength relative to the scalewidth of the inhomogeneity. In this way we may determine the dispersive properties of modes propagating along the particular inhomogene-

ity under consideration, be it a single surface or a duct. Note that $c_p > 0$ for propagation in the direction of the applied magnetic field $\mathbf{B}_0$, while $c_p < 0$ for propagation in the opposite direction.

2.3.1 Propagation windows

Prior to solving for $c_p(ka)$, we can establish propagation windows for stable solutions of each mode type. These are the ranges of c_p satisfying the constraints on the signs of ${m_e}^2$ and ${m_0}^2$ under which the dispersion relations were derived and have real solutions.

Consider the static case. Rewrite expression (2.47) for m^2 as

$$\frac{m^2}{k^2} = \frac{({c_{max}}^2 - {c_p}^2)({c_p}^2 - {c_{min}}^2)}{({c_{min}}^2 + {c_{max}}^2)({c_p}^2 - {c_T}^2)}, \qquad \text{with} \quad \begin{aligned} c_{min} &= \min(c_s, v_A), \\ c_{max} &= \max(c_s, v_A). \end{aligned} \tag{2.72}$$

Then we have

$$m^2 > 0 \iff {c_p}^2 < {c_T}^2 \quad \text{or} \quad {c_{min}}^2 < {c_p}^2 < {c_{max}}^2 \tag{2.73}$$

$$m^2 < 0 \iff {c_T}^2 < {c_p}^2 < {c_{min}}^2 \quad \text{or} \quad {c_p}^2 > {c_{max}}^2 \tag{2.74}$$

with $m^2/k^2 \to \infty$ as ${c_p}^2 \to {c_T}^2$ and $m^2/k^2 = 0$ when ${c_p}^2 = {c_{min}}^2,\ {c_{max}}^2$. This is illustrated in Figure 2.6 where we plot m^2/k^2 against ${c_p}^2$ for various ratios of ${c_{min}}^2/{c_{max}}^2$. We note that (for ${c_T}^2 > 0$) the curve for m^2/k^2 has two branches separated by the asymptote at ${c_p}^2 = {c_T}^2$; the first branch is monotonic increasing with minimum $m^2/k^2 = 1$ at ${c_p}^2 = 0$ while the second branch has zeroes at ${c_p}^2 = {c_{min}}^2,\ {c_{max}}^2$ and a maximum (marked by a diamond) at ${c_p}^2 = 2{c_T}^2$, $m^2/k^2 = 1 - 4{c_T}^4/({c_s}^2{v_A}^2)$.

For a given set of parameter values (v_{Ai}, c_{si}; $i = 0$ or e) we can plot each ${m_i}^2/k^2$ and determine for what values of ${c_p}^2$ it is positive or negative. For all modes under consideration we take ${m_e}^2 > 0$, and hence we are restricted to ${c_p}^2 < {c_{Te}}^2$ or ${c_p}^2 \in ({c_{se}}^2, {v_{Ae}}^2)$. [1] This provides a basic range of c_p to which all non-leaky modes are restricted. We similarly obtain ranges for which ${m_0}^2 > 0$ (surface modes: ${c_p}^2 < {c_{T0}}^2$ or ${c_p}^2 \in ({c_{s0}}^2, {v_{A0}}^2)$) and ${m_0}^2 < 0$ (body modes: ${c_{T0}}^2 < {c_p}^2 < \min({c_{s0}}^2, {v_{A0}}^2)$ or ${c_p}^2 > \max({c_{se}}^2, {v_{Ae}}^2)$). The overall propagation window for *body modes* is given by the intersection of the positive parts of the ${m_e}^2/k^2$ curve with the negative parts of the ${m_0}^2/k^2$ curve, irrespective of

[1] We use set notation here to indicate that ${c_p}^2$ lies *between* ${c_{se}}^2$ and ${v_{Ae}}^2$, their order not being specified.

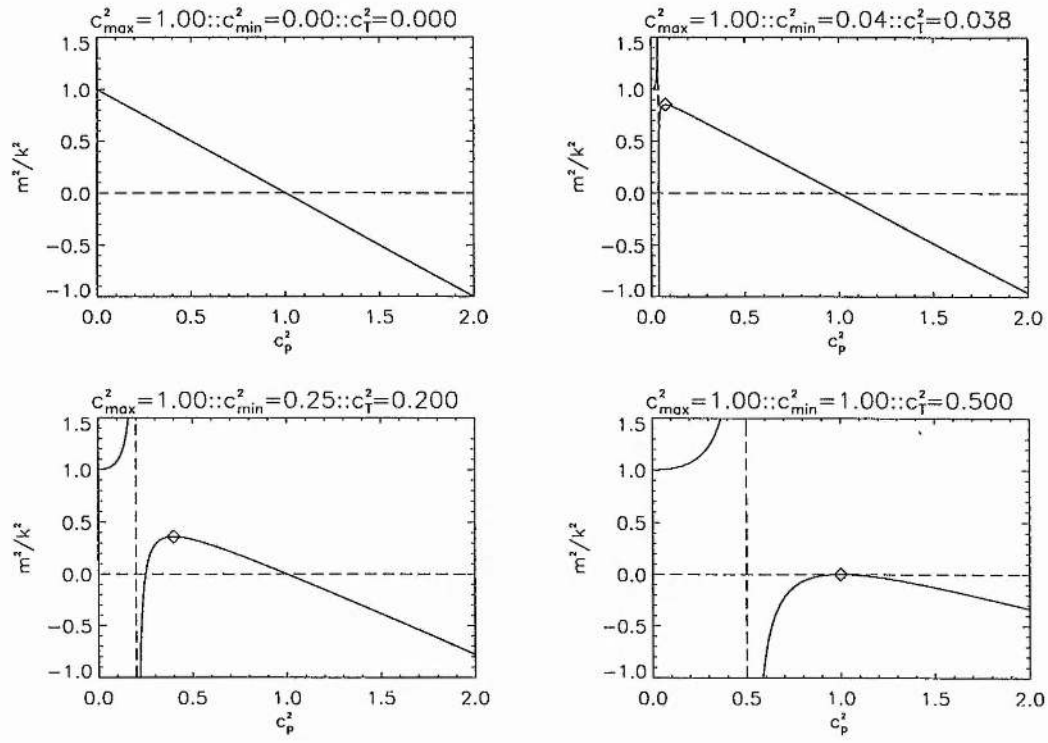

Figure 2.6: Plots of m^2/k^2 against ${c_p}^2$ for $c_{min}/c_{max} = 0,\ 0.2,\ 0.5,\ 1.0$; see equation (2.72). Long-dashed lines indicate the vertical asymptote at ${c_p}^2 = {c_T}^2$ and the horizontal line $m^2/k^2 = 0$. For ${c_T}^2 \neq 0$ the curve for m^2/k^2 has two branches separated by the asymptote at ${c_p}^2 = {c_T}^2$; the first branch is monotonic increasing with $m^2/k^2 \geq 1$ while the second branch has $m^2/k^2 < 1$ with zeroes at ${c_p}^2 = {c_{min}}^2,\ {c_{max}}^2$ and a maximum (marked by a diamond) at ${c_p}^2 = 2{c_T}^2$, $m^2/k^2 = 1 - 4{c_T}^4/({c_s}^2{v_A}^2)$. In the presence of field-aligned steady flow U_i, ${c_p}^2$ is replaced by $(c_p - U_i)^2$.

whether c_{max} within each medium is the sound speed or Alfvén speed. For *surface modes*, we are restricted to the intersection of the positive parts of both curves; however, there is an additional requirement that ${c_p}^2 \in ({v_{A0}}^2, {v_{Ae}}^2)$ (see below) which further reduces the propagation window, and hence for these modes the relative ordering of sound and Alfvén speeds in each medium is important. For example, if $c_{s0} < v_{A0}$ and $c_{se} < v_{Ae}$ (typical of the corona) then it is impossible to satisfy all the criteria for surface modes; hence no surface modes exist when both media are low-β plasmas (for which $c_{si} \ll v_{Ai}$). (Note, however, that our discussion is restricted to the special case of field-aligned propagation. It is found (Jain and Roberts 1991) that for $c_{s0} < v_{A0}$ and $c_{se} < v_{Ae}$, surface modes exist for all angles of propagation except those parallel or perpendicular to the applied magnetic field.)

We note that depending on how the curves for ${m_0}^2/k^2$ and ${m_e}^2/k^2$ overlap, there may be two ranges of c_p satisfying all the requirements for a given mode type. In such cases we obtain two sets of modes, which are termed *fast* and *slow* modes of the given type (surface or body). Hence the very existence of each mode type for a given configuration depends on the relative orderings of all the speeds involved. For a detailed discussion of the mode types which may arise for different orderings of c_{s0}, v_{A0}, c_{se}, v_{Ae} in the static case, see Abdelatif (1988).

The above discussion is for the static case. When flows are introduced then there are qualitative changes in the propagation windows, due to the fact that in ${m_e}^2/k^2$ we replace ${c_p}^2$ by $(c_p - U_e)^2$ while in ${m_0}^2/k^2$ the replacement is $(c_p - U_0)^2$. The evolution of the propagation windows with increasing relative flow is discussed in Chapter 3, with particular reference to the case of incompressible surface modes, where it proves to be a surprisingly useful tool in the investigation of the properties of the solutions as a function of the relative flow.

2.3.2 Properties of solutions

Once the propagation windows have been established, and we know *which* modes may exist and *where*, it is quite another matter to find out *how* their phase speeds vary with vertical wavelength. The propagation windows tell us where solutions *may* lie, this being independent of the geometry. However, in order to determine where, within this allowed

range, the solutions actually *do* lie, we need to take into account the specific forms of the functions involved for each mode type and geometry.

The determination of the solution for $c_p(ka)$ is not a straightforward task. One reason for this is that all the dispersion relations contain the factors m_e and m_0 (or n_0), each of which are radical rational functions of c_p. While radicals may be eliminated by squaring the dispersion relations, this process introduces spurious roots so that care must be taken in order to ensure that any solutions obtained satisfy the original dispersion relation, a partial check being that they lie within the propagation window. Further, the slab and cylinder dispersion relations each contain transcendental functions of m_0 (and also of m_e for the cylinder), with the result that an analytical treatment is generally only possible in certain limits such as the vertical wavelength extremes $ka \to 0$ and $ka \to \infty$, with numerical methods required elsewhere. While for the static case c_p always appears as ${c_p}^2$, with steady flows included c_p appears in two combinations, $(c_p - U_0)^2$ and $(c_p - U_e)^2$, which makes the problem of solving for c_p doubly difficult.

Rather than treating the nine cases on an individual basis, we first consider them together by treating the dispersion relations in a general form. This allows us to discuss some general properties shared by the dispersion relations, and to point to some differences between surface and body modes, and to some effects of geometry. Here we make some preliminary comments about the mathematical features of the dispersion relations, and their implications for the physical properties of the modes. In doing so we review results found in the literature on the above dispersion relations.

From our general derivation in Section 2.2, we know that all the dispersion relations take the form

$$\frac{\varepsilon_e}{\varepsilon_0} = \frac{\hat{p}_{T0}}{d\hat{p}_{T0}/dx_\perp} \frac{d\hat{p}_{Te}/dx_\perp}{\hat{p}_{Te}} \tag{2.75}$$

with the right-handside evaluated at $x_\perp = a$. The left-handside is an essential feature of the problem, having come from the matching conditions at the interface. The right-handside is characterised by the geometry, with its form being determined by the choice of solutions for the regions either side of the interface. We can compare and contrast the properties of the functions in the right-handside of (2.75) for surface and body mode separately, as differences between these modes can be related to the form of the right-handside.

In the following we will consider *stable modes*, so that c_p, ${m_0}^2$, and ${m_e}^2$ are real. Note however that our discussion is not restricted to the static case; it is also valid for stable modes modified by the presence of structured steady flows.

Surface modes

We consider the right-handside of (2.75) in terms of a function of two variables, $x_0 \equiv m_0 a$ and $x_e \equiv m_e a$, representing the effective *transverse* dimensionless wavenumbers of the disturbance in each medium. Note that in general $x_0 \neq x_e$. This approach is in contrast to the usual one of examining dependence on the dimensionless *vertical* wavenumber ka. Note that $(m_i a)^2 = {\lambda_i}^2 (ka)^2$, where ${\lambda_i}^2 = {m_i}^2/k^2$ (> 0 for surface modes) is given by (2.72) with the appropriate subscripts; λ_i is a function of c_p but is not explicitly a function of ka. From Figure 2.6 we see that for $(c_p - U_i)^2 < {c_{Ti}}^2$ we have $m_i a > ka$, while if $(c_p - U_i)^2 \in ({c_{si}}^2, {v_{Ai}}^2)$ then $m_i a < ka$.

We split the right-handside of dispersion relation (2.75) into two factors, one for each of x_0 and x_e, and consider the dependence of that factor on the given variable. In this way we can separate and compare the contributions to the right-handside from the internal and external variables, x_0 and x_e. Writing

$$f_0(x_0) \equiv \frac{\hat{p}_{T0}}{d\hat{p}_{T0}/dx_0}, \qquad f_e(x_e) \equiv -\frac{\hat{p}_{Te}}{d\hat{p}_{Te}/dx_e}, \tag{2.76}$$

the general dispersion relation (2.75) becomes

$$\frac{\varepsilon_e}{\varepsilon_0} = -\frac{x_e}{x_0}\frac{f_0(x_0)}{f_e(x_e)} \tag{2.77}$$

where the functions $f_0(x_0)$ and $f_e(x_e)$ are given for each case in Table 2.1. We refer to $f_0(x_0)/x_0$ as the *internal factor* and $f_e(x_e)/x_e$ as the *external factor*.

For the single interface both f_0 and f_e are unity, as is f_e for both surface mode types of the uniform slab. For the slab and cylinder, f_0 is a transcendental function of x_0, hence also of c_p, ka and the internal speed parameters v_{A0}, c_{s0} and U_0. For the cylinder, f_e is a transcendental function of x_e, which involves c_p, ka and the external speed parameters v_{Ae}, c_{se} and U_e The dependence on ka renders the modes dispersive, and their properties further depend on the relative ordering of c_p with the various speed parameters.

geometry	mode type	$f_0(x_0)$	$f_e(x_e)$
single interface	—	1	1
slab	sausage	$\coth(x_0)$	1
	kink	$\tanh(x_0)$	1
cylinder	sausage	$\frac{I_0(x_0)}{I_0'(x_0)}$	$-\frac{K_0(x_e)}{K_0'(x_e)}$
	kink	$\frac{I_1(x_0)}{I_1'(x_0)}$	$-\frac{K_1(x_e)}{K_1'(x_e)}$

Table 2.1: Forms of the functions $f_0(x_0)$ and $f_e(x_e)$ in the general dispersion relation (2.77) for the surface modes of the given geometries and mode types, where $x_0 = m_0 a$ and $x_e = m_e a$. In all cases $f_i(x_i) > 0$ for x_i real and positive. Note that for the slab case the sausage and kink mode factors are reciprocals of each other.

This in general necessitates the use of numerical methods in order to solve for $c_p(ka)$, for a given set of speed orderings. Most treatments consider the solutions at either extreme in ka, representing long ($ka \to 0$) or short ($ka \to \infty$) vertical wavelengths (with respect to the lengthscale, a, of the inhomogeneity), in which analytical solutions may be obtained from use of approximations to the transcendental functions for small or large arguments. Here care must be taken since each vertical wavelength extreme has more than one possible equivalent in terms of transverse wavelengths, see Table 2.2. However, as a general rule (concluded from results in the literature, see below) it would appear that for *surface* modes (we discuss body modes separately below) the solutions in a given vertical wavelength extreme are obtained in the same extreme for transverse wavelengths, that is $ka \to 0$ corresponds to $x_0, x_e \to 0$ and $ka \to \infty$ corresponds to $x_0, x_e \to \infty$. The only exception is the cylinder slow kink mode (see below), for which the long wavelength extreme corresponds to $x_i \to 0$ for only *one* of $i = 0, e$, the other tending to some finite value.

Hence, tracing the dispersion curves for c_p with increasing ka may be considered in terms of simultaneously tracing (at different rates) the internal and external factors with increasing x_0, x_e. In Figure 2.7 we plot the reciprocals of the internal and external factors, that is $x_i/f_i(x_i)$ against x_i, with $i = 0, e$ (taken to be real since stable solutions are assumed). Taking $m_0 > 0$ and $m_e > 0$ we need only plot for $x_i > 0$ in each case. In all

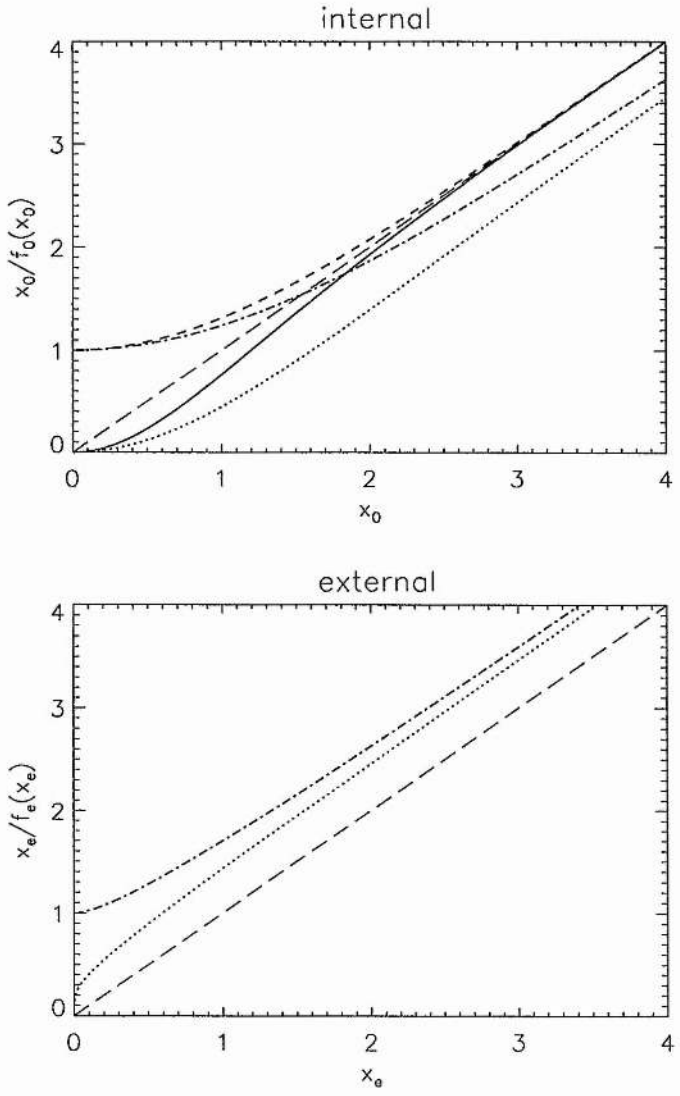

Figure 2.7: Plots of the reciprocals of the internal and external factors, namely $x_0/f_0(x_0)$ and $x_e/f_e(x_e)$, for the given geometries and surface mode types, with $x_0 = m_0 a$, $x_e = m_e a$, both real. See Table 2.1 for the forms of $f_0(x_0)$ and $f_e(x_e)$. Slab curves are solid (sausage modes) and dashed (kink modes). Cylinder curves are dotted (sausage modes) and dot-dashed (kink modes). Single interface solutions are long-dashed. For the internal factors, the curve for the cylinder kink mode crosses that for the single interface mode at $x_0 \approx 1.6$. For the external factors, the curves for slab sausage and kink modes coincide with that for the single interface mode, and all three are shown by the long-dashed line.

vertical wavelength extreme	equivalents for transverse wavelengths	implications for limiting phase speeds	applications in the literature	case label
$ka \to 0$	$m_i a \to 0$	?	all modes except case(b)	(a)
	$m_i a \to \nu$, $\lvert\lambda_i^2\rvert \to \infty$	${c_p}^2 \to {c_{Ti}}^2$	some surface; all slow body	(b)
$ka \to \infty$	$m_i a \to \infty$	?	all surface; all $\text{body}_{(i=e)}$	(c)
	$n_0 a \to \nu$, ${\lambda_0}^2 \to 0$	${c_p}^2 \to {v_{A0}}^2, {c_{s0}}^2$	all body	(d)

Table 2.2: Vertical wavelength extremes each with two possible equivalents for transverse wavelengths. Here ν is a finite constant and $\lambda_i^2 = m_i^2/k^2 = -n_i^2/k^2$, with $i = 0$ or e in each case unless otherwise specified. Question marks (?) indicate limiting ${c_p}^2$ depends on the given mode, with caution required if ${c_p}^2 \to {c_{Ti}}^2$ in case (a). Cases (a) and (b) apply to both surface and body modes. Applications are for the static case (Roberts 1981b, Edwin 1984). Where flows are included ${c_p}^2$ is replaced by $(c_p - U_i)^2$.

our plots for the slab and cylinder we will adopt the following *linestyle convention*: where plots are for one geometry only we use solid lines for sausage solutions and dashed lines for kink solutions; where slab and cylinder solutions are plotted on the same diagram the usual linestyle convention is used for the slab while for the cylinder we use dotted lines for sausage solutions and dot-dashed lines for kink solutions. In Figure 2.7 we also show, for comparison, the lines for the single interface, using a long-dashed line.

An immediate conclusion from the plots in Figure 2.7 is that all surface mode curves exhibit broadly similar behaviour, this behaviour being that of the single interface (shown by the long-dashed curves), particularly for large values of x_0 and x_e. Indeed, in the case of the slab, the external curves for both mode types (sausage and kink) *coincide* with that of the single interface (since $f_e(x_e) \equiv 1$ in each of these cases), while the two internal curves converge on the single interface one (since $\lim_{x_0 \to \infty} f_0(x_0) = 1$ for both mode types). In the limit of large x_i the cylinder curves for $x_i/f_i(x_i)$ also have the same behaviour as those for the single interface, but differ by a constant: as $x_0, x_e \to \infty$, both cylinder modes have $x_0/f_0(x_0) \to x_0 - 0.5$ and $x_e/f_e(x_e) \to x_e + 0.5$. These limits can be shown analytically by considering the asymptotic expansions for the modified Bessel functions (Abramowitz

and Stegun 1965), from which we obtain the results

$$\frac{I_n(x)}{I_n'(x)} \approx 1 + \frac{1}{2x}, \qquad -\frac{K_n(x)}{K_n'(x)} \approx 1 - \frac{1}{2x} \tag{2.78}$$

for any fixed n (real and non-negative) and x large and positive.

Hence for large values of x_0 and x_e, that is short transverse wavelengths in each medium, we have $f_i(x_i) \to 1$ for surface modes, all surface mode dispersion relations reduce to that for the single interface, namely

$$\frac{\varepsilon_e}{\varepsilon_0} = -\frac{x_e}{x_0}. \tag{2.79}$$

Indeed, it is found in the dispersion diagrams for the static case (Edwin and Roberts 1982, Edwin and Roberts 1983, Edwin 1984) that in the short vertical wavelength limit $ka \to \infty$ (equivalent to $x_0, x_e \to \infty$ for surface modes) the solutions for c_p for the sausage and kink surface modes of the slab and cylinder all asymptote to those for a single interface. We note that this ought to continue to hold for stable surface modes modified by the presence of structured steady flows. That is, for a given configuration with given physical properties (including flows) of the internal and external media, all stable surface modes of the slab and cylinder ought to be indistinguishable from those of the "equivalent" single interface in the limit that in each region the wavelength of the mode is small compared to the lengthscale of the inhomogeneity.

We consider now the opposite extreme of small x_0 and x_e. This corresponds to transverse wavelengths in each region which are long compared to the inhomogeneity lengthscale. This limit is also used in the investigation of the long vertical wavelength extreme, that is $ka \to 0$. From Figure 2.7 we see that for the slab

$$\lim_{x_0 \to 0} \frac{x_0}{f_0(x_0)} = \begin{cases} 0, & \text{sausage} \\ 1, & \text{kink} \end{cases} \qquad \lim_{x_e \to 0} \frac{x_e}{f_e(x_e)} = \begin{cases} 0, & \text{sausage} \\ 0, & \text{kink} \end{cases} \tag{2.80}$$

while for the cylinder

$$\lim_{x_0 \to 0} \frac{x_0}{f_0(x_0)} = \begin{cases} 0, & \text{sausage} \\ 1, & \text{kink} \end{cases} \qquad \lim_{x_e \to 0} \frac{x_e}{f_e(x_e)} = \begin{cases} 0, & \text{sausage} \\ 1, & \text{kink.} \end{cases} \tag{2.81}$$

These limits can be obtained analytically by considering approximations to the $f_i(x_i)$ valid for small x_i, which we now consider.

In the literature such approximations are used to obtain reduced forms of the full dispersion relation (2.77), to be applied to the given mode in this limit. The reduced dispersion relation may be used to obtain the possible limiting phase speeds together with their leading order corrections for $0 < ka \ll 1$. The existence of a mode with a given limiting phase speed depends on the relative ordering of the various speed parameters and the limiting solution for c_p, and on whether the leading order corrections have $c_p(ka)$ increasing or decreasing.

Consider the slab. The external factors are identical to that for the single interface, so that $x_e/f_e(x_e) \equiv x_e$. For the sausage modes, with $f_0(x_0) \approx 1/x_0$ we obtain $x_0/f_0(x_0) \approx {x_0}^2$, while for the kink modes we use the approximation $f_0(x_0) \approx x_0 - x_0^3/3$ to yield $x_0/f_0(x_0) \approx 1 + {x_0}^2/3$, in agreement with the limiting values (2.80) seen from Figure 2.7. The slab dispersion relations then reduce to

$$\frac{\varepsilon_e}{\varepsilon_0} = \begin{cases} -\frac{x_e}{{x_0}^2}, & \text{sausage} \\ -\frac{x_e}{1+{x_0}^2/3}, & \text{kink} \end{cases} \tag{2.82}$$

in agreement with the long wavelength leading order reductions for the static case given by Edwin and Roberts (1982), and also Roberts (1981b) in his treatment of the isolated slab ($v_{Ae} = 0$); with flows included, Nakariakov and Roberts (1995) gave the reduction for the sausage mode taking $U_0 = 0$, $v_{Ae} = 0$. For the static case, Equations (2.82) yield the possible limiting phase speeds as ${c_p}^2 \to {c_{se}}^2, {c_{T0}}^2$ for sausage modes and ${c_p}^2 \to {v_{Ae}}^2, {c_{Te}}^2$ for kink modes. With flows included we obtain similar expressions with ${c_p}^2$ replaced by $(c_p - U_i)^2$ where $i = 0, e$ as appropriate (Chakraborty 1968, Nakariakov and Roberts 1995a); leading order corrections are given by Chakraborty (1968). Leading order corrections for the static case (Edwin 1984, and references therein) confirm that the solution ${c_p}^2 \to {c_{T0}}^2$ does not violate $x_0 \to 0$ as $ka \to 0$. The sausage mode with ${c_p}^2 \to {c_{se}}^2$ exists as a result of structuring in pressure, density or temperature, and is absent for the case $c_{se} = c_{s0}$, and hence overlooked in studies (Cram and Wilson 1975) of the isothermal case. The sausage solution ${c_p}^2 \to {c_{T0}}^2$ was also derived by Roberts (1981b) by an alternative analysis, based on the thin tube approximation.

Turning now to the cylinder, for the internal factors we use the results (Abramowitz

and Stegun 1965)

$$I_n(x) \approx \left(\frac{1}{2}x\right)^n \frac{1}{n!} \quad \text{as } x \to 0, \qquad I_n'(x) = I_{n+1}(x) + \frac{n}{x} I_n(x) \tag{2.83}$$

to write (for all integers $n \geq 0$ and x_0 small)

$$\frac{x_0}{f_0(x_0)} \approx n + \frac{{x_0}^2}{2(n+1)}. \tag{2.84}$$

For the external factors, the results (Abramowitz and Stegun 1965)

$$K_n(x) \approx \frac{\frac{1}{2}(n-1)!}{\left(\frac{1}{2}x\right)^n} \quad \text{as } x \to 0 \quad (\text{integer } n > 0) \tag{2.85}$$

$$-K_n'(x) = K_{n-1}(x) + \frac{n}{x} K_n(x), \qquad -K_0'(x) = K_1(x) \tag{2.86}$$

yield the approximations for small x_e

$$\frac{x_e}{f_e(x_e)} \approx \begin{cases} \frac{1}{K_0(x_e)}, & n = 0 \\ 1 + {x_e}^2 K_0(x_e), & n = 1 \\ n + \frac{{x_e}^2}{2(n-1)}, & n \geq 2 \end{cases} \tag{2.87}$$

where $K_0(x) \approx -\ln(x) = \ln(1/x)$ in the limit $x \to 0$. These results are in agreement the limiting values (2.81) seen from Figure 2.7, and with the leading order approximations obtained by Spruit (1982) for the static case.

The reduced dispersion relation for the cylinder sausage mode ($n = 0$) is then

$$\frac{\varepsilon_e}{\varepsilon_0} = \frac{2}{{x_0}^2 \ln(x_e)} \tag{2.88}$$

in agreement with that given for the static case by Roberts and Webb (1978, 1979), who considered the isolated tube ($v_{Ae} = 0$) and by Edwin and Roberts (1983). Equation (2.88) yields the limiting phase speeds ${c_p}^2 \to {c_{se}}^2, {c_{T0}}^2$, coinciding with those given above for the sausage surface modes for the slab. The latter limit (${c_p}^2 \to {c_{T0}}^2$) was also found by Spruit (1982). For the case of an isolated tube ($v_{Ae} = 0$), assumed to be slender, this limit was found by Defouw (1976) and by Roberts and Webb (1978, 1979) using the "slender flux tube approximation".

For the kink ($n = 1$), and fluting ($n \geq 2$), modes (2.84) and (2.87) yield the reduced dispersion relation

$$\frac{\varepsilon_e}{\varepsilon_0} = -1 \tag{2.89}$$

in agreement with results in the literature for the static case (Spruit 1982, Edwin and Roberts 1982, Edwin 1984, Abdelatif 1988, Evans and Roberts 1990). Equation (2.89) coincides with the dispersion relation for surface modes of an incompressible single interface (see Chapter 3), which for the static case yields the limiting phase speed ${c_p}^2 = {c_k}^2 \equiv (\rho_0 {v_{A0}}^2 + \rho_e {v_{Ae}}^2)/(\rho_0 + \rho_e)$; c_k is termed the kink speed. This phase speed was given by Parker (1979b) for the $n = 1$ mode of a slender incompressible cylinder, while (2.89) shows that it may also apply to all nonaxisymmetric modes of a slender compressible cylinder.

Edwin and Roberts (1983) and Edwin (1984) additionally found for kink modes the limiting phase speeds ${c_p}^2 \to {c_{Ti}}^2$, $i = 0, e$ by respectively taking the limits $x_i \to \nu, x_j \to 0$ (each of these have existence conditions on the relative orderings of v_{Ai}, c_{si}), and for the solution with ${c_p}^2 \to {c_{T0}}^2$ the cylinder slow surface waves are all almost identical (Evans and Roberts 1990). Hence the kink (and fluting) modes of a cylinder generally have different limiting phase speeds to the kink modes of a slab.

Overall we see that in the long wavelength extreme, surface modes are very much affected by the geometry, in marked contrast to the short wavelength extreme discussed above. For both geometries, the sausage and kink modes exhibit quite different behaviour to each other in the long wavelength limit, as demonstrated in dispersion diagrams for the static case for the slab (Roberts 1981b, Edwin and Roberts 1982, Edwin 1984) and for the cylinder (Edwin and Roberts 1983, Evans and Roberts 1990). Further, while the sausage modes of both geometries are found to have the same limiting phase speeds, those of the kink modes differ between the geometries. The basic difference between sausage and kink modes is related to the internal factors, while the difference between the kink modes of the two geometries is due to differences in the external factors (despite the strong similarity between the kink internal factors in this limit). This difference in kink modes was explained on physical grounds by Parker (1979b), on the basis that a cylinder oscillating transversely displaces less of its surroundings than a slab does.

We have examined the properties of the solutions at the extremes in x_0 and x_e and our analysis shows that similar effects are to be expected for stable surface modes modified by the presence of steady flows. However, this does not exhaust the number of interesting results, since special features may also occur at finite wavelengths. It appears in the literature (Edwin and Roberts 1982, Evans and Roberts 1990) that all $n \neq 0$ cylinder

modes which have ${c_p}^2 \to {c_k}^2$ in the long wavelength limit, possess a turning point in c_p at finite ka, while all other surface modes are monotonic in $c_p(ka)$. This feature has not to the author's knowledge been explained, other than as some mysterious quirk of the cylinder. However, we argue that this behaviour may be related to the mathematical properties of the internal and external factors of a cylinder. We have noted that in the long wavelength extreme $x_i/f_i(x_i) \to n$ for all cylinder surface modes. Then, in this limit, all the cylinder curves for $x_i/f_i(x_i)$ lie *above* those for the single interface, provided $n > 0$. In the opposite extreme of x_0 and x_e large, we have $x_0/f_0(x_0) \to x_0 - 0.5$ and $x_e/f_e(x_e) \to x_e + 0.5$ for all cylinder modes. Hence, while the limiting curve for the external factors is still above that for the single interface, the curve for the internal factors now lies *below* it. Hence all cylinder modes with $n > 0$ have a peculiarity in that the internal kink factor "crosses" that for the single interface, unlike all other factors. We argue that this peculiarity manifests itself as the turning points in the dispersion diagrams of Edwin and Roberts (1983) and Evans and Roberts (1990). This is demonstrated for the incompressible case (see Chapter 3), for which $m_0 = m_e = k$, where it is found that the kink mode has a turning point for $ka \approx 1.6$, in agreement with the crossing at $x_0 \approx 1.6$ in Figure 2.7.

Finally, we note from Figure 2.7 that

$$f_0(x_0) > 0, \quad f_e(x_e) > 0 \tag{2.90}$$

for x_0, x_e real and positive. For the single interface and slab, (2.90) is obvious from the form of these functions in Table 2.1. For the cylinder, we can easily prove conditions (2.90) for *all* surface modes (including fluting modes, $n \geq 2$) on noting (see Abramowitz and Stegun 1965) the general properties of Bessel functions (for $n > -1$ and $x > 0$)

$$I_n(x) > 0, \quad K_n(x) > 0, \quad I_n'(x) > 0, \quad K_n'(x) < 0. \tag{2.91}$$

Conditions (2.90) may also be deduced intuitively from the general form of the dispersion relation (2.75). The characteristic feature of surface modes is that the perturbations are monotonic either side of the interface (up to the axis of symmetry for the finite width inhomogeneities), with maximum disturbance at the interface itself. Continuity of p_T requires that $\hat{p}_T$ have the same sign either side of the interface, while the nature of surface modes suggests that $d\hat{p}_T/dx_\perp$ changes sign. Then $\hat{p}_{T0}$ and $d\hat{p}_{T0}/dx_\perp$ share the same sign,

while $\hat{p}_{Te}$ and $d\hat{p}_{Te}/dx_\perp$ have opposite signs, from which (2.90) follows. We note that conditions (2.90) do not necessarily hold for body modes, since they no longer have the requirement that $d\hat{p}_T/dx_\perp$ changes sign at the interface.

Conditions (2.90) are an essential feature of all stable surface modes of the given configurations, independently of compressibility and geometry, and lead to the *general requirement for surface modes* that

$$\varepsilon_e \text{ and } \varepsilon_0 \text{ have opposite signs.} \tag{2.92}$$

This requirement has important implications for the properties of surface modes: it imposes a constraint on the propagation window for surface modes (which we referred to in Section 2.3.1 above). For the static case the constraint is that the phase speed must lie between the two Alfvén speeds (Wentzel 1979, Roberts 1981b, Edwin and Roberts 1982, Abdelatif 1988). It is more complicated than that if relative flow is included, as the propagation windows change qualitatively according to the value of the flow relative to the difference and the sum of the two Alfvén speeds. This point will be discussed further in Chapter 3, and in fact proves to be a surprisingly useful tool in our investigation into the properties of the modes in the presence of flow.

Body modes

We now turn our attention to the body modes, occurring for the uniform slab and uniform cylinder (but not the single interface). Each of these geometries may be thought of as forming a duct in which the modes are trapped. Body modes are related to the fast and slow magnetoacoustic waves in an infinite uniform medium, and represent the modifications to these modes due to the bounded nature of the duct.

The requirement that $m_0^2 < 0$ restricts the phase speeds of body modes to two basic ranges, namely $c_{T0}^2 < (c_p - U_0)^2 < \min(c_{s0}^2, v_{A0}^2)$ and $(c_p - U_0)^2 > \max(c_{s0}^2, v_{A0}^2)$, in common with the constraints on slow and fast magnetoacoustic modes in an unbounded medium with the same properties as the interior of the duct. Hence a body mode may be similarly classified as slow or fast according to its phase speed relative to the speeds c_{s0}, v_{A0} and c_{T0}. However, the requirement that the mode be trapped within the duct imposes further conditions from $m_e^2 > 0$, that is $(c_p - U_e)^2 < c_{Te}^2$ or $(c_p - U_e)^2 \in (c_{se}^2, v_{Ae}^2)$.

While for the unbounded case the modes are nondispersive, with field-aligned phase speeds given by $(c_p - U_0)^2 = {c_{s0}}^2, {v_{A0}}^2$, the presence of the interfaces renders the body modes dispersive, as modes of different wavelengths "notice" the interfaces to different extents. With the interfaces parallel to the magnetic field, the extent to which the modes are affected by the structuring is related to their ability to propagate across the magnetic field. Slow magnetoacoustic modes are strongly field guided, and therefore slow body modes are only weakly dispersive. On the other hand fast magnetoacoustic modes are almost isotropic, with the result that fast body modes are strongly dispersive. Fast and slow body modes are usually treated separately, due to the differences between them.

In this thesis we are more concerned with surface modes, but to illustrate the features we consider the internal and external factors of body modes for comparison. Following the same approach as for the surface modes, we consider separately the contributions to the right hand side of the general dispersion relation (2.75) from the internal factors and external factors. The external factors are the same as for surface modes, as both mode types have evanescent behaviour in the environment of the inhomogeneity. However, since stable body modes are characterised by ${m_0}^2 < 0$ we retain real variables by changing the internal variable from $x_0 = m_0 a$ to $y_0 = n_0 a$, where ${n_0}^2 = -{m_0}^2 > 0$. Since the disturbance in the internal medium is now oscillatory, the variable y_0 is indeed a measure of transverse wavelength, in the conventional sense of the word, with respect to the width of the inhomogeneity. We may again compare the transverse and vertical wavelengths using the relation $(m_0 a)^2 = {\lambda_0}^2 (ka)^2$, where ${\lambda_0}^2 = {m_0}^2/k^2 < 0$. When negative, as for body modes, the factor ${\lambda_0}^2$ is unrestricted in magnitude. Therefore the variables $n_0 a$ and ka are not generally of the same order. However, the dispersive properties of a given mode may still be related to tracing the curves for the internal and external factors.

As for the surface modes we split the right hand side of (2.75) into internal and external factors, where for body modes we write

$$\frac{\hat{p}_{T0}}{d\hat{p}_{T0}/dx_\perp} \frac{d\hat{p}_{Te}/dx_\perp}{\hat{p}_{Te}} = -\frac{x_e}{y_0} \frac{g_0(y_0)}{f_e(x_e)} \tag{2.93}$$

where $y_0 = n_0 a$, $x_e = m_e a$ and

$$g_0(y_0) = \frac{\hat{p}_{T0}}{d\hat{p}_{T0}/dy_0}, \qquad f_e(x_e) = -\frac{\hat{p}_{Te}}{d\hat{p}_{Te}/dx_e}. \tag{2.94}$$

geometry	mode type	$g_0(y_0)$	$f_e(x_e)$
slab	sausage	$-\cot(y_0)$	1
	kink	$\tan(y_0)$	1
cylinder	sausage	$\frac{J_0(y_0)}{J_0'(y_0)}$	$-\frac{K_0(x_e)}{K_0'(x_e)}$
	kink	$\frac{J_1(y_0)}{J_1'(y_0)}$	$-\frac{K_1(x_e)}{K_1'(x_e)}$

Table 2.3: Forms of $g_0(y_0), f_e(x_e)$ in the general dispersion relation (2.77) for the body modes of the given geometries and mode types, where $y_0 = n_0 a$ and $x_e = m_e a$. There are no body modes for the single interface. In each case $f_e(x_e)$ is the same as for the corresponding surface mode, so that $f_e(x_e) > 0$ for x_e real and positive. Meanwhile each $g_0(y_0)$ may have either sign for y_0 real and positive.

Each mode has the same external factor, $f_e(x_e)/x_e$ as for the corresponding surface mode, while the internal factor is now $g_0(y_0)/y_0$. Then the general dispersion relation becomes

$$\frac{\varepsilon_e}{\varepsilon_0} = -\frac{x_e}{y_0}\frac{g_0(y_0)}{f_e(x_e)} \tag{2.95}$$

where the functions $g_0(y_0)$ and $f_e(x_e)$ are given for each case in Table 2.3. We note that there are no body modes for the single interface geometry. As for the surface modes, for the slab the internal factor is a transcendental function of the internal variable, while the external factor is constant; for the cylinder, both factors are transcendental functions of their respective variables.

Following our approach for the surface modes, we investigate the internal factors by plotting the reciprocal, which for body modes is $y_0/g_0(y_0)$. We do this for the sausage and kink modes separately, see Figure 2.8, where we show the curves for the given mode type for the slab and cylinder on the same plot using the linestyle convention described above (for the external factors see Figure 2.7).

An immediate conclusion from Figure 2.8 is that there is a remarkable similarity in the qualitative behaviour of the internal factors between the two geometries for each mode type. This similarity is more marked than was found for surface modes. Hence body modes are less strongly affected by the geometry of the structure. The main difference between the geometries for body modes is in the solutions for kink modes which have $x_e \to 0$, since the external factors are the same as for surface modes. We also note that for all body

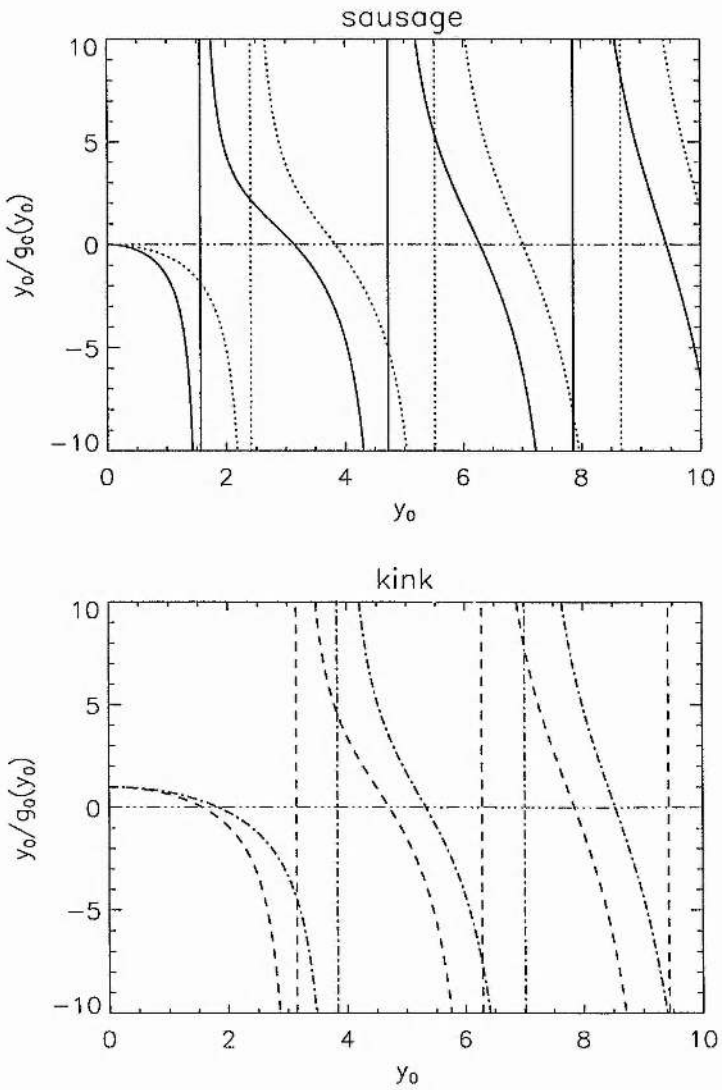

Figure 2.8: Plots of the reciprocals of the internal factors, namely $y_0/g_0(y_0)$ (where $y_0 = n_0 a$, real), for the given geometries and body mode types. See Table 2.1 for the forms of $g_0(y_0)$ and Figure 2.7 for the reciprocals of the external factors. We show sausage and kink curves separately. Slab curves are solid (sausage modes) and dashed (kink modes). Cylinder curves are dotted (sausage modes) and dot-dashed (kink modes). There are no body modes for the single interface. The vertical lines are asymptotes, where $\hat{p}_{T0}(y_0) = 0$ for the given mode, and the horizontal dot-dot-dot-dashed line shows where $y_0/g_0(y_0) = 0$.

modes the $y_0/g_0(y_0)$ curve alternates in sign and has an infinite number of branches, in contrast to those for surface modes which have a single branch which is always positive. The result of this is that there are an infinite number of body modes of each type within each of their propagation ranges, while for surface modes there is only one mode of each type within each propagation range. However, the limits for body modes of $y_0/g_0(y_0)$ as $y_0 \to 0$ coincide with those for surface modes of $x_0/f_0(x_0)$ as $x_0 \to 0$.

Let us consider the long wavelength extreme, $ka \to 0$, for slow body modes. Here we use case (b) in Table 2.2 for the transverse wavelength equivalent $y_0 \to \nu$, and the solution is of the form $(c_p - U_0)^2 \to {c_{T0}}^2(1 + Ak^2a^2/\nu^2)$ (Roberts and Webb 1979, Roberts 1981b, Edwin 1984, Nakariakov and Roberts 1995a) where A is a constant and ν is a zero of $y_0/g_0(y_0)$, of which there are an infinite number; see Figure 2.8. This leads to an infinite number of modes of each type, all with limiting phase speed given by $(c_p - U_0)^2 = {c_{T0}}^2$. This limiting phase speed is to be expected, since it is the field-aligned phase speed for slow modes in the limit of propagation transverse to the magnetic field. Here the presence of the interfaces constrains the modes to "fit" between them: the choices for ν correspond to zeroes in $d\hat{p}_{T0}/dy_0$, or maximum total pressure perturbation at each interface, and the larger the value of ν the greater the number of (complete) transverse oscillations there are between the interfaces. Note that for both geometries this limiting phase speed for the slow *body* modes of a slender structure, was also found for symmetric (i.e. sausage) *surface* modes of such a structure.

For the fast modes we have a different story. While the range of ${c_p}^2$ satisfying ${m_0}^2 < 0$ for the fast modes has no upper limit, the constraint that ${m_e}^2 > 0$ imposes that ${c_p}^2 < \max({c_{se}}^2, {v_{Ae}}^2)$ which cuts short this propagation window. This leads to the appearance of *cut-offs*, in that while, as for the slow body modes, there are an infinite number of fast body modes, here each mode only exists for ka greater than some critical value. The cut-off wave numbers of fast body waves are important in the theory of fast coronal pulsations (Roberts, Edwin and Benz 1984, Aschwanden 1987). The location of these cutoffs is related to the asymptotes of $y_0/g_0(y_0)$, and they occur where $x_e = 0$. While all sausage modes have finite cutoffs, in certain cases the lowest order kink modes exist for all ka. For such modes we may consider the long wavelength ($ka \to 0$) behaviour in a similar way to surface modes, using case (a) in Table 2.2 for the internal transverse

wavelength equivalent, the external factors being the same as for surface modes. For the slab kink modes we obtain $y_0/g_0(y_0) \approx 1 - {y_0}^2/3$ while for the cylinder we use the results (Abramowitz and Stegun 1965)

$$J_n(x) \approx \left(\frac{1}{2}x\right)^n \frac{1}{n!} \quad \text{as } x \to 0, \qquad J_n'(x) = -J_{n+1}(x) + \frac{n}{x}J_n(x) \tag{2.96}$$

to write (for all integers $n \geq 0$ and x_0 small)

$$\frac{y_0}{g_0(y_0)} \approx n - \frac{{y_0}^2}{2(n+1)} \tag{2.97}$$

These results are identical to those for surface modes, with the substitution ${y_0}^2 = -{x_0}^2$, hence we recover identical dispersion relations, with the same limiting solution. We note that this approach is not valid for slow body modes and it is found that there are no sausage body modes of this type. This is to be expected, since for small values of a there is little difference between the surface and body profiles of $\hat{p}_{T0}$ for kink modes, however for sausage surface modes $\hat{p}_{T0}$ decreases within the duct while for body modes it increases. Hence for fast body modes existing for all ka the possible limiting phase speeds are ${c_p}^2 \to {v_{Ae}}^2$ for the slab kink modes and ${c_p}^2 \to {c_k}^2$ for the cylinder kink modes. Whether or not they actually occur for a given configuration depends on the limits of the propagation window for fast body modes. Consider the static case. While for slow body modes $c_p(ka)$ is always increasing, for the fast body modes $c_p(ka)$ is always decreasing, hence it is the upper limit which is most important for the fast modes. We noted above that the upper limit is always defined by either c_{se} or v_{Ae}. Then if $v_{Ae} > c_{se}$ (and also $v_{Ae} > \max(c_{s0}, v_{A0})$) the first (fundamental) kink mode exists for all ka for the slab with limiting phase speed v_{Ae}, while for the cylinder the fundamental kink mode exists for all ka with limiting phase speed c_k, provided c_k lies within the propagation window for fast body modes. In each case, all other fast body modes have cutoffs, which alternate between sausage and kink, as do the positions of the asymptotes of $y_0/g_0(y_0)$. The cutoffs of fast body modes corresponds to zeroes in $\hat{p}_{T0}$, with an integer number of half-oscillations within the duct and no motion outside. The higher the cutoff, the greater the number of half-oscillations.

Turn now to the opposite extreme of $ka \to \infty$. In Table 2.2 the appropriate equivalent for internal transverse wavelengths is case (d), with $y_0 \to \nu$ and ${c_p}^2 \to {c_{s0}}^2, {v_{A0}}^2$, so that we recover the phase speeds of the fast and slow magnetoacoustic modes for field-aligned propagation. This is to be expected, since in this limit we have fast and slow

magnetoacoustic modes propagating essentially along the field in a very wide box, where the only influence of the boundaries is to quantise the modes into a discrete spectrum of wavenumbers. The slow body waves tend to $\min(c_{s0}, v_{A0})$, with $c_p(ka)$ increasing, while the fast body modes tend to $\max(c_{s0}, v_{A0})$, with $c_p(ka)$ decreasing. The slow body modes also exist in the opposite extreme $ka \to 0$, and approach their $ka \to \infty$ limit at smaller values of ka than do their fast counterparts, whose cutoffs are at increasingly large values of ka. This is reflective of the fact that fast body modes are more strongly affected by the duct width than are the slow body modes. The development of $c_p(ka)$ in each case may be thought of in terms of tracing a given branch of $y_0/g_0(y_0)$ from its starting value (a zero for slow modes, an asymptote for fast modes), to the value of ν appropriate to the given mode: with $y_0/(ka) \to 0$ the increase in y_0 is increasingly slower than that of ka and eventually grinds to a halt, while x_e continues to increase with ka. The choice of ν is beyond our interest, and the reader is referred to Edwin(1984).

For body modes we see similar overall behaviour between the two geometries, the main difference being in the long wavelength behaviour of the fast kink mode, where it exists for $ka \to 0$. In common with the kink surface modes, this difference between the geometries is due to the form of the external factor. The only other difference between any of the body modes (of either geometry or mode type) is in the location of the zeroes and asymptotes of $y_0/g_0(y_0)$. The former affects the dispersive properties of the slow body modes at long wavelengths, while the latter determines the cutoffs for fast body modes. We note that due to the strong similarity between the curves for the slab and cylinder body modes in Figure 2.8, as compared to those for surface modes in Figure 2.7 the qualitative features of body modes are in general less strongly affected by geometry than those of surface modes. This was found numerically for the static case by Edwin and Roberts (1982, 1983) and is to be expected on physical grounds since surface modes, by their very nature, are dependent on the geometry of the surface meanwhile the body modes may be thought of as "confined" versions of the modes arising in the infinite uniform medium.

2.3.3 Summary

Surface modes

The overall propagation window is the overlap of the ranges given by the requirement that ε_e and ε_0 have opposite signs, together with those satisfying ${m_0}^2 > 0$ and ${m_e}^2 > 0$. These ranges depend on the relative ordering of the sound and Alfvén speeds involved, making the dispersion relation difficult to treat generally, even for the static case, and each parameter case must be considered separately.

A necessary first step is to establish the propagation windows, this being particularly important for the case with flow as the windows evolve with increasing relative flow, see Chapter 3. Even for the simplest case, the single interface, the dispersion relation must be squared up in order to make analytical progress. This process introduces spurious roots, which may be discarded on the basis of their lying outside the propagation windows or failing to satisfy the unsquared dispersion relation.

Once the propagation windows have been established, we generally require a numerical treatment in order to determine where in the the propagation window the solutions actually do lie, due to the fact that the dispersion relation is transcendental, with internal and external factors each being transcendental functions of ω. Analytical treatment may be possible in certain limits. However, perhaps not all the important features are present in this limit. The problem is more complicated if relative flows are included, as ω occurs in two combinations, so that there is no direct analog with the static case.

We are therefore as well to get everything we can out of a case for which we can obtain analytical solutions, in order to gain an insight into the general features of surface modes. This case is the incompressible case, which is studied in detail in Chapter 3, and we also consider to what extent the results obtained for the incompressible chapter may tell us anything about the properties of compressible surface modes. Our investigation of the incompressible case allows us to uncover certain features that are not apparent in other treatments.

Body modes

Similar things hold for body modes, in that the propagation window depends on the relative ordering of the speeds and that each case tends to be considered separately. However, here g can be positive or negative, so the only ranges requirements are those imposed by ${m_0}^2 < 0$ and ${m_e}^2 > 0$. The periodic nature of the internal factor has a different implication for the properties of the modes: since a given value may correspond to a number of values of ka, there are an infinite number of body modes for each propagation window in which they may exist, while for surface modes there were at most two of each type.

In this thesis we are mainly concerned with surface modes, using the incompressible approximation to gain a deeper insight into their nature. For (fast) body modes, it is the cold plasma approximation that is usually used, with applications to the corona.

Chapter 3

Effects of field-aligned steady flows on incompressible surface modes

3.1 Introduction

We have seen in Chapter 2 that the dispersion relations of the form (2.75) for structured media are considerably more complicated than those for the unstructured case, given by (2.2). This complication is largely due to the fact that the dispersion relations for structured media, instead of being algebraic, contain functions of $m_0 a$ and $m_e a$, which are themselves functions of ω, rendering the relations highly transcendental. The transcendental nature of the dispersion relations makes them difficult to treat analytically in general. Therefore, while we can identify propagation windows for each type of mode, determined by the signs of ${m_0}^2$ and ${m_e}^2$, in general we require numerical methods to determine exactly *where* in the propagation window the solutions lie. Moreover, the propagation windows themselves depend on the relative ordering of the sound and Alfvén speeds in the media involved. Hence a large number of cases must be considered. A comprehensive treatment for the static case is provided by Edwin (1984). Again for the static case, Cramer (1995) has reviewed recent developments in the theory of the effects of non-ideal and nonlinear terms in the equations for surface waves in nonuniform magnetised plasmas.

The situation is more complicated if relative flows are involved, as ω then appears in two different combinations, namely ${\Omega_0}^2$ and ${\Omega_e}^2$, in the dispersion relations. This

leads to qualitative changes from the static case, and this area of investigation is a developing subject. As will be discussed in this chapter, flows may lead to altered propagation properties of stable modes (Satya Narayanan and Somasundaram 1985, Somasundaram and Satya Narayanan 1987, Ryutova 1988, Satya Narayanan 1991, Nakariakov and Roberts 1995a, Nakariakov et al. 1996, Joarder et al. 1997b), such as shifts in phase speed, reversal of dispersion properties, the appearance of backward or negative energy modes, and changes in mode character from trapped to radiative or from surface to body, and vice versa. Flows may also lead to the Kelvin-Helmholtz instability and unstable body modes (Chandrasekhar 1961, Parker 1964, 1979a, Gerwin 1968, Chakraborty 1968, Ferrari, Trussoni and Zaninetti 1981, Rae 1983, Pu and Kivelson 1983, Bodo, Rosner, Ferrari and Knobloch 1989, Birkinshaw 1991, Singh and Talwar 1994, Hardee 1995) We will show that all these features may be discussed in terms of the qualitative evolution of the propagation windows (that is the ranges of c_p in which stable solutions may lie) with increasing relative flow.

The threshold for the appearance of negative energy waves is lower than that for the onset of the Kelvin-Helmholtz instability, which occurs due to the linear interaction of a positive and negative energy wave. Negative energy waves may also be subject to dissipative instability (Cairns 1979, Ruderman and Goossens 1995, Joarder et al. 1997b) and nonlinear three-wave explosive instability (Cairns 1979, Craik and Adam 1979). Linear and nonlinear negative energy wave effects are also discussed in the context of hyperelastic fluid-filled tubes such as blood vessels (Ropchan and Swaters 1993). For continuously structured media, the presence of flows may cause enhancements or reductions in resonant absorption processes (Hollweg, Yang, Cadez and Gakovic 1990, Goossens, Hollweg and Sakurai 1992, Erdélyi and Goossens 1996, Csik, Erdélyi and Cadez 1997), and small but sharply structured steady flows may lead to enhanced efficiency of heating in dissipative phase mixing (Nakariakov, Roberts and Murawski 1998).

In this chapter we concentrate on the case of ideal MHD for small perturbations to discretely structured steady states with field-aligned flow and parallel propagation, so that dispersion relations of the form (2.75) apply. We are interested in the qualitative effects of flows on the propagation of *stable* waves, and the conditions under which they become unstable due to the relative flow.

While for the static case it is sufficient to consider only one root of the dispersion relation (equation (3.7)), in the presence of flows the asymmetry makes it necessary to consider both roots (see equation (3.8)) for the field-aligned phase speed $c_p \equiv \omega/k$. In Section 2.1.1 we noted that sufficiently large flows may lead to a propagation direction "reversal" for the mode formerly propagating against the flow, so that both solutions for c_p have the same sign. This is also found for surface and body waves in structured plasmas: a wave that in a static medium would propagate anti-parallel to the applied magnetic field is found in the presence of sufficiently large field-aligned flow to propagate in the same direction as the magnetic field and flow. Such waves are termed "backward modes" (Nakariakov and Roberts 1995a, Nakariakov et al. 1996, Joarder et al. 1997b), and were shown by Joarder et al. (1997a) to be "negative energy waves" in the given frame of reference (see Section 2.1.1). Joarder et al. (1997a) provided a detailed discussion of flow effects on stable ducted modes in a uniform slab, but they largely confined their attention to *body* modes. Our interest here is in flow effects on *surface* modes of the single interface, slab and cylinder.

We have noted the complications involved in attempting a general discussion of the dispersion relations. However, in the treatment of surface modes the analysis simplifies greatly if we consider the incompressible approximation, allowing us to gain valuable insight into the nature of surface modes. The nature of MHD wave propagation in a structured but static incompressible medium is well known (Roberts 1981a, 1981b; Edwin and Roberts 1982, 1983; see also reviews in Edwin (1991, 1992), Roberts (1991b, 1992) and Roberts and Ulmschneider (1997)), and will be considered in this chapter. The aim of this chapter is to examine the modifications to these stable modes in the presence of steady flows, and the conditions under which they may go unstable.

3.1.1 The incompressible approximation

We start with a discussion of the incompressible approximation, given formally by $\gamma \to \infty$, $c_s \to \infty$. Then $c_T \to v_A$, and $m^2/k^2 \to 1$ for any value of $(c_p - U)^2 \neq {v_A}^2 (= {c_T}^2)$. Thus m is necessarily real (even when ω or c_p is complex); only surface modes are possible.

We note that in the general compressible case it is possible for up to two bands of surface modes to exist, depending on the relative magnitudes of the sound and Alfvén

speeds in the two media; these two bands are referred to as fast and slow surface modes. The properties of the fast and slow surface modes differ, since they correspond to different branches of the m_i^2/k^2 curves (see Figure 2.6): fast surface modes have $(c_p - U_i)^2 > {c_{Ti}}^2$, for both $i = 0$ and e, corresponding to the second branch ($0 < m_i^2/k^2 < 1$) of both curves; slow surface modes have $(c_p - U_i)^2 < {c_{Ti}}^2$ for at least one of $i = 0$ or e, for which the first branch ($m_i^2/k^2 > 1$) applies.

For the incompressible case we have ${v_{Ai}}^2 = {c_{Ti}}^2$. Then, by the general requirement for surface modes that the $\varepsilon_i \equiv \rho_i k^2({v_{Ai}}^2 - (c_p - U_i)^2)$ have opposite signs, there is only the slow surface mode. Therefore in this approximation we obtain the incompressible limit of the *slow* surface mode. However, since the mode is characterised by the Alfvén speeds, it is often termed the "Alfvén surface mode" (e.g. Uberoi and Somasundaram 1980, Somasundaram and Satya Narayanan 1987). This is in fact a misnomer, as the mode is quite distinct from the Alfvén mode which is incompressible for all sound speeds, whereas all surface modes are compressible except in this special limit (Roberts 1991b).

Propagation windows

For the incompressible case, the surface mode conditions ${m_0}^2 > 0$ and ${m_e}^2 > 0$ are trivially satisfied (even for complex ω) so long as ω/k is not equal to any of the shifted Alfvén speeds, i.e. neither of the terms ε_e, ε_0 are equal to zero. Hence for the incompressible case our only restriction in ranges for stable surface modes is the general requirement for all stable surface modes that ε_0 and ε_e have opposite signs. For the static case this implies that ${c_p}^2 \in ({v_{A0}}^2, {v_{Ae}}^2)$. However, this condition evolves in the presence of field-aligned steady flows (see Section 3.3.1). The implications of this evolution are discussed in more detail below, and prove to be a key feature in our analysis of the flow effects on incompressible surface modes in media structured by discontinuities. Indeed, the evolution of the propagation windows (i.e. the dependence of their limits on the relative flow velocity) may be used to predict and explain some of the effects we see through mathematical analysis and computational solution of the dispersion relation, as will be discussed in Section 3.3. Further, since the condition that ε_0 and ε_e have opposite signs is a fundamental feature of surface modes, we propose in Section 3.3.5 that similar approaches may usefully be applied in the compressible case also.

3.1.2 General dispersion relation for incompressible surface modes

Let us consider the incompressible case in the context of our general analysis of the dispersion relations in Section 2.3, where we noted that for the geometries under consideration, surface modes satisfy dispersion relations of the general form

$$\frac{\varepsilon_e}{\varepsilon_0} = -\frac{x_e}{x_0}\frac{f_0(x_0)}{f_e(x_e)} \tag{3.1}$$

where (with $i = 0, e$) $\varepsilon_i = \rho_i(k^2 {v_{Ai}}^2 - \Omega_i^2)$, $x_i = m_i a$ and the forms of $f_i(x_i)$ relevant to each geometry and mode type are given in Table 2.1 (see Section 2.3).

We noted that for the general compressible case the internal and external variables, x_0 and x_e, are not necessarily equal. Each x_i is $|k|a$ multiplied by m_i/k (> 0). Then, tracing the solutions $c_p(ka)$ to the dispersion relation may be considered in terms of simultaneously tracing, at different rates, the curves for $x_0/f_0(x_0)$ and $x_e/f_e(x_e)$; these curves are plotted in Figure 2.7 (see Section 2.3). The tracing rate for each of these functions is related to the value of ${m_i}^2/k^2$, that is to the value of ${c_p}^2$ (or $(c_p - U_i)^2$ for flows) relative to the squares of c_{si}, v_{Ai} and c_{Ti} (where $i = 0$ or e as appropriate). Hence the general dispersion relation (3.1) for surface modes expresses c_p in terms of functions of two multiples of $|k|a$, namely x_0 and x_e, where each multiplying factor varies with c_p.

For the incompressible case, ${m_i}^2/k^2 \to 1$ for both $i = 0, e$. Then with $m_e = m_0 = |k|$ we have $x_0 = x_e = |k|a$, and both transverse spatial scales are equal to the vertical wavelength. Therefore all tracing rates are equal. In the general dispersion relation (3.1) the factor x_e/x_0 cancels and the right hand side is reduced to a single function f of a single variable $|k|a$, that is

$$f(|k|a) \equiv \frac{f_0(|k|a)}{f_e(|k|a)}. \tag{3.2}$$

The forms of $f_i(|k|a)$ are given in Table 3.1 for each geometry and mode type.

Then the general dispersion relation for incompressible surface modes is

$$\frac{\varepsilon_e}{\varepsilon_0} = -f(|k|a), \tag{3.3}$$

where

$$\frac{\varepsilon_e}{\varepsilon_0} = \frac{\rho_e\left[{v_{Ae}}^2 - (c_p - U_e)^2\right]}{\rho_0\left[{v_{A0}}^2 - (c_p - U_0)^2\right]}. \tag{3.4}$$

geometry	mode type	$f_0(x)$	$f_e(x)$
single interface	—	1	1
slab	sausage	$\coth(x)$	1
	kink	$\tanh(x)$	1
cylinder	sausage	$\frac{I_0(x)}{I_0'(x)}$	$-\frac{K_0(x)}{K_0'(x)}$
	kink	$\frac{I_1(x)}{I_1'(x)}$	$-\frac{K_1(x)}{K_1'(x)}$

Table 3.1: Forms of $f_0(x)$ and $f_e(x)$, where $x = |k|a$, in the general incompressible surface mode dispersion relation (3.3), for the given geometries and mode types. The properties of the solutions for a given mode type are characterised by the function $f(|k|a) \equiv f_0(|k|a)/f_e(|k|a)$, see Figure 3.1.

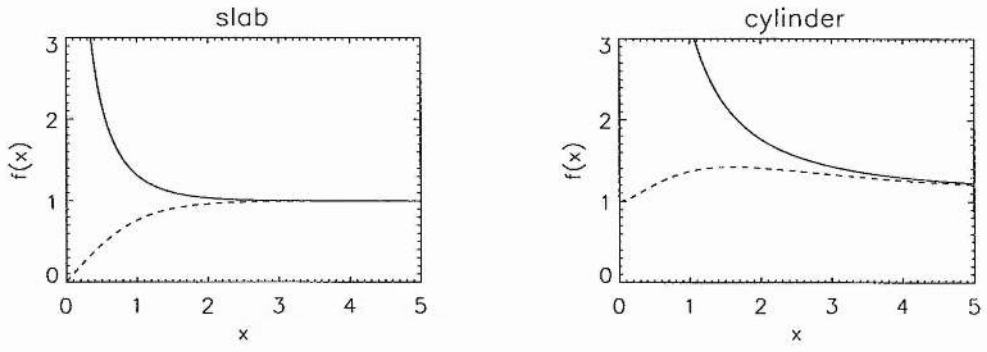

Figure 3.1: Sketches of $f(x) \equiv f_0(x)/f_e(x)$, with $x = |k|a$, for slab and cylinder incompressible surface modes (see Table 3.1). Sausage modes are given by solid lines, kink modes by dashed lines. The cylinder kink curve has a maximum at $f(1.6) \approx 1.4$; all other curves are monotonic. In all cases $f(x) > 0$ for all $x > 0$ and $\lim_{x\to\infty} f(x) = 1$, recovering the single interface.

The dispersive properties of $c_p(|k|a)$ for each geometry and mode type are directly related to the variation of $f(|k|a)$. In Figure 3.1 we plot $f(|k|a)$ for the slab and cylinder; for both geometries, we use the usual linestyle convention of solid lines for sausage modes and dashed lines for kink modes. Our cylinder plots in Figure 3.1 are equivalent to those in Figure 1 of Uberoi and Somasundaram (1980) whose definition of $f(|k|a)$ is the reciprocal of ours.

Our formulation of the problem in terms of a general function $f(|k|a)$, specified for each geometry and mode type, allows us to treat the cases in parallel. In this way we may highlight features common to all incompressible surface modes, as well as dispersive effects. In particular we note that for all modes

$$f(|k|a) > 0 \quad \text{for all } |k|a > 0, \tag{3.5}$$

leading to the ranges constraint noted above that ε_0, ε_e have opposite signs.

For all slab and cylinder modes, $f(|k|a) \to 1$ as $|k|a \to \infty$, so that in the short wavelength limit ($|k|a \gg 1$), the dispersion relation (3.3) reduces to

$$\frac{\varepsilon_e}{\varepsilon_0} = -1, \tag{3.6}$$

thereby recovering the incompressible single interface results. This is in agreement with the general results for surface modes (see discussions in Sections 2.3, 3.2.2 and 3.3.3) in that the corresponding single interface case is recovered in the short wavelength limit.

Consider now the opposite extreme of long wavelengths ($|k|a \ll 1$) for the slab and cylinder. This limit is examined in more detail in Sections 3.2.2 and 3.3.3 below, but for the moment we consider the limiting phase speeds for each case, drawing on the properties of $f(|k|a)$. For the sausage modes of both geometries, $f(|k|a) \to \infty$ as $|k|a \to 0$, giving $\varepsilon_0 \to 0$, or $c_p \to U_0 \pm v_{A0}$. For the kink modes of the slab, $f(|k|a) \to 0$ as $|k|a \to 0$, giving $\varepsilon_e \to 0$, or $c_p \to U_e \pm v_{Ae}$. For the cylinder kink modes, $f(|k|a) \to 1$ as $|k|a \to 0$, and we recover the single interface results. These limiting phase speeds are in agreement with the incompressible limit of those given in Section 2.3 for the compressible case.

Advantages of the reduction for the incompressible case

We noted that for the compressible case, the existence and nature of the solutions depends strongly on the relative ordering of the speeds v_{Ai}, c_{si}, c_{Ti} (and also U_i where flows are

included). Therefore each parameter regime must be considered separately. Furthermore, the dispersion relation is transcendental in c_p so that explicit analytical solutions may only be obtained in certain extreme cases, such as very small or very large $|k|a$. However, such analytical treatments fail to reveal features occurring at finite $|k|a$, an example of which is the turning point in the cylinder kink surface mode.

In contrast, for the incompressible case a general analysis is possible. There is only one band of surface modes, namely slow modes, for which the propagation windows are always bounded by shifted Alfvén speeds. With the internal and external variables x_0 and x_e now equal to $|k|a$, the dispersion relation is no longer transcendental in c_p and the dispersive properties are characterised by a single function $f(|k|a)$, which is independent of the internal and external parameters and may be treated as constant when solving for c_p for a given ka. This is the real advantage of the incompressible approximation, as it allows us to obtain explicit analytical solutions, at all values of $|k|a$, whose structure may be thoroughly investigated, thereby providing insight into the nature of the modes.

3.1.3 Solutions of the general dispersion relation

We have noted that for the incompressible case the dispersion relation is no longer transcendental in c_p. Indeed, the dispersion relation (3.3) may be written as a quadratic equation for c_p, the longitudinal phase speed ω/k:

$$(f\rho_0 + \rho_e){c_p}^2 - 2(f\rho_0 U_0 + \rho_e U_e)c_p - \left[f\rho_0(v_{A0}^2 - U_0^2) + \rho_e(v_{Ae}^2 - U_e^2)\right] = 0. \qquad (3.7)$$

Note that $c_p \equiv \omega/k$ may be positive or negative depending on whether propagation is in the positive or negative z-direction. Equation (3.7) has explicit solutions:

$$c_p = \frac{f\rho_0 U_0 + \rho_e U_e}{f\rho_0 + \rho_e} \pm \frac{1}{f\rho_0 + \rho_e}\left\{(f\rho_0 + \rho_e)(f\rho_0 v_{A0}^2 + \rho_e v_{Ae}^2) - f\rho_0\rho_e(U_0 - U_e)^2\right\}^{1/2}. \qquad (3.8)$$

The general incompressible dispersion relation (3.7) and solutions (3.8) are in agreement with those given in the literature for the specific cases of the incompressible *single interface* (static: Roberts 1981a, Somasundaram and Uberoi 1982; with flow: Chandrasekhar 1961, Parker 1979a, Rae 1983 and references therein, Hollweg et al. 1990, *uniform slab* (static: Parker 1974, Roberts 1981b, Edwin and Roberts 1982, Singh and

Talwar 1993; with flow: Parker 1964, 1979a Chakraborty 1968, Geronicolas 1977, Rae 1983, Satya Narayanan and Somasundaram 1985, Singh and Talwar 1994, Nakariakov and Roberts 1995, Nakariakov, Roberts and Mann 1996), and *uniform cylinder* (static: Roberts and Webb 1978, Uberoi and Somasundaram 1980, Edwin and Roberts 1983; with flow: Trehan and Singh 1978, Ray 1981, Roberts 1987, Somasundaram and Satya Narayanan 1987, Satya Narayanan 1991, Goossens, Hollweg and Sakurai 1992).

The explicit form of (3.8) is convenient for investigating analytically the dispersive and stability properties of the solutions, at all wavenumbers. The stability properties are determined by the sign of the term in braces: unstable solutions exist wherever

$$f\rho_0\rho_e(U_0 - U_e)^2 > (f\rho_0 + \rho_e)(f\rho_0 {v_{A0}}^2 + \rho_e {v_{Ae}}^2), \tag{3.9}$$

in which case the solutions for c_p are complex conjugates. This is the Kelvin-Helmholtz instability. In the absence of relative flows, $U_e = U_0$ and (3.9) cannot be satisfied; hence all modes are stable. We may think of (3.9) as defining a threshold value of the relative flow, greater than which a given mode becomes unstable. This threshold is independent of the frame of reference. At the threshold, the two solutions for c_p are real and equal. In the absence of magnetic fields, the right-handside of (3.9) is zero, so that any nonvanishing relative flow renders all modes unstable at all wavelengths. Magnetism has a stabilising effect, due to the tension restoring force. In the presence of a magnetic field, stable modes may exist for sufficiently small relative flows. Such modes represent modifications to those occurring for the static case, which become unstable when the relative flow exceeds the threshold value given by criterion (3.9). Note that since criterion (3.9) involves $f(|k|a)$, the stability properties are dispersive; that is, the flow threshold for the onset of the Kelvin-Helmholtz instability may vary with geometry, mode type and wavenumber.

A further point to note is that the two solutions (3.8) for c_p share the same sign when

$$f\rho_0(U_0^2 - v_{A0}^2) + \rho_e(U_e^2 - v_{Ae}^2) > 0;, \tag{3.10}$$

therefore (3.10) gives us a general criterion for the existence of backward incompressible surface modes. This criterion is similarly dispersive (through $f(|k|a)$), although the threshold relative flow it defines is dependent on the choice of reference frame. At the threshold, one of the solutions is given by $c_p = 0$. As well as being dispersive, criteria

(3.9) and (3.10) also depend on the strength of the inhomogeneity, given by the ratios of density, ρ_e/ρ_0, and Alfvén speed, v_{Ae}/v_{A0}.

Outline of Chapter

In Section 3.2 we review the results for the static case, the remainder of the Chapter being concerned with the effects of flows on such modes. In Section 3.3 we consider the ways in which the stable solutions for the static case are modified by an increasing relative flow, drawing on basic ideas about flow effects (from Section 2.1.1) and dispersion (from Section 3.2). These effects of flow on incompressible surface modes are put in the context of the qualitative evolution of the propagation windows, from which we may define three regimes for the relative flow (see Section 3.3.1). After first considering the single interface in Section 3.3.2, we then in Section 3.3.3 perform a generalised approach applicable to all mode types of the incompressible single interface, slab and cylinder, and discuss the results in terms of an effective density ratio $f\rho_0/\rho_e$ (with $f = f(|k|a)$ given by (3.2)). Sufficiently large relative flows may lead to the onset of instability in a given mode, and the conditions under which this occurs are examined in detail. The effects of dispersion and plasma inhomogeneity are discussed in terms of the critical case $f = f^* \equiv (\rho_e v_{Ae})/(\rho_0 v_{A0})$. Our unique and thorough approach to this problem leads to new results, in the light of which previous literature studies of the same model are discussed in Section 3.3.4, while in Section 3.3.5 we consider the implications for the compressible case. Finally, in Section 3.4 we summarise our results and present conclusions.

3.2 Static case

As a necessary preliminary to our discussion of the effects of steady flows on incompressible surface modes, we must consider the modes arising for a static equilibrium. This problem has been extensively investigated, and so in this section we present briefly the main results, referring the reader to the original papers for details.

Recall that the general dispersion relation (3.7) is a quadratic in c_p, thereby yielding two solutions (3.8) for c_p, which may propagate in the positive ($c_p > 0$) or negative ($c_p < 0$) magnetic field direction. For the static case, the coefficient of c_p in (3.7) vanishes, yielding

symmetric solutions for c_p that represent two waves propagating at the same speed $|c_p|$ but in opposite directions. Thus, for the static case, we need consider only one of these solutions, say $c_p > 0$.

3.2.1 Single interface

Consider first the single interface. We obtain

$$c_p{}^2 = \frac{\rho_0 v_{A0}{}^2 + \rho_e v_{Ae}{}^2}{\rho_0 + \rho_e} \equiv c_k{}^2 \tag{3.11}$$

The characteristic speed c_k of these modes is termed the *kink speed*, and first appeared in the work of . (Kruskal and Schwarzschild (1954); see also Wentzel (1979) and Roberts (1981a). This speed also arises in the description of the modes of a slender flux tube (Ryutov and Ryutova 1976, Parker 1979b, Spruit and Roberts 1983, Roberts 1990, Roberts and Ulmschneider 1997), as noted in Section 2.3.

There are a number of points to be noted about the kink speed c_k. It is a weighted average of the two Alfvén speeds (squared), and hence represents a *"mean" Alfvén speed*, which reflects the fact that the mode involves two media, each with different properties. The weights of each speed in this average are the respective densities, and since these are necessarily positive $c_k{}^2$ must lie between $v_{A0}{}^2$ and $v_{Ae}{}^2$. This confirms that the phase speed satisfies the general requirement for surface modes (given a static equilibrium) that it is intermediate between the two Alfvén speeds. The value of $c_k{}^2$ depends on the density ratio ρ_0/ρ_e, and is nearer to the square of the Alfvén speed of the medium with higher density.

3.2.2 Slab and cylinder

For the single interface the surface wave propagation speed is independent of wavelength, rendering the mode nondispersive. This is not surprising, given that there is no natural lengthscale to measure wavelengths against. However, for a finite-width inhomogeneity, such as a slab or cylinder, there *is* a natural lengthscale, and this will be "noticed" to different extents by modes of different wavelengths, with short wavelengths being the least affected. Hence, the surface modes of a slab or cylinder, while analogous to those of a single interface, differ from the interface modes in the important respect that they are

dispersive. Also, we obtain two types of modes, termed kink or sausage according to whether or not the centre of the slab or cylinder is displaced. The dispersive properties depend not only on wavelength but also on geometry, leading to differences between slab and cylinder results, as well as between kink and sausage modes.

Despite these differences, in all cases we may write the characteristic speed in the general form

$$c_p{}^2 = \frac{f\rho_0 v_{A0}{}^2 + \rho_e v_{Ae}{}^2}{f\rho_0 + \rho_e} \equiv c_{k_{eff}}{}^2 \tag{3.12}$$

with $f \equiv f(|k|a)$ defined by (3.2), from which we may alternatively write (3.12) as

$$c_p{}^2 = \frac{f_0\rho_0 v_{A0}{}^2 + f_e\rho_e v_{Ae}{}^2}{f_0\rho_0 + f_e\rho_e}; \tag{3.13}$$

$f_0(|k|a)$ and $f_e(|k|a)$ are defined for each mode in Table 3.1. The expressions (3.12) and (3.13), being closely similar to (3.11), demonstrate clearly the analogy between the incompressible surface modes of single interface, slab and cylinder. We therefore refer to $c_{k_{eff}}$, defined in (3.12), as representing an *"effective" kink speed*, which instead of being constant, depends on both the wavelength and the type of mode, through $f(|k|a)$.

Treating $c_{k_{eff}}$ as a weighted average of v_{A0} and v_{Ae}, we note that in all cases both weights are positive, since $f(|k|a) > 0$. Hence we may note immediately that for all mode types and at all wavenumbers, the effective kink speed satisfies the usual requirement for the propagation speed of surface modes in static media to be intermediate between the two Alfvén speeds. Whereas for the single interface case the (constant) value that $c_p{}^2 = c_k{}^2$ takes within this range depends on the density ratio ρ_0/ρ_e, for the dispersive modes of the slab or cylinder it is an *"effective" density ratio*, $f\rho_0/\rho_e$, that comes into play. Then the incompressible surface modes of the slab and cylinder are basically analogous to those of the single interface, and we may think of the dispersive effects in terms of the given mode behaving like a single interface mode which *perceives* this effective density ratio rather than the true density ratio ρ_0/ρ_e, where the effective density ratio depends on geometry, mode type and wavelength.

In Figures 3.2 and 3.3, taking $v_{A0} > v_{Ae}$ and $v_{A0} < v_{Ae}$ respectively, we plot the dispersion curves for each geometry and mode type, and various values of the density ratio ρ_e/ρ_0. We note that our parameter choices in Figures 3.2 and 3.3 allow us to demonstrate the symmetry properties of $c_{k_{eff}}$, on which we now comment. From the form of $c_{k_{eff}}{}^2$ we

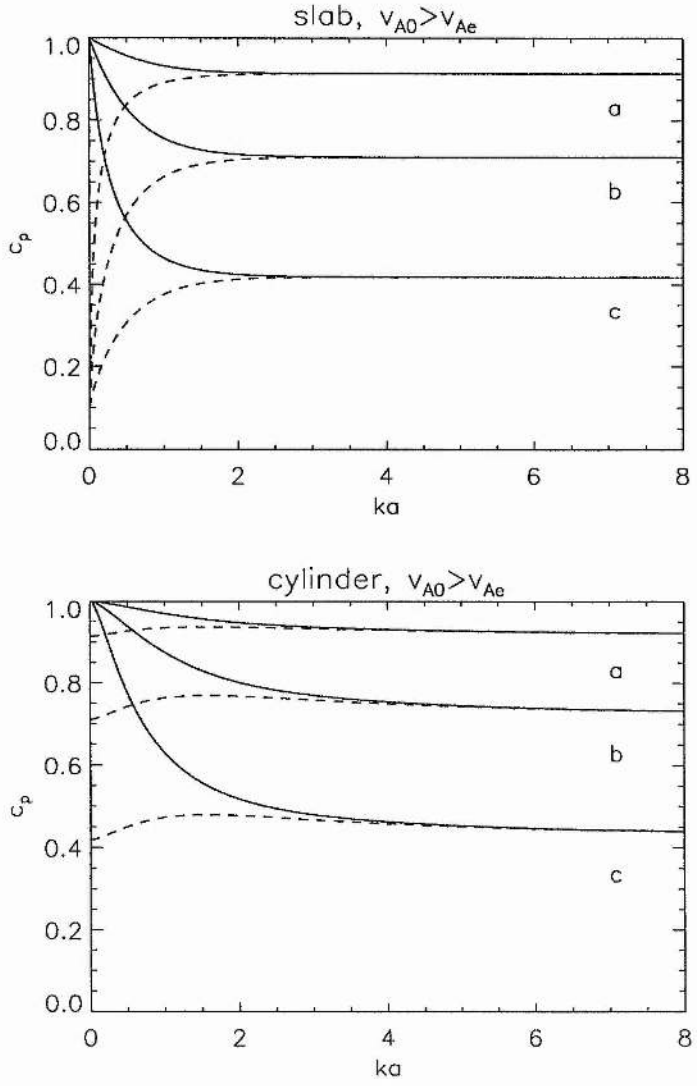

Figure 3.2: Dispersion diagrams for the incompressible slab and cylinder in the absence of flows, for $v_{Ae} = 0.1v_{A0}$, and various density ratios ρ_e/ρ_0. All speeds are expressed in units of the internal Alfvén speed v_{A0}. In each plot of the phase speed c_p v. dimensionless wavenumber ka, curves a, b and c correspond to density ratio $\rho_e/\rho_0 = 0.2$, 1.0 and 5.0 respectively. Solid lines correspond to sausage modes, dashed lines to kink modes. With $v_{A0} > v_{Ae}$, each kink curve of the cylinder has a maximum at $|k|a \approx 1.6$; all other dispersion curves are monotonic in ka.

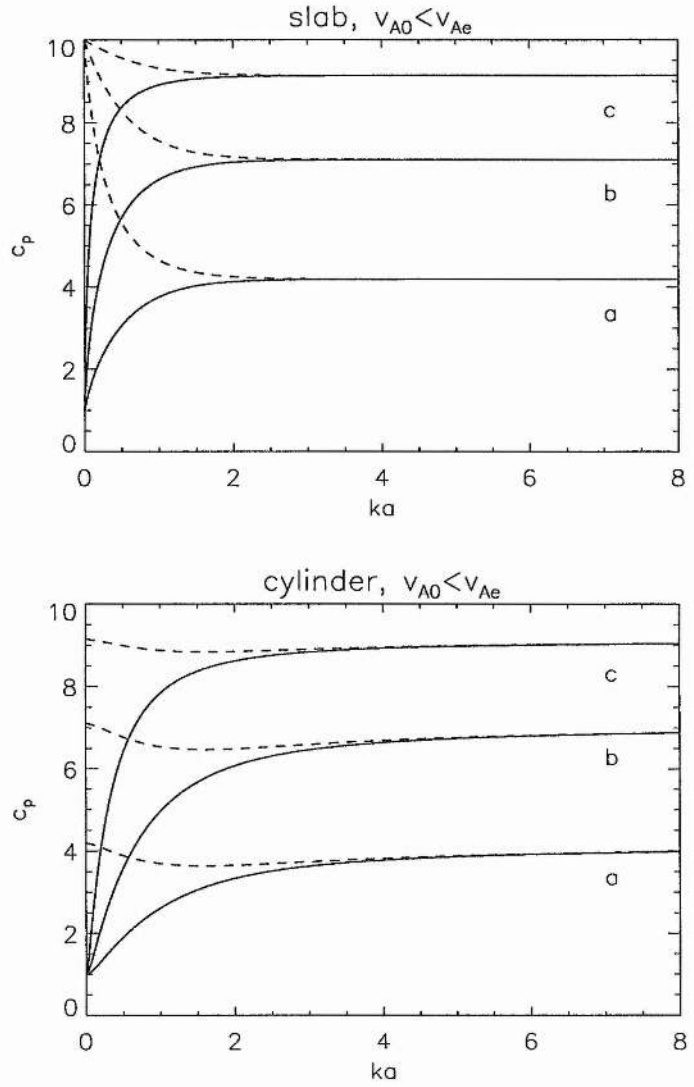

Figure 3.3: Dispersion diagrams for the incompressible slab and cylinder in the absence of flows, for $v_{Ae} = 10.0v_{A0}$. The density ratios considered (cases a, b and c) are as given in Figure 3.2, and again all speeds are expressed in units of the internal Alfvén speed v_{A0}. With $v_{A0} < v_{Ae}$, each kink curve of the cylinder has a minimum at $|k|a \approx 1.6$; all other dispersion curves are monotonic in ka.

note that if we take the reciprocals of the ratios ρ_e/ρ_0 and v_{Ae}/v_{A0}, then we obtain the same value of $c_{k_{eff}}$ if we also take the reciprocal of f, i.e. if we swap f_0 and f_e. For the slab we have $f_{saus} \equiv 1/f_{kink}$, so that there is a direct equivalence between the sausage (kink) modes of a given configuration of plasmas and the kink (sausage) modes of a configuration in which the plasmas are interchanged (so that the internal medium is now the external medium and vice versa). Therefore the slab diagrams in Figures 3.2 and 3.3 are identical apart from the linestyles and vertical scale. For the cylinder, there is no exact equivalence between f and $1/f$ for the sausage and kink modes, as can be seen by the fact that the two diagrams are different (particularly for small values of $|k|a$).

Consider now the extreme $|k|a \to \infty$, corresponding to short wavelengths with respect to the width of the inhomogeneity. On physical grounds, we may expect that modes of short enough wavelengths or in a wide enough inhomogeneity will "notice" only one of the interfaces, the other being too far away to have a strong influence on the modes. Hence sausage and kink modes ought to behave similarly to each other in such cases, and be essentially the same as if only one interface were present, this holding true for both slab and cylinder. That all cases reduce to the single interface result in this limit is also apparent on mathematical grounds, as was shown for the general compressible case in Section 2.3, and therefore holds also for the incompressible case. For each mode, c_k and $c_{k_{eff}}$ coincide in this limit, since $\lim_{|k|a\to\infty} f(|k|a) = 1$ for all sausage and kink modes (Uberoi and Somasundaram 1980, Roberts 1981b, Edwin and Roberts 1982, 1983). This is clear from the plots in Figure 3.1 of $f(|k|a)$ for each mode type.

In the opposite extreme $|k|a \to 0$, corresponding to wavelengths that are long with respect to the slab or cylinder width, we intuitively expect the modes to be strongly affected by the presence of *both* interfaces and also to be strongly influenced by the geometry (slab or cylinder) of the inhomogeneity and the particular mode (sausage or kink) it supports. The variation of $f(|k|a)$ shown in Figure 3.1 supports this view, where for $|k|a$ of order 1 or smaller we see very different curves for the sausage modes compared with the kink modes and also for the slab geometry compared with the cylinder geometry.

We may derive approximations to the phase speeds for each mode at small values of $|k|a$. For the slab these long wavelength approximations are given by (Edwin and

Roberts 1982)

$$\frac{\omega^2}{k^2} \approx \begin{cases} {v_{A0}}^2 \left[1 + \frac{\rho_e}{\rho_0}\left(\frac{{v_{Ae}}^2}{{v_{A0}}^2} - 1\right)|k|a\right], & \text{sausage} \\ {v_{Ae}}^2 \left[1 + \frac{\rho_0}{\rho_e}\left(\frac{{v_{A0}}^2}{{v_{Ae}}^2} - 1\right)|k|a\right], & \text{kink} \end{cases} \tag{3.14}$$

while for the cylindrical case the results are (Edwin and Roberts 1983)

$$\frac{\omega^2}{k^2} \approx \begin{cases} {v_{A0}}^2 \left[1 + \frac{\rho_e}{\rho_0}\left(\frac{{v_{Ae}}^2}{{v_{A0}}^2} - 1\right)\frac{(ka)^2}{2} K_0(|k|a)\right], & \text{sausage} \\ {c_k}^2 \left[1 + \frac{\rho_0\rho_e}{\rho_0+\rho_e}\left(\frac{{v_{A0}}^2 - {v_{Ae}}^2}{\rho_0 {v_{A0}}^2 + \rho_e {v_{Ae}}^2}\right)(ka)^2 K_0(|k|a)\right], & \text{kink.} \end{cases} \tag{3.15}$$

These analytical results explain the general features demonstrated in Figures 3.2 and 3.3. The sausage modes of both geometries have limiting phase speed v_{A0}, and while the slab kink mode has limiting phase speed v_{Ae}, that of the cylinder kink mode is c_k. If $v_{Ae} > v_{A0}$, then for both geometries ${c_p}^2$ is an increasing function of $|k|a$ for sausage modes and decreasing for kink modes; the reverse is the case if $v_{A0} > v_{Ae}$. We have already noted that in the opposite extreme, $|k|a \to \infty$, the single interface is recovered for all modes and there is no distinction between either geometry or mode type since as far as the mode is concerned there is only one interface and it is flat. Hence all dispersion curves converge for $|k|a \to \infty$ with ${c_p}^2 \to {c_k}^2$. We noted above that the value of ${c_k}^2$ is nearest to the squared Alfvén speed of the medium with higher density. The effect of this is that for $\rho_0 \gg \rho_e$ the sausage modes of both geometries are almost nondispersive, while the slab kink mode is almost nondispersive for $\rho_e \gg \rho_0$. The cylinder kink mode is always only weakly dispersive, with the same limiting phase speed, c_k, for both extremes in $|k|a$. For this mode $c_p(ka)$ has a turning point at the same value of $|k|a$ as does $f(|k|a)$, namely $|k|a \approx \pi/2$, corresponding to the longitudinal wavelength being approximately equal to twice the diameter of the tube.

In summary, we note that in the static incompressible case, the surface modes of the uniform slab and cylinder are closely similar to those for the single interface. However, for the slab and cylinder the frequencies are determined by the "effective" density ratio, $f\rho_0/\rho_e$, as "perceived" by a particular mode with a given wavenumber for a particular geometry (that is, for a given value of $f(|k|a) \equiv f_0(|k|a)/f_e(|k|a)$). In all cases the effective density ratio approaches the true density ratio in the short wavelength extreme, while in the opposite extreme of long wavelengths the effective density ratio depends strongly on the mode type and geometry. In the static case, all modes are stable.

3.3 Development of incompressible surface modes with increasing relative flow

We now consider how the solutions obtained for the static case are modified by the presence of field-aligned steady flows, and in particular the evolution of these solutions with increasing relative flow. This evolution of stable solutions is discussed in terms of the changing qualitative properties of the propagation windows. Sufficiently large relative flows may cause a given mode to go unstable, and we analyse in detail the conditions under which this occurs.

In this, we apply a generalised treatment applicable to the single interface, uniform slab and uniform cylinder, for all modes and wavenumbers. This allows us to compare the results, identifying general features and formulating differences between cases in terms of the effective density ratio $f\rho_0/\rho_e$, for which a critical value is obtained.

3.3.1 Evolution of propagation windows with flow

We consider in detail the properties of the solutions to the dispersion relation, for each geometry. As a preliminary, we resume our discussion of the propagation windows, describing the ranges of c_p for which stable modes *may* exist, and from which we may glean useful information about the properties of the solutions.

The propagation windows for stable incompressible surface modes are defined by the general surface mode condition noted earlier that the terms ε_0 and ε_e have opposite signs, where $\varepsilon_i = \rho_i k^2({v_{Ai}}^2 - (c_p - U_i)^2)$. That is, given a real solution $c_p \equiv \omega/k$ of the form (3.8), this condition implies that if, say, ${v_{Ae}}^2 > (c_p - U_e)^2$ then ${v_{A0}}^2 < (c_p - U_0)^2$, and vice versa. In general, these conditions yield two ranges in which stable (i.e. real) solutions for c_p may lie. We will refer to the range containing larger values of c_p as the *first range* and the other range as the *second range*. The ranges are bounded by the lines $c_p = U_i \pm v_{Ai}$, through which $\varepsilon_i = 0$, corresponding to degenerate cases.

The nature of the propagation windows depends on the relative ordering of these range limits, which for given v_{A0}, v_{Ae} is in turn determined by the magnitude U_D of the relative flow, given by

$$U_D \equiv |U_0 - U_e|. \tag{3.16}$$

Note that $U_D > 0$ is independent of the reference frame. In Figure 3.4 we illustrate the evolution of the propagation windows as U_D is increased from zero, taking as an example the parameter case $v_{Ae} > v_{A0}$ (specifically $v_{Ae} = 3v_{A0}$) and reference frame $U_0 \geq U_e = 0$ (then $U_D = U_0$), so that the region labelled "0" is moving in the positive z-direction, the other region being static. The propagation windows are given by the unshaded regions.

As U_D increases within a fixed reference frame, we find that for any given v_{A0} and v_{Ae} there are two crossings of range limits. The *first crossing* occurs when $U_D = |v_{Ae} - v_{A0}|$, and corresponds to a reversal of the upper and lower limits of one of the two ranges. The *second crossing* occurs when $U_D = v_{Ae} + v_{A0}$, where the lower limit of the first range becomes the upper limit of the second range, and vice versa. Prior to the second crossing the ranges may generally be written (in set notation so that the ordering of limits is unspecified) as $c_p \in (U_0 + v_{A0}, U_e + v_{Ae})$ and $c_p \in (U_0 - v_{A0}, U_e - v_{Ae})$, while for $U_D > v_{A0} + v_{Ae}$ they are $c_p \in (U_0 - v_{A0}, U_0 + v_{A0})$ and $c_p \in (U_e - v_{Ae}, U_e + v_{Ae})$.

We may therefore define three flow regimes, *independently of parameter case and reference frame*: $0 < U_D < |v_{Ae} - v_{A0}|$, $|v_{Ae} - v_{A0}| < U_D < v_{Ae} + v_{A0}$ and $U_D > v_{Ae} + v_{A0}$, which we refer to as the *first regime*, *second regime* and *third regime* respectively. The critical relative flow speeds involved, namely $U_D = |v_{Ae} - v_{A0}|$ and $U_D = v_{A0} + v_{Ae}$, can be expected to correspond to critical cases for the qualitative properties of the solutions. The implications of the evolution of the propagation windows for the properties of the modes will be discussed in detail below, in a thorough analysis of the solutions in the presence of flows.

We have defined our three flow regimes in terms of general criteria for the *ordering* of the range limits. Since they involve the *relative* flow U_D they are independent of the frame of reference. They are also independent of the parameter case. It is also of interest to consider critical flows for the *sign* of the range limits, as the conditions under which range limits change sign yield necessary criteria for the appearance of backward modes. However, the critical flow and affected range does depend on reference frame and parameter case. In the case illustrated in Figure 3.4, we obtain $U_D = U_0 > v_{A0}$ as a necessary criterion for the appearance of backward modes in the second range. However, if in our illustration we had instead taken $U_0 = 0$, $U_D = -U_e \geq 0$, corresponding to a different frame of reference for the same relative flow, then we would have obtained the criterion $U_D = -U_e > v_{Ae}$,

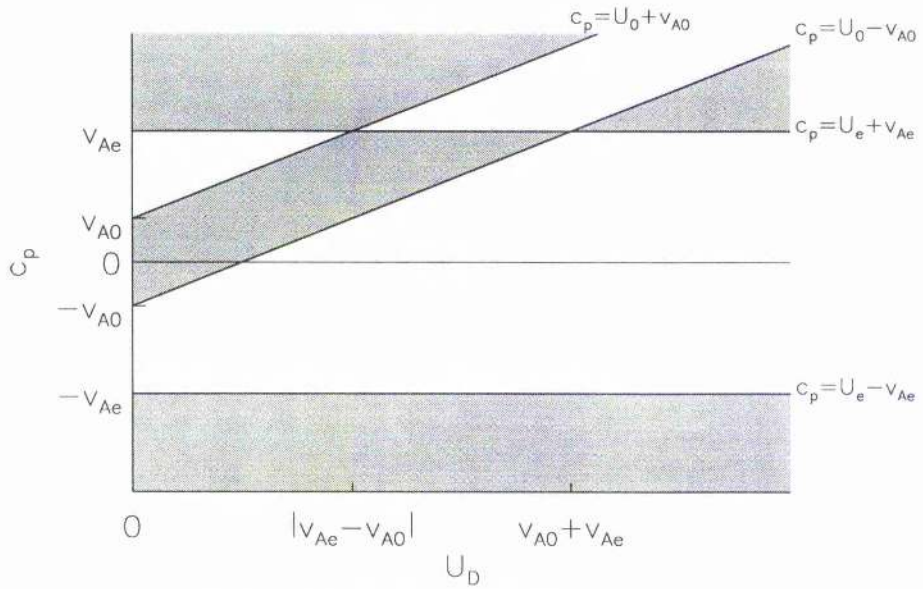

Figure 3.4: Evolution with increasing relative flow $U_D \equiv |U_0 - U_e|$ of the propagation windows for incompressible surface modes, taking as an example $v_{Ae} = 3v_{A0}$, $U_e = 0$ and $U_0 \geq 0$. Stable modes are confined to the unshaded regions, which are bounded by the labelled lines $c_p = U_0 \pm v_{A0}$, $U_e \pm v_{Ae}$. Propagation windows change qualitatively through the critical relative flow values $U_D = |v_{Ae} - v_{A0}|$ and $U_D = v_{A0} + v_{Ae}$.

with the first range being affected.

When either medium is field-free the two crossings coincide and the second regime vanishes, as does the spacing between the ranges within the first regime. When both media are field-free there are no ranges in which stable solutions may lie, so that for any $U_D > 0$ all solutions are unstable, in agreement with results for the hydrodynamic case. For equal fluids there are no incompressible surface modes for the static case (as there is no surface!), although they may exist in the presence of relative flows. With $v_{A0} = v_{Ae}$, the first flow regime vanishes.

3.3.2 Single interface

We now turn to a detailed analysis of the properties of the solutions for c_p in the presence of relative flows. For any given mode type (e.g. slab sausage, or single interface) there are two solutions for c_p, corresponding to the plus ("+") and minus ("−") sign in (3.8). Stable (i.e. real) solutions for c_p may be positive or negative according to the direction of propagation (in the given frame of reference) relative to the positive magnetic field direction. We will discuss the properties of the solutions with increasing flow in terms of the changing qualitative nature of the propagation windows, but first we consider how the stable solutions for the static case are qualitatively modified by flow and ultimately go unstable.

We start with the single interface in order to identify the main features associated with incompressible surface modes of media structured by velocity as well as by plasma properties, reserving a discussion of dispersive effects until the following section, in which the slab and cylinder are studied.

Separation of components and qualitative effects of flow

For the single interface, the solutions for c_p are given by (3.8) with $f = 1$. Rewriting these solutions in terms of those for the static case, given by ${c_p}^2 = {c_k}^2$ (see (3.11) in Section 3.2), we obtain

$$c_p = \frac{\rho_0 U_0 + \rho_e U_e}{\rho_0 + \rho_e} \pm \left\{ {c_k}^2 - \frac{\rho_0 \rho_e}{(\rho_0 + \rho_e)^2} (U_0 - U_e)^2 \right\}^{1/2}. \tag{3.17}$$

Recall our results of Section 2.1.1 for modes of an unstructured medium with a uniform steady field-aligned flow U relative to the given frame of reference. There it was found that where the solutions for the static case are $c_p = \pm c_{ps}$ with $c_{ps} > 0$ specified according to the mode, then for a uniform bulk flow U we obtain $c_p = U \pm c_{ps}$. Then in a uniform bulk flow, both solutions are subject to the same shift U relative to their values for the static case, which is recovered after a change of reference frame so as to be moving with the bulk flow. It is the speed c_{ps} which characterises the mode, since for any U the two solutions are separated by $2c_{ps}$. We therefore refer to c_{ps}, the positive solution to c_p for the static case, as the *basic speed* of the mode, and write the solutions in a uniform bulk flow U as

$$\begin{aligned} c_p &= U \pm c_{ps} \\ &= \mathit{shift} \pm \mathit{basic\ speed}. \end{aligned} \tag{3.18}$$

Comparing this result with (3.17), which gives the solutions for the incompressible surface modes of a single interface allowing for relative flows, we see that we may similarly formulate the solutions for c_p in terms of a shift and a basic speed, although these components are both modified by relative flows. Writing

$$U_m = \frac{\rho_0 U_0 + \rho_e U_e}{\rho_0 + \rho_e}, \qquad c_{pm} = \left\{ {c_k}^2 - \frac{\rho_0 \rho_e}{(\rho_0 + \rho_e)^2}(U_0 - U_e)^2 \right\}^{1/2}, \tag{3.19}$$

(3.17) becomes

$$\begin{aligned} c_p &= U_m \pm c_{pm} \\ &= \mathit{mean\ shift} \ \pm \ \mathit{modified\ basic\ speed}. \end{aligned} \tag{3.20}$$

The shift component U_m is now a *mean shift*, intermediate between the flow speeds U_0 and U_e in the media to either side of the interface and weighted by their respective densities. Note that U_m depends on the density ratio and frame of reference. For any U_m, the two solutions for c_p are now separated by $2c_{pm}$, so that it is the speed c_{pm} which characterises the mode, independently of reference frame. We term c_{pm} the *modified basic speed*, since in the presence of relative flows it is modified from the basic speed $c_{ps} (= c_k$ for the incompressible surface modes of a single interface) arising for an unstructured flow. Our

expression for c_{pm} has been termed in the literature the "phase speed in the centre-of-mass reference frame" (Hollweg et al. 1990, Goossens et al. 1992). In the centre-of-mass reference frame, which satisfies $U_e = -U_0\rho_0/\rho_e$, the mean shift U_m is eliminated to leave symmetric solutions $c_p = \pm c_{pm}$.

In the presence of flow (in the given reference frame) in either or both media, all solutions are shifted from their values $\pm c_{ps}$ for the static case. For a uniform bulk flow $U_0 = U_e = U$ we obtain similar results to those given above for modes of an unstructured medium, here with basic speed $c_{ps} = c_k$ applying to incompressible surface modes of a single interface. For a small relative flow $U_D > 0$, $c_{pm} \approx c_{ps}$ so that both roots are shifted by approximately the same amount, U_m, from their values for the static case, although this shift varies with density ratio whereas for a bulk flow all solutions are subject to the same shift. As U_D increases, c_{pm} decreases from c_{ps} and there is an increasing discrepancy in the shifts to the two roots: the one propagating with the mean flow U_m is shifted by less than U_m, the other root is shifted by more than U_m, both shifts being taken relative to the appropriate static solution and measured in the direction of the mean flow. The latter root becomes a backward mode when $|U_m| > c_{pm}$, in agreement with the general criterion (3.10) for the appearance of backward incompressible surface modes, with $f = 1$ for the single interface. Then the two solutions for c_p share the same sign, and have "opposite energies"in the given frame of reference. For U_D such that $c_{pm} = 0$ the two solutions coalesce and are marginally stable, while for larger relative flows we have ${c_{pm}}^2 < 0$ so that the solutions are complex conjugates, corresponding to the onset of the Kelvin-Helmholtz instability.

The general criterion for the Kelvin-Helmholtz instability for the incompressible case to occur is given by (3.9), which for the single interface $f = 1$ yields (Chandrasekhar 1961)

$$ {U_D}^2 > \left(\frac{\rho_0 + \rho_e}{\rho_0\rho_e}\right)(\rho_0 {v_{A0}}^2 + \rho_e {v_{Ae}}^2) \equiv {U_{KHI}}^2 \tag{3.21} $$

where we denote by U_{KHI} the critical relative flow magnitude at which the incompressible single interface is marginally stable for given $v_{A0}, v_{Ae}, \rho_0, \rho_e$. Criterion (3.21) is in agreement with (2.25) and follows from the reduction of Syrovatskii's conditions (see Landau and Lifshitz 1960, Axford 1960, Sen 1963, Todd 1966) in the special case of magnetic fields, flow and propagation vector all parallel to each other and to the interface.

The general qualitative evolution of a stable incompressible surface mode with increasing relative flow has been similarly discussed (but without reference to negative energy waves) by Parker (1979a), for the case $v_{Ae} = U_0 = 0$ and $\rho_0 = \rho_e$, for which $U_{KHI}{}^2 = 2v_{A0}{}^2$.

Discussion in terms of propagation windows

Having discussed the general features, we now turn to a discussion of the solutions in terms of the evolution of the propagation windows. Let us consider the qualitative features associated with each of the three flow regimes, and their relation to the properties of the solutions. By means of illustration, we use the same parameter regimes and reference frame as we did in our example of Figure 3.4 which showed the evolution of the propagation windows with increasing relative flow, for the case $v_{Ae} > v_{A0}$ (specifically $v_{Ae} = 3v_{A0}$) and $U_e = 0$, $U_D = U_0 \geq 0$. In Figure 3.5 we repeat the information contained in Figure 3.4, but now overplot using broken lines typical solutions for the single interface, taking various values of the density ratio ρ_0/ρ_e, which for the incompressible case may be chosen arbitrarily. We show below that, for v_{Ae} and v_{A0} specified, a critical value of this density ratio is v_{Ae}/v_{A0}. Therefore in Figure 3.5 we chose density ratios greater than, equal to, and less than this critical value. The particular values chosen and corresponding linestyles are $\rho_0/\rho_e = 4v_{Ae}/v_{A0}$ (dotted), $\rho_0/\rho_e = v_{Ae}/v_{A0}$ (dot-dashed) and $\rho_0/\rho_e = 0.25v_{Ae}/v_{A0}$ (dashed), where $v_{Ae}/v_{A0} = 3$. The general qualitative evolution with increasing U_D of the curves for each case is in agreement with our discussion above. Parker (1979a, Figure 1) showed similar curves for the case $v_{Ae} = U_0 = 0$ and $\rho_0 = \rho_e$, although the propagation windows were not included in the plot or the discussion.

For the static case, given by the left hand extreme ($U_D = 0$) of Figure 3.5, the ranges and solutions are symmetric about the horizontal line $c_p = 0$. From Section 3.2 the solutions are $c_p = \pm c_k$ and represent two waves propagating in opposite directions at the same speed c_k, where the kink speed c_k is defined by (3.11). Note that c_k is closer to v_{Ae} for larger values of ρ_e/ρ_0. Thus the curves in Figure 3.5 (for which $v_{Ae} > v_{A0}$) are ordered, as c_p decreases, by increasing values of ρ_0/ρ_e in the first range, with this ordering being reversed in the second range.

Throughout the first flow regime, given by $0 < U_D < |v_{Ae} - v_{A0}|$, one of the ranges

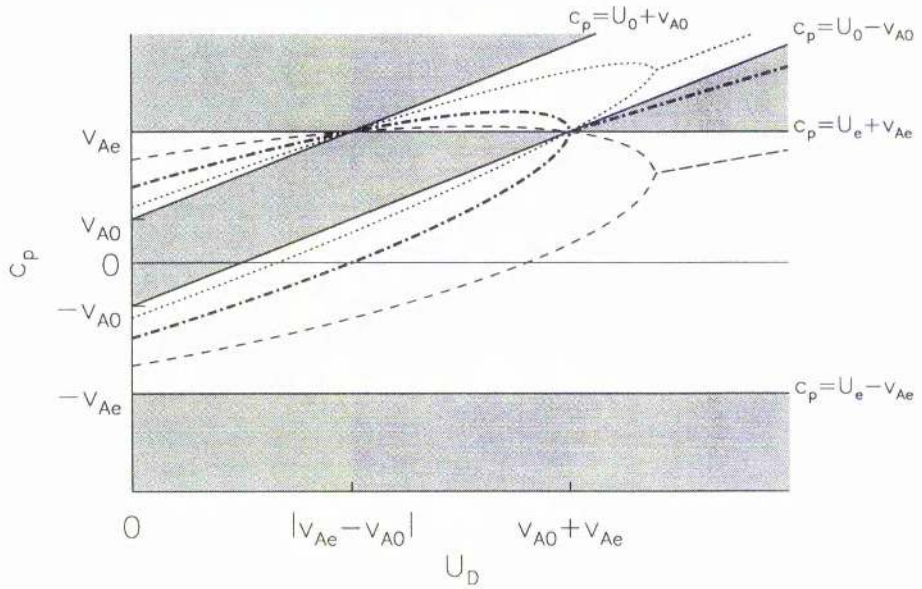

Figure 3.5: As in Figure 3.4, we show the evolution, with increasing relative flow $U_D \equiv |U_0 - U_e|$, of propagation windows (given by the unshaded regions) for incompressible surface modes, for the case $v_{Ae} > v_{A0}$ (specifically $v_{Ae} = 3v_{A0}$), $U_e = 0$ and $U_D = U_0 \geq 0$. Here we also plot using broken lines typical solutions for the single interface for density ratios satisfying $\rho_0/\rho_e > v_{Ae}/v_{A0}$ (dotted), $\rho_0/\rho_e = v_{Ae}/v_{A0}$ (dot-dashed) and $\rho_0/\rho_e < v_{Ae}/v_{A0}$ (dashed). Backward modes exist in the second range when ${U_D}^2 > {v_{A0}}^2 + {v_{Ae}}^2\rho_e/\rho_0$. The two single interface solutions for given ρ_0/ρ_e coalesce when $U_D = U_{KHI}$ (see (3.21), (3.27)), where $U_{KHI}(\geq v_{A0} + v_{Ae}$, with equality for the critical case $\rho_0/\rho_e = v_{Ae}/v_{A0}$) is the threshold for the Kelvin-Helmholtz instability in the incompressible single interface; they are unstable for larger values of U_D, for which we plot the real part of the complex conjugate solutions for $c_p \equiv \omega/k$.

widens while the other shrinks in width, their respective upper and lower limits being shifted by different amounts. Within the first regime, the fixed distance between the ranges ensures that $c_{pm} \in (v_{A0}, v_{Ae})$. In Figure 3.5 the solution curves retain their ordering as for the static case, although in each range they become accordingly more or less spaced. Since $U_m > 0$ in this case, it is the "$-$" root which becomes a backward mode, and with $f = 1$ and $U_e = 0$ the general criterion (3.10) for this to occur reduces to

$$U_0{}^2 > v_{A0}{}^2 + \frac{\rho_e}{\rho_0} v_{Ae}{}^2 \tag{3.22}$$

in agreement with the minimum criterion $U_0 > v_{A0}$ yielded from consideration of the propagation windows.

At the critical case $U_D = |v_{Ae} - v_{A0}|$, the shrinking range vanishes as its limits coincide. Here (3.19) yields

$$c_{pm} = \frac{\rho_0 v_{A0} + \rho_e v_{Ae}}{\rho_0 + \rho_e}. \tag{3.23}$$

All solutions in the shrinking range pass through the first crossing, at which point they are degenerate since $\varepsilon_0 = \varepsilon_e = 0$.

In the second flow regime, given by $|v_{Ae} - v_{A0}| < U_D < v_{A0} + v_{Ae}$, the reversal of the limits of the previously shrinking range is accompanied by a reversal in the ordering of the solution curves within that range: in Figure 3.5, the solutions in the first range are now ordered by decreasing values of ρ_0/ρ_e, in common with those in the second range. The spacing between the ranges now decreases, thereby reducing the lower bound for c_{pm}. Throughout the second regime both ranges widen, although spacing of the various solution curves within each range in Figure 3.5 does not necessarily increase with its width. Note that $d^2 c_p / dU_D{}^2$ varies with density ratio ρ_0/ρ_e and is negative for the "$+$" root and positive for the "$-$" root, so that for $U_m > 0$ the "$+$" root has a turning point at some U_D, as the shift to the solution propagating with the mean flow U_m is held in check by the increasing relative flow, allowing the backward mode to catch up. This turning point may be in the second or third flow regime, depending on the density ratio.

At the critical case $U_D = v_{Ae} + v_{A0}$, the spacing between the ranges vanishes as the lower limit of the first range coincides with the upper limit of the second range. From Figure 3.5 we see that for each value of ρ_e/ρ_0, either or both of the solutions for c_p passes through the second crossing, at which point they are degenerate since $\varepsilon_0 = \varepsilon_e = 0$. For

$U_D = v_{Ae} + v_{A0}$, (3.19) yields

$$c_{pm} = \left| \frac{\rho_0 v_{A0} - \rho_e v_{Ae}}{\rho_0 + \rho_e} \right|, \tag{3.24}$$

from which we may note the critical density ratio $\rho_0/\rho_e = v_{Ae}/v_{A0}$, for which (3.24) reduces to $c_{pm} = 0$, so that *both* roots pass through the second crossing, at which they are marginally stable, with $U_D = U_{KHI}$. This critical density ratio separates those whose "+" or "−" root passes through the second crossing, although the root appropriate to each density ratio case depends on parameter regime; see below. This critical density ratio also yields the smallest value of the stability threshold U_{KHI} for given v_{A0} and v_{Ae}, a point which we return to below.

When U_D is increased further, these coinciding limits swap ranges, and in cases where one root passed through the second crossing, this root also swaps ranges. The third and final regime, given by $U_D > v_{A0} + v_{Ae}$, is qualitatively quite different from the previous two. For $U_D < v_{A0} + v_{Ae}$, the two solutions for c_p for any given case lie within separate ranges, each of whose two limits involve parameters from separate media. However, in the third regime the two limits of each range involve parameters from only one of the media, and the two solutions (where stable) both lie in the same range. The range in which the two solutions lie depends upon the density ratio: for $\rho_0/\rho_e > v_{Ae}/v_{A0}$ both roots, where stable, satisfy $U_0 - v_{A0} < c_p < U_0 + v_{A0}$, while for $\rho_0/\rho_e < v_{Ae}/v_{A0}$ stable solutions lie in the range $U_e - v_{Ae} < c_p < U_e + v_{Ae}$. The ordering of these ranges determines which root passes through the second crossing for a given density ratio case. Therefore it is in the third regime that it first becomes possible for the two solutions to coalesce, yielding a simple *necessary* condition for instability of incompressible surface modes, namely

$$U_D > v_{A0} + v_{Ae}, \tag{3.25}$$

while stability is guaranteed for $U_D < v_{Ae} + v_{A0}$.

Analysis of stability condition

Defining the parameter

$$f^* \equiv \frac{\rho_e v_{Ae}}{\rho_0 v_{A0}}, \tag{3.26}$$

we see that (3.21), which gives the exact stability threshold U_{KHI} for the incompressible single interface, may alternatively be written as

$$U_{KHI}{}^2 = (v_{A0} + f^* v_{Ae}) \left(v_{A0} + \frac{1}{f^*} v_{Ae} \right). \tag{3.27}$$

Thus,

$$U_{KHI}{}^2 - (v_{A0} + v_{Ae})^2 = \frac{(f^* - 1)^2}{f^*} v_{Ae} v_{A0}. \tag{3.28}$$

When $f^* = 1$ the right-handside of (3.28) is zero; for $f^* \neq 1$ the right-handside is positive. We may also use (3.26) to obtain an alternative form for our expression (3.11) for the kink speed c_k:

$$c_k{}^2 = v_{A0} v_{Ae} \left(\frac{v_{A0} + f^* v_{Ae}}{v_{Ae} + f^* v_{A0}} \right), \tag{3.29}$$

reducing to $c_k{}^2 = v_{A0} v_{Ae}$ when $f^* = 1$. The alternative forms (3.27)-(3.29) do not appear be available in the literature.

Then given v_{A0} and v_{Ae}, the smallest value of U_{KHI} is for the critical density ratio $\rho_0/\rho_e = v_{Ae}/v_{A0}$, for which $f^* = 1$ and $U_{KHI} = v_{A0} + v_{Ae}$; this critical case being significant in that it corresponds to the kink speed c_k being equal to the geometric mean of the Alfvén speeds v_{A0} and v_{Ae}. The more extreme f^* is relative to unity, i.e. the more the density ratio ρ_0/ρ_e deviates from the critical value v_{Ae}/v_{A0}, the greater the difference between the actual threshold U_{KHI} and its minimum value $v_{A0} + v_{Ae}$, with the same value of U_{KHI} (but not of c_k) being obtained if f^* is replaced by its reciprocal.

Discussion of approach used

Let us comment on our chosen approach, namely to fix v_{A0} and v_{Ae}, then solve for $c_p \equiv \omega/k$ as a function of U_D for various values of ρ_0/ρ_e. It may be argued that this is a rather unnatural approach in that our chosen parameters are not independent, a more appropriate choice being to fix instead the magnetic field strengths B_0 and B_e. However, our chosen approach has several advantages, as follows.

Firstly, the same propagation windows apply to any given value of ρ_0/ρ_e, and examining the dependency on ρ_0/ρ_e in terms of the evolution of the propagation windows as U_D increases forms a basis for studying the effects of flows on the dispersive modes of the slab and cylinder of a given configuration of plasma parameters. This point is elaborated on in the Section 3.3.3 below.

Secondly, our approach points to a clear definition of a minimum value of the stability threshold U_{KHI}: this minimum, given by $v_{A0} + v_{Ae}$, is determined by the choice of fixed parameters v_{A0} and v_{Ae} and is attained for a particular value of our free parameter ρ_0/ρ_e, for which $f^* = 1$. In such a case, marginal stability occurs at the earliest possible point in the propagation windows diagram, namely at the second crossing of ranges limits. This is a new result. This sense of U_{KHI} having a minimum proves to be of importance in the discussion of dispersive modes.

When considering the effect on U_{KHI}, in absolute terms, of a change in physical parameters (density or magnetic field strength) of either medium, say region "e", it may be useful to instead use the more "natural" parameters ρ_e/ρ_0 and B_e/B_0. Let us apply such an approach to the equal fluids case, for which $\rho_e = \rho_0$, $B_e = B_0$ and $v_{Ae} = v_{A0}$. This case is included in the critical case $f^* = 1$ for which U_{KHI} attains its minimum value (in our sense of the word), with $U_{KHI} = v_{A0} + v_{Ae} = 2v_{A0}$. Holding region "0" fixed, clearly any change in region "e" which increases v_{Ae} will increase U_{KHI}, while a decrease in v_{Ae} may lead to a decrease in U_{KHI}. For the case where a uniform magnetic field $B_e = B_0$ is retained, we may show that for any ratio of densities, $f^* = 1$ so that $U_{KHI} = v_{A0} + v_{Ae}$. Then with B_e fixed, U_{KHI} increases as ρ_e decreases and decreases as ρ_e increases, and has a lower bound of v_{A0} for $\rho_e \gg \rho_0$; at all values of ρ_e, U_{KHI} attains its minimum in our sense of the word. Returning to the equal fluids case, let us this time retain a uniform density $\rho_e = \rho_0$ and alter the magnetic field strength B_e in region "e". Then with $B_e \neq B_0$ we have $f^* \neq 1$, and so $U_{KHI} > v_{A0} + v_{Ae}$. Allowing for oppositely directed magnetic fields, the case $|B_e| > |B_0|$ leads to an increase in U_{KHI}, while for $|B_e| < |B_0|$ the vanishing field case $B_e = 0$ yields the lower bound of $\sqrt{2}v_{A0}$ for U_{KHI}. For $B_e = 0$ we may further reduce U_{KHI} to its minimum value v_{A0} by increasing ρ_e. Therefore a parameter change which reduces U_{KHI} in absolute terms may in fact increase $U_{KHI}/(v_{A0} + v_{Ae})$, so that marginal stability occurs *after* the second crossing of range limits (although the value of U_D at which this occurs may also vary as a result of the parameter change).

Further comments

Returning to our discussion of Figure 3.5, we have seen that the critical case $\rho_0/\rho_e = v_{Ae}/v_{A0}$ acts as a separator for the topological properties of the solution curves for different

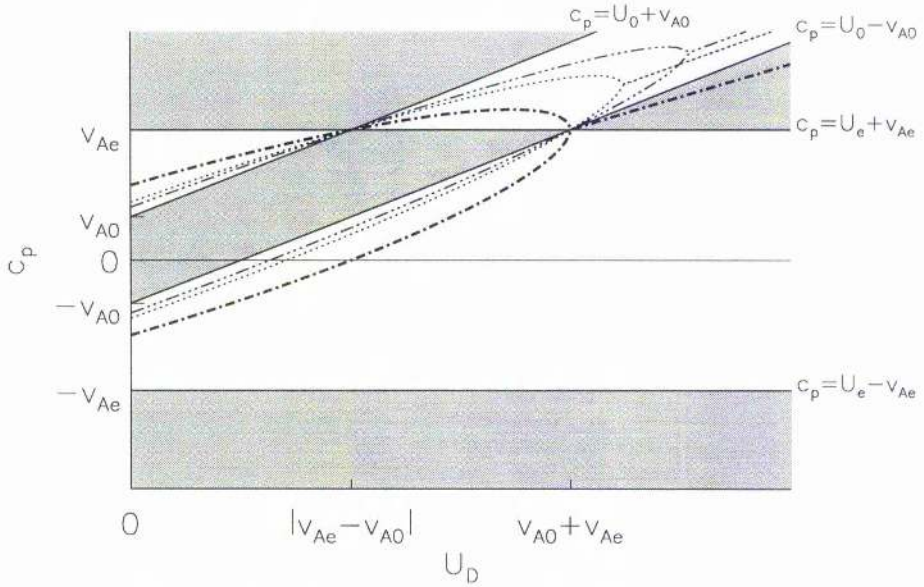

Figure 3.6: As Figure 3.5, but with $\rho_0/\rho_e \geq v_{Ae}/v_{A0}$, specifically $\rho_0/\rho_e = v_{Ae}/v_{A0}$ (heavy dot-dashed), $\rho_0/\rho_e = 3v_{Ae}/v_{A0}$ (dotted) and $\rho_0/\rho_e = 5v_{Ae}/v_{A0}$ (dot-dot-dot-dashed).

values of ρ_0/ρ_e, given v_{Ae}/v_{A0}. In Figures 3.6 and 3.7 we show further examples of the cases $\rho_0/\rho_e \geq v_{Ae}/v_{A0}$ and $\rho_0/\rho_e \leq v_{Ae}/v_{A0}$ respectively, which demonstrate the topological features characteristic of each case and the effects of varying ρ_0/ρ_e within each case. The features are in agreement with the above analysis.

Finally, we comment on the effect on the solution curves of a change of reference frame for the same relative flow $U_0 - U_e$. Figure 3.8 shows solution curves for the same parameter sets as in Figure 3.5, but in a reference frame in which region "0" is stationary and the flow in region "e" is in the negative z-direction, i.e. we take $U_0 = 0$, $U_D = -U_e > 0$. We see that a change of reference frame only leads to quantitative changes, with the main differences being associated with backward modes. Neglecting differences in the sign of c_p, the topological properties of Figures 3.5 and 3.8 are the same. This reflects the invariance of physics with reference frame.

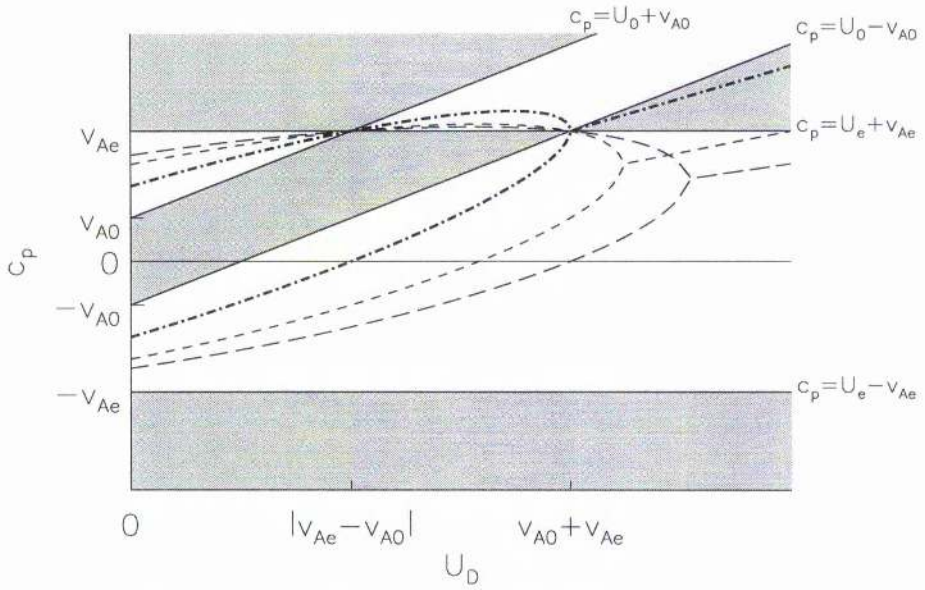

Figure 3.7: As Figure 3.5, but with $\rho_0/\rho_e \leq v_{Ae}/v_{A0}$, specifically $\rho_0/\rho_e = v_{Ae}/v_{A0}$ (heavy dot-dashed), $\rho_0/\rho_e = v_{Ae}/(3v_{A0})$ (dashed) and $\rho_0/\rho_e = v_{Ae}/(5v_{A0})$ (long-dashed).

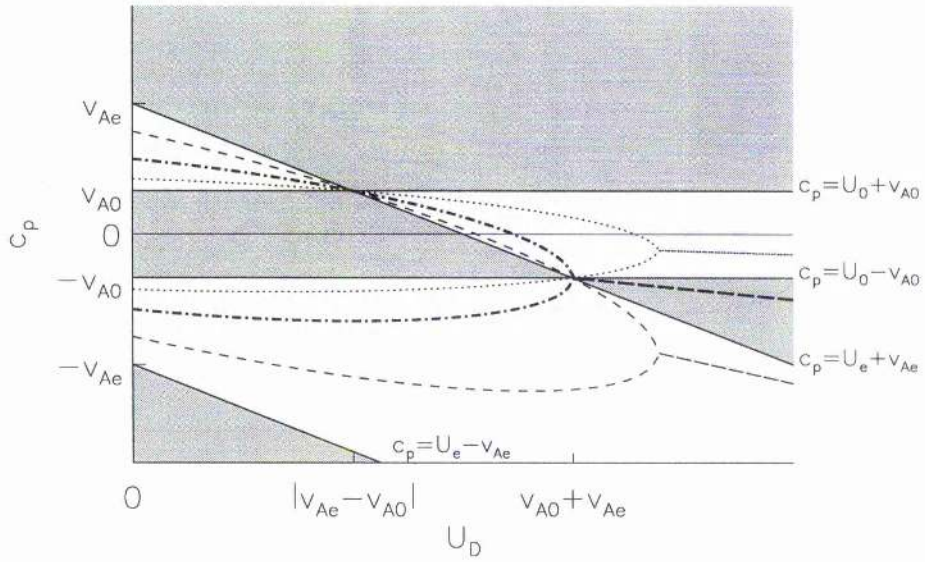

Figure 3.8: As Figure 3.5, but with a change of reference frame such that $U_0 = 0$ and $U_e \leq 0$, i.e. $U_D = -U_e$.

3.3.3 Slab and cylinder

Separation of components and generalised model

Following our discussion for a single interface, we may consider the cases of a slab or cylinder, and write the general solutions (3.8) in terms of a shift component and a basic speed component:

$$\begin{aligned} c_p &= \frac{f\rho_0 U_0 + \rho_e U_e}{f\rho_0 + \rho_e} \pm \left\{ {c_{k_{eff}}}^2 - \frac{f\rho_0\rho_e}{(f\rho_0+\rho_e)^2}(U_0 - U_e)^2 \right\}^{1/2} \\ &= U_m \pm c_{pm} \\ &= \textit{mean shift } \pm \textit{ modified basic speed} \end{aligned} \tag{3.30}$$

where now the mean shift U_m and modified basic speed c_{pm} are

$$U_m = \frac{f\rho_0 U_0 + \rho_e U_e}{f\rho_0 + \rho_e}, \qquad c_{pm} = \left\{ {c_{k_{eff}}}^2 - \frac{f\rho_0\rho_e}{(f\rho_0+\rho_e)^2}(U_0 - U_e)^2 \right\}^{1/2} \tag{3.31}$$

with $f = f(|k|a)$ defined according to the geometry and mode type (see Table 3.1 and Figure 3.1). The effective kink speed $c_{k_{eff}}$ is given by (3.12). In the absence of relative flows, i.e. for $U_0 = U_e = U$, (3.31) yields $U_m = U$ and $c_{pm} = c_{k_{eff}}$.

Comparing (3.31) with (3.19) we see that when allowing for relative flows, just as for the static case (see Section 3.2), the incompressible surface modes of the uniform slab or cylinder are basically analogous to those of the single interface, but with the effective density ratio $f\rho_0/\rho_e$ (as perceived by a particular mode at a particular wavelength) replacing the true density ratio ρ_0/ρ_e, so that $c_{k_{eff}}$ replaces c_k as the basic speed c_{ps} in the absence of relative flows. For all modes, the results for the single interface of density ratio ρ_0/ρ_e are recovered in the short wavelength limit $|k|a \to \infty$, in which $f = 1$ and $c_{k_{eff}} = c_k$.

We may think of (3.30) and (3.31) as a generalised case which, in addition to describing the modes of the slab and cylinder, contains the special case of a single interface (given by $f = 1$). In the general case we are interested in the effects of dispersion, associated with the variation of $f(|k|a)$, for each mode type.

Long wavelength solutions for slab and cylinder

Let us examine the long wavelength extreme, given by $|k|a \ll 1$. In our general discussion of surface modes in Section 2.3, we derived reduced forms of the dispersion relation (2.77)

applicable to each particular mode, for the case $x_0 \ll 1$, $x_e \ll 1$ where $x_0 = m_0 a$ and $x_e = m_e a$. For the incompressible case, $x_0 = x_e = |k|a$, and we may similarly derive reduced forms of (3.3) for small values of the parameter $x \equiv |k|a$, corresponding to the long wavelength extreme $|k|a \ll 1$. Given the appropriate reduced dispersion relation, we then seek for $x \ll 1$ a series solution of the form $c_p = C_0 + C_1 x + C_2 x^2 + \ldots$, the coefficients C_i to be determined for each geometry and mode type.

Consider the incompressible slab. To lowest order in $x \equiv |k|a$, the reduced dispersion relations obtained are

$$\frac{\varepsilon_e}{\varepsilon_0} = \begin{cases} -\frac{1}{x}, & \text{sausage} \\ -x, & \text{kink.} \end{cases} \tag{3.32}$$

For the slab sausage modes we obtain the solutions

$$c_p \approx U_0 + v_{A0} + \frac{\rho_e}{2\rho_0 v_{A0}} \left[{v_{Ae}}^2 - (U_o - U_e + v_{A0})^2 \right] |k|a \tag{3.33}$$

$$c_p \approx U_0 - v_{A0} - \frac{\rho_e}{2\rho_0 v_{A0}} \left[{v_{Ae}}^2 - (U_o - U_e - v_{A0})^2 \right] |k|a \tag{3.34}$$

while for the slab kink modes we find

$$c_p \approx U_e + v_{Ae} + \frac{\rho_0}{2\rho_e v_{Ae}} \left[{v_{A0}}^2 - (U_o - U_e - v_{Ae})^2 \right] |k|a \tag{3.35}$$

$$c_p \approx U_e - v_{Ae} - \frac{\rho_0}{2\rho_e v_{Ae}} \left[{v_{A0}}^2 - (U_o - U_e + v_{Ae})^2 \right] |k|a. \tag{3.36}$$

For the static case we recover the symmetric solutions for c_p given by Edwin (1984), and the solutions given here for flows are in agreement with the incompressible limit of those in Chakraborty (1968).

Turning now to the cylinder, to lowest order in $x \equiv |k|a$ the reduced dispersion relations obtained are

$$\frac{\varepsilon_e}{\varepsilon_0} = \begin{cases} -\frac{2}{x^2 K_0(x)}, & \text{sausage} \\ -\left[\frac{1+x^2 K_0(x)}{1+x^2/4}\right], & \text{kink.} \end{cases} \tag{3.37}$$

For the cylinder sausage modes we obtain

$$c_p \approx U_0 + v_{A0} + \frac{\rho_e K_0(|k|a)}{4\rho_0 v_{A0}} \left[{v_{Ae}}^2 - (U_o - U_e + v_{A0})^2 \right] (ka)^2 \tag{3.38}$$

$$c_p \approx U_0 - v_{A0} - \frac{\rho_e K_0(|k|a)}{4\rho_0 v_{A0}} \left[{v_{Ae}}^2 - (U_o - U_e - v_{A0})^2 \right] (ka)^2. \tag{3.39}$$

For the cylinder kink modes the two roots may be written as

$$c_p = C_0 + \frac{\rho_0 K_0(|k|a) \left[{v_{A0}}^2 - (C_0 - U_0)^2 \right]}{2\left[\rho_0 (C_0 - U_0) + \rho_e (C_0 - U_e)\right]} (ka)^2 \tag{3.40}$$

where C_0 is either of the roots for the single interface, which satisfy

$$\rho_e \left((C_0 - U_e)^2 - {v_{Ae}}^2 \right) + \rho_0 \left((C_0 - U_0)^2 - {v_{A0}}^2 \right) = 0. \tag{3.41}$$

For the static case, the solutions for both mode types are in agreement with those obtained by Edwin (1984). With flows included the sausage mode solutions reduce to those given by Roberts (1987) for the case $v_{Ae} = U_e = 0$.

All the long wavelength expansions given above show clearly that, apart from the basic shift in phase speed, the dispersive properties differ from the static case (see (3.14)–(3.15)) only in the presence of *relative* flows ($U_e \neq U_0$). Further, in certain cases the relative flow may cause a mode to undergo a reversal of its dispersive properties, so that $c_p(|k|a)$ changes from increasing to decreasing, or vice versa. We note that our long wavelength solutions, derived in the linear regime, may also be applied in the investigation of weakly nonlinear effects such as soliton propagation, for which the reader is referred to Roberts (1987). Another nonlinear effect is the steepening of wavefronts (Hollweg 1987); see Section 3.3.4 below.

Discussion of approach and qualitative effects of flow

Our method of investigation of the properties of the solutions (3.30) will be similar to that used in Section 3.3.2 for the single interface: we fix v_{A0} and v_{Ae}, and investigate the evolution of the stable solutions for c_p as the relative flow magnitude $U_D \equiv |U_0 - U_e|$ increases from zero (within a fixed reference frame), for given ρ_0/ρ_e. By this approach, the propagation windows for a given U_D are determined by the choice of Alfvén speeds and reference frame (see Section 3.3.1), and apply to all incompressible surface modes under consideration, irrespective of $f\rho_0/\rho_e$. The results may therefore be compared to those obtained for the single interface: features which for the single interface are dependent on density ratio, are now similarly dependent on $f(|k|a)$ in the case of the slab or cylinder, and we may infer the dependence on $|k|a$ from our knowledge of $f(|k|a)$ for each geometry and mode type. Further, we may discuss the qualitative evolution of the solutions with increasing U_D with reference to the three general flow regimes we defined earlier in terms of the sum $v_{A0} + v_{Ae}$ and difference $|v_{Ae} - v_{A0}|$ of the Alfvén speeds.

A specific illustration is of interest, for which we refer to Figures 3.9–3.18. We use

the same parameter regime and reference frame as for our previous examples (Figures 3.4–3.7), namely $v_{Ae} = 3v_{A0}$, $U_e = 0$, $U_D = U_0 \geq 0$, so that for any given incompressible surface mode the propagation windows are given by Figure 3.4. We choose a fixed density ratio $\rho_0/\rho_e = 1$.

Figure 3.9 is discussed below. In each of Figures 3.10–3.17, we choose a particular value of U_0 and display the two solutions (3.30) for $c_p(|k|a)$ for each mode type, with sausage and kink modes indicated by solid and dashed lines respectively; the slab and cylinder modes are shown in separate plots. All speeds are expressed in units of v_{A0}. In cases where the solutions for c_p are complex conjugates their real part is shown (this occurs in Figures 3.15–3.17), with the magnitude of the corresponding imaginary part of c_p is shown in Figure 3.18. The magnitude of imag (kc_p) gives the growth rate of an unstable mode.

For all modes, as $|k|a \to \infty$, $f \to 1$ and the "+" and "–" roots (3.30) tend to their single interface counterparts (equation (3.17) with density ratio $\rho_0/\rho_e = 1$), which are indicated at the right-handside of each plot by an asterisk and a diamond respectively.

There are two ways in which we can relate the solutions for the slab or cylinder to those of the single interface:

1. At a fixed value of U_D, that is for a particular one of Figures 3.10–3.17, the dispersion of the solutions for c_p is related to the dependence on density ratio for the single interface at the given value of U_D, for which we may refer to back Figure 3.5.

   In the context of the propagation windows, this variation with density ratio was shown to differ within each flow regime. Hence for the slab and cylinder we can expect qualitative changes in the dispersive properties of a given mode as U_D enters each flow regime.

2. At a fixed value of $|k|a$, the two solutions for any given mode type in Figures 3.10–3.17 may may thought of as snapshots of the curves of $c_p(U_D)$ for the single interface of density ratio $f\rho_0/\rho_e$, with typical curves given in Figure 3.5. Then, as noted also by Parker (1979a) for the slab case, at any given wavelength of a particular mode the general behaviour of the two solutions for c_p as U_D increases is the same as for the single interface: compared to their values for the static case, both solutions are shifted in the direction of the mean flow U_m, the solution propagating against the

mean flow becomes a backward mode when $|U_m| > c_{pm}$ and coalesces with the other solution when $c_{pm} = 0$, leading to the Kelvin-Helmholtz instability with complex conjugate solutions for c_p as U_D is increased further.

The thresholds for the appearance of the backward mode and the occurrence of marginal stability, depend on the density ratio for the single interface and on $f(|k|a)$ for the slab or cylinder. In the context of the propagation windows, for the single interface the critical case $\rho_0/\rho_e = v_{Ae}/v_{A0}$ acts as a topological separator for the $c_p(U_D)$ curves for different density ratios, this being particularly evident in the third flow regime, and also yields the minimum value (for given v_{A0} and v_{Ae}) of the stability threshold U_{KHI}. This minimum value, given by $U_D = v_{A0} + v_{Ae}$, marks the beginning of the third flow regime and is the smallest relative flow at which the two solutions for c_p may coalesce. For the slab and cylinder we expect the critical effective density ratio $f\rho_0/\rho_e = v_{Ae}/v_{A0}$ to feature in a similar way. For a fixed ρ_0/ρ_e this yields a critical value f^* of $f(|k|a)$, namely $f(|k|a) = (\rho_e v_{Ae})/(\rho_0 v_{A0}) \equiv f^*$.

Figure 3.9 is identical to Figure 3.5, except here we mark with vertical lines the values of U_D chosen in Figures 3.10–3.17, and show single interface solutions for the density ratios of particular interest to our illustrated slab and cylinder results: these values and corresponding linestyles are $\rho_0/\rho_e = 1$ (dotted), $\rho_0/\rho_e = 1.42$ (dot-dot-dot-dashed) and $\rho_0/\rho_e = 3$ (dot-dashed), which respectively correspond to the short wavelength limit of all modes (and long wavelength limit of the cylinder kink mode), the turning point of the cylinder kink mode (at which $f(|k|a) = f_{max} \approx 1.42$), and the critical case $f = f^*$.

Then for the illustrative case the basic properties of the slab and cylinder modes shown in Figures 3.10–3.17, may be inferred from Figures 3.1 and 3.9. The lines $c_p = U_0 \pm v_{A0}$ give the long wavelength limits of the sausage modes of both geometries and the lines $c_p = U_e \pm v_{Ae}$ give the long wavelength limits of the slab kink mode, the other cases of interest being noted from the solution curves in Figure 3.9. The behaviour of $c_p(|k|a)$ between these values is determined by the form of $f(|k|a)$ for the given mode type, shown in Figure 3.1.

Consider the static case, shown in Figure 3.10. The dispersion diagrams are similar to those of Figure 3.3, extended here to $c_p < 0$ so as to include both solutions $c_p = \pm c_{k_{eff}}$

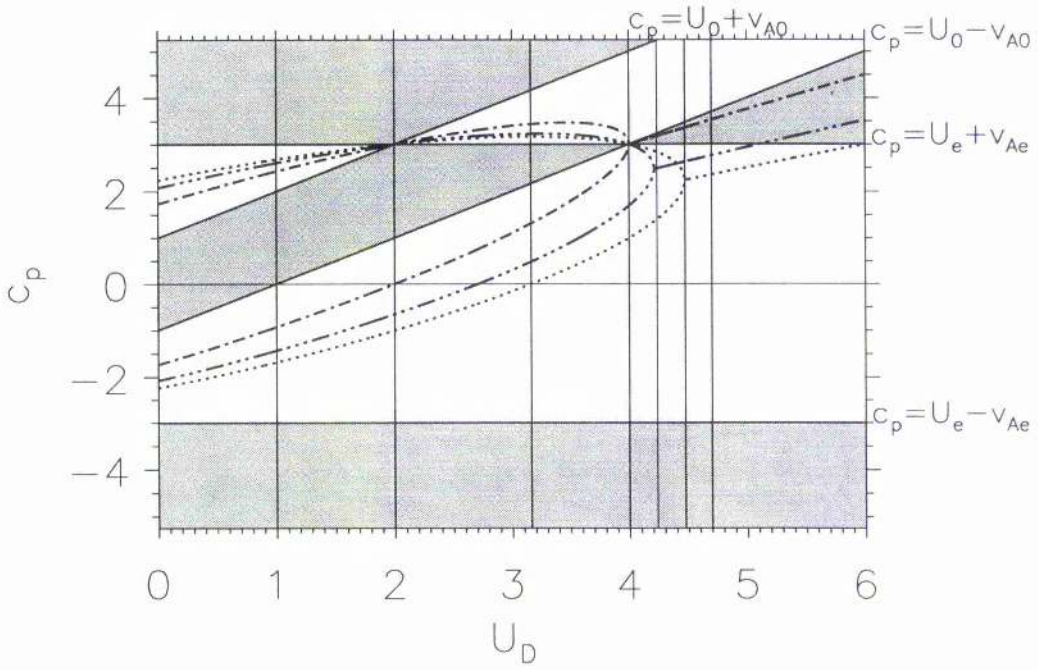

Figure 3.9: As Figure 3.5, but for density ratios of interest to the slab and cylinder illustration in Figures 3.10–3.17, namely $\rho_0/\rho_e = 1.0$ (dotted), $\rho_0/\rho_e = 1.42$ (dot-dot-dot-dashed) and $\rho_0/\rho_e = 3.0$ (dot-dashed), respectively, corresponding to the short wavelength limit of all modes (and long wavelength limit of the cylinder kink mode), the turning point of the cylinder kink mode, and the critical case $f = f^*$. We also mark with vertical lines the values of U_D chosen in Figures 3.10–3.17.

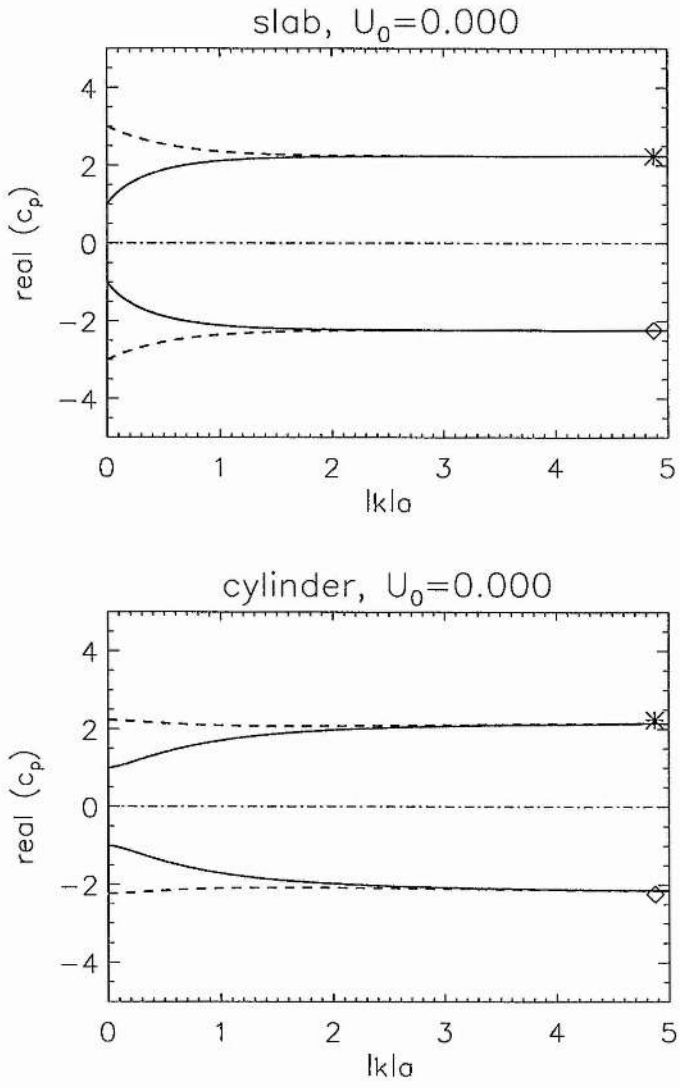

Figure 3.10: Plots of real (c_p) against $|k|a$ for the slab and cylinder, $\rho_e = \rho_0$ and $v_{Ae} = 3v_{A0}$. All speeds are expressed in units of the internal Alfvén speed v_{A0}, and the environment is taken to be static ($U_e = 0$). Solid lines are sausage modes, dashed lines are kink modes. There are two solutions of each mode type, which we refer to as the "+" and "−" root according to the sign in (3.30). The "+" and "−" single interface solutions (3.17) are shown on the right-handside with an asterisk and a diamond respectively. For this parameter set the Kelvin-Helmholtz threshold for the single interface is $U_0 = U_{KHI} = 4.472$.

The above also applies to Figures 3.11–3.17. Here $U_0 = 0$, giving the purely static case. All solutions are stable. All solutions are symmetric about $c_p = 0$ (the dot-dashed line), representing waves propagating in opposite directions at the same speed.

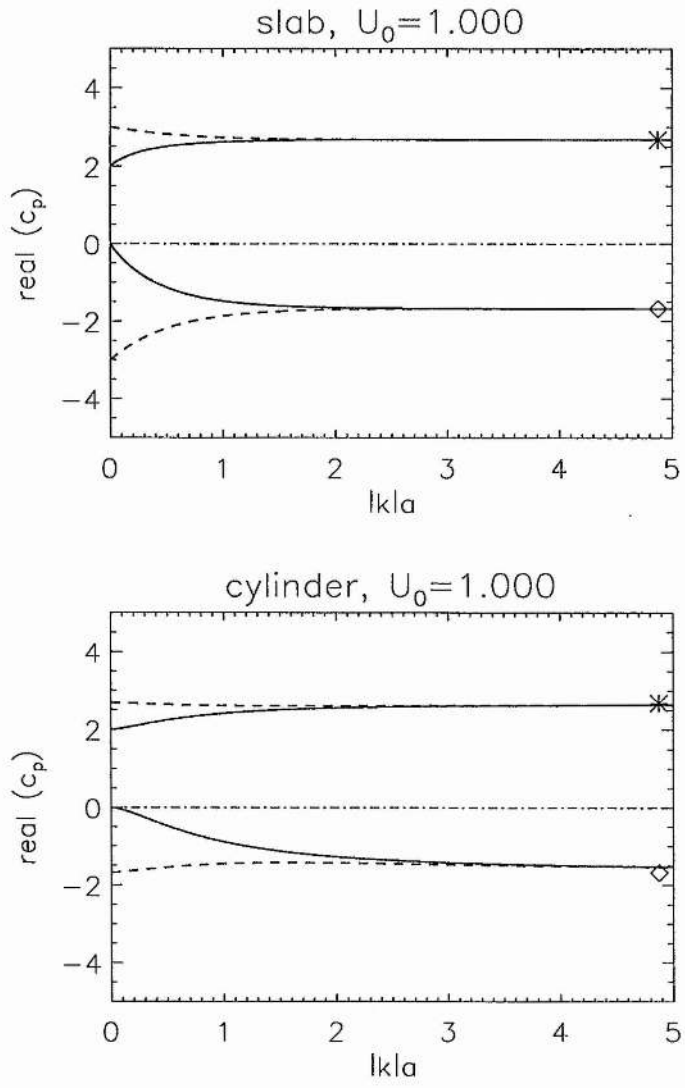

Figure 3.11: As Figure 3.10, but with $U_0 = v_{A0} = 1.0$. All solutions are stable. Solutions are no longer symmetric, but are qualitatively similar to the static case, being distorted reflections of each other. The main effect of the flow is the Doppler shift, and the upper and lower solutions become less and more dispersive as they respectively correspond to propagation with and against the flow. The propagation ranges are $U_0 + v_{A0} < c_p < v_{Ae}$ and $-v_{Ae} < c_p < U_0 - v_{A0}$.

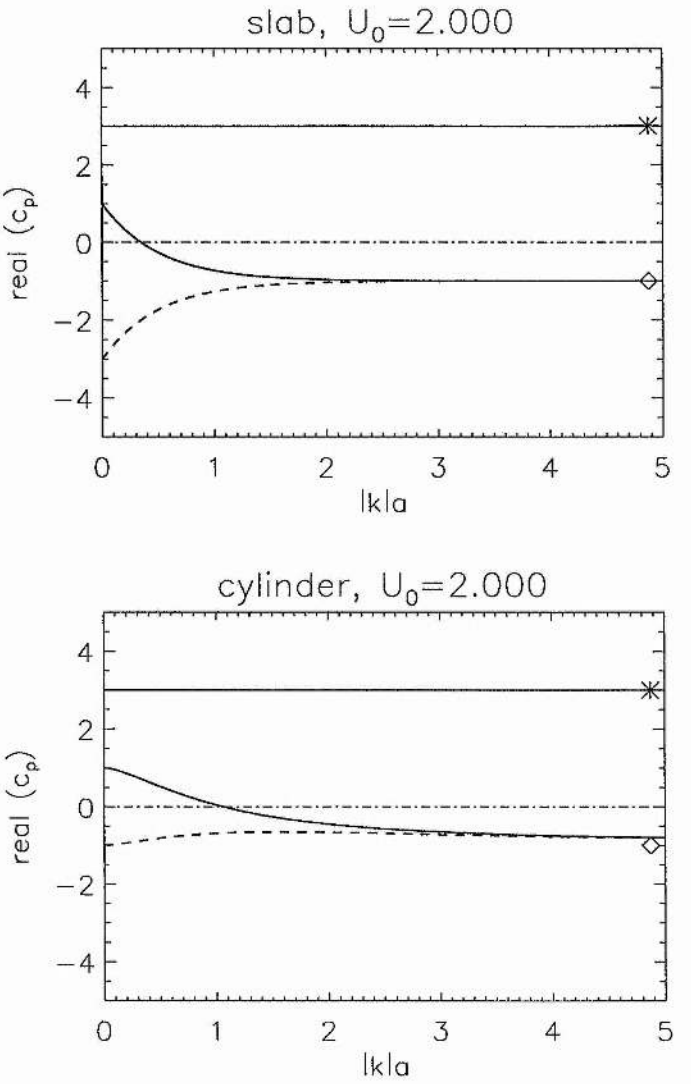

Figure 3.12: As Figure 3.10, but with $U_0 = |v_{Ae} - v_{A0}| = 2.0$, corresponding to the first critical relative flow determined by the propagation windows. The "+" sausage and kink modes of each geometry become degenerate as their propagation window collapses. All solutions are stable. The "–" sausage modes of both geometries are "backward" for sufficiently long wavelengths, having been swept forward by the flow (since $U_0 - v_{A0} > 0$).

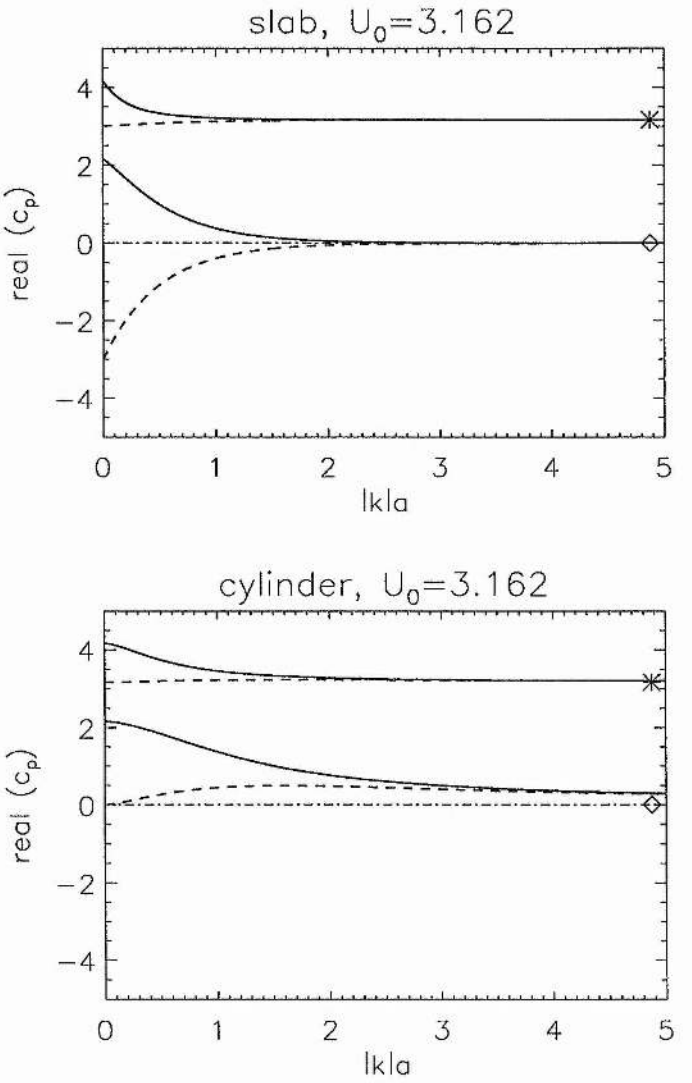

Figure 3.13: As Figure 3.10, but with $U_0{}^2 = v_{A0}{}^2 + v_{Ae}{}^2\rho_e/\rho_0 = 10.0$, so that the "−" single interface solution is stationary. All solutions are stable. The "+" sausage and kink solutions have reversed their ordering: since $U_0 + v_{A0} > v_{Ae}$, the limits of the upper propagation range have reversed. The solution curves are now distorted translations of each other. The "−" sausage modes of both geometries are now "backward" for all $|k|a$, as is the "−" cylinder kink mode, so that there is no propagation of these mode types against the flow.

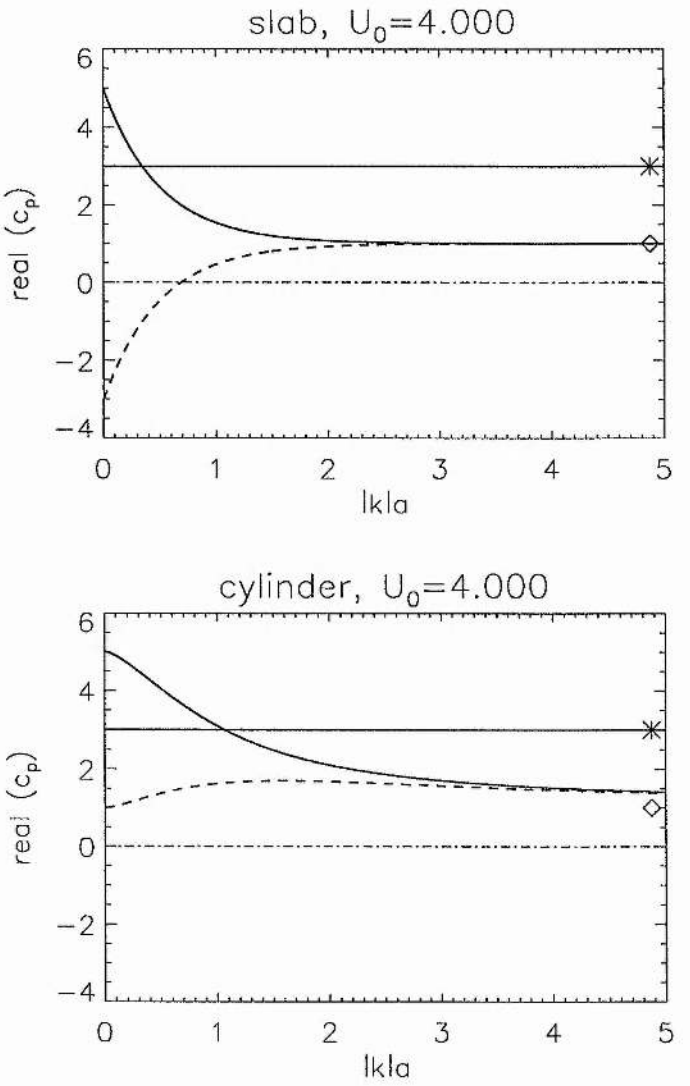

Figure 3.14: As Figure 3.10, but with $U_0 = v_{A0} + v_{Ae} = 4.0$, corresponding to the second critical relative flow determined by the propagation windows. All solutions are stable. However, the sausage modes of each geometry are marginally stable at the point where the upper and lower solutions come into contact; this occurs where $f(|k|a) = f^*(= 3.0)$, that is at $|k|a = 0.35$ for the slab sausage mode and at $|k|a = 1.08$ for the cylinder sausage mode. Solutions along the line real $(c_p) = v_{Ae} = U_0 - v_{A0}$ are degenerate. Both single interface solutions are in the flow direction, so that the "−" slab kink mode is now backward for sufficiently short wavelengths, while the other "−" modes are backward for all wavelengths.

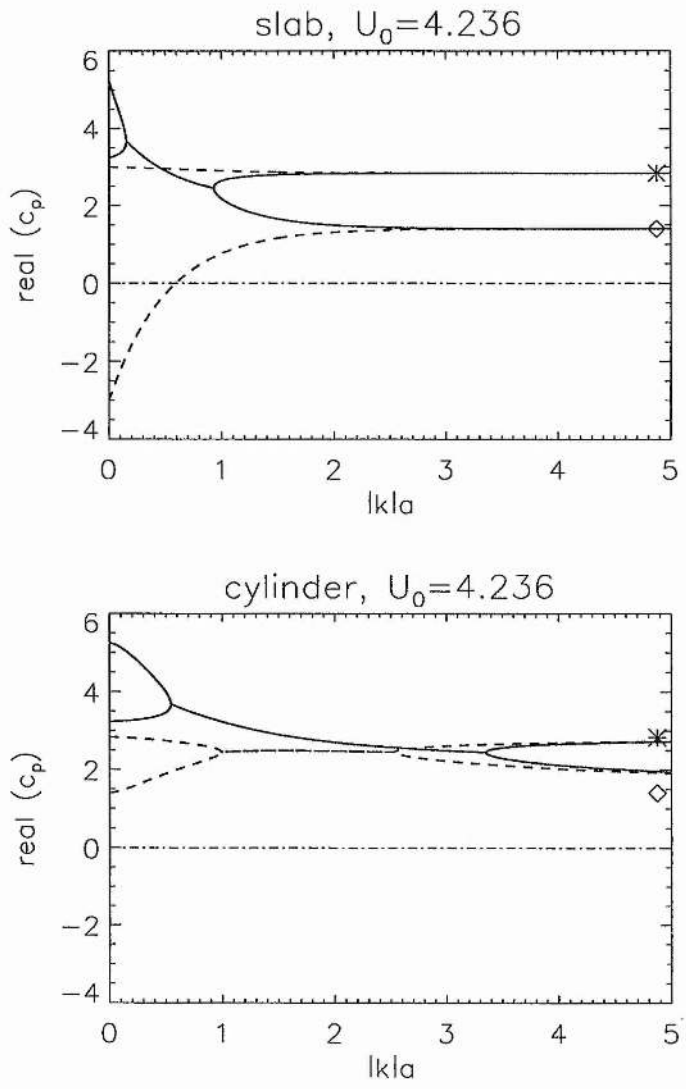

Figure 3.15: As Figure 3.10, but with $U_0 = 4.236$. With $U_0 < U_{KHI}$, all solutions are stable in the single interface ($|k|a \to \infty$) limit. However, *unstable solutions exist at finite* $|k|a$ for the slab and cylinder sausage modes and the cylinder kink mode. Marginal stability occurs where stable solutions of the same mode type touch: at $|k|a = 0.15$ and 0.93 for the slab sausage mode; at $|k|a = 0.55$ and 3.36 for the cylinder sausage mode, and at $|k|a = 1.00$ and 2.53 for the cylinder kink mode. The slab kink mode is stable for all $|k|a$. Since $U_0 > v_{A0} + v_{Ae}$ the propagation ranges for stable modes are now $U_0 - v_{A0} < c_p < U_0 + v_{A0}$ (containing the long wavelength stable sausage solutions, for which $f(|k|a) > f^*$) and $-v_{Ae} < c_p < v_{Ae}$ (containing the short wavelength stable sausage solutions, all kink solutions, and *both* single interface solutions, for which $f(|k|a) < f^*$). See Figure 3.18 for imag (c_p).

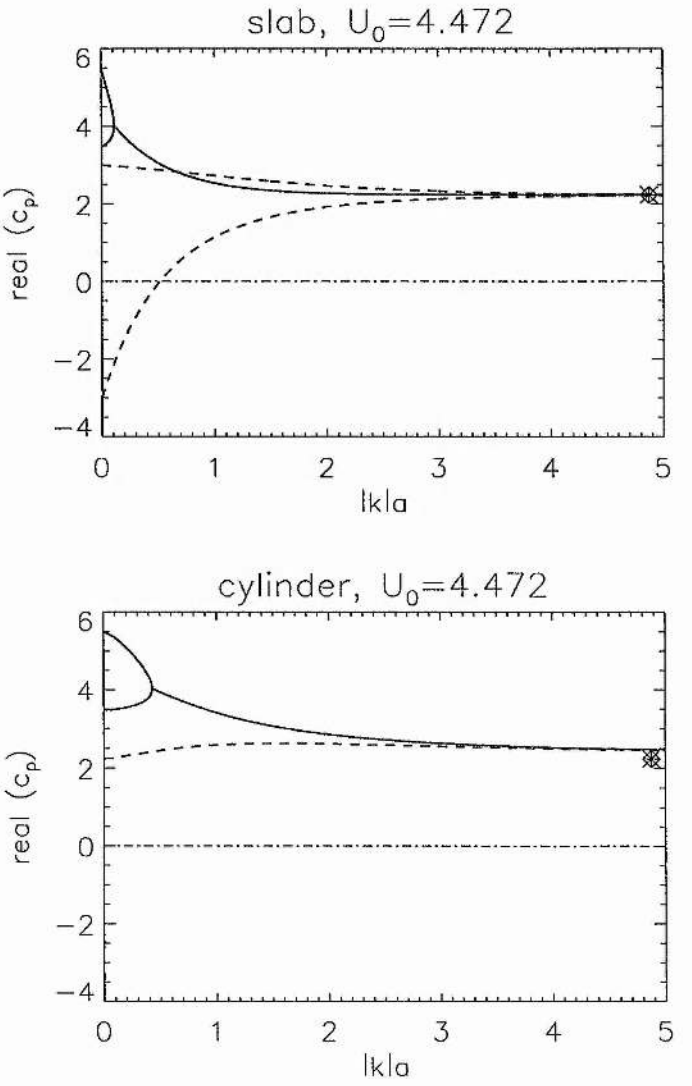

Figure 3.16: As Figure 3.10, but with $U_0 = U_{KHI} = 4.472$ so that the single interface is marginally stable (real, equal roots). Then all modes are marginally stable in the limit $|k|a \to \infty$, hence the short wavelength stable branches of Figure 3.15 have disappeared; and the cylinder kink mode is also marginally stable as $|k|a \to 0$, so that its long wavelength stable branch has disappeared. Sausage modes are additionally marginally stable at $|k|a = 0.11$ for the slab, and at $|k|a = 0.44$ for the cylinder. See Figure 3.18 for imag (c_p).

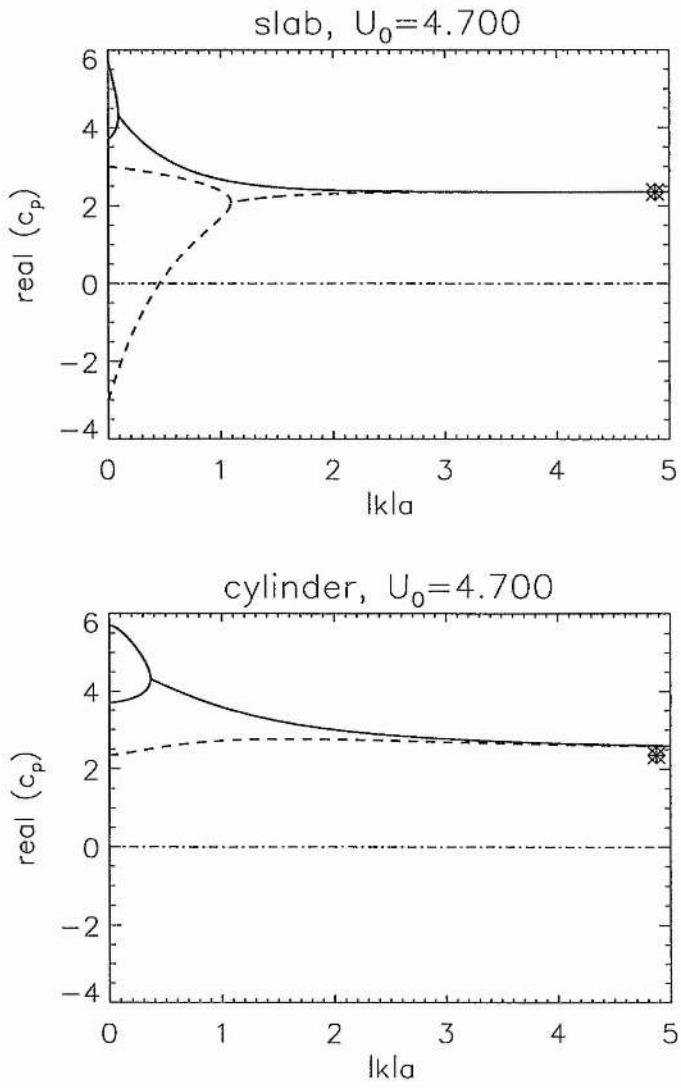

Figure 3.17: As Figure 3.10, but with $U_0 = 4.7 > U_{KHI}$. For the slab, both mode types are unstable for $|k|a$ sufficiently large, with marginal stability at $|k|a = 0.09$ for the sausage mode, $|k|a = 1.09$ for the kink mode. The cylinder sausage mode has a similar behaviour, with marginal stability at $|k|a = 0.37$, while the cylinder kink mode is unstable for all $|k|a$. See Figure 3.18 for imag (c_p).

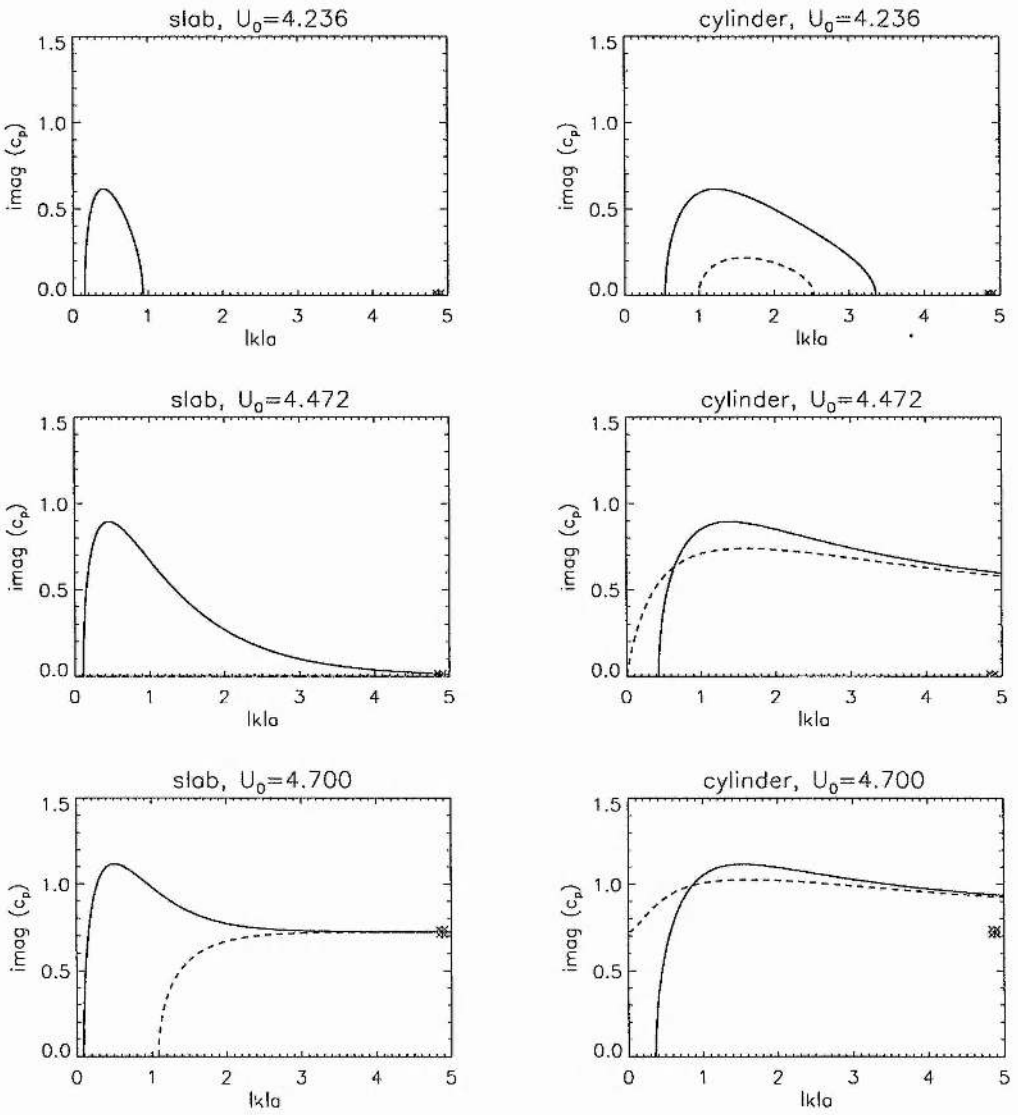

Figure 3.18: Plots of imag (c_p) against $|k|a$, to be compared with those of real (c_p) for the same parameter values in Figures 3.15–3.17. Where imag (c_p) is non-zero, the solutions for c_p are complex conjugates, hence we may restrict the plots to positive values of imag (c_p). The magnitude of imag (kc_p) gives the growth rate of an unstable mode.

for each mode type, which in the absence of relative flows are mirror images of each other since $U_m = 0$. These curves may be compared to the left hand extreme of Figure 3.9. While the single interface solution c_k is closer to $v_{Ae}(v_{A0})$ for smaller(larger) values of ρ_0/ρ_e, here $c_{k_{eff}}$ is closer to $v_{Ae}(v_{A0})$ for smaller(larger) values of $f(|k|a)$.

For nonzero relative flow, U_m is nonzero and dispersive so that the two solutions for c_p for any given mode type are not mirror images of each other in any fixed reference frame, thereby necessitating the consideration of *both* solutions. In our illustration, $U_m > 0$ so that as U_D increases from zero all solutions for c_p increase from their values for the static case, although the long wavelength limit of the slab kink modes remain fixed at $c_p = \pm v_{Ae}$ since $U_e = 0$. Then the "$-$" root of (3.30) becomes a backward mode when $U_m > c_{pm}$, which for $U_e = 0$ yields

$$U_0{}^2 > v_{A0}{}^2 + \frac{\rho_e}{f\rho_0} v_{Ae}{}^2 \tag{3.42}$$

in agreement with the general criterion (3.10).

Then, for our illustrated case, the backwards threshold is at least as large as v_{A0}, as indicated by the propagation windows, and increases as $f(|k|a)$ decreases. Figure 3.11 shows the dispersion diagrams for the case $U_0 = v_{A0}$; for larger U_0 as in Figure 3.12 there are long wavelength backward sausage modes for both geometries. In Figure 3.13 we have $U_0{}^2 = 10 v_{A0}{}^2$, which for our chosen parameter values is the backwards threshold for $f = 1$. Here it is also the threshold at which there is no propagation against the mean flow, at any wavelength, of the sausage mode for either geometry and the kink mode for the cylinder, while for larger values of U_0 as in Figures 3.14–3.17 the backward slab kink mode exists for sufficiently short wavelengths.

Turning now to the stability threshold, the general criterion (3.9) for the occurrence of the Kelvin-Helmholtz instability may be rewritten as

$$U_D{}^2 > \left(\frac{f\rho_0 + \rho_e}{f\rho_0\rho_e}\right)\left(f\rho_0 v_{A0}{}^2 + \rho_e v_{Ae}{}^2\right) \equiv U_C{}^2, \tag{3.43}$$

where we denote by U_C the critical relative flow magnitude at which an incompressible surface mode is marginally stable for given v_{A0} and v_{Ae}, and a particular effective density ratio $f\rho_0/\rho_e$. We may also obtain the general stability threshold U_C by writing $c_{pm} = 0$ using (3.31). Writing $f = 1$ in (3.43), we recover the single interface result (3.21), with (3.43) reducing to $U_C = U_{KHI}$.

The forms of (3.43) applicable to the sausage and kink modes of the slab have been given in the literature (Parker 1964, Singh and Talwar 1994, Nakariakov and Roberts 1995a, Nakariakov et al. 1996), together with its reduction for the kink mode of the isolated ($v_{Ae} = 0$) slab (Geronicolas 1977). An equivalent to (3.43) for the slab case is given in Chakraborty (1968). Rae (1983) noted that the stability criteria for the slab may be obtained from those for the single interface, since the dispersion relations for the two geometries were "equivalent to [each other] with a suitable change of density". The analogy between the slab and single interface was also noted by Parker (1979a), who considered the single interface and both slab modes for the case $v_{Ae} = U_0 = 0$ and $\rho_0 = \rho_e$. The form of (3.43) applicable to the cylinder has been given by Trehan and Singh (1978) for the case of an isolated ($v_{Ae} = 0$) tube.

While the stability condition (3.43) has appeared in the literature in various forms, it has not until now been subjected to detailed analysis, nor have the three geometries been considered in parallel. Previous investigations have been restricted to certain limiting or special cases, such as wavelength extremes or equal fluids, for a particular geometry. These treatments do not reveal the full structure of the equation, nor do they explain all the features to be seen in our illustration. We return to this point in Section 3.3.4 below, where we discuss the literature results in the light of our analysis of the problem.

For our chosen parameter values, ${U_{KHI}}^2 = 20{v_{A0}}^2$. The case $U_0 = U_{KHI} \approx 4.472$ is shown in Figure 3.16, in which all modes are marginally stable in the limit $|k|a \to \infty$. However, for some modes in our illustration marginal stability first occurs for $U_0 = 4v_{A0} = v_{A0} + v_{Ae}$ at a finite value of $|k|a$; see Figure 3.14. For $v_{A0} + v_{Ae} < U_0 < U_{KHI}$, as in Figure 3.15, instability may occur in a finite $|k|a$-range so that a given mode has two stable branches. For $U_0 > U_{KHI}$, as in Figure 3.17, all modes are unstable for a semi-infinite range of $|k|a$, except the cylinder kink mode which is unstable at all $|k|a$. Figure 3.18 shows the corresponding imaginary parts of c_p for each of Figures 3.15–3.17.

The dispersive and stability properties of a given mode may be quantified in terms of its variation of $f(|k|a)$ relative to the critical value f^*. This point is elaborated on below, but we first discuss the properties of the solutions for c_p in the context of the evolution of the propagation windows with increasing relative flow.

Discussion in terms of propagation windows

In the first flow regime, which for our illustration corresponds to $0 < U_0 < 2v_{A0}$, we have $c_{pm} \in (v_{A0}, v_{Ae})$ and the solutions are qualitatively similar to the static case. The main effect is due to the shift term, which leads to increased(reduced) dispersion of solutions in the widening(shrinking) range, together with the possibility of backward modes. Although asymmetric, the two solutions for a given mode type are *distorted reflections* of each other about the line $c_p = U_D$. These general qualitative features of the first flow regime are illustrated in Figure 3.11, where we show the dispersion curves for the case $U_0 = v_{A0}$. As noted above, this case also corresponds in our illustration to the minimum threshold for the appearance of backward modes.

At the critical case $U_D = |v_{Ae} - v_{A0}|$, corresponding to the first crossing of range limits, we have in general

$$c_{pm} = \frac{f\rho_0 v_{A0} + \rho_e v_{Ae}}{f\rho_0 + \rho_e}. \tag{3.44}$$

This case is illustrated in Figure 3.12, in which $U_0 = 2v_{A0}$ and for all $f(|k|a)$ the "+" root lies along the crossing and is degenerate, while the sausage mode "−" root represents a backward mode for sufficiently small $|k|a$.

In the second flow regime, given in our illustrated case by $2v_{A0} < U_0 < 4v_{A0}$, the reversal of range limits in the previously shrinking range is accompanied by a reversal in the dispersive properties of the solutions within that range, in that wherever $c_p(|k|a)$ was previously decreasing it is now increasing, and vice versa. Also within that range the sausage and kink curves reverse their ordering. For either geometry, the solutions are now ordered *alternately* by mode type, with the "+" and "−" solutions being *distorted translations* of each other. These general qualitative features of the second flow regime are illustrated in Figure 3.13, where we show the dispersion curves for the case $U_0 = 10^{1/2} v_{A0} \approx 3.162 v_{A0}$. As noted above, this case also corresponds to the threshold for the appearance of the backward mode when $f = 1$.

At the critical case $U_D = v_{A0} + v_{Ae}$, corresponding to the second crossing of range limits, we have in general

$$c_{pm} = \left| \frac{f\rho_0 v_{A0} - \rho_e v_{Ae}}{f\rho_0 + \rho_e} \right|, \tag{3.45}$$

from which we may note the critical effective density ratio $f\rho_0/\rho_e = v_{Ae}/v_{A0}$, for which

(3.45) yields $c_{pm} = 0$ so that marginal stability occurs. This critical case may also be written as $f = (\rho_e v_{Ae})/(\rho_0 v_{A0}) \equiv f^*$, and as well as yielding the minimum stability threshold $v_{A0} + v_{Ae}$ for given v_{A0} and v_{Ae} (we elaborate on this point below), it also separates those whose "+" or "−" root lies along the second crossing, where the given root is degenerate. For the single interface, for which $f(|k|a) \equiv 1$, marginal stability occurs at $U_D = v_{A0} + v_{Ae}$ only if $f^* = 1$, that is for the critical density ratio $\rho_0/\rho_e = v_{Ae}/v_{A0}$ noted above. In the generalised case, if f^* lies within the range of $f(|k|a)$ for a given mode type, then there is marginal stability at $U_D = v_{A0} + v_{Ae}$ for the corresponding wavelength, $|k|a = f^{-1}(f^*)$, which may be read off from Figure 3.1.

The behaviour of $c_p(|k|a)$ at the second crossing is illustrated in Figure 3.14, in which $U_0 = 4v_{A0}$. For our chosen parameter set $f^* = 3$, which for both geometries lies within the range of $f(|k|a)$ for the sausage modes but outwith the range of $f(|k|a)$ for kink modes. Then in Figure 3.14 the curves for the sausage mode coalesce at the second crossing for the appropriate value of $|k|a$, while the curves for the kink mode are well separated; and we have $c_p = -v_{A0} + U_0 = v_{Ae} + U_e$ for the "−" root wherever $f(|k|a) \geq 3$ and for the "+" root wherever $f(|k|a) \leq 3$, the given solution being degenerate in each case. As $U_D \to v_{A0} + v_{Ae}$ from below, the two sausage curves for each geometry pinch at the appropriate value of $|k|a$, for which $c_{pm} \to 0$.

Throughout the third flow regime, the behaviour of $c_p(|k|a)$ is determined by the value of $f(|k|a)$ relative to f^*, and is entirely different to the behaviour in the previous two flow regimes. For the single interface we found that in the third regime, if solutions are stable then both roots lie in the same range, this range being determined by the value of ρ_0/ρ_e relative to v_{Ae}/v_{A0}. In the generalised case we find that for $f > f^*$ both roots, where stable, satisfy $U_0 - v_{A0} < c_p < U_0 + v_{A0}$, while for $f < f^*$ stable solutions lie in the range $U_e - v_{Ae} < c_p < U_e + v_{Ae}$. This leads to the possibility of a given mode type having two stable branches, one in each propagation range. This behaviour is illustrated in Figure 3.15, where it affects the sausage modes of both geometries and the cylinder kink mode. In general the occurrence of this feature for a given mode type depends on the form of $f(|k|a)$ and the values of f^* and U_D.

Analysis of stability condition

Let us consider in more detail the importance of the parameter f^*. In terms of f^* we may rewrite (3.43) as

$$U_C{}^2 = \left(v_{A0} + \frac{f^*}{f} v_{Ae}\right)\left(v_{A0} + \frac{f}{f^*} v_{Ae}\right), \tag{3.46}$$

which yields

$$U_C{}^2 - (v_{A0} + v_{Ae})^2 = \frac{(f^*/f - 1)^2}{f^*/f} v_{Ae} v_{A0}, \tag{3.47}$$

while we may rewrite our expression (3.12) for the effective kink speed $c_{k_{eff}}$ in terms of f^* as

$$c_{k_{eff}}{}^2 = v_{A0} v_{Ae} \left(\frac{v_{A0} + \frac{f^*}{f} v_{Ae}}{v_{Ae} + \frac{f^*}{f} v_{A0}}\right). \tag{3.48}$$

We may alternatively write (3.46) as

$$\frac{f}{f^*} = \frac{U_C{}^2 - (v_{A0}{}^2 + v_{Ae}{}^2)}{2 v_{A0} v_{Ae}} \pm \frac{1}{2 v_{A0} v_{Ae}} \left\{\left[(v_{A0} - v_{Ae})^2 - U_C{}^2\right]\left[(v_{A0} + v_{Ae})^2 - U_C{}^2\right]\right\}^{1/2} \tag{3.49}$$

to obtain the marginally stable values of f/f^* for a given relative flow. The various forms (3.46)–(3.49) have not been found in the literature.

The right-handside of our expressions (3.46)–(3.48) for the generalised case are identical in form to those of (3.27)–(3.29), given earlier for the special case of single interface, but with f^* now replaced by f^*/f; for $f = 1$ we recover the earlier results with $U_C = U_{KHI}$ and $c_{k_{eff}} = c_k$. With f and f^* real and positive, we have $U_C \geq v_{A0} + v_{Ae}$, so that marginal stability is possible only in the third flow regime, as indicated by the propagation windows. The minimum value, $v_{A0} + v_{Ae}$, of the stability threshold U_C is attained for the critical case $f = f^*$, which corresponds to the repeated root case in (3.49) and yields $c_{k_{eff}}{}^2 = v_{A0} v_{Ae}$.

For a given value of U_D in the third flow regime there are two marginally stable values of f/f^*, each the reciprocal of the other, between which solutions are unstable. For fixed f, as in the single interface case, this yields a range of density ratios for which solutions are unstable at the given U_D. For fixed f^*, as in the case of the slab or cylinder, we obtain a range of $f(|k|a)$ in which solutions are unstable, so that the stability properties of a given mode at this particular value of U_D depend on whether this given range intersects its own range of $f(|k|a)$: for both geometries the sausage mode has $f(|k|a) > 1$; the slab kink mode has $0 < f(|k|a) < 1$; the cylinder kink mode has $1 < f(|k|a) < f_{max} \approx 1.42$

where f_{max} is the value of $f(|k|a)$ at its turning point. Then the dispersive and stability properties of each mode type in the third flow regime depend on the value of f^* relative to unity and also, in the case of the cylinder kink mode, f_{max}.

In Figure 3.19 we plot using a heavy solid line U_C/v_{A0} as a function of f/f^*, using (3.46) with the parameter values of our illustration, for which $v_{Ae} = 3v_{A0}$ and $f^* = 3$. The dark shaded region above the U_C/v_{A0} curve contains unstable solutions, while the region below this curve contains stable solutions, and is shaded into zones covering different mode types. The zones are labelled "S" or "K" to indicate sausage or kink modes, with subscript "slab" or "cyl" to denote the geometry to which the label applies. The zones are separated by vertical lines corresponding to the cases $f = 1$ (dotted) and $f = f_{max}$ (dot-dot-dot-dashed). With $f^* = 3$ the minimum in the U_C/v_{A0} curve lies in the zone covering the sausage modes of both geometries, for which marginal stability first occurs at the value $|k|a = f^{-1}(f^*)$.[1] As U_C/v_{A0} increases, there are two marginally stable values of $f(|k|a)$ between which solutions are unstable. For any choice of parameter values, U_C has a minimum of $v_{A0} + v_{Ae}$ when $f = f^*$ (see (3.47)), leading to a qualitatively similar diagram to Figure 3.19, although the locations of the zones covering each mode type depend on the value of f^*. A diagram of the type Figure 3.19 may also be used to show the variation of U_{KHI} with density ratio ρ_0/ρ_e, with the minimum corresponding to the critical case $\rho_0/\rho_e = v_{Ae}/v_{A0}$ discussed in Section 3.3.2.

A diagram of the type Figure 3.19 is applicable to all geometries and mode types and shows how the instability spreads through the modes as the relative flow increases, according to the zones covered by the unstable region for the particular parameter set. The detailed variation of U_C with $|k|a$ for any given mode may be obtained by combining these results with the form of $f(|k|a)$ as shown in Figure 3.1. In Figures 3.20 and 3.21 we show this variation, giving in separate plots curves of U_C against $|k|a$ for sausage (solid lines) and kink (dashed lines) modes. In both figures we fix the Alfvén speeds such that $v_{Ae} = 3v_{A0}$, as in our illustration in Figures 3.10–3.17, plotting U_C in units of v_{A0}, and for comparative purposes choose a variety of density ratios with $f^* \geq 1$ in Figure 3.20 and $f^* \leq 1$ in Figure 3.21. In each case, $U_C \geq v_{A0} + v_{Ae}$ with this minimum being attained for $|k|a = f^{-1}(f^*)$ wherever f^* lies in the $f(|k|a)$ range of a given mode, so that for $f^* < 1$ the

[1] Note that $f^{-1}(x)$ denotes the inverse of $f(x)$.

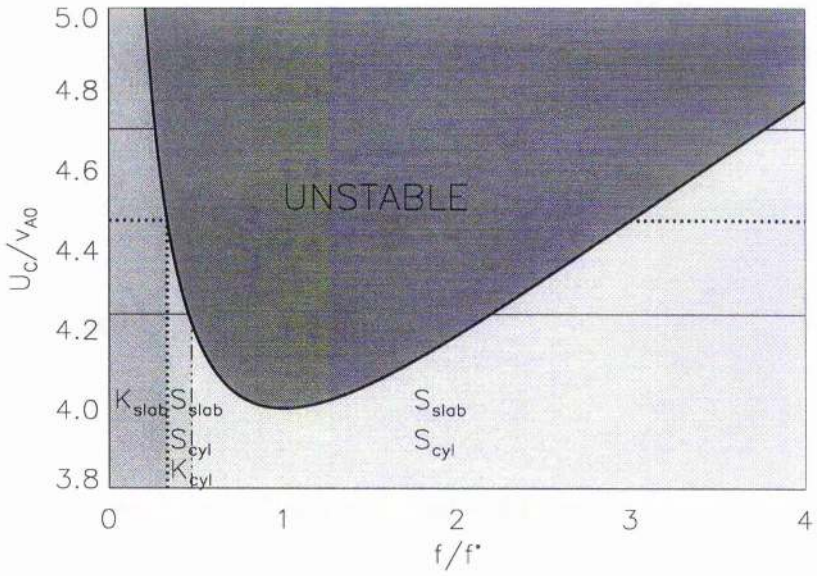

Figure 3.19: The variation of the critical relative flow magnitude U_C/v_{A0} with f/f^*, with U_C and f^* defined by (3.46) and (3.26) respectively, taking the same parameter values as in our illustration of Figures 3.10–3.17. The dark shaded region above the curve contains unstable solutions. The region below the curve contains stable solutions, and is shaded into zones covering different mode types. The zones are labelled "S" or "K" to indicate sausage or kink modes, with subscript "slab" or "cyl" to denote the geometry to which the label applies. The zones are separated by vertical lines corresponding to the cases $f = 1$ (dotted) and $f = f_{max}$ (dot-dot-dot-dashed). With $f^* = 3$ the minimum in the U_C/v_{A0} curve lies in the zone covering the sausage modes of both geometries, for which marginal stability first occurs at the value $|k|a = f^{-1}(f^*)$. As U_C/v_{A0} increases from its minimum value, there are two marginally stable values of $f(|k|a)$ between which solutions are unstable. For any choice of parameter values, U_C has a minimum of $v_{A0} + v_{Ae}$ when $f = f^*$ (see (3.47)), leading to a qualitatively similar diagram to that given here, although the locations of the zones covering each mode type depend on the value of f^*.

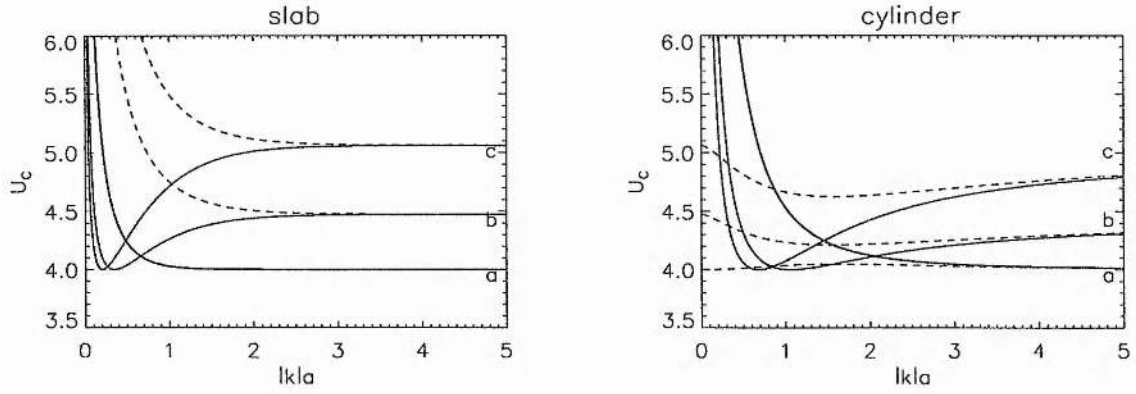

Figure 3.20: Variation of U_C (in units of v_{A0}) with $|k|a$, with U_C defined by (3.46), taking $v_{Ae} = 3v_{A0}$ as in our illustration of Figures 3.10–3.17, and with various density ratios corresponding to $f^* \geq 1$. Separate plots for the slab and cylinder show curves for sausage (solid lines) and kink (dashed lines) for each density ratio. For $U_D > U_C$ solutions are unstable. The density ratios and corresponding labels are $\rho_0/\rho_e = 3$ (curves a, $f^* = 1$, slab curves coincide), $\rho_0/\rho_e = 1$ (curves b, $f^* = 3$, same as in our illustration), $\rho_0/\rho_e = 0.6$ (curves c, $f^* = 5$).

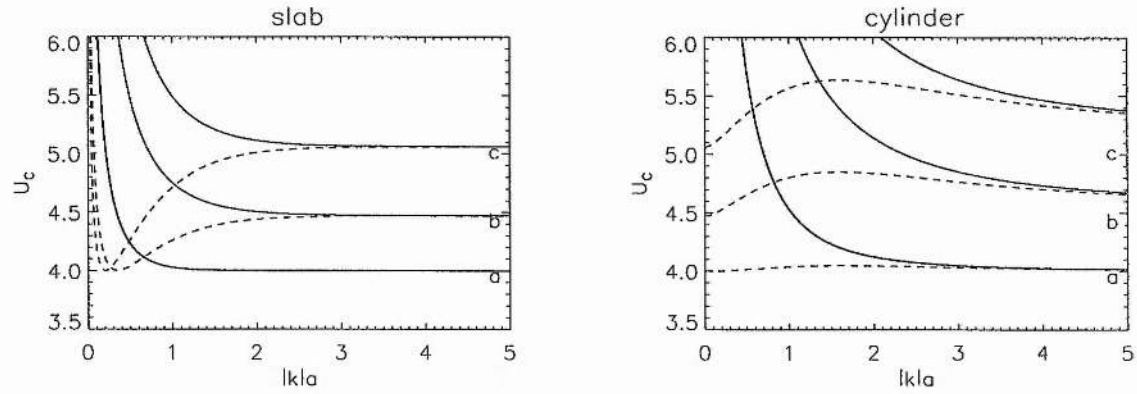

Figure 3.21: Variation of U_C (in units of v_{A0}) with $|k|a$, with U_C defined by (3.46), taking $v_{Ae} = 3v_{A0}$ as in our illustration of Figures 3.10–3.17, and with various density ratios corresponding to $f^* \leq 1$. Separate plots for the slab and cylinder show curves for sausage (solid lines) and kink (dashed lines) for each density ratio. For $U_D > U_C$ solutions are unstable. The density ratios and corresponding labels are $\rho_0/\rho_e = 3$ (curves a, $f^* = 1$, slab curves coincide), $\rho_0/\rho_e = 9$ (curves b, $f^* = 1/3$), $\rho_0/\rho_e = 15$ (curves c, $f^* = 1/5$).

smallest value of U_C for the cylinder is $U_{KHI} > v_{A0} + v_{Ae}$. Note that for $f^* = 1$ (curves a in both figures) the slab sausage and kink curves coincide and are monotonic decreasing. The parameters used in curves b in Figure 3.20 are the same as in our illustration of Figures 3.10–3.17.

Similar plots to those in Figures 3.20 and 3.21 have appeared in papers by Satya Narayanan and Somasundaram (1985, Figure 5) and Singh and Talwar (1994, Figure 1) for the slab, and Somasundaram and Satya Narayanan (1987, Figure 5) for the cylinder. These results are discussed in Section 3.3.4 below.

Special cases

We have discussed the properties of the dispersion relation with reference to a particular illustration. The features for other parameter values may be easily derived from our general analysis and discussion. In particular we may consider some special cases.

For the case $v_{Ae} = 0$, that is an isolated slab or tube, or magnetic-nonmagnetic interface, we have $f > f^* = 0$ for all finite density ratios and wavenumbers, and we obtain

$$U_C{}^2 = v_{A0}{}^2 \left(1 + \frac{f\rho_0}{\rho_e}\right). \tag{3.50}$$

Then for given v_{A0}, U_C attains its minimum value of v_{A0} in the long wavelength limit of the slab kink mode, independently of density ratio, while for all other modes the onset of instability occurs at $f = 1$ when $U_C{}^2 = v_{A0}{}^2(1 + \rho_0/\rho_e)$. For all modes except the cylinder kink mode, $U_C(|k|a)$ is monotonic.

For the case $v_{A0} = 0$, that is an nonmagnetic slab or tube in a magnetic environment ($v_{Ae} \neq 0$), or magnetic-nonmagnetic interface, we have $f < f^* = \infty$ for all finite density ratios and wavenumbers, and we obtain

$$U_C{}^2 = v_{Ae}{}^2 \left(1 + \frac{\rho_e}{f\rho_0}\right). \tag{3.51}$$

Then, for given v_{Ae}, U_C attains its minimum value of v_{Ae} in the long wavelength limit of the slab sausage mode, independently of density ratio, while for the slab kink mode and the cylinder sausage mode the onset of instability occurs at $f = 1$ when $U_C{}^2 = v_{Ae}{}^2(1 + \rho_e/\rho_0)$. For the cylinder kink mode, instability first sets in at $f = f_{max}(\approx 1.42)$

when $U_C{}^2 = v_{A0}{}^2(1+\rho_e/(f_{max}\rho_0))$. For all modes except the cylinder kink mode, $U_C(|k|a)$ is monotonic.

For the case of equal fluids $v_{A0} = v_{Ae}$ and $\rho_0 = \rho_e$, we have $f^* = 1$ and

$$U_C{}^2 = v_{A0}{}^2(1+f)\left(1+\frac{1}{f}\right) \tag{3.52}$$

so that U_C attains its minimum value of $2v_{A0}$ at $f = 1$. For the slab modes, the values of U_C for the sausage and kink modes coincide at all $|k|a$. For all modes except the cylinder kink mode, $U_C(|k|a)$ is monotonic.

The results of authors who considered these special cases are discussed in Section 3.3.4 below. We make the comment that, as noted in Section 3.3.1 above, where either medium is field-free the second flow regime vanishes, while for $v_{A0} = v_{Ae}$ the first flow regime vanishes.

Dispersive properties of backward modes

Finally we comment on the dispersive properties of backward modes. Since the criterion (3.10) is dispersive, it is possible for a given mode to have a cutoff wavelength at which it changes propagation direction in the given reference frame. In our illustration, the qualitative dispersive properties (by this we mean $c_p(|k|a)$ either increasing or decreasing) of the backward sausage and kink modes are unchanged up to the onset of instability, since the dispersion reversal in the second flow regime affects the solutions propagating with the mean flow U_m. In such a case, a mode which first becomes a backward mode for sufficiently long(short) wavelengths, has $c_p(|k|a)$ that is decreasing(increasing) for the same solution in the static case.

However, this is not always so. Depending on the parameter values, the dispersion reversal in the second flow regime may affect either the "+" or the "−" solutions for c_p. When it affects the solutions propagating against the mean flow U_m, this reversal occurs prior to the sign change of these solutions. In such a case, the qualitative dispersive properties of the backward modes are the *opposite* to those of the same solutions in the static case. This occurs where $U_0 - U_e$ and $v_{A0} - v_{Ae}$ share the same sign, that is where the net flow in the positive z-direction is in the medium of higher Alfvén speed.

3.3.4 Discussion of literature

Incompressible slab and cylinder

We noted above that while particular forms of our generalised solutions (3.30) and stability condition (3.43) have appeared in the literature, the detailed structure of these equations, as revealed by our analysis, had not been fully brought out in earlier studies. We now discuss these previous investigations in the light of our results, explaining the limitations of the approaches used and why they failed to reveal fully the features seen in our more general and thorough analysis.

Parker (1964) gave the separate forms of the stability condition (3.43) applicable to the sausage and kink modes of the slab case, together with their respective reductions for the extremes $\rho_0 \gg \rho_e$ and $\rho_0 \ll \rho_e$, noting that in the former case the kink (or "serpentine") mode is more unstable than the sausage mode (that is, has smaller U_C at given $|k|a$) while in the latter case the sausage mode is more unstable than the kink mode. Hence it was appreciated that the density ratio can influence the stability threshold and affects the different mode types in different ways. However, by confining the investigation of the effect of ρ_0/ρ_e to extreme values, the existence of a critical density ratio was overlooked. Turning to a consideration of wavelength extremes, which similarly obscures the existence of a critical value of $|k|a$, Parker (1964) noted that in the short wavelength case $|k|a \to \infty$ the single interface result (3.21) is recovered, while for long wavelengths $|k|a \to 0$ the requirement for instability is said to be ${U_D}^2 > ({v_{A0}}^2\rho_0)/(\rho_e|k|a)^{\,2}$. The conclusion drawn from the results is that *"instability is most likely when ρ_e/ρ_0 is of order unity and when the wavelength of the disturbance is not long compared with the width of the stream"* (Parker 1964). While this statement hints that the strength of density inhomogeneity and dispersion have a *combined* effect on the stability properties, our more extensive analysis fully quantifies this effect and gives a detailed description of it in terms of the effective density ratio $f\rho_0/\rho_e$.

An equivalent form to (3.43) for the slab case is given in Chakraborty (1968), from

[2] We note that this expression is (3.43) to leading order in $|k|a \ll 1$ for the slab sausage mode, while for the slab kink mode its right-handside is replaced by $({v_{Ae}}^2\rho_e)/(\rho_0|k|a)$. This does not alter the conclusion that for both slab mode types the stability threshold increases as $|k|a \to 0$ (unless either medium is field-free).

which it is deduced that if both ${v_{A0}}^2 > {U_0}^2$ and ${v_{Ae}}^2 > {U_e}^2$ are satisfied then the jet is stable. That this condition is similarly *sufficient* for stability in our generalised case can be seen from our Equation (3.7), while our results reveal that a *necessary* (and frame-independent) condition for stability is $|U_0 - U_e| < v_{A0} + v_{Ae}$.

Parker (1979a) considered the single interface and both slab modes for the case $v_{Ae} = 0$, $U_0 = 0$ and $\rho_0 = \rho_e$, while Geronicolas (1977) considered the kink mode of the isolated ($v_{Ae} = 0$) slab, both authors obtaining stability criteria in agreement with our generalised form (3.43). Noting that the most rapid growth occurs for the shortest wavelength (the growth rate of an unstable mode is $|\text{imag}(\omega)|$), Geronicolas (1977) considered the $|k|a \gg 1$ extreme for the case $\rho_0 = \rho_e$, in which case instability occurs if ${U_D}^2 > 2{v_{A0}}^2$ (Parker 1979a). Trehan and Singh (1978) compared the slab results of Geronicolas (1977) with those for the isolated cylinder, obtaining the condition ${U_D}^2 > 4{v_{A0}}^2$ for the same parameter case ($v_{Ae} = 0$, $\rho_0 = \rho_e$). Although these authors examined the stability condition for particular parameter values only, we note that when either medium is field-free f^* is either zero or infinity, so that the minimum U_C for any given mode is attained in either the long or the short wavelength extreme (with the exception of the kink mode of the field-free ($v_{A0} = 0$) cylinder which has its minimum value of $U_C (> v_{A0} + v_{Ae} = v_{Ae})$ when $f = f_{max} (< f^* = \infty)$). Hence the full structure of the problem cannot be revealed through a study restricted to either $v_{A0} = 0$ or $v_{Ae} = 0$.

Singh and Talwar's (1994) formulation allowed for different relative orientations of magnetic fields, steady flows and propagation vector, all of which are in the plane of the interface. With flow internal to the slab and aligned to propagation, the stability conditions given for the slab sausage and kink modes agree with our general condition (3.43) with each v_{Ai} now denoting the component of Alfvén velocity in the direction of propagation and flow. While the stability conditions were not analysed, U_C/v_{A0} was plotted against $|k|a$ for two particular cases, both of which had equal densities ($\rho_0 = \rho_e$) and equal magnetic field strengths: the parallel case had magnetic fields of both regions aligned to the propagation vector and flow (yielding the case $v_{Ae} = v_{A0}$ of our model); the orthogonal case had the magnetic field aligned to the propagation and flow in one medium and transverse to it in the other. Both cases yielded monotonic curves of U_C/v_{A0}, recovering the single interface results for large $|k|a$. Further, for the parallel case the

curves for sausage and kink modes coincide and are decreasing with limit $2v_{A0}$, as is also predicted from our analysis: with $f^* = 1$ the sausage and kink U_C curves coincide with minimum value $v_{A0} + v_{Ae}$ of U_C being attained in the short wavelength ($f = 1$) extreme; the additional constraint of equal fluids means $v_{A0} + v_{Ae} = 2v_{A0}$. By being restricted to very special cases, their treatment does not reveal the possibility of a minimum U_C at a finite $|k|a$, nor does it bring out the different stability properties of the two mode types for the parallel case. Further, with no analysis of the stability condition and propagation windows, there is no mention of the sum $v_{A0}+v_{Ae}$ of the Alfvén speeds as a critical relative flow, nor of results to be expected for other parameter values.

Parhi (1992) also allowed for arbitrary orientations of magnetic field, flow and propagation vector in the plane of the interface, in a three-layer model corresponding to an incompressible slab having different plasma properties to either side. A sufficient stability condition was obtained analytically, valid under certain conditions, and in a numerical investigation it was seen that the corresponding flow threshold varies with the ratios of densities in each medium, although this effect was not investigated in detail.

Nakariakov and Roberts (1995a) and Nakariakov et al. (1996) also gave the general stability condition (3.43) for the slab case, noting that for the case $\rho_0 = \rho_e$ and $v_{A0} = v_{Ae}$ the minimum threshold U_C is $2v_{A0}$ and is attained in the limit $|k|a \to \infty$ in which the single interface result is recovered for both mode types. There was no further investigation of stability properties, the primary aim being to yield qualitative and quantitative results for stable waves in the presence of small steady flows for parameter values realistic to particular solar applications. They noted qualitative changes associated with changes in propagation windows, but in concentrating on small steady flows they did not take this beyond the second flow regime, hence the general significance of the sum of the Alfvén speeds was not brought out.

The slab and cylinder cases of our generalised incompressible model were considered by Satya Narayanan and Somasundaram (1985) and Somasundaram and Satya Narayanan (1987) respectively, and both dispersive and stability properties were considered in a numerical investigation of the appropriate forms of our general solution (3.8), for particular parameter values. Positive solutions for c_p/v_{A0} were plotted as a function of $|k|a$, showing on the same diagram the curves for several values of $\beta \equiv B_e/B_0$, with fixed $\eta \equiv \rho_e/\rho_0$

and U_0/v_{A0}. This approach and parameter choice obscures the full nature of the solutions as revealed by our own analysis: although it was noted that in some cases the flow may lead to a dispersion reversal for a particular mode, this was neither fully quantified nor put in the context of the evolution of the propagation windows, and indeed each choice of the free parameter β leads to a different propagation window; the sum and difference of Alfvén speeds were not noted as critical flow speeds; we further note that since all chosen parameter sets satisfied $U_0 < v_{A0} + v_{Ae}$, all solutions were stable and the existence of a finite $|k|a$-range instability was not revealed.

Without giving an analytical expression for the threshold flow U_C, they also plotted U_C/v_{A0} against $|k|a$ for each mode type, again for various $\beta \equiv B_e/B_0$ and fixed $\eta \equiv \rho_e/\rho_0$. This demonstrated the fact that different modes have different dispersive stability properties. For the slab case, Satya Narayanan and Somasundaram (1985) observed, without analysis, that the ordering of the sausage and kink stability curves depends on the combination $\eta\beta^2$ ($= f^{*2}$ in our notation) and coincide when $\eta\beta^2 = 1$ (that is, $f^* = 1$). They also noted a minimum in the kink stability curve at $|k|a = \tanh^{-1}(\sqrt{\beta^2\eta})$ for the parameter set satisfying $\eta\beta^2 = 0.8 < 1$, as predicted by our analysis, but they did not note the corresponding minimum threshold $U_C = v_{A0} + v_{Ae}$ nor give the implications for the dispersion diagram. Our analysis also predicts a minimum in the sausage stability curve at $|k|a = \coth^{-1}(\sqrt{\beta^2\eta})$ for $\eta\beta^2 > 1$, and although this is present in the curve shown for $\eta\beta^2 = 1.5$ the minimum is less marked than for the kink mode, and is not noted by Satya Narayanan and Somasundaram (1985). For the cylinder case (Somasundaram and Satya Narayanan 1987), stability curves were similarly plotted, although the significance of the parameter $\eta\beta^2$ was neither commented on nor obvious from their choice of parameters.

Hence, while the studies of Satya Narayanan and Somasundaram indicate some of the features predicted by our own analysis, namely the dispersion reversal for some $c_p(|k|a)/v_{A0}$ curves and the existence of a minimum turning point in one particular $U_C(|k|a)/v_{A0}$ curve, these features were merely observed from numerical plots of particular parameter cases and are neither fully discussed nor supported by detailed analysis of the equations. There is no general discussion of the effects of flows on the dispersive and stability properties of incompressible surface modes, no discussion of the propagation windows and critical flows, no indication of what to expect for other parameter values,

and no attempt to compare the modes for the different geometries.

Other related studies for the incompressible case

The problem of incompressible surface modes in discretely structured media with relative flows has been extended to a four-layer model applied to the magnetosphere (Lee, Wang, Wei and Tsurutani 1988). Solutions and stability criteria of a similar form to (3.8) and (3.43) respectively were given for the sausage and kink modes separately, and for each mode the single interface results were recovered in the short wavelength limit $|k|a \to \infty$. Growth rates of unstable solutions for both mode types were plotted for a particular relative flow. It was found that the mode type having the faster growth rate depended critically on the density ratio ρ_p/ρ_∞ relative to some critical value; also, in the same paper, similar results were found for the compressible case, in a numerical study yielding the growth rate and eigenmode structures of the fastest growing streaming instability (sausage or kink) in a continuously structured configuration. In the notation of Lee et al. (1988), ρ_p is the density at the centre of the inhomogeneity and ρ_∞ is the density at large distances from the centre: in each case the sausage (kink) mode has the faster growth rate for ρ_p/ρ_∞ greater (less) than the critical value.

We noted above that the linear long wavelength solutions may be applied to the weakly nonlinear effect of soliton propagation (Roberts 1987). Another nonlinear effect is the steepening of propagating waves due to second-order terms in the wave amplitude (Hollweg 1987). Hollweg (1987) considered some nonlinear properties of incompressible surface waves, and found that the steepening rate is a function of the zeroth order velocity shear across the surface, and becomes very large as the velocity shear approaches the threshold U_{KHI} for the linear Kelvin-Helmholtz instability in the single interface. He therefore suggests that the instability may be modified by nonlinear effects. However, we note from Figure 2 of his paper that the steepening rate is zero at relative flows corresponding to the first and second crossings of range limits in the propagation windows. Therefore we might expect the onset of instability at $U_D = v_{A0} + v_{Ae}$ to occur even in the nonlinear case, although further investigation is required in order to test this supposition.

In our general model, the propagating medium is discretely structured, while some authors consider continuous structuring. For an incompressible plasma with magnetic field

and field-aligned flow both varying arbitrarily transversely to their direction, stability is assured if $U^2 < {v_A}^2$ everywhere (Kent 1968), in agreement with the sufficient conditions noted by Chakraborty (1968). This condition ensures that magnetic energy always exceeds the kinetic energy, and for a uniform magnetic field the sufficient condition for stability is then $U_{0M} < 2v_{A0}$ (Lau and Liu 1980), where U_{0M} is the difference between the extremes in velocity. This result corresponds to the minimum stability threshold given in our analysis for a discretely structured configuration with relative flow $U_D = U_{0M}$, and has been confirmed numerically (Ray and Ershkovich 1983) for the case of a linear shear layer replacing the single interface between two equal uniform media in relative motion.

3.3.5 Implications for the effects of flows on compressible surface modes

For the incompressible case we made sense of the results by starting from the static case, in which all modes are stable, and considering how these modes develop as the relative flow increases within a fixed reference frame, leading to the Kelvin-Helmholtz instability for sufficiently large relative flows. This development, and its dependence on the (effective) density ratio, was discussed in terms of the changing qualitative properties of the propagation windows, for which we may define three flow regimes which are fixed by the Alfvén speeds, and are independent of reference frame and effective density ratio. It was found that the beginning of the third flow regime, that is $U_D = v_{A0} + v_{Ae}$, corresponds to the minimum stability threshold, being attained for the critical case on the effective density ratio, given by $f = f^*$ (recall that $f^* \equiv (\rho_e v_{Ae})(\rho_0 v_{A0})$). This case acts as a topological separator of the stable solutions: in the third flow regime both solutions, where stable, lie in the *same* range, which is $U_0 - v_{A0} < c_p < U_0 + v_{A0}$ for $f > f^*$ and $U_e - v_{Ae} < c_p < U_e + v_{Ae}$ for $f < f^*$.

The main point to note is that the above knowledge, when combined with the form of $f(|k|a)$ for each mode type and the solution for the $f = 1$ case, may be used to infer the dispersion diagrams and stability properties for the slab and cylinder, without having to solve the equations. We now consider the possibility of similarly inferring properties for the compressible case, although this is considerably more complicated than the incompressible case.

Relating dispersive and stability properties to propagation window evolution

Consider first the propagation windows. For all surface modes under consideration, we have the requirement that ε_0 and ε_e have opposite signs. This requirement leads to the propagation windows for the incompressible case (see Section 3.3.1) which are therefore fundamental to all surface modes. From these propagation windows we defined three flow regimes, separating different qualitative classes of solutions: throughout the first regime ($0 < U_D < |v_{Ae} - v_{A0}|$) the solutions are qualitatively similar to the static case but for the asymmetry, leading them to be distorted reflections of each other; in the second flow regime ($|v_{Ae} - v_{A0}| < U_D < v_{A0} + v_{Ae}$) the dispersion of solutions in one of the ranges reverses so that they are distorted translations of each other; in the third regime ($U_D > v_{A0} + v_{Ae}$) both solutions, where stable, lie within either of the two ranges for which the ranges constraint is satisfied (see Figures 3.9–3.17).

For the stable surface modes of the compressible case we similarly expect these qualitative features to be associated with each flow regime. Further, since the case $U_D = v_{A0} + v_{Ae}$ is the earliest point in the propagation window at which the two solutions for c_p for any given mode may possibly coalesce, it ought to similarly represent a minimum value of the stability threshold. Whether or not this minimum is actually *attained* in the compressible case remains to be seen.

While all stable surface modes (compressible or otherwise) must lie within the propagation windows defined for the incompressible case, for the compressible case these basic propagation windows may be reduced or split according to the relative ordering of the shifted Alfvén speeds $U_i \pm v_{Ai}$, sound speeds $U_i \pm c_{si}$ and tube speeds $U_i \pm c_{Ti}$ ($i = 0, e$), so that they may contain stable radiative (${m_e}^2 < 0$) or body (${m_0}^2 < 0$, ${m_e}^2 > 0$) modes as well as surface modes (${m_0}^2 > 0$, ${m_e}^2 > 0$), all of which may be fast or slow. Sub-regimes of U_D may be defined in terms of sums and differences of the v_{Ai}, c_{si} and c_{Ti}, so that as U_D passes through a given critical value the corresponding qualitative change in the propagation window may imply that, for example, a surface or body mode changes character, becoming a radiative mode.

This means that the development of a given surface mode with increasing relative flow may not necessarily be the same as for the incompressible case: we might expect that for

small relative flows, the main effect is the asymmetry whereby the solution propagating with the flow is shifted by more than the backward solution; however, while for the incompressible case this discrepancy increases right up to the onset of instability, we might find that a compressible surface changes character to a radiative or body mode before the onset of instability. The detailed development to instability of a given mode is to be determined through numerical solution of the dispersion relation for a particular ordering of the various Alfvén, sound and tube speeds, although greater insight into the results from this approach may be obtained if it is coupled with analysis of the evolving propagation windows.

Determining critical cases

While for compressible surface modes the basic features associated with the main flow regimes defined in Section 3.3.1 ought to remain as for the incompressible case, the splitting of the propagation window makes it difficult to attempt a study of the type we carried out for the incompressible case, that is the determination of a critical effective density ratio which acts as a topological separator of stable solutions and yields the minimum relative flow for coalescence of solutions. For the compressible case, we may similarly relate the dispersive properties for each geometry to an effective density ratio, hence the determination of a critical value would have implications for the dispersive and stability properties with increasing relative flow. Unlike the incompressible case, where the density ratio is arbitrary, for the compressible case it is determined by pressure balance across interfaces and expressed in terms of the sound and Alfvén speeds in each medium, so that varying the density ratio may vary the propagation windows. This is in contrast to the incompressible case where for fixed Alfvén speeds the same propagation windows apply to all modes. Thus it is more difficult to compare solutions for single interfaces of different density ratios. Further, for dispersive modes the "effective"component of the dispersion relation (that is, the ratio $f_0(x_0)/f_e(x_e)$ in (3.1)) is transcendental in c_p, making it more difficult to relate the single interface results to the dispersive properties of the slab or cylinder.

In a stability study of the compressible single interface, Prialnik, Eviatar and Ershkovich (1986) obtained the growth rate of the Kelvin-Helmholtz instability as a function

of the density jump between the plasmas. Their results indicate that for a fixed value of the relative flow (at which unstable solutions exist), there is a critical density ratio at which the growth rate is a maximum.

Literature on the compressible case

In studies of the effects of flows on compressible modes by Nakariakov and Roberts (1995a) and Nakariakov and Roberts (1996) attention was restricted to stable modes of the slab, taking small values of the relative flow as deemed realistic for particular solar applications. In our terminology, their attention was restricted to the first and second flow regimes, and hence the full development to the Kelvin-Helmholtz instability was not investigated. However, by considering the changes in range limits for stable modes as a result of the flow, Nakariakov and Roberts (1995a) and Nakariakov et al. (1996) noted, in agreement with our comments above, that relative flows may not only cause the appearance of backward modes but also lead to the "disappearance" of a given surface or body mode, or more strictly a change in their behaviour from trapped to radiative modes (for which an alternative dispersion relation applies), as they now leak their energy to the external medium. The study of backward modes was further developed by Joarder et al. (1997a), who confirmed these modes as negative energy waves, so that in the presence of dissipation they are subject to dissipative instability, so that they grow rather than decay in amplitude.

Satya Narayanan (1991) considered compressible surface waves in a moving ($U_0 = 0$, $U_e \neq 0$) cylinder, obtaining a dispersion relation equivalent to (2.69) of Section 2.2.4 above. The dispersion relation was solved numerically, plotting positive solutions for c_p/v_{A0} against the "compressibility parameter" c_{s0}/v_{A0} for one parameter set and fixed wavenumber, for which all solutions were stable. This demonstrated the existence of two surface modes (that is, fast and slow) as occurs for the static case, and it was noted that the results of the incompressible case apply to the incompressible limit of the slow surface mode. However, their limited approach does not provide insight into the effects of flows on stable compressible surface modes, nor were the stability conditions considered.

We turn now to the effect of compressibility on the Kelvin-Helmholtz instability. In the absence of magnetic fields ($v_{A0} = v_{Ae} = 0$), a compressible single interface with $\rho_0 = \rho_e$ and $c_{s0} = c_{se}$ is stable for ${U_D}^2 \geq 8{c_{s0}}^2$ (Miles 1958), whereas in the incompressible case there

is instability for all $U_D > 0$. Hence in this case the introduction of compressibility has a stabilising effect for sufficiently large relative flows. However, in other cases compressibility may have a destabilising effect. In a consideration of the compressible magnetic single interface for the case of a very "stiff" plasma ($c_{si} \gg v_{Ai}$), it was found by Sen (1964) that *"the effect of slight compressibility is to always destabilise an otherwise neutrally stable stationary state of motion"*. This was done through performing a perturbation analysis for large c_{s0} and c_{se} of the compressible dispersion relation, taking as the zeroth order solution a marginally stable solution for the incompressible case. Fejer (1964) reached the same conclusion by considering corrections to the incompressible dispersion relation for the single interface when taking large but finite sound speeds $c_{si} \gg v_{Ai}$, which leads to a reduced stability threshold compared to U_{KHI}.

Certain other special cases have been considered analytically, including cases with the propagation vector and/or magnetic fields orientated transverse to the flow; see the reviews by Gerwin (1968) and Rae (1983). The compressible case is generally complicated by the possibility of *two* surface modes, namely fast and slow, each with different properties, and this must be borne in mind when comparing results. Further, for investigations based on the squared form of the dispersion relation, care must be taken to exclude spurious roots which do not satisfy the original dispersion relation and conditions under which it is derived. These points have not been appreciated by all authors, and the resulting errors and discrepancies between results have been discussed in the literature (Gerwin 1968, Pu and Kivelson 1983, Kirtskhalia 1994).

In agreement with our own discussion, Kirtskhalia (1994) argues that stability conditions may be deduced from the propagation windows, noting that for stable surface modes the conditions ${m_0}^2 > 0$ and ${m_e}^2 > 0$ must be satisfied simultaneously with the constraint corresponding to our ε_0 and ε_e having opposite signs. Although critical of earlier authors for neglecting this latter requirement, Kirtskhalia (1994) does not properly analyse its implications, and hence fails to note the critical relative flows $U_D = |v_{Ae} - v_{A0}|$ and $U_D = v_{A0} + v_{Ae}$ revealed by our rigorous analysis in Section 3.3.1 above. Further, by restricting consideration to only one of the two positive branches of each ${m_i}^2$ curve it was found that the constraints for stable surface modes cannot all be simultaneously satisfied. Kirtskhalia (1994) therefore concludes that *"the tangential discontinuity is ab-*

solutely unstable", and that results of previous studies are invalid. While this conclusion is obviously false, as evidenced by the stable surface waves in the above-mentioned papers of Nakariakov and co-authors, the discussion contains valid points.

Pu and Kivelson (1983) state that fast and slow surface modes each have *two* critical values of the relative flow, between which they are unstable. The unstable ranges of U_D for fast and slow modes are non-overlapping, with that of the slow mode occupying smaller values, and that of the fast mode containing the stability threshold for the incompressible case for the parameter sets chosen typical of the magnetosphere. They suggest that when the relative flow exceeds the upper threshold for the fast mode, the unstable fast mode becomes a stable body mode, with phase speed in excess of the fast speed $c_f = ({c_s}^2 + {v_A}^2)^{1/2}$ of each medium, noting that for the incompressible case $c_f \rightarrow \infty$ and hence there is no upper stability threshold. Indeed, they note that previous authors agree that *"compressibility has a stabilising effect when the relative flow speed sufficiently exceeds the magnetoacoustic speed"*, that is for $U_D > c_f$.

The existence of two critical relative flows was also noted in a numerical study of the compressible single interface (Ferrari, Trussoni and Zaninetti 1980), the authors saying the lower value is *"due to the 'rigidity' of magnetic field lines inhibiting perturbations of the contact surface for low velocities"* while the upper value *"arises when the flow velocity is too large to be matched by perturbations moving at typical speeds* $\approx c_f$*"*. They also noted that the stability properties may vary with the strength of inhomogeneity in density and magnetic field strength. This was also found in their extension of the model to the cylinder (Ferrari, Trussoni and Zaninetti 1981), where it was noted that different mode types had different stability properties, which vary with $|k|a$, and that the effects of a finite width inhomogeneity are also manifested in the appearance of a new branch of unstable modes, called *"reflection modes"*, occurring at shorter wavelengths than "ordinary", i.e. surface, modes.

These new modes correspond to unstable body modes, and their existence had been previously indicated for the hydrodynamic slab case (Gill 1965), and they were further investigated in a stability study (Bodo, Rosner, Ferrari and Knobloch 1989) of the sausage modes of the compressible isolated cylinder, in which unstable *slow* body modes were discovered. Bodo et al. (1989) interpreted the destabilisation of body modes in terms

of negative energy waves (that is, backward body modes) which for sufficiently large flows couple to external propagating waves (that is, radiative waves) leading to a loss of energy from the cylinder. Further, the stability properties of the various mode types were seen to depend on the parameter regime for sound and Alfvén speeds. These authors recently extended this work to nonaxisymmetric ($n \geq 1$) modes (Bodo, Rosner, Ferrari and Knobloch 1996).

Unstable body modes were also found in the stability studies of the MHD compressible slab and cylinder by Hardee and co-authors (Hardee, Cooper, Norman and Stone 1992, Hardee 1995, Hardee, Clarke and Rosen 1997), who in a linear stability analysis also gave analytical expressions for the maximum growth rates and solutions in the low and high frequency limits. In their nonlinear simulations, the linear analysis was found to provide a reasonable description of the spatial stability properties of the jet, and for the cylinder (Hardee et al. 1997) the jet structure at large amplitudes was seen to depend on the density ratio. Similarly, in nonlinear temporal stability studies of the hydrodynamic compressible slab and cylinder (Bodo, Massaglia, Ferrari and Trussoni 1994, Bodo, Massaglia, Rossi, Rosner, Malagoli and Ferrari 1995), the initial stages were well described by linear analysis while the long term evolution of the jet, as determined by the fastest growing linear mode, depended critically on the density ratio. For further discussion of the stability of jets and references to earlier stability studies, see the review by Birkinshaw (1991).

Compressibility clearly has a complex role to play in the onset of the Kelvin-Helmholtz instability as well as in the dispersion of stable waves, with the fast and slow modes having different properties which may depend on the particular parameter regime. Although there is a wealth of literature on the compressible Kelvin-Helmholtz instability, of which we have discussed only a relevant sample, the problem is not entirely understood, even for the single interface. A useful approach may be to carry out a combined study of stable and unstable waves, by tracing the development of stable solutions for the static case as relative flow increases, up to the onset of instability. This development may be better understood when considered in terms of the evolving propagation windows [3], in which one ought to include

[3]Note that for nonparallel orientations of magnetic field, flow and propagation vector, the propagation windows are defined in terms of the solutions, in the given reference frame and for the particular propagation direction, for the fast, slow and Alfvén modes of each (moving) medium treated separately as infinite and

the shifted fast speeds $U_i \pm c_{fi}$ $(i = 0, e)$. As has been found here for the incompressible case, a detailed study of this type for the compressible single interface may also provide a basis for understanding the slab and cylinder. In this, it is important to include the full effects of inhomogeneity in the plasma parameters in order to reveal the full structure of the equations and gain insight into dispersive effects. Such a qualitative study may cast additional light on the results of the various numerical investigations of the stability of the compressible single interface, slab and cylinder, and provide greater insight into dispersive effects and the role of compressibility in the Kelvin-Helmholtz instability.

3.4 Summary and conclusions

We have carried out a generalised treatment of incompressible surface modes, which allows us to more easily compare and contrast the different geometries and mode types, thereby separating the general features from dispersive effects and gaining an insight into the nature of incompressible surface modes in the presence of relative flows.

After discussing the static case in Section 3.2, we showed in Section 3.3 how the basic effect of flow is to cause the solutions for the longitudinal phase velocity $c_p \equiv \omega/k$ to be shifted (in the given frame of reference) relative to their symmetric values $c_p = \pm c_{ps}$ for the static case, with c_{ps} defined according to the mode and referred to as its basic speed. Sufficiently large flows may lead to a change in sign of one of the solutions for c_p, that is a reversal (in the given frame of reference) in the direction of propagation of the given mode; such a mode being referred to as a backward mode when this occurs. For a bulk flow U there is a uniform shift of solutions, so that $c_p = U \pm c_{ps}$, while in the presence of relative flows we may write $c_p = U_m \pm c_{pm}$, where ${c_{pm}}^2 \leq {c_{ps}}^2$ (see equation (3.31)), referring to U_m as the mean shift and c_{pm} as the modified basic speed. The two solutions for c_p are shifted by different amounts relative to their respective values for the static case, so that they share the same sign when $|U_m| > c_{pm}$ and may ultimately coalesce for sufficiently large relative flows. The condition for coalescence, $c_{pm} = 0$, yields the threshold relative flow U_C for the Kelvin-Helmholtz instability; see equation (3.43). For larger relative flows ${c_{pm}}^2 < 0$ and the solutions for c_p are complex conjugates, indicating instability.

uniform. See Section 2.1.1 for the case of field-aligned flow and arbitrary propagation direction.

These general features may be discussed in terms of the propagation windows that delineate the ranges in which stable solutions for c_p may lie. In Section 3.3.1 we discussed how the propagation windows undergo qualitative changes as the increasing relative flow $U_D \equiv |U_0 - U_e|$ passes through the critical values $|v_{Ae} - v_{A0}|$ and $v_{Ae} + v_{A0}$ (taking the Alfvén speeds v_{A0} and v_{Ae} to be fixed). This allows us to define three flow regimes, characterised by different qualitative properties: the dispersive properties of the solutions in the first regime ($0 < U_D < |v_{Ae} - v_{A0}|$) are qualitatively similar to the static case, being distorted reflections of each other; in the second regime ($|v_{Ae} - v_{A0}| < U_D < v_{A0} + v_{Ae}$) there is a reversal in the dispersive properties of solutions in one of the two ranges, so that they are distorted translations of each other; in the third regime ($U_D > v_{A0} + v_{Ae}$) both solutions, where stable, lie within the same range so that coalescence is now possible, leading to the Kelvin-Helmholtz instability. The appearance of backward modes may also be discussed in terms of the propagation windows. Note that the definition of the three flow regimes, and the general qualitative properties associated with each regime, are independent of choice of Alfvén speeds and reference frame. Further, once the Alfvén speeds and reference frame are fixed, the same propagation windows apply to all incompressible surface modes, hence they are a useful framework on which to base a comparative study of different geometries and mode types.

The dispersive effects have been shown to be associated with an "effective" density ratio $f\rho_0/\rho_e$, which may vary (through $f = f(|k|a)$, see Table 3.1 and Figure 3.1) with mode type and wavenumber as well as with the density ratio ρ_0/ρ_e. This allows us to discuss the dependence of c_p on $f(|k|a)$ for the slab or cylinder in terms of its dependence on ρ_0/ρ_e for the single interface, taking fixed Alfvén speeds v_{A0} and v_{Ae}.

It is by this approach that we have been able to define a critical case, written generally as $f = f^* \equiv (\rho_e v_{Ae})/(\rho_0 v_{A0})$, which in the context of the propagation windows acts as a topological separator of the solution curves for c_p. This critical case yields the minimum value $v_{A0} + v_{Ae}$ of the stability threshold U_C, as can be seen from our alternative expression (3.46) for U_C in terms of f^*. This minimum value of U_C marks the beginning of the third flow regime, and hence is the earliest possible point in the propagation windows for coalescence of the two solutions for c_p for a particular mode. We may also note that for this critical case the basic phase speed c_{ps} in the absence of relative flows is the geometric

mean of the two Alfvén speeds, that is ${c_{ps}}^2 = v_{A0}v_{Ae}$. We have shown how knowledge of the evolution of the propagation window combined with the critical case $f = f^*$ and the form of $f(|k|a)$ together yields information about the dispersive and stability properties of a given mode and configuration of plasmas, without requiring solution of the dispersion relation itself.

To our knowledge, detailed discussion of the above points is absent from the literature; we present this discussion for the first time here in this Chapter. Hence, as well as formulating a general treatment covering the single interface, uniform slab and uniform cylinder, which had previously been given separate treatments, we have also uncovered a number of features overlooked in published studies. We have also explained why these features are not readily apparent in the less extensive approaches used by earlier authors. Our analysis of the evolution of the propagation windows has proved particularly invaluable. We have also discussed in physical terms the qualitative evolution of the well known stable solutions for the static case, as the relative flow is increased up to the onset of the Kelvin-Helmholtz instability, and as such have gained a deeper insight into the effects of flows on incompressible surface modes. Finally, we have provided a framework on which to base a future study of the dispersive and stability properties of compressible surface modes in the presence of flows.

Chapter 4

Compressible surface modes on a static magnetic-nonmagnetic interface

4.1 Introduction

In the previous chapter, we found that for surface modes the incompressible approximation simplifies the equations dramatically, in that the dispersion relation is no longer transcendental in c_p. We have already seen the advantage of this tractability from the previous chapter when we were able to gain great insight into surface modes with flow using a largely analytical approach. It is clearly advantageous to determine the situations in which the incompressible approximation can be applied.

While the incompressible approximation is widely used in this context, it appears that little study has been made as to its applicability to the compressible case. Studies of compressible surface modes usually give the reduced form of the dispersion relation for the incompressible limit, but do not then compare the results they obtain with those given by the incompressible limit of the dispersion relation.

Here we consider the applicability of the incompressible case to the compressible surface modes of a simple case, that of the static magnetic-nonmagnetic interface. In this case it is straightforward to obtain the exact solutions to the full dispersion relation, so that one

may question the need to consider the incompressible limit as a means of investigating the dispersion relation. However, this simplicity actually makes it an ideal case to examine, as the results may be easily compared.

We determine the variation of the phase speed c_p in terms of the parameters involved, considering both fast and slow surface modes. The applicability of the incompressible results is assessed by comparing the calculated compressible c_p with the value of c_k for an incompressible medium with the density ratio ρ_e/ρ_0 determined by the pressure balance in equilibrium. We also consider the other features associated with the incompressible case, namely $m_0/k = 1$, $m_e/k = 1$ so that $m_0 = m_e$.

4.2 The model

Consider the static magnetic-nonmagnetic interface. With $v_{Ae} = 0$ the full dispersion relation for the single interface may be written as

$$\frac{\rho_e}{\rho_0}\left(\frac{{c_p}^2}{{v_{A0}}^2 - {c_p}^2}\right) = \frac{m_e}{m_0} \tag{4.1}$$

where

$$\frac{{m_0}^2}{k^2} = \frac{({v_{A0}}^2 - {c_p}^2)({c_p}^2 - {c_{s0}}^2)}{({c_{s0}}^2 + {v_{A0}}^2)({c_p}^2 - {c_{T0}}^2)}, \qquad \frac{{m_e}^2}{k^2} = 1 - \frac{{c_p}^2}{{c_{se}}^2}. \tag{4.2}$$

Equilibrium pressure balance (see (2.30)) implies that

$$\frac{\rho_e}{\rho_0} = \frac{{c_{s0}}^2}{{c_{se}}^2} + \frac{\gamma}{2}\frac{{v_{A0}}^2}{{c_{se}}^2}. \tag{4.3}$$

In most solar applications we take $\gamma = 5/3$, which is the value used in all our numerical illustrations in this chapter.

For the static case there only exist *stable* (ω real) solutions to the dispersion relation (4.1). With m_e real we have $c_p < c_{se}$, while the requirement that m_0 is real implies that either $c_p < c_{T0}$ or $c_p \in (c_{s0}, v_{A0})$, where the set notation is shorthand for "c_p lies between c_{s0} and v_{A0}, with the order of these limits unspecified". The additional ranges requirement for surface waves in a static medium that ${c_p}^2 \in ({v_{A0}}^2, {v_{Ae}}^2)$ (see Section 2.3) implies that $0 < c_p < v_{A0}$. With $v_{Ae} = 0$, only the fast branch to ${m_e}^2/k^2$ exists, with $0 < c_p < c_{se}$. Depending on the relative ordering of the speeds c_{se}, c_{s0} and v_{A0}, there may be one or two surface modes, according to whether the positive branch of ${m_e}^2/k^2$ overlaps with one

or both positive branches of the curve for m_0^2/k^2. We obtain two possible ranges: one with

$$c_p < \min(c_{T0}, c_{se}) \qquad (\textit{slow surface wave}) \tag{4.4}$$

and the other with

$$c_{s0} < c_p < \min(c_{se}, v_{A0}) \qquad (\textit{fast surface wave}). \tag{4.5}$$

The former case is referred to as the *slow surface wave*, the latter as the *fast surface wave* (Roberts 1981a). The slow surface mode always exists for finite non-zero sound speeds, i.e.

$$c_{s0} > 0, \tag{4.6}$$

while for the fast surface mode we require

$$v_{A0} > c_{s0}, \quad c_{se} > c_{s0}. \tag{4.7}$$

In (4.7), the latter requirement implies that the magnetic region is cooler than the non-magnetic one, the former includes the case where the magnetic region is low β. We note that in the limit of a cold (zero β) magnetic plasma, $c_{s0} \to 0$, the slow mode disappears and only the fast mode remains.

The solutions of the dispersion relation (4.1) have been examined by Miles and Roberts (1989). The compressible single interface was also investigated by Wentzel (1979), although he did not note the existence of two surface modes. Jain and Roberts (1991) extended the work of Miles and Roberts (1989) by considering non-parallel propagation for the magnetic-nonmagnetic interface and parallel propagation for the magnetic-magnetic interface. Equation (4.1) was also given by Roberts (1981b) to describe surface waves in a wide slab, the exterior of which is field-free.

The dispersion relation (4.1) must in general be treated numerically, due to the presence of radicals. However, we can make analytical progress by squaring the dispersion relation (4.1) to obtain (Roberts 1981a, Miles and Roberts 1989)

$$({c_{T0}}^2 - {c_p}^2)({v_{A0}}^2 - {c_p}^2)({c_{se}}^2 - {c_p}^2) = \Lambda^2 {c_p}^4({c_{s0}}^2 - {c_p}^2) \tag{4.8}$$

where

$$\Lambda^2 = \left(\frac{\rho_e}{\rho_0}\right)^2 \frac{{c_{se}}^2}{{c_{s0}}^2 + {v_{A0}}^2} \tag{4.9}$$

and ρ_e/ρ_0 is given by (4.3). It should be noted, however, that the process of squaring introduces spurious roots, that is solutions to (4.8) but not the original dispersion relation (4.1). Such spurious roots may be eliminated on use of the ranges constraints described above.

4.3 Explicit analytical solutions for special cases

We may obtain explicit analytical expressions for the phase speed c_p for certain specific values of the sound speed c_{s0} in the magnetic medium. The specific cases we consider are: case (i) $c_{s0} = 0$; case (ii) $c_{s0} = c_{se}$; and case (iii) $c_{s0} = v_{A0}$. A fourth case, namely case (iv) $\Lambda = 1$, is discussed separately below in Section 4.3.2. See also Mundie and Roberts (1998).

4.3.1 Treatment for cases $(i) - (iii)$

In each of cases $(i) - (iii)$, the squared dispersion relation (4.8) contains a spurious factor (corresponding to one or more of c_p, m_e, m_0 being zero) which may be eliminated to leave a quadratic in ${c_p}^2$. While case (i) was noted by Miles and Roberts (1989) and case (ii) by Roberts (1981a), the third case was overlooked, as was the fact that all three cases could be treated together by writing the obtained quadratic equation in the general form

$$(1-\Lambda^2){c_p}^4 - (a^2+b^2){c_p}^2 + a^2b^2 = 0. \tag{4.10}$$

In equation (4.10) we have

$$\begin{aligned}
&\text{case } (i): \quad c_{s0} = 0, \quad \{a,b\} = \{c_{se}, v_{A0}\} \\
&\text{case } (ii): \quad c_{s0} = c_{se}, \quad \{a,b\} = \{v_{A0}, c_{T0}\} \\
&\text{case } (iii): \quad c_{s0} = v_{A0}, \quad \{a,b\} = \{c_{se}, c_{T0}\} \ .
\end{aligned}$$

The labels of the speeds in the curly brackets are interchangeable. For the purposes of a general treatment it is convenient to choose a to be the larger of the two speeds in each case, so that $a \geq b$. In case (ii) we then necessarily have $a = v_{A0}$ and $b = c_{T0}$ but for the other cases the labelling depends on the relative magnitudes of the speeds involved.

The roots of the quadratic (4.10) are given by

$$2(1-\Lambda^2){c_p}^2 = (a^2+b^2) \pm \left\{(a^2-b^2)^2 + 4\Lambda^2a^2b^2\right\}^{1/2}. \tag{4.11}$$

The plus root may be rejected as a spurious solution introduced by the squaring: it yields ${c_p}^2 < 0$ for $\Lambda^2 > 1$ and ${c_p}^2 > (a^2 + b^2)$ for $\Lambda^2 < 1$, thus violating the ranges constraint that $0 < {c_p}^2 < \min({c_{se}}^2, {v_{A0}}^2)$. We therefore restrict attention to the minus root, which for $\Lambda^2 \neq 1$ may be written as (Mundie and Roberts 1998)

$$ {c_p}^2 = \frac{2a^2b^2}{(a^2+b^2) + \{(a^2-b^2)^2 + 4\Lambda^2 a^2 b^2\}^{1/2}}. \tag{4.12} $$

We obtain (4.12) from (4.11) as follows. Using the minus root of (4.11), multiply the numerator and denominator of its right-handside, by the right-handside of the plus root of (4.11), in order to remove the radical from the numerator. Both sides of the obtained equation then contain a factor $2(1-\Lambda^2)$, which may be cancelled (provided $\Lambda \neq 1$) to obtain (4.12). The case $\Lambda = 1$ is considered separately, and it too leads to a quadratic in ${c_p}^2$; see Section 4.3.2.

Our ultimate aim is to assess the applicability to the compressible case of results obtained for the incompressible case, and so it is of interest to compare the obtained phase speed with the equivalent kink speed. By "equivalent" kink speed we mean the phase speed of the surface wave on a single interface separating two incompressible media having the same ratio of magnetic field strengths and densities as for the compressible case being considered here. For the case of one of the media being field-free ($v_{Ae} = 0$) the kink speed c_k is given by

$$ {c_k}^2 = \frac{\rho_0}{\rho_0 + \rho_e} {v_{A0}}^2. \tag{4.13} $$

For the incompressible case we may choose the density ratio ρ_e/ρ_0 arbitrarily, whereas for compressible media this ratio is determined by the sound and Alfvén speeds, and is given by equation (4.3). With (4.3), we obtain

$$ {c_k}^2 = \frac{{v_{A0}}^2}{1 + \frac{{c_{s0}}^2}{{c_{se}}^2} + \frac{\gamma {v_{A0}}^2}{2{c_{se}}^2}}. \tag{4.14} $$

We will also consider whether the other characteristics of the incompressible case (namely $m_e/k = m_0/k = m_e/m_0 = 1$) go hand in hand with the closeness of the kink speed approximation c_k to the phase speed c_p.

Equation (4.12) gives ${c_p}^2$ explicitly. Nonetheless, it is of interest to obtain bounds on ${c_p}^2$ as follows. First, rewrite (4.12) as

$$ {c_p}^2 = \frac{2a^2}{(\frac{a^2}{b^2}+1)+\left\{(\frac{a^2}{b^2}-1)^2+4\Lambda^2\frac{a^2}{b^2}\right\}^{1/2}}. \tag{4.15} $$

Then, with $a \geq b$, the denominator of (4.15) is greater than or equal to $(2+2\Lambda)$, so that ${c_p}^2 \leq a^2/(1+\Lambda)$. Similarly, ${c_p}^2 \geq b^2/(1+\Lambda)$. Overall, we obtain

$$ \frac{b^2}{1+\Lambda} \leq {c_p}^2 \leq \frac{a^2}{1+\Lambda}. \tag{4.16} $$

If $a = b$ we immediately obtain ${c_p}^2 = a^2/(1+\Lambda)$. Note that since $\Lambda = \Lambda(c_{se}, v_{A0}, c_{s0})$ is a function of a and b, varying either a or b uniformly does not lead to a corresponding uniformity in these bounds and they may for some parameter values be even less tight than the ranges constraints (4.4) and (4.5) for each mode type.

Having given the formulae in their general form, we now turn to consideration of each case in turn. Note that in all our numerical illustrations we set $\gamma = 5/3$.

Case (i): $c_{s0} = 0$ (fast mode only)

Consider first case (i). This case corresponds to the magnetic medium having a very low plasma β: the magnetic pressure dominates the plasma pressure. We may set the plasma pressure p_0 to be zero, which in turn implies a sound speed c_{s0} of zero: we apply the "cold plasma" approximation to the magnetic medium. For this case we obtain the fast mode only.

For this case we have $c_{s0} \equiv 0$ and $\{a, b\} = \{c_{se}, v_{A0}\}$. From (4.3) and (4.9) we have

$$ \frac{\rho_e}{\rho_0} = \frac{\gamma {v_{A0}}^2}{2{c_{se}}^2}, \quad \Lambda^2 = \frac{\gamma^2 {v_{A0}}^2}{4{c_{se}}^2} \tag{4.17} $$

so that from (4.12) the phase speed c_p is given by

$$ {c_p}^2 = \frac{2{v_{A0}}^2{c_{se}}^2}{({v_{A0}}^2+{c_{se}}^2)+\{({v_{A0}}^2-{c_{se}}^2)^2+\gamma^2{v_{A0}}^4\}^{1/2}} \tag{4.18} $$

while the equivalent kink speed ${c_k}^2$ is given from (4.14) by

$$ {c_k}^2 = \frac{2{v_{A0}}^2{c_{se}}^2}{2{c_{se}}^2+\gamma{v_{A0}}^2}. \tag{4.19} $$

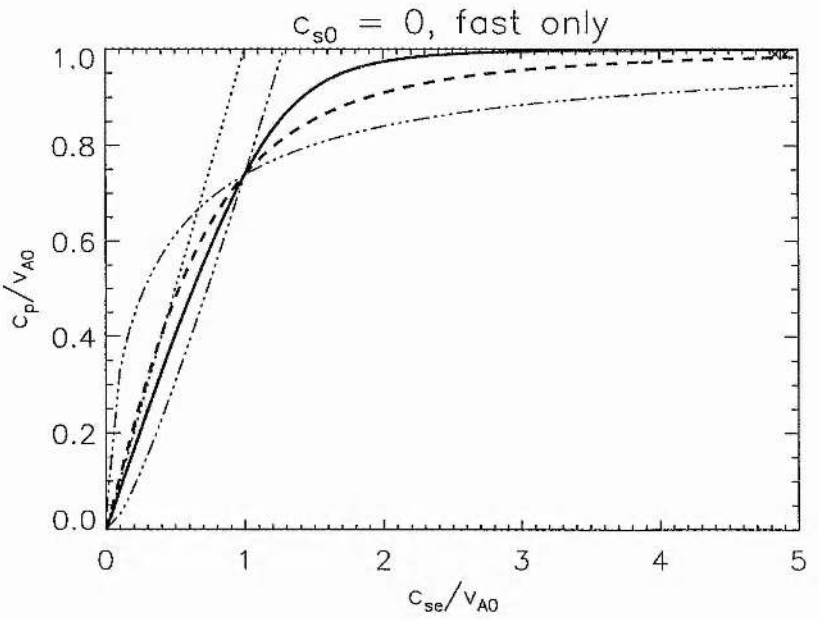

Figure 4.1: Magnetic-nonmagnetic interface, case (i): $c_{s0} = 0$, for which we obtain the fast mode only. The variation of c_p/v_{A0} (see equation (4.18) with $\gamma = 5/3$) as a function of c_{se}/v_{A0} is shown with a heavy solid line. The fast mode satisfies $c_{s0} < c_p < \min(c_{se}, v_{Ae})$, so that the solution is confined to the plot area on the right-handside of the inclined dotted line, along which $c_p = c_{se}$. The dot-dot-dot-dashed lines are the bounds given by (4.16). The heavy dashed line shows the normalised "equivalent" kink speed c_k/v_{A0}, given by (4.19). The limiting values of c_p/v_{A0} and c_k/v_{A0} as $c_{se}/v_{A0} \to \infty$ (see (4.21)) are shown on the right-handside of the plot with a diamond and an asterisk respectively (these symbols overlap and are on the upper edge of the plot), and correspond to $c_p \approx v_{A0}$ and $c_k \approx v_{A0}$; the limits as $c_{se}/v_{A0} \to 1$ are given by (4.20). Note that $c_p = c_k$ when $c_{se} = v_{A0}$ and $c_{s0} = v_{Ae} = 0$, and c_k lies outside the allowed range for c_p when $c_{se}/v_{A0} < (1 - \gamma/2)^{1/2} \approx 0.4$.

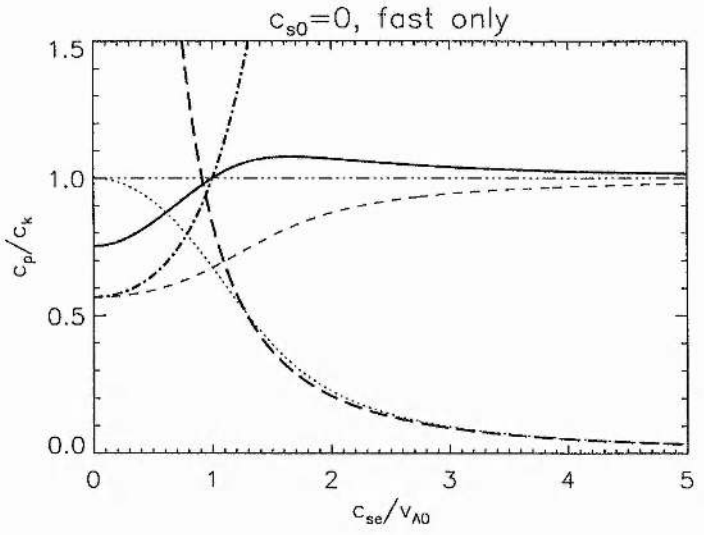

Figure 4.2: Magnetic-nonmagnetic interface, case (*i*): $c_{s0} = 0$, for which we obtain the fast mode only (see Figure 4.1). Here we further compare with the results from the incompressible case, again with $\gamma = 5/3$. The variation of c_p/c_k as a function of c_{se}/v_{A0} is shown with a heavy solid line. Intersections with the dot-dot-dot-dashed line shows where plotted quantities are equal to unity. The other lines are m_0/k (dotted), m_e/k (dashed), m_e/m_0 (heavy dot-dashed) and ρ_e/ρ_0 (heavy long-dashed).

In Figure 4.1 we show the variation of the phase speed c_p with the sound speed c_{se} of the nonmagnetic medium, for fixed Alfvén speed v_{A0}, plotting c_p/v_{A0} as a function of c_{se}/v_{A0} using a heavy solid line. We set $\gamma = 5/3$. The fast mode satisfies $c_{s0} < c_p < \min(c_{se}, v_{A0})$, so that the solution is confined to the plot area to the right-handside of the inclined dotted line, along which $c_p = c_{se}$. The dot-dot-dot-dashed lines are the bounds given by (4.16). The heavy dashed line shows the normalised "equivalent" kink speed c_k/v_{A0}, given by (4.19). Note that $c_k > c_{se}$ for $c_{se}/v_{A0} < (1-\gamma/2)^{1/2} \approx 0.4$; in this case c_k lies outside the allowed range for c_p and is therefore an unsatisfactory choice of approximation, despite being numerically close to c_p.

In Figure 4.2 we carry out further comparisons with the results for the incompressible case, by plotting c_p/c_k (heavy solid curve) as a function of c_{se}/v_{A0}. Also shown are plots of m_0/k (dotted), m_e/k (dashed), m_e/m_0 (heavy dot-dashed) and ρ_e/ρ_0 (heavy long-dashed). For the fast mode, $m_0/k < 1$ and $m_e/k < 1$.

Let us consider limiting values of the phase speed c_p and the kink speed c_k, given by (4.18) and (4.19) respectively. For $c_{se}/v_{A0} \to 0$ we obtain

$$c_p{}^2 \approx \frac{2c_{se}{}^2}{1+\{1+\gamma^2\}^{1/2}}, \qquad c_k{}^2 \approx \frac{2}{\gamma}c_{se}{}^2, \qquad \rho_e \gg \rho_0 \qquad (v_{A0} \gg c_{se},\ c_{s0} = v_{Ae} = 0) \tag{4.20}$$

which for $\gamma = 5/3$ yields $c_p \approx 0.824 c_{se}$ and $c_k \approx 1.095 c_{se}$. The limiting phase speed c_p in (4.20) was given by Miles and Roberts (1989), for the case $v_{A0}/c_{se} \to \infty$ with c_{s0}/c_{se} arbitrarily fixed (here $c_{s0}/c_{se} = 0$). This limit was also given by Roberts (1981b) for the wide isolated ($v_{Ae} = 0$) slab under coronal conditions, namely $v_{A0} \gg c_{s0}, c_{se}$.

As c_{se}/v_{A0} increases from zero, the normalised phase speed c_p/v_{A0} and normalised kink speed c_k/v_{A0} increase monotonically, so that as $c_{se}/v_{A0} \to \infty$ we have

$$c_p{}^2 \approx v_{A0}{}^2, \qquad c_k{}^2 \approx v_{A0}{}^2, \qquad \rho_e \ll \rho_0 \qquad (c_{se} \gg v_{A0},\ c_{s0} = v_{Ae} = 0). \tag{4.21}$$

These limiting values for the phase speed c_p and kink speed c_k are indicated on the right-handside of Figure 4.1 by a diamond and an asterisk respectively (these symbols overlap and are on the upper edge of the plot).

From Figure 4.1 and 4.2 we may note that $c_p \approx c_k$ for $c_{se}/v_{A0} \geq 1$, with equality for $c_{se} = v_{A0}$ (at which $m_0/k = m_e/k < 1$ and $\rho_e \approx \rho_0$) and in the limit $c_{se}/v_{A0} \to \infty$. In the latter case, the equality is due to the fact that the same limiting value v_{A0} is obtained

for both c_p (since $m_0/k \to 0$) and c_k (since $\rho_e/\rho_0 \to 0$), as opposed to a recovery of the results from the incompressible case. This is not surprising for the fast mode.

Case (ii): $c_{s0} = c_{se}$ (slow mode only)

Now let us consider case (ii). This case corresponds to both media having equal temperatures, and from (4.3) we necessarily have $\rho_e > \rho_0$ (unless $v_{A0} = 0$, which yields the hydrodynamic, equal fluids, case for which there are no surface modes). For the isothermal case $c_{s0} = c_{se}$ we obtain the slow mode only, since the existence of the fast mode requires that $c_{se} > c_{s0}$.

Here $c_{s0} \equiv c_{se}$, $a = v_{A0}$ and $b = c_{T0}$, where ${c_{T0}}^2 = {v_{A0}}^2 {c_{se}}^2/({v_{A0}}^2 + {c_{se}}^2)$. From (4.3) and (4.9) we have

$$\frac{\rho_e}{\rho_0} = 1 + \frac{\gamma {v_{A0}}^2}{2{c_{se}}^2}, \quad \Lambda^2 = \frac{({c_{se}}^2 + \frac{\gamma}{2}{v_{A0}}^2)^2}{{c_{se}}^2({c_{se}}^2 + {v_{A0}}^2)}, \tag{4.22}$$

so that from (4.12) the phase speed c_p is given by

$${c_p}^2 = \frac{2{v_{A0}}^2{c_{se}}^2}{({v_{A0}}^2 + 2{c_{se}}^2) + \{{v_{A0}}^4 + (2{c_{se}}^2 + \gamma {v_{A0}}^2)^2\}^{1/2}} \tag{4.23}$$

while the equivalent kink speed c_k is given from (4.14) by

$${c_k}^2 = \frac{2{v_{A0}}^2{c_{se}}^2}{4{c_{se}}^2 + \gamma {v_{A0}}^2}. \tag{4.24}$$

In Figure 4.3 we show variation of the phase speed c_p with the sound speed c_{se} of the nonmagnetic medium, for fixed Alfvén speed v_{A0}, plotting c_p/v_{A0} as a function of c_{se}/v_{A0} using a heavy solid line. We set $\gamma = 5/3$. The slow mode satisfies $c_p < \min(c_{T0}, c_{se})$, so that the solution is confined to the plot area to the right-handside of the inclined dotted line, along which $c_p = c_{se}$, and to the right-handside of the curved dotted line, along which $c_p = c_{T0}$. The dot-dot-dot-dashed lines are the bounds given by (4.16). The heavy dashed line shows the normalised "equivalent" kink speed c_k/v_{A0}, given by (4.24). Note that $c_k > c_{T0}$ for $c_{se}/v_{A0} < (1 - \gamma/2)^{1/2} \approx 0.4$, for which c_k lies outside the allowed range for c_p and therefore $c_p \approx c_k$ does not provide an appropriate approximation.

In Figure 4.4 we perform further comparisons with the results from the incompressible case, plotting c_p/c_k (heavy solid curve) as a function of c_{se}/v_{A0}, against which we also plot m_0/k (dotted), m_e/k (dashed), m_e/m_0 (heavy dot-dashed) and ρ_e/ρ_0 (heavy long-dashed). For the slow mode, $m_0/k > 1$ and $m_e/k < 1$.

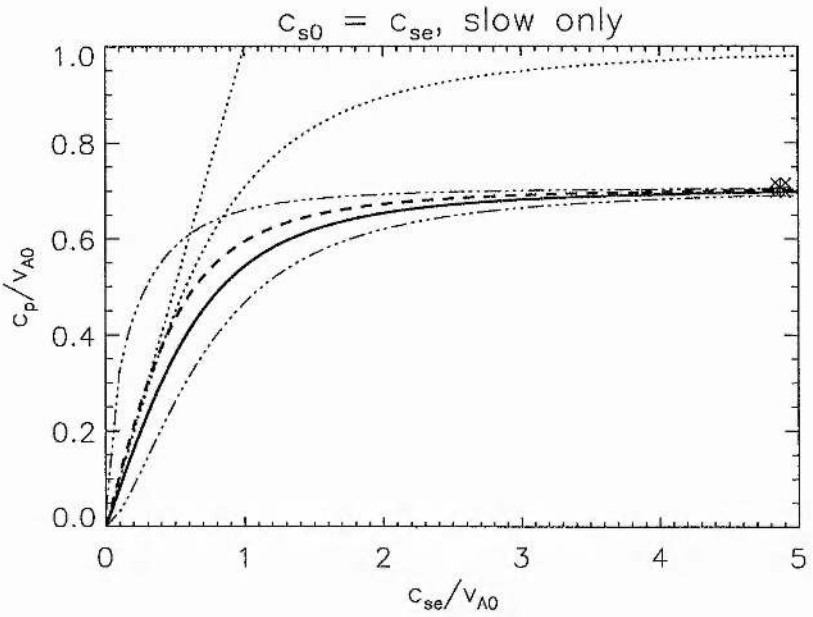

Figure 4.3: Magnetic-nonmagnetic interface, case (*ii*): $c_{s0} = c_{se}$, for which we obtain the slow mode only. The variation of c_p/v_{A0} (see equation (4.23) with $\gamma = 5/3$) as a function of c_{se}/v_{A0} is shown with a heavy solid line. The slow mode satisfies $c_p < \min(c_{T0}, c_{se})$, so that the solution is confined to the plot area to the right-handside of the inclined dotted line, along which $c_p = c_{se}$, and to the right-handside of the curved dotted line, along which $c_p = c_{T0}$. The dot-dot-dot-dashed lines are the bounds given by (4.16). The heavy dashed line shows the normalised "equivalent" kink speed c_k/v_{A0}, given by (4.24). The limiting values of c_p/v_{A0} and c_k/v_{A0} as $c_{se}/v_{A0} \to \infty$ (see (4.26)) are shown on the right-handside of the plot with a diamond and an asterisk respectively (these symbols overlap), and correspond to $c_p \approx v_{A0}/\sqrt{2}$ and $c_k \approx v_{A0}/\sqrt{2}$; the limits as $c_{se}/v_{A0} \to 1$ are given by (4.25). Note that c_k lies outside the allowed range for c_p when $c_{se}/v_{A0} < (1-\gamma/2)^{1/2} \approx 0.4$.

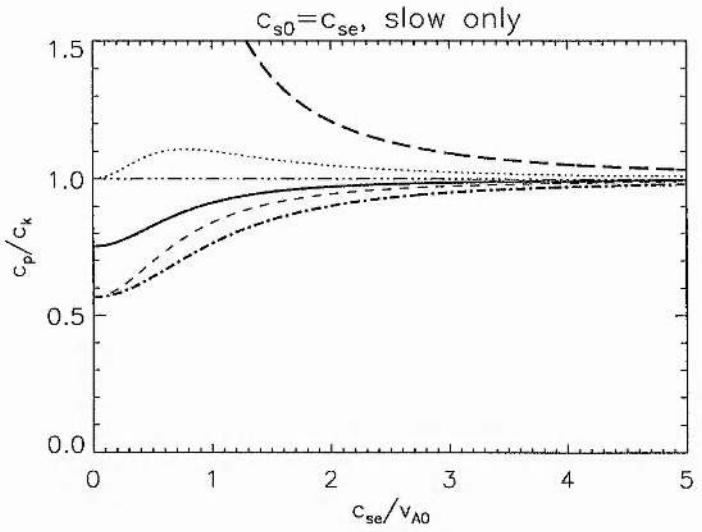

Figure 4.4: Magnetic-nonmagnetic interface, case (*ii*): $c_{s0} = c_{se}$, for which we obtain the slow mode only (see Figure 4.3). Here we further compare with the results from the incompressible case, again with $\gamma = 5/3$. The variation of c_p/c_k as a function of c_{se}/v_{A0} is shown with a heavy solid line. Intersections with the dot-dot-dot-dashed line shows where plotted quantities are equal to unity. The other lines are m_0/k (dotted), m_e/k (dashed), m_e/m_0 (heavy dot-dashed) and ρ_e/ρ_0 (heavy long-dashed).

Let us consider limiting values of the phase speed c_p and the kink speed c_k, given by (4.23) and (4.24) respectively. In the limit $c_{se}/v_{A0} \to 0$ we obtain

$$c_p{}^2 \approx \frac{2c_{se}{}^2}{1+\{1+\gamma^2\}^{1/2}}, \qquad c_k{}^2 \approx \frac{2}{\gamma}c_{se}{}^2, \qquad \rho_e \gg \rho_0 \qquad (v_{A0} \gg c_{se} = c_{s0},\ v_{Ae} = 0) \tag{4.25}$$

which for $\gamma = 5/3$ yields $c_p \approx 0.824 c_{se}$ and $c_k \approx 1.095 c_{se}$. These results coincide with those for case (i), so that the limiting phase speed c_p in (4.25) is similarly in agreement with the value given by Roberts (1981a) and Miles and Roberts (1989) for the case $v_{A0}/c_{se} \to \infty$ with c_{s0}/c_{se} fixed arbitrarily (this time $c_{s0}/c_{se} = 1$). Wentzel (1979) also gave the limiting phase speed for this case, although he used $\gamma = 1$ (which gave a higher phase speed of $c_p \approx 0.910 c_{se}$). We also note that our solution takes the value $c_p/v_{A0} \approx 0.542$ when $c_{se}/v_{A0} = 1$, thereby recovering the value obtained by Roberts (1981a) for the special case $c_{se} = c_{s0} = v_{A0}$.

As c_{se}/v_{A0} increases from zero, the normalised phase speed c_p/v_{A0} and normalised kink speed c_k/v_{A0} increase monotonically, and as $c_{se}/v_{A0} \to \infty$ we have

$$c_p{}^2 \approx \frac{v_{A0}{}^2}{2}, \qquad c_k{}^2 \approx \frac{v_{A0}{}^2}{2}, \qquad \rho_e \approx \rho_0 \qquad (c_{se} = c_{s0} \gg v_{A0},\ v_{Ae} = 0) \tag{4.26}$$

These limiting values for the phase speed $c_p \approx 0.7 v_{A0}$ and kink speed $c_k \approx 0.7 v_{A0}$ are indicated on the right-handside of Figure 4.3 by a diamond and an asterisk respectively (these symbols overlap).

Note that the limiting values (4.26) for case (ii) are not the same as the corresponding results (4.21) for case (i). This contrasting behaviour between the cases as $c_{se}/v_{A0} \to \infty$ is similarly evident when we compare Figures 4.2 and 4.4. From Figure 4.4, we see that for case (ii),

$$c_p \approx c_k, \qquad \frac{m_0}{k} \approx 1, \qquad \frac{m_e}{k} \approx 1, \qquad m_0 \approx m_e \qquad (c_{se} = c_{s0} \gg v_{A0},\ v_{Ae} = 0) \tag{4.27}$$

so that the *full* features of the incompressible case are recovered in the limit $c_{se}/v_{A0} \to \infty$. This is as expected for the slow mode with $c_{s0}, c_{se} \gg v_{A0}, v_{Ae}$.

Indeed, from Figures 4.3 and 4.4 we may conclude that extreme ratios between the sound and Alfvén speeds are not required in order for the results of the incompressible case to be applicable to the slow mode of case (ii), where it is sufficient, say, that the two

sound speeds c_{s0} and c_{se} merely exceed the Alfvén speed v_{A0} of the magnetic medium. That is, for

$$c_{s0} = c_{se} > v_{A0}, \quad v_{Ae} = 0 \tag{4.28}$$

we may apply the incompressible case to the slow mode, for which the full features of the incompressible case are recovered (see (4.27)).

Case (iii): $c_{s0} = v_{A0}$ (slow mode only)

We now consider case (iii). Here the sound and Alfvén speeds in the magnetic medium are equal, and $\rho_e/\rho_0 > {c_{s0}}^2/{c_{se}}^2$. For this case we obtain the slow mode only, since existence of the fast mode requires that $v_{A0} > c_{s0}$.

Here $c_{s0} \equiv v_{A0}$, and $\{a, b\} = \{c_{se}, c_{T0}\}$, where ${c_{T0}}^2 = {v_{A0}}^2/2$. From (4.3) and (4.9) we have

$$\frac{\rho_e}{\rho_0} = \left(1 + \frac{\gamma}{2}\right) \frac{{v_{A0}}^2}{{c_{se}}^2}, \quad \Lambda^2 = \frac{{v_{A0}}^2}{2{c_{se}}^2} \left(1 + \frac{\gamma}{2}\right)^2, \tag{4.29}$$

so that from (4.12) the phase speed c_p is given by

$${c_p}^2 = \frac{2{v_{A0}}^2{c_{se}}^2}{({v_{A0}}^2 + 2{c_{se}}^2) + \{({v_{A0}}^2 - 2{c_{se}}^2)^2 + (2+\gamma)^2{v_{A0}}^4)\}^{1/2}} \tag{4.30}$$

while the equivalent kink speed c_k is given from (4.14) by

$${c_k}^2 = \frac{2{v_{A0}}^2{c_{se}}^2}{2{c_{se}}^2 + (2+\gamma){v_{A0}}^2}. \tag{4.31}$$

In Figure 4.5 we show variation of the phase speed c_p with the sound speed c_{se} of the nonmagnetic medium, for fixed Alfvén speed v_{A0}, plotting c_p/v_{A0} as a function of c_{se}/v_{A0} using a heavy solid line. We set $\gamma = 5/3$. The slow mode satisfies $c_p < \min(c_{T0}, c_{se})$, so that the solution is confined to the plot area to the right-handside of the inclined dotted line, along which $c_p = c_{se}$, and below the horizontal dotted line, along which $c_p = c_{T0}$. The dot-dot-dot-dashed lines are the bounds given by (4.16). The heavy dashed line shows the normalised "equivalent" kink speed c_k/v_{A0}, given by (4.31). Note that $c_k > c_{T0}$ for $c_{se}/v_{A0} > (1 + \gamma/2)^{1/2} \approx 1.35$, for which c_k lies outside the allowed range for c_p and therefore $c_p \approx c_k$ does not provide an appropriate approximation.

In Figure 4.6 we perform further comparisons with the results from the incompressible case, plotting c_p/c_k (heavy solid curve) as a function of c_{se}/v_{A0}, against which we also plot

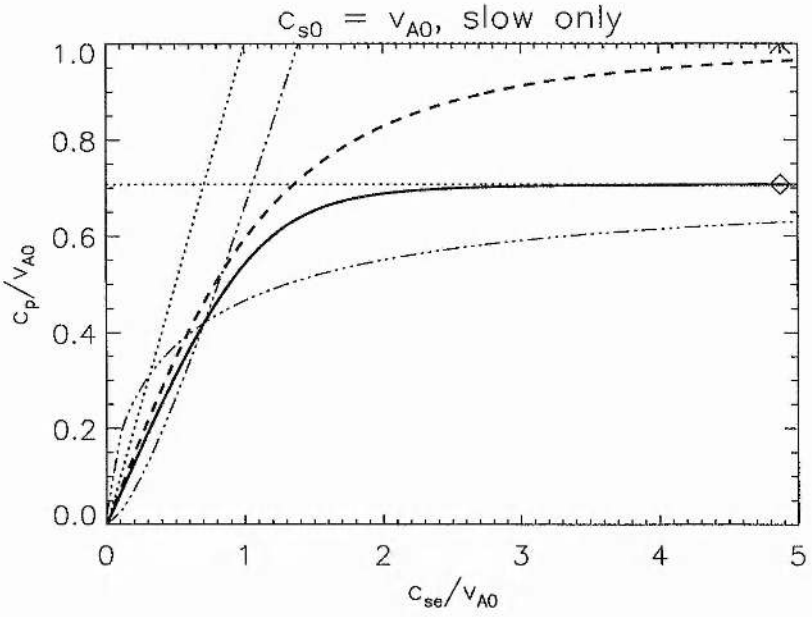

Figure 4.5: Magnetic-nonmagnetic interface, case (*iii*): $c_{s0} = v_{A0}$, for which we obtain the slow mode only. The variation of c_p/v_{A0} (see equation (4.30) with $\gamma = 5/3$) as a function of c_{se}/v_{A0} is shown with a heavy solid line. The slow mode satisfies $c_p < \min(c_{T0}, c_{se})$, so that the solution is confined to the plot area to the right-handside of the inclined dotted line, along which $c_p = c_{se}$, and below the horizontal dotted line, along which $c_p = c_{T0}$. The dot-dot-dot-dashed lines are the bounds given by (4.16). The heavy dashed line shows the normalised "equivalent" kink speed c_k/v_{A0}, given by (4.31). The limiting values of c_p/v_{A0} and c_k/v_{A0} as $c_{se}/v_{A0} \to \infty$ (see (4.33)) are shown on the right-handside of the plot with a diamond and an asterisk respectively (the asterisk is on the upper edge of the plot), and correspond to $c_p \approx v_{A0}/\sqrt{2} = c_{T0}$ and $c_k \approx v_{A0}$; the limits as $c_{se}/v_{A0} \to 1$ are given by (4.32). Note that c_k lies outside the allowed range for c_p when $c_{se}/v_{A0} > (1+\gamma/2)^{1/2} \approx 1.35$.

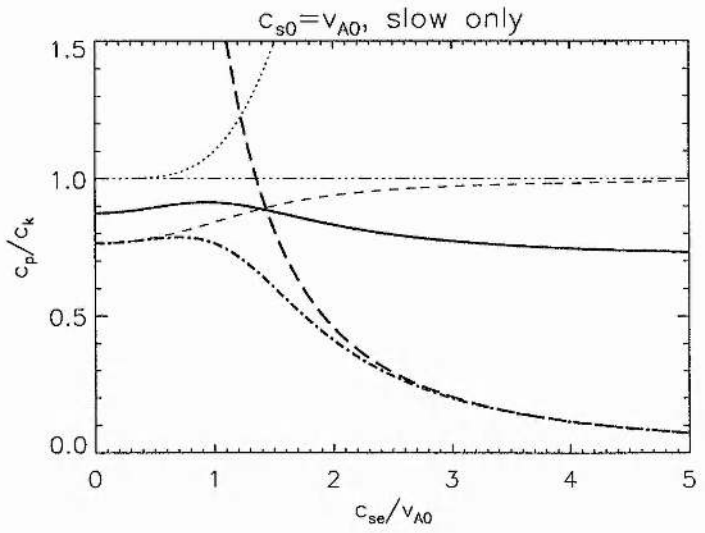

Figure 4.6: Magnetic-nonmagnetic interface, case (*iii*): $c_{s0} = v_{A0}$, for which we obtain the slow mode only (see Figure 4.5). Here we further compare with the results from the incompressible case, again with $\gamma = 5/3$. The variation of c_p/c_k as a function of c_{se}/v_{A0} is shown with a heavy solid line. Intersections with the dot-dot-dot-dashed line shows where plotted quantities are equal to unity. The other lines are m_0/k (dotted), m_e/k (dashed), m_e/m_0 (heavy dot-dashed) and ρ_e/ρ_0 (heavy long-dashed).

m_0/k (dotted), m_e/k (dashed), m_e/m_0 (heavy dot-dashed) and ρ_e/ρ_0 (heavy long-dashed). For the slow mode, $m_0/k > 1$ and $m_e/k < 1$.

Let us consider limiting values of the phase speed c_p and the kink speed c_k. In the limit $c_{se}/v_{A0} \to 0$ we obtain

$$c_p{}^2 \approx \frac{2{c_{se}}^2}{1+\{1+(2+\gamma)^2\}^{1/2}}, \qquad {c_k}^2 \approx \frac{2}{2+\gamma}{c_{se}}^2, \qquad \rho_e \gg \rho_0 \qquad (c_{s0} = v_{A0} \gg c_{se},\ v_{Ae} = 0) \tag{4.32}$$

which for $\gamma = 5/3$ yields $c_p \approx 0.645 c_{se}$, $c_k \approx 0.739 c_{se}$. These results do not coincide with the previous cases.

As c_{se}/v_{A0} increases from zero, the normalised phase speed c_p/v_{A0} and normalised kink speed c_k/v_{A0} increase monotonically, and as $c_{se}/v_{A0} \to \infty$ we have

$$c_p{}^2 \approx \frac{{v_{A0}}^2}{2} = {c_{T0}}^2, \qquad {c_k}^2 \approx {v_{A0}}^2, \qquad \rho_e \ll \rho_0 \qquad (c_{se} \gg v_{A0} = c_{s0},\ v_{Ae} = 0). \tag{4.33}$$

These limiting values for the phase speed $c_p \approx 0.7 v_{A0}$ and kink speed $c_k \approx v_{A0}$ are indicated on the right-handside of Figure 4.5 by a diamond and an asterisk respectively (the asterisk is on the upper edge of the plot).

From Figures 4.5 and 4.6 we may conclude that for c_{se} only slightly greater than $v_{A0} = c_{s0}$, the tube speed c_{T0} is a good approximation to the phase speed c_p of the slow mode in case (iii), that is

$$c_p \approx c_{T0}, \qquad \text{for} \qquad c_{se} > v_{A0} = c_{s0}, \quad v_{Ae} = 0. \tag{4.34}$$

With c_k outwith the allowed range of values of c_p when $c_{se}/v_{A0} > 1.35$, we may conclude from Figures 4.5 and 4.6 that the results of the incompressible case may be fairly applied to the slow mode of case (iii) when $c_{se}/v_{A0} < 1$. Hence, for

$$c_{s0} = v_{A0} > c_{se}, \quad v_{Ae} = 0 \tag{4.35}$$

the incompressible case roughly "applies" to the slow mode, for which $c_p \approx c_k$ and $m_e \approx m_0$, although without such good agreement as is obtained in case (ii) subject to (4.28).

4.3.2 Treatment for case (iv): $\Lambda = 1$ (fast and slow modes)

We noted above that the formulae derived in Section 4.3.1 for cases (i)–(iii) are valid provided $\Lambda \neq 1$, with Λ given by (4.9). For the case $\Lambda = 1$, the squared up dispersion

relation (4.8) may be reduced (on neglect of the root $c_p = 0$) to a quadratic in ${c_p}^2$ (Mundie and Roberts 1998):

$$({c_{T0}}^2+{v_{A0}}^2+{c_{se}}^2-{c_{s0}}^2){c_p}^4-({c_{T0}}^2{v_{A0}}^2+{c_{T0}}^2{c_{se}}^2+{v_{A0}}^2{c_{se}}^2){c_p}^2+{c_{T0}}^2{v_{A0}}^2{c_{se}}^2 = 0. \quad (4.36)$$

With $\Lambda = 1$ in (4.9), we have

$${c_{se}}^2 = \frac{({c_{s0}}^2 + \frac{\gamma}{2}{v_{A0}}^2)^2}{{c_{s0}}^2 + {v_{A0}}^2}, \qquad \frac{\rho_e}{\rho_0} = \frac{{c_{s0}}^2 + {v_{A0}}^2}{{c_{s0}}^2 + \frac{\gamma}{2}{v_{A0}}^2}. \quad (4.37)$$

Then, for this case, the kink speed c_k is given by

$${c_k}^2 = \frac{{v_{A0}}^2(2{c_{s0}}^2 + \gamma{v_{A0}}^2)}{4{c_{s0}}^2 + (2+\gamma){v_{A0}}^2}. \quad (4.38)$$

In Figure 4.7 we plot the solutions for c_p/v_{A0} as a function of c_{s0}/v_{A0}, using a heavy solid line. Whereas the other cases were each limited to one only of the two surface modes, this case illustrates both modes. The fast mode satisfies $c_{s0} < c_p < \min(c_{se}, v_{A0})$, and therefore exists only for $c_{s0}/v_{A0} < 1$, being confined to the plot area between the upper dotted curve, along which $c_p = c_{se}$, and the inclined dotted line, along which $c_{s0} = v_{A0}$. The slow mode exists for all $c_{s0}/v_{A0} > 0$, and satisfying $c_p < \min(c_{T0}, c_{se})$ it is confined to the plot area below the lower dotted curve, along which $c_p = c_{T0}$. As for the other cases, the heavy dashed line shows the normalised "equivalent" kink speed c_k/v_{A0}, given by (4.38).

In Figure 4.8 we perform further comparisons with the results from the incompressible case, by plotting c_p/c_k (heavy solid curve) as a function of c_{se}/v_{A0}, against which we also plot m_0/k (dotted), m_e/k (dashed), m_e/m_0 (heavy dot-dashed) and ρ_e/ρ_0 (heavy long-dashed). Curves for the fast and slow modes are given in separate plots. For the slow mode, $m_0/k > 1$ and $m_e/k < 1$; for the fast mode, whose existence is restricted to $c_{s0}/v_{A0} < 1$, we have $m_0/k < 1$ and $m_e/k < 1$.

In the "cold" extreme, $c_{s0} = 0$, we recover case (i) above, for the particular value of c_{se} given by (4.37), namely $c_{se} = v_{A0}\gamma/2$ ($\approx 0.833 v_{A0}$ for $\gamma = 5/3$). With $c_{s0} = 0$ the slow mode disappears (with $c_p = 0$) while the fast mode remains. From (4.36) we can write the solution for the fast mode for $c_{s0} = 0$ as

$${c_p}^2 = \frac{{v_{A0}}^2{c_{se}}^2}{{v_{A0}}^2 + {c_{se}}^2} \quad (4.39)$$

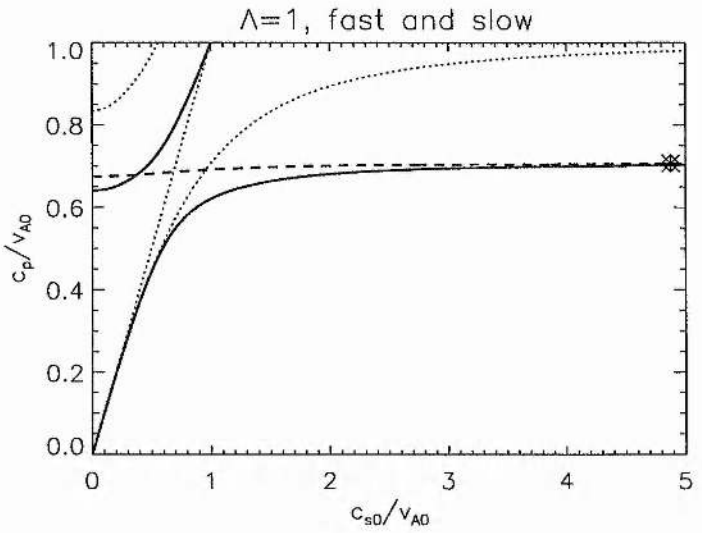

Figure 4.7: Magnetic-nonmagnetic interface, case (*iv*): $\Lambda = 1$, illustrating both fast and slow modes. The variation of c_p/v_{A0} (see equation (4.36) with $\gamma = 5/3$) as a function of c_{s0}/v_{A0} is shown with a heavy solid line. The fast mode satisfies $c_{s0} < c_p < \min(c_{se}, v_{A0})$, and therefore exists only for $c_{s0}/v_{A0} < 1$, being confined to the plot area between the upper dotted curve, along which $c_p = c_{se}$, and the inclined dotted line, along which $c_{s0} = v_{A0}$. The slow mode exists for all $c_{s0}/v_{A0} > 0$, and satisfying $c_p < \min(c_{T0}, c_{se})$ it is confined to the plot area below the lower dotted curve, along which $c_p = c_{T0}$. The heavy dashed line shows the normalised "equivalent" kink speed c_k/v_{A0}, given by (4.38). The asymptotic values ($c_{s0} \gg v_{A0}$) for the normalised phase speed and normalised kink speed are shown on the right-handside of the plot with a diamond and an asterisk respectively (these symbols overlap), and correspond to $c_p \approx v_{A0}/2^{1/2}$ and $c_k \approx v_{A0}/2^{1/2}$.

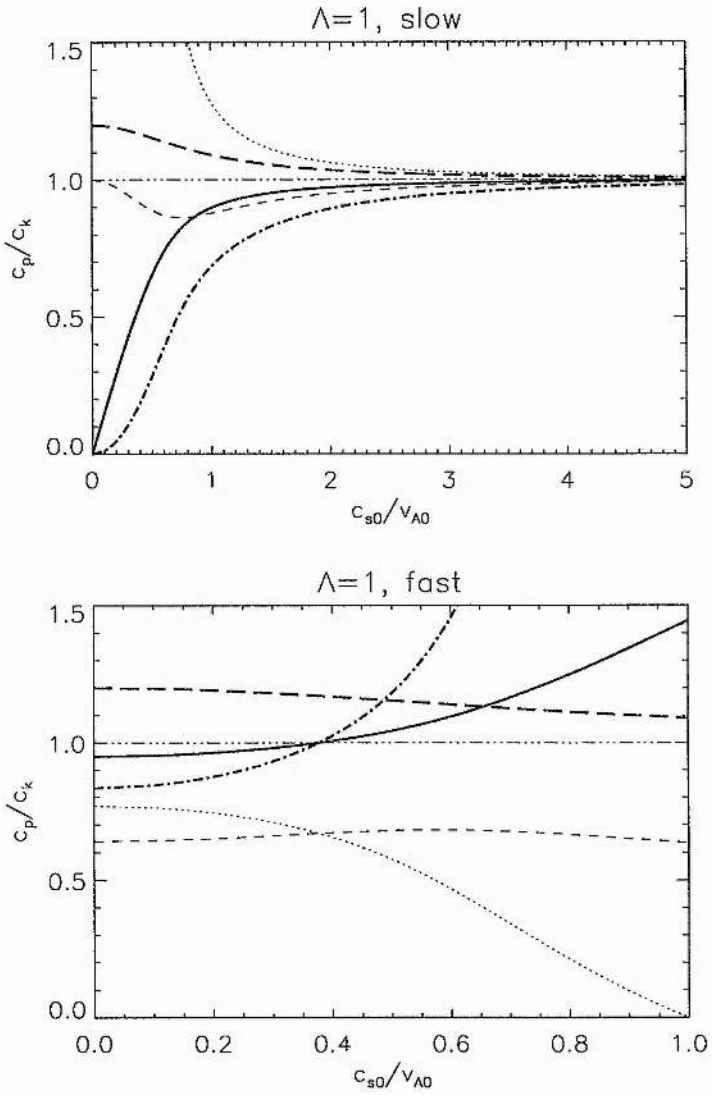

Figure 4.8: Magnetic-nonmagnetic interface, case (*iv*): $\Lambda = 1$, illustrating the existence of both the fast mode and the slow mode (see Figure 4.7). Here we further compare with the results from the incompressible case, again with $\gamma = 5/3$. The variation of c_p/c_k as a function of c_{s0}/v_{A0} is shown with a heavy solid line, with separate plots for the slow and fast mode. Intersections with the dot-dot-dot-dashed line shows where plotted quantities are equal to unity. The other lines are m_0/k (dotted), m_e/k (dashed), m_e/m_0 (heavy dot-dashed) and ρ_e/ρ_0 (heavy long-dashed). Note that the fast mode is confined to $c_{s0}/v_{A0} < 1$.

which yields $c_p < \min(v_{A0}, c_{se})$, in agreement with the ranges requirement (4.5) for the fast surface mode. With $c_{se} = v_{A0}\gamma/2$ we obtain the phase speed c_p of the fast mode from ${c_p}^2/{v_{A0}}^2 = \gamma^2/(4+\gamma^2)$, while the kink speed c_k (see (4.38)) is given by ${c_k}^2/{v_{A0}}^2 = \gamma/(2+\gamma)$. For $\gamma = 5/3$ we obtain $c_p \approx 0.640 v_{A0}$ and $c_k \approx 0.674 v_{A0}$, in agreement with Figure 4.1 for $c_{se}/v_{A0} \approx 0.833$. We also find that for the fast mode in case (i), equation (4.39) yields an approximation to c_p which is very slightly better, at all values of c_{se}/v_{A0}, than the kink speed c_k.

For $0 < c_{s0}/v_{A0} \ll 1$, equation (4.39) is found to give a good approximation to the phase speed c_p of the fast mode, for c_{se} given by (4.37). Here it is also found that for this mode $c_p \approx c_k$, since $m_e \approx m_0$ (see Figure 4.8), although this is without recovery of the full features of the incompressible case (for the fast mode, the full recovery of the incompressible case is not expected). For the slow mode with $0 < c_{s0}/v_{A0} \ll 1$, we see from Figures 4.7 and 4.8 that $c_p \approx c_{T0}$ with $m_0/k \gg 1$.

As $c_{s0}/v_{A0} \to 1$, the fast mode disappears with $c_p \to c_{s0}$ and $m_0/k \to 0$ (see Figure 4.8). For the slow mode we recover case (iii) for the particular value of c_{se} given by (4.37), which for $c_{s0} = v_{A0}$ yields ${c_{se}}^2/{v_{A0}}^2 = (1+\gamma/2)^2/2$, so that $c_{se}/v_{A0} \approx 1.296$ for $\gamma = 5/3$. From (4.36) we can write the solution for the slow mode, for $c_{s0} = v_{A0}$, as

$$ {c_p}^2 = \frac{{c_{T0}}^2 {c_{se}}^2}{{c_{T0}}^2 + {c_{se}}^2}, \tag{4.40} $$

with ${c_{T0}}^2 = {v_{A0}}^2/2$ and ${c_{se}}^2 = (1+\gamma/2)^2 {v_{A0}}^2/2$. Note that (4.40) yields $c_p < \min(c_{T0}, c_{se})$, in agreement with the ranges requirement (4.4) for the slow surface mode. For $\gamma = 5/3$ we obtain $c_p \approx 0.621 v_{A0}$. Also, the kink speed is given by ${c_k}^2/{v_{A0}}^2 = (2+\gamma)/(6+\gamma)$, which for $\gamma = 5/3$ yields $c_k \approx 0.692 v_{A0}$. These values are in agreement with the curves of Figure 4.5 for $c_{se}/v_{A0} = 1.296$. We also find that for the slow mode in case (iii), equation (4.40) yields a good approximation to c_p for $c_{se}/v_{A0} \gg 1$, while for $c_{se}/v_{A0} < 1$ a better approximation is $c_p \approx c_k$, since $m_e \approx m_0$.

Returning to case (iv), for $c_{s0}/v_{A0} \gg 1$ equation (4.37) yields $c_{se} \approx c_{s0}$, and we recover the $c_{se}/v_{A0} \gg 1$ limit of the slow mode in case (ii). Setting ${c_{se}}^2 = {c_{s0}}^2 (\gg {v_{A0}}^2)$ in equation (4.36), we obtain ${c_p}^2 = {v_{A0}}^2/2$ (provided $v_{A0} \neq 0$). Similarly, (4.38) yields ${c_k}^2 = {v_{A0}}^2/2$ in this limit. The limiting values for the normalised phase speed c_p/v_{A0} of the slow mode and normalised kink speed c_k/v_{A0} are marked on the right-handside of

Figure 4.7 with a diamond and an asterisk respectively. From Figure 4.8 we may note that in this limit for the slow mode we recover the full features of the incompressible case, as was found in the same limit for case (ii) above.

4.4 Further investigation of the dispersion relation

The results obtained so far have provided insight into the compressible fast and slow surface modes of the magnetic-nonmagnetic interface, and into the situations in which the incompressible approximation may be applicable to these modes.

We have found that for the slow surface mode we recover all the features of the incompressible case ($c_p \to c_k$; m_0/k, m_e/k, $m_e/m_0 \to 1$) when $c_{s0}, c_{se} \gg v_{A0}$, in which case we have $\rho_e/\rho_0 \to 1$. The other parameter regimes in which c_k is a fair approximation to c_p all have $m_0/k, m_e/k, m_e/m_0$ not far from 1, and while the density ratio appears to be of secondary importance, the best approximations for the slow mode obtained so far have $\rho_e/\rho_0 \approx 1$.

Turning to the fast mode, the results obtained suggest that the incompressible case may also be applicable here in certain situations, having found that $c_p = c_k$ for particular parameter cases ($c_{s0} = 0, c_{se} = v_{A0}$ from case (i) and $c_{s0} \ll v_{A0}, c_{se} \approx v_{A0}$ from case (iv)) for which $m_0/k = m_e/k < 1$.

Cases $(i)-(iii)$ were respectively restricted to c_{s0} being equal to one of the other three speeds $v_{Ae}(=0)$, c_{se}, v_{A0}, making it impossible to satisfy the existence criteria (4.6) and (4.7) for both slow and fast modes, so that only one mode is obtained. (The only case of equality between characteristic speeds which has not been examined so far is $c_{se} = v_{A0}$; see Section 4.4.1, Figures 4.9 and 4.10.) While case (iv) was not restricted to any pair of speeds being equal, thereby allowing the demonstration of both modes, it is difficult to make any general claims from this case on the applicability criteria for the incompressible case due to the fact that there is an associated variation of c_{se}/v_{A0} as c_{s0}/v_{A0} varies.

To gain greater insight into the applicability of the incompressible approximation, particularly for the fast mode, we now carry out further investigation, using the full dispersion relation (4.1) for our problem of the magnetic-nonmagnetic interface. We again fix v_{A0}, and consider the variation of the normalised phase speed of c_p/v_{A0} in terms of

c_{s0}/v_{A0}, for $c_{se}/v_{A0} = \lambda$, where λ is a fixed ratio which we specify. Again, we compare the results with those of the equivalent incompressible case, and consider its applicability.

4.4.1 Treatment for fixed c_{se}/v_{A0} (fast and slow modes)

Consider the case of fixed $c_{se}/v_{A0} \equiv \lambda$, with c_{s0}/v_{A0} allowed to vary. In Figure 4.9 we show the variation of c_p/v_{A0} with increasing c_{s0}/v_{A0} for the case $\lambda = 1$, while in Figure 4.11 we have similar plots for the cases $\lambda = 0.5,\ 0.8,\ 1.2,\ 2.0$. The slow mode exists for all non-zero c_{s0}/v_{A0}, while the fast mode exists where $c_{s0}/v_{A0} < \min(1, \lambda)$. In the limit $c_{s0}/v_{A0} \to 0$ we recover the results of case (i) for the fast mode, when taking the appropriate value of c_{se}/v_{A0}.

Let us now consider the applicability of the equivalent incompressible case. Following our earlier approach, in Figures 4.9 and 4.11 we plot c_k/v_{A0} for comparison, using a heavy dashed line, with c_k given by (4.14). We also show in Figures 4.10, 4.12 and 4.13, the associated variation of c_p/c_k, m_0/k, m_e/k, m_e/m_0 and ρ_e/ρ_0, treating fast and slow modes separately.

For the slow mode we see that for all considered values of λ, we have $c_p/c_k \to 1$, together with $m_e/k, m_0/k, m_e/m_0 \to 1$, as $c_{s0}/v_{A0} \to \infty$, with each of these quantities being close to unity for moderately large c_{s0}/v_{A0} (> 3, say). Hence for the slow mode the full recovery of the incompressible case demands only that c_{s0}/v_{A0} be sufficiently large, while it is not necessary for c_{se}/v_{A0} to be large also.

For the fast mode, on the other hand, the closeness of c_k to c_p depends more strongly on the value of λ, although for $\lambda = 1$ we have $c_p \approx c_k$ for moderately small c_{s0}/v_{A0} (< 0.4, say).

Finally, we note that in all plots for the fast mode c_p/v_{A0} is almost uniform (as are the other plotted quantities) for c_{s0}/v_{A0} small. This indicates that wherever the magnetic medium has low plasma β, setting $c_{s0} = 0$ (as in case (i)) yields good results for the fast mode, whatever the value of c_{se}. Hence a "cold" (magnetic) plasma approximation may safely be applied to such fast surface modes, just as it is applied to fast *body* modes in coronal loops. While this approximation yields no information about the slow modes, we see here that the slow mode satisfies $c_p \approx c_{T0}$ for $c_{s0}/v_{A0} \ll 1$.

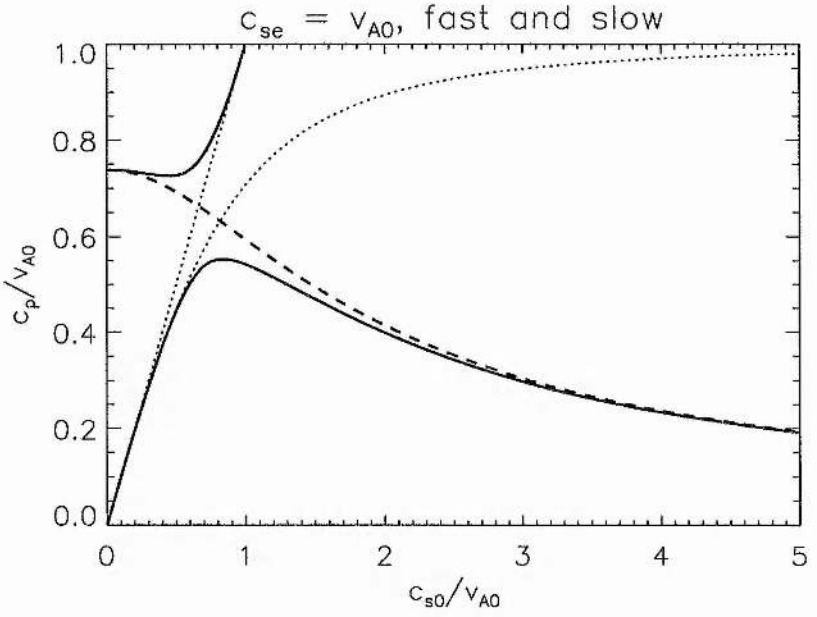

Figure 4.9: Magnetic-nonmagnetic interface, with $c_{se} = v_{A0}$. The variation of c_p/v_{A0} as a function of c_{s0}/v_{A0} is shown with a heavy solid line: the slow mode exists for all non-zero c_{s0}/v_{A0} while the fast mode is limited to $c_{s0}/v_{A0} < 1$. The variation of c_k/v_{A0} is shown with a heavy dashed line. The dotted lines are $c_p = c_{s0}$ (inclined) and $c_p = c_{T0}$ (curved).

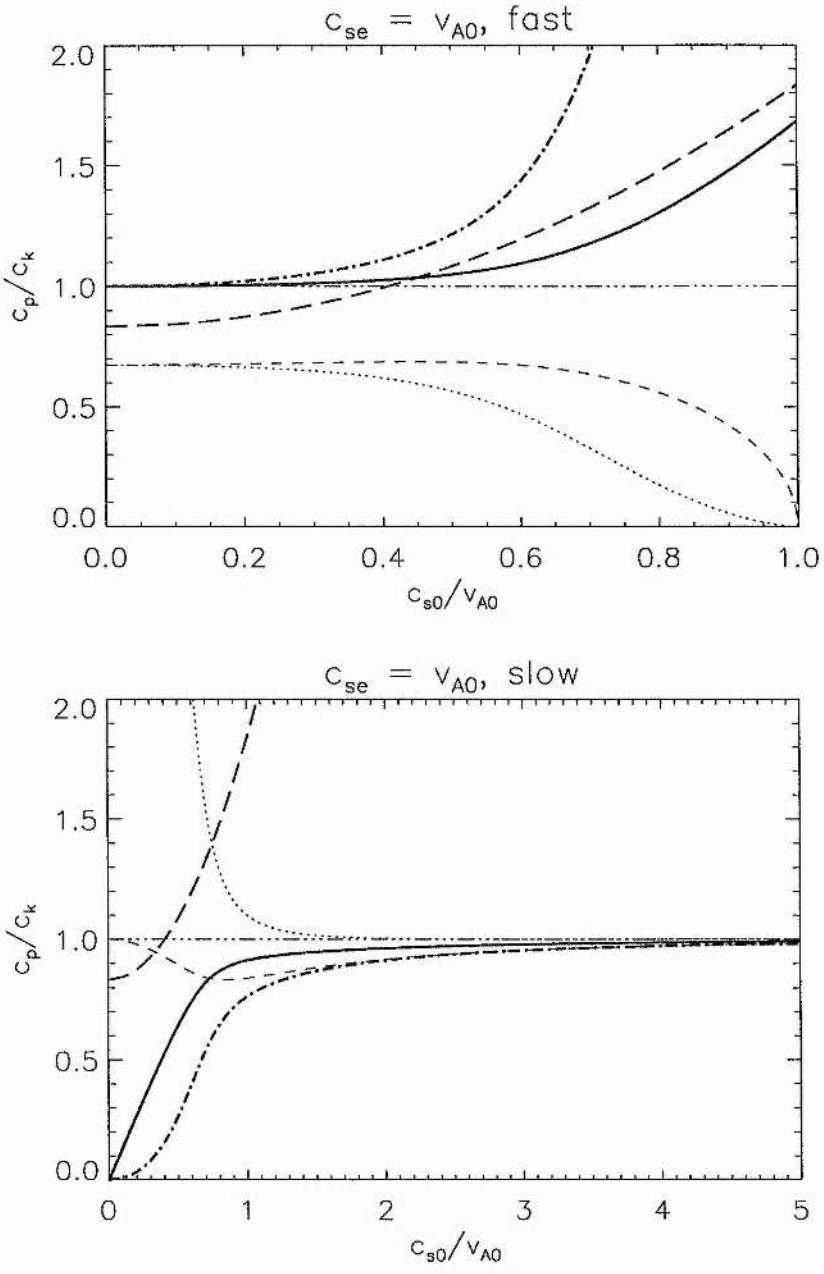

Figure 4.10: Magnetic-nonmagnetic interface, $c_{se} = v_{A0}$ (see Figure 4.9). The variation of c_p/c_k as a function of c_{s0}/v_{A0} is shown with a heavy solid line, for fast and slow modes displayed separately. Intersections with the dot-dot-dot-dashed line shows where plotted quantities are equal to unity. The other lines are m_0/k (dotted), m_e/k (dashed), m_e/m_0 (heavy dot-dashed) and ρ_e/ρ_0 (heavy long-dashed).

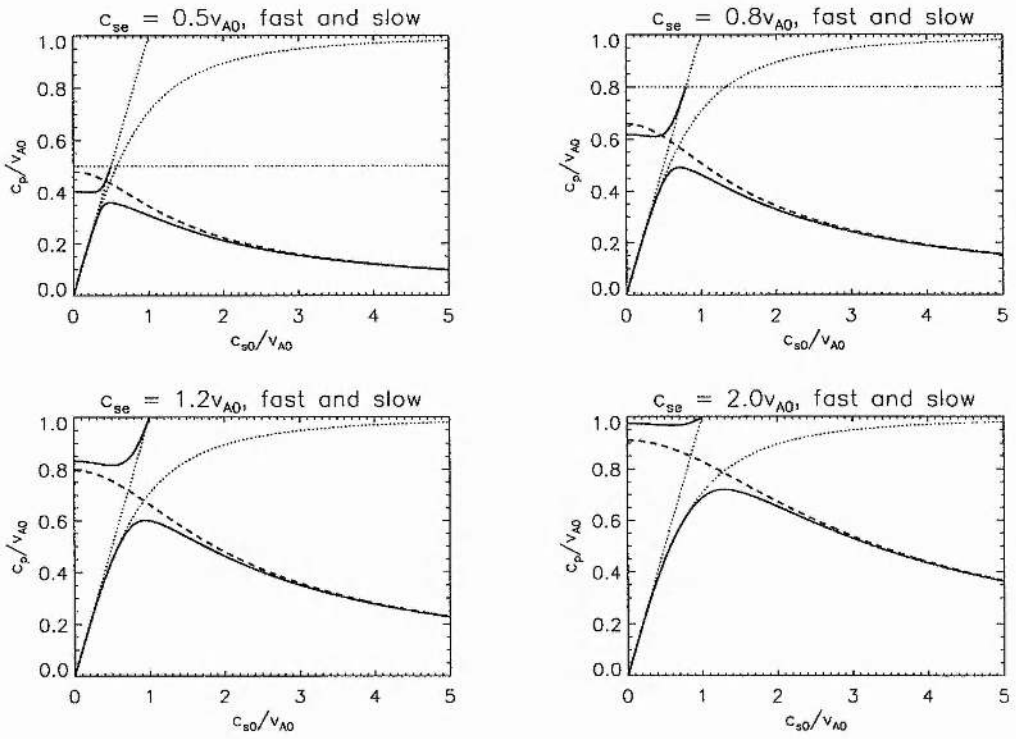

Figure 4.11: Magnetic-nonmagnetic interface, $c_{se} = \lambda v_{A0}$ with $\lambda = 0.5,\ 0.8,\ 1.2,\ 2.0$. The variation of c_p/v_{A0} as a function of c_{s0}/v_{A0} is shown with a heavy solid line: the slow mode exists for all value of c_{s0}/v_{A0} while the fast mode is limited to $c_{s0}/v_{A0} < \min(1, \lambda)$. The variation of c_k/v_{A0} is shown with a heavy dashed line. The dotted lines are $c_p = c_{se}$ (horizontal), $c_p = c_{s0}$ (inclined) and $c_p = c_{T0}$ (curved).

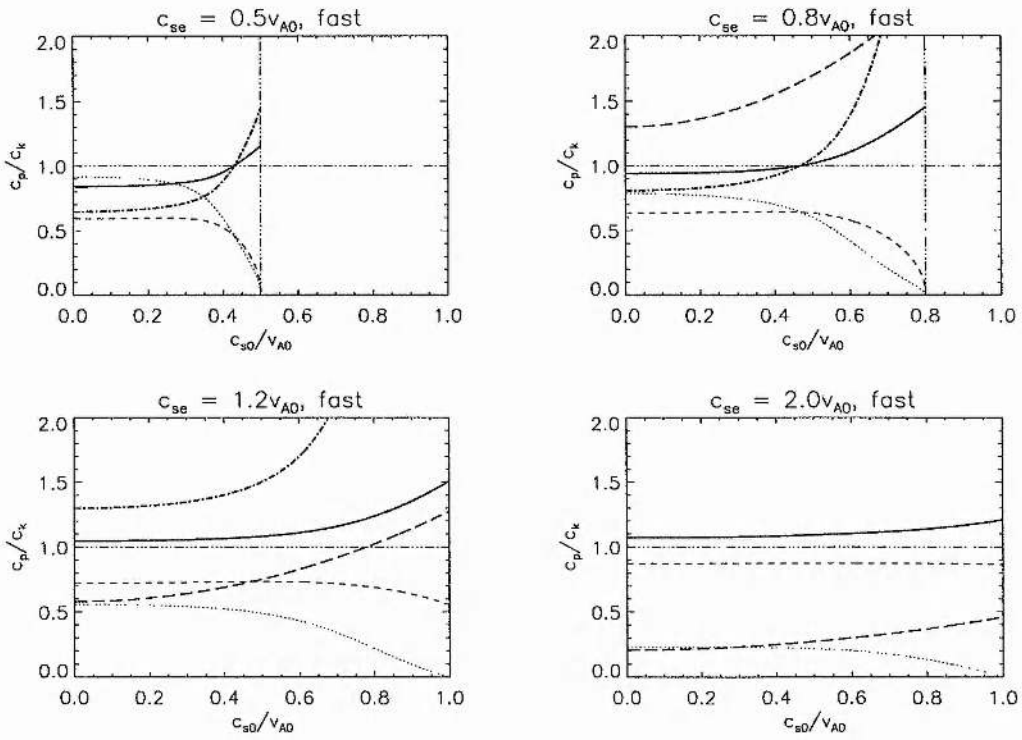

Figure 4.12: Magnetic-nonmagnetic interface, $c_{se} = \lambda v_{A0}$ with $\lambda = 0.5,\ 0.8,\ 1.2,\ 2.0$ (see Figure 4.11). The variation of c_p/c_k as a function of c_{s0}/v_{A0} for the fast surface wave is shown with a heavy solid line. Other plotted quantities are: m_0/k (dotted linestyle), m_e/k (dashed), m_e/m_0 (heavy dot-dashed) and ρ_e/ρ_0 (heavy long-dashed). Intersections with the horizontal dot-dot-dot-dashed line shows where plotted quantities are equal to unity. The fast mode is limited to $c_{s0}/v_{A0} < \min(1, \lambda)$, this limit being shown by a vertical dot-dot-dot-dashed line for cases with $\lambda < 1$. For $\lambda = 2.0$ the curve for m_e/m_0 lies outside the plotted range, as does the curve for ρ_e/ρ_0 for $\lambda = 0.5$.

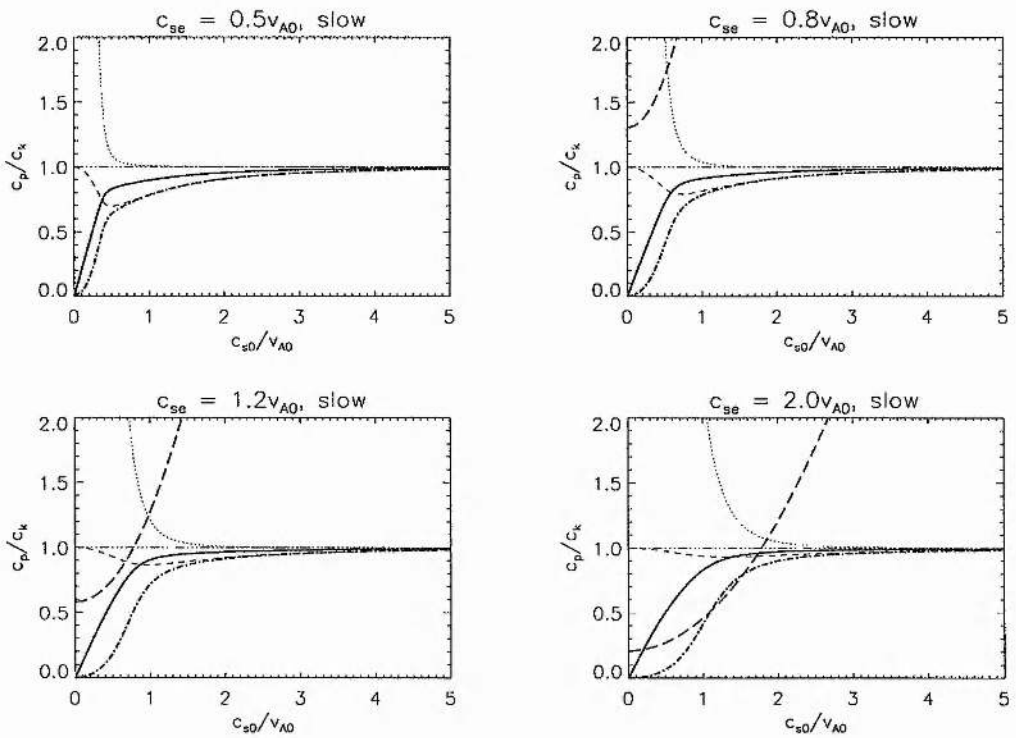

Figure 4.13: Magnetic-nonmagnetic interface, $c_{se} = \lambda v_{A0}$ with $\lambda = 0.5$, 0.8, 1.2, 2.0. Variation of c_p/c_k as a function of c_{s0}/v_{A0} for the slow surface wave is shown with a heavy solid line. Other plotted quantities are: m_0/k (dotted linestyle), m_e/k (dashed), m_e/m_0 (heavy dot-dashed) and ρ_e/ρ_0 (heavy long-dashed). Intersections with the horizontal dot-dot-dot-dashed line shows where plotted quantities are equal to unity. The slow mode exists for all non-zero values of c_{s0}/v_{A0}. For $\lambda = 0.5$ the curve for ρ_e/ρ_0 lies outside the plotted range.

4.5 Summary and conclusions

We have considered compressible surface modes on a magnetic-nonmagnetic interface, which are governed by the dispersion relation (4.1). We have analysed four cases in which simple explicit solutions for the phase speed $c_p \equiv \omega/k$ are obtained. We have considered the variation of c_p with the sound and Alfvén speeds within the two media, considering both slow and fast surface waves.

Additionally, we have incorporated an investigation into the applicability of results obtained for the "equivalent" incompressible case, by comparing the obtained phase speed c_p with the kink speed c_k (see (4.14)) for the same density ratio ρ_e/ρ_0 and Alfvén speed v_{A0}, and also considering the values of m_0/k, m_e/k and m_e/m_0, all of which are equal to unity in the incompressible case.

The properties of the slow mode depend on the relative magnitudes of c_{s0} and v_{A0}. Overall, for the slow mode:

$$c_{s0} \ll v_{A0}, \quad \text{all} \quad c_{se} \quad \Rightarrow \quad {c_p}^2 \approx \frac{{v_{A0}}^2 {c_{s0}}^2}{{v_{A0}}^2 + {c_{s0}}^2} \equiv {c_{T0}}^2 \tag{4.41}$$

$$c_{s0} \approx v_{A0}, \quad c_{se} > v_{A0} \quad \Rightarrow \quad {c_p}^2 \approx \frac{{c_{T0}}^2 {c_{se}}^2}{{c_{T0}}^2 + {c_{se}}^2} \tag{4.42}$$

$$c_{s0} \approx v_{A0}, \quad c_{se} < v_{A0} \quad \Rightarrow \quad {c_p}^2 \approx {c_k}^2 \quad (\text{since } m_e \approx m_0) \tag{4.43}$$

$$c_{s0} \gg v_{A0}, \quad \text{all} \quad c_{se} \quad \Rightarrow \quad {c_p}^2 \approx {c_k}^2 \quad (\text{incompressible case recovered}) \tag{4.44}$$

For the slow surface mode, the full recovery of results from the incompressible case demands only that c_{s0}/v_{A0} be sufficiently large, say $c_{s0}/v_{A0} > 3$; it is not necessary that c_{se}/v_{A0} be large also.

Where both the fast and slow surface modes exist, we have $c_p \approx c_{T0}$ for the slow mode while the incompressible case may yield a good approximation to the phase speed of the fast mode in cases where $m_e \approx m_0$.

For the fast mode we find that for given c_{se}, the phase speed c_p is almost constant for small c_{s0}/v_{A0}, and as such is well approximated by its value when $c_{s0} = 0$. Hence the "cold" (magnetic) plasma approximation may be applied to fast surface modes, just as it is applied to fast body modes in coronal loop applications. The appropriate approximation to use here depends on the relative magnitudes of c_{se} and v_{A0}. For small values of c_{se}/v_{A0}, the approximation to c_p for $c_{s0} = 0$ is given by (4.20). For $c_{se} \approx v_{A0}$, equation (4.39)

yields a good approximation to c_p, although we also obtain $c_p \approx c_k$ since $m_e \approx m_0$. For $c_{se} \gg v_{A0}$, the fast mode satisfies $c_p \approx v_{A0}$ for $0 \leq c_{s0}/v_{A0} < 1$. For all values of c_{se}, for the fast mode we have $c_p \to v_{A0}$ as $c_{s0} \to v_{A0}$.

In this Chapter we have presented an approach for assessing the applicability of the incompressible approximation to compressible surface modes, and we have applied this approach to the particular case of a static magnetic-nonmagnetic interface. Our results show that in many instances, particularly for the slow mode, the relevance of the incompressible surface modes to compressible situations is high. Further investigations based on similar approaches may help shed additional light on this issue.

Chapter 5

Prominence oscillations

5.1 Introduction

Solar quiescent prominences are extremely complicated and mysterious objects. They are dense clouds of material suspended above the photosphere, and threaded by magnetic fields which support the prominence against the downward pull of gravity and anchor it to the solar surface. Also known as filaments (when observed on the solar disk), they are vertical sheet-like structures, with typical width ($\approx$ 5000km) very much less than height ($\approx 50,000$km) or length ($\approx 200,000$km). They have rich fine structure, but their average density is typically 100 times greater than the surrounding corona. The temperature is similarly structured, with prominences being much cooler than their environment. Thus they represent a large-scale inhomogeneity in the solar atmosphere.

Quiescent prominences are remarkably stable objects, with their global structure remaining virtually unchanged for many days through their passage from limb to limb as the Sun rotates. However, after hanging eerily for so long, they may erupt explosively, often with an associated coronal mass ejection or a solar flare. Prominence mysteries are many. How do they form, what is their equilibrium configuration, why do they remain so stable for so long, and what brings about their abrupt end? These puzzles and general prominence properties are discussed in several reviews (Tandberg-Hanssen 1974, Priest 1982, Poland 1986, Ballester and Priest 1987, Priest 1988, Ruzdjak and Tandberg-Hanssen 1989, Démoulin 1991).

The high density of a prominence brings with it high opacity, so that it is difficult to observe their internal structure. It is also difficult to observe the 3D magnetic field threading the prominence, as we are generally restricted to line-of-sight measurements. However, what has been observed is that the magnetic field threading the prominence is predominantly horizontal, making a small angle $\phi \approx 20°$ with the prominence long axis and having a moderate field strength of 5-20G. The magnetic field suffers a slight dip of around 10 degrees as it goes through the prominence, and is anchored in the dense photosphere; see Figure 5.1.

The modelling of prominence equilibria is a complicated business. While numerous models have emerged (e.g. Menzel 1951, Kippenhahn and Sclüter 1957, Kuperus and Raadu 1974, Poland and Anzer 1971, Low and Wu 1981, Priest, Hood and Anzer 1989, Hood and Anzer 1989) prominences nonetheless remain one of the great enigmas in solar physics.

An alternative approach to gaining an understanding of the makeup of a prominence is through its dynamics, in particular the study of its oscillations. It has been known for some time that prominences oscillate, although it is only in recent years that significant progress has been made in the observation and theoretical modelling of oscillatory phenomena in prominences, as we now discuss.

5.1.1 Observations of prominence oscillations

The first observations of oscillatory phenomena in prominences were in the so-called "winking filaments" (Ramsey and Smith 1966, Hyder 1966, Kleczek and Kuperus 1969). These were horizontal oscillations of the entire prominence, with periods of around 20 min, most likely triggered by a shock wave generated by a solar flare.

The advent of more sophisticated observational techniques in the 1980's made possible the discovery of lower amplitude, non-flare related oscillations of quiescent prominences. This led to many observational studies, the results of which are summarised in reviews (Tsubaki 1988, Schmieder 1988, Schmieder 1989, Vrsnak 1993) and may be classified into three period ranges as follows.

The existence of *long periods*, of the order of an hour, are well established (Bashkirtsev, Kobanov and Mashnich 1983, Bashkirtsev and Mashnich 1984, Wiehr, Stellmacher and

Balthasar 1984, Balthasar, Knölker, Stellmacher and Wiehr 1986, Balthasar, Stellmacher and Wiehr 1988, Balthasar, Wiehr and Stellmacher 1988, Mashnich and Bashkirtsev 1990, Bashkirtsev and Mashnich 1993, Balthasar and Wiehr 1994, Molowny-Horas, Oliver, Ballester and Baudin 1997), being evident in every observation with a sufficiently long time series. Being characteristic of prominences in general, they are considered (e.g. Vrsnak (1993), Mashnich et al. (1993), Balthasar et al. (1993)) to be global oscillations of the prominence.

Short periods, of up to 5 min, have also been reported by many observers (Wiehr et al. 1984, Balthasar et al. 1986, Tsubaki and Takeuchi 1986, Tsubaki, Ohnishi and Suematsu 1987, Balthasar, Stellmacher and Wiehr 1988, Balthasar, Wiehr and Stellmacher 1988, Thompson and Schmieder 1991, Yi Zhang, Engvold and Keil 1991, Yi Zhang and Engvold 1991, Balthasar and Wiehr 1994), and are believed by some (e.g. Balthasar et al. (1986, 1988), Yi Zhang et al. (1991)) to be a forced response to the photospheric 5 min and chromospheric 3 min oscillations. A 30 s oscillation was observed by Balthasar et al. (1993), who suggested they are fast ducted modes (Roberts et al. 1984) in the prominence fine structure.

Oscillations in the *intermediate period* range of 10-20 min have also been observed (Tsubaki et al. 1987, Tsubaki, Toyoda and Suematsu 1988, Balthasar, Stellmacher and Wiehr 1988, Balthasar, Wiehr and Stellmacher 1988, Suematsu, Yoshinaga, Terao and Tsubaki 1990, Yi Zhang et al. 1991, Yi Zhang and Engvold 1991, Balthasar, Wiehr, Schleicher and Wöhl 1993, Bashkirtsev and Mashnich 1993, Mashnich, Druzhinin, Pevtsov and Levkovsky 1993, Balthasar and Wiehr 1994), and interpreted (e.g. Balthasar and Wiehr (1994)) as eigenmodes of the prominence and surrounding coronal arcade.

The majority of the above results are for prominences observed at the limb. While early studies (Engvold 1981, Malherbe, Schmieder and Mein 1981, Malherbe, Schmieder, Mein and Tandberg-Hanssen 1987) of disk filaments reported no clear evidence of oscillations, short and intermediate periods were later found in the disk observations of Thompson and Schmieder (1991), Yi Zhang et al. (1991) and Yi Zhang and Engvold (1991), and attributed by Jensen, Yi Zhang and Engvold (1994) as Alfvén modes propagating along the prominence fine structure. Bashkirtsev and Mashnich (1993) found both intermediate and long periods in a number of limb prominences and disk filaments.

In general, oscillations may be inferred from variations in Doppler shifts, line widths or intensities of spectral lines, although the majority of observations of prominence oscillations are in Doppler shifts. Indeed, it has been suggested (Gheonjian, Klepikov and Stepanov 1990) that in ground-based observations of prominence oscillations, only the variations in the Doppler shifts are of solar origin, while variations of other parameters may be associated with wave phenomena in the terrestrial atmosphere. This problem is avoided in observations made from space. Recent observations (Blanco, Bocchialini, Costa, Domenech, Rovira and Vial 1998) from the SOHO spacecraft have revealed short and intermediate period oscillations, through wavelet analysis of intensity fluctuations.

5.1.2 Theory of prominence oscillations

The theoretical modelling of prominence oscillations is an inherently complicated business, given the complex nature of prominences themselves. It is however an important area to pursue, since together with detailed observations it has the potential to provide seismic information about conditions within and around the prominence, just as heliosiemology is now used to delve deep within the solar interior.

The main aim of a first theoretical model is to obtain periods in the correct ranges given by observations, and to gain an insight into the basic physical nature of the modes. This necessitates the use of simple models yielding analytical results, so that the main physical factors determining the periods may be found.

Models based on simple prominence-like equilibira, treating the prominence as a whole, should give a good guide, since a more complex structure ought to oscillate globally in a similar manner. Preliminary investigations using elementary models (Roberts 1991a) indicated that at least some of the observed periods ought to be obtained from global oscillations, and so it is worth pursuing this approach using more sophisticated models.

One of the elementary models considered by Roberts (1991a) was that of a uniform elastic string with its ends tied, representing the coronal arcade threading the prominence and anchored in the photosphere, and loaded with a point mass M at its centre, representing the prominence. For $M >> 2\rho l$, where $2l$ is the length of the string and ρ is its mass density per unit length, the frequency ω and period $\tau = (2\pi/\omega)$ of the fundamental

mode of oscillation are approximated by the formulae (see Section 5.2.2 below)

$$\omega = \left(\frac{2\mathcal{T}}{Ml}\right)^{1/2}, \qquad \tau = \pi\left(\frac{2lM}{\mathcal{T}}\right)^{1/2}. \tag{5.1}$$

where $\mathcal{T}$ is the tension in the string.

Models using ideal linear MHD theory include work by Joarder and Roberts (Joarder and Roberts 1992a, 1992b, 1993a, 1993b, Joarder 1993, Roberts and Joarder 1994, Joarder, Nakariakov and Roberts 1997b) and Oliver and co-authors (Oliver, Ballester, Hood and Priest 1992, 1993, Oliver and Ballester 1995, 1996).

The prominence may be modelled as a vertical sheet of cool, dense material embedded within a hot, rarefied corona, with structuring in the transverse (x) direction only. The prominence is threaded by a magnetic field, which is horizontal at the centre of the prominence ($x = 0$) and anchored to the photosphere, this line-tying effect being represented by rigid walls at $x = \pm l$. Joarder and Roberts (1992a, 1992b, 1993b) used this approach, neglecting gravity in order to concentrate on the effects of the large-scale structuring due to the prominence-corona inhomogeneity, which is represented by a uniform slab configuration; see Figures 5.1 and 5.2. Analytical dispersion relations were derived for arbitrary propagation directions and for the separate cases of the horizontal magnetic field threading the prominence longitudinally (Joarder and Roberts 1992a, $\phi = 0$), transversely (Joarder and Roberts 1992b, $\phi = \pi/2$) or at an arbitrary angle ϕ to the prominence long axis (Joarder and Roberts 1993b).

Investigations have also been carried out using more complicated magnetostatic equilibria, such as the Poland and Anzer model (see Oliver et al. 1992, 1993), the Menzel (1951) model (see Joarder and Roberts 1992a), and the Low and Wu (1981) model (see Oliver and Ballester 1995, 1996). In these models the magnetic field is transverse to the prominence, and the solutions are computed numerically.

It is found (Roberts 1991a, Joarder and Roberts 1992a, 1992b, 1993b, Oliver et al. 1993, Roberts and Joarder 1994) that the basic modes of oscillation of the prominence sheet are analogous to the oscillation modes of a stretched elastic string of nonuniform density (see Section 5.2.2 below). These modes are termed *string modes* (or "hybrid" modes in Oliver et al. (1993)), and for propagation across the prominence at a wavelength which

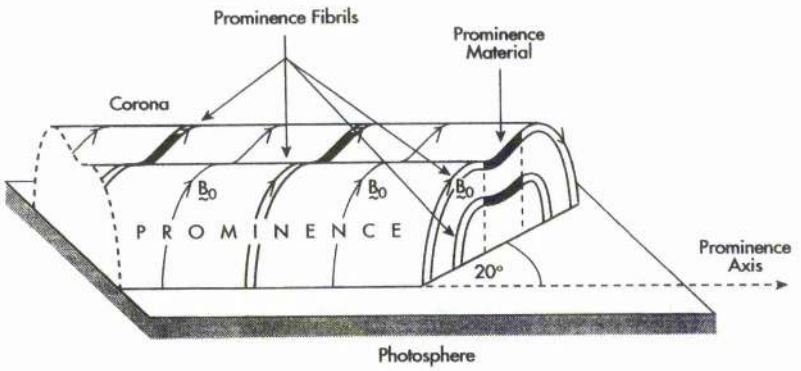

Figure 5.1: A schematic diagram of a prominence and surrounding coronal arcade. The prominence, composed of an array of fibrils, is threaded by a magnetic field $\mathbf{B}_0$ at an angle $\phi \approx 20°$ to its long axis. Predominantly horizontal through the prominence (although with a slight dip due to gravity acting vertically), $\mathbf{B}_0$ also passes through the arcade before being anchored in the dense photosphere. (After Joarder et al. 1997b.)

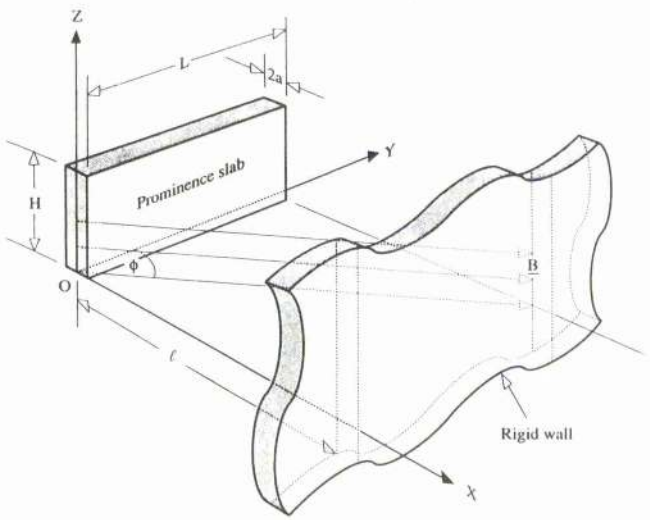

Figure 5.2: A schematic diagram of prominence-coronal representation adopted in the uniform slab model of Joarder and Roberts (1992a, 1992b, 1993b). Gravity is neglected and the prominence is represented by a dense uniform slab of width $2a$, length L and height H in the x-, y- and z-directions respectively (typically $2a \ll H < L$), embedded in a uniform coronal environment. Both media are threaded by a uniform magnetic field at an angle $\phi \approx 20°$ to the prominence long axis and tied to rigid walls at $x = \pm l$, representing photospheric line-tying. (After Joarder and Roberts 1993b.)

is long compared to the prominence dimensions they have periods of the form

$$\tau = \frac{2\pi}{c_p}(al)^{1/2} \tag{5.2}$$

where c_p is the propagation speed characterising the mode, $2a(\approx 5000$ km) is the width of the prominence sheet whose threading magnetic field is anchored at a distance $l(\approx 10a)$ to either side of the prominence sheet. With $\tau = 2\pi/\omega$, we may compare the result (5.25) with the formula (5.1) of the point mass analogy, writing $\mathcal{T} = {c_p}^2\rho_p$ and $M = 2a\rho_p$, where ρ_p is the prominence density.

There are three types of string mode, each characterised by the propagation speeds of the three MHD modes in an infinite uniform medium, for propagation across[1] the prominence, that is at an angle $\pi/2 - \phi$ to the magnetic field, which is inclined at an angle ϕ to the prominence long axis: the *Alfvén string mode* has $c_p \approx v_A \sin\phi$, the *fast magnetoacoustic string* mode has $c_p \approx ({c_s}^2 + {v_A}^2)^{1/2}$, the *slow magnetoacoustic string mode* has $c_p \approx c_s v_A \sin\phi/({c_s}^2 + {v_A}^2)^{1/2}$ (Joarder and Roberts 1993b, Roberts and Joarder 1994, Joarder 1993, Joarder, Nakariakov and Roberts 1997a). Here v_A and c_s are typical Alfvén and sound speeds within the prominence.

For a "typical" prominence with plasma density $\rho_p = 2 \times 10^{-13}$ g cm^{-3} (or a number density of 10^{11} cm $^{-3}$, temperature $T_p = 10^4$ K, magnetic field strength $B_0 = 8$ G we obtain a prominence Alfvén speed of $v_A \approx 55$ km s^{-1} and sound speed $c_s \approx 12$ km s^{-1}. Then, with $\phi \approx 20°$, $2a = 5000$ km and $l = 10a$, the approximation (5.2) yields $\tau \approx 45$ min for the Alfvén string mode, $\tau \approx 15$ min for the fast string mode and $\tau > 3$ h for the slow string mode. The Alfvén and slow string modes are anisotropic, with longer period estimates resulting for smaller values of ϕ. The estimated periods of the Alfvén and fast string modes are respectively consistent with the long and intermediate periods of observed oscillation, while the slow string mode is unlikely to be observed due to the long time series required.

It is also found (Joarder and Roberts 1992b, Oliver, Ballester, Hood and Priest 1992) that there exist *internal modes* of the prominence, which propagate acros the prominence and have a node at the centre of the prominence, appreciable kinetic energy within the prominence, and are evanescent in the corona. The period of an internal mode is basically

[1]That is, in the transverse direction.

its transit time back and forth across the prominence, i.e.

$$\tau = \frac{4a}{c_p} \tag{5.3}$$

where the three internal modes (Alfvén , and fast and slow magnetoacoustic) are characterised by the same values of c_p as for the corresponding string modes. Using the above values of v_A, c_s and ϕ we obtain from (5.3) the period estimates of 9 min, 3 min and 42 min for the internal Alfvén, fast and slow modes respectively, which are respectively consistent with the intermediate, short and long periods of oscillation observed in prominences.

In the above mentioned numerical models for prominence oscillations, which adopt more complex equilibrium configurations, the calculated periods for long wavelength modes propagating across the prominence are in good agreement with the above simple formulae for the string modes (given by (5.2) and obtained where the magnetic field is line-tied) and internal modes (given by (5.3)) obtained from the uniform slab models. The results from the numerical models, which all adopt a transverse magnetic field ($\phi = \pi/2$), suggest that the main factors determining the periods of the string modes are the strength of the prominence-corona inhomogeneity, the strength of the magnetic field threading the prominence horizontally, and the photospheric line-tying effect. Investigations by Joarder & Roberts (1993b) with a uniform prominence and corona indicate that the field angle ϕ is also important in determining the periods.

Edwin and Roberts (1988) and Nakariakov and Roberts (1995b) considered the effects of different density profiles on the results of discretely structured models (Edwin and Roberts 1982, 1983) for ducted magnetic Love and Pekeris modes in a dense coronal loop, concluding that the essence of the problem is contained in the slab model. Prompted by these results, and those of the numerical investigations noted above, we consider the effects of different density profiles on the periods given by slab models for the long wavelength string modes of a thin, dense prominence. We aim to show that, under suitable conditions, the basic nature of the string mode is independent of the details of structuring, and rather depends on the average properties within the prominence and its environment, so that the results from the uniform slab calculation (Joarder and Roberts 1992b, 1993b) are indeed applicable to models with more realistic profiles of the prominence-corona inhomogeneity.

5.2 Model

Consider the magnetostatic equilibrium sketched in Figure 5.3. Gravity is neglected ($\mathbf{g} = 0$). The plasma pressure p_0 and magnetic field B_0 are both uniform, while the the density $\rho_0(x)$ and temperature $T_0(x)$ are structured in the x-direction. There is density enhancement of scalewidth $2a$ centred on the y-axis (which represents the prominence long axis) with $\rho_0(x)$ taking its maximum value ρ_p at the centre of the prominence and declining to a minimum value ρ_c in the corona outside the prominence. The temperature $T_0(x)$ is structured in inverse proportion to the density $\rho_0(x)$, so that $\rho_0(x)T_0(x)$ is a constant. The uniform magnetic field $\mathbf{B}_0 = (B_{0x}, B_{0y}, 0)$ threads the prominence horizontally at an angle ϕ to the prominence long axis, with field strength $B_0 = (B_{0x}^2 + B_{0y}^2)^{1/2}$ and components $B_{0x} = B_0 \sin\phi$, $B_{0y} = B_0 \cos\phi$. Rigid walls at a distance l to either side of the prominence centre represent the line-tying effect of the high density photosphere (the coronal loop has been "straightened"). For a typical prominence, $a \ll l$, $\rho_p \gg \rho_c$ and $\phi \approx 20°$. [2]

For perturbations of the form (1.23) about the magnetostatic ($\mathbf{v}_0 = 0$) equilibrium sketched in Figure 5.3, the linearised MHD equations (1.25)-(1.28) yield

$$\rho_0 \frac{\partial^2 \mathbf{v}_1}{\partial t^2} = c_s^2 \rho_0 \,\text{grad div}\, \mathbf{v}_1 - \text{grad}\left[\frac{\mathbf{B}_0}{\mu} \cdot \frac{\partial \mathbf{B}_1}{\partial t}\right] + \left[\frac{\mathbf{B}_0}{\mu} \cdot \text{grad}\right] \frac{\partial \mathbf{B}_1}{\partial t} \tag{5.4}$$

$$\frac{\partial \mathbf{B}_1}{\partial t} = (\mathbf{B}_0 \cdot \text{grad})\, \mathbf{v}_1 - \mathbf{B}_0 \,\text{div}\, \mathbf{v}_1 \,. \tag{5.5}$$

Using (5.5) and vector identities to expand the magnetic terms in (5.4), we obtain

$$\begin{aligned} -\text{grad}\left[\frac{\mathbf{B}_0}{\mu} \cdot \frac{\partial \mathbf{B}_1}{\partial t}\right] &= -\left[\frac{\mathbf{B}_0}{\mu} \cdot \text{grad}\right] [\text{grad}\,(\mathbf{B}_0 \cdot \mathbf{v}_1)] + \frac{B_0^2}{\mu} \,\text{grad div}\, \mathbf{v}_1 \\ &= -\left[\frac{\mathbf{B}_0}{\mu} \cdot \text{grad}\right] \{(\mathbf{B}_0 \times \text{curl}\, \mathbf{v}_1) + \mathbf{B}_0 \,\text{div}\, \mathbf{v}_1\} + \frac{B_0^2}{\mu} \,\text{grad div}\, \mathbf{v}_1 \end{aligned} \tag{5.6}$$

$$\left[\frac{\mathbf{B}_0}{\mu} \cdot \text{grad}\right] \frac{\partial \mathbf{B}_1}{\partial t} = \left[\frac{\mathbf{B}_0}{\mu} \cdot \text{grad}\right] [\mathbf{B}_0 \cdot \text{grad}]\, \mathbf{v}_1 - \left[\frac{\mathbf{B}_0}{\mu} \cdot \text{grad}\right] (\mathbf{B}_0 \,\text{div}\, \mathbf{v}_1)\,, \tag{5.7}$$

[2] Most of this Chapter's results are concerned with the special case where $\mathbf{B}_0$ is transverse to the prominence long axis, as is the wave propagation (i.e. $\phi = \pi/2$ and $\mathbf{B} \parallel \hat{\mathbf{x}} \parallel \mathbf{k}$). See Equations 5.17 and following.

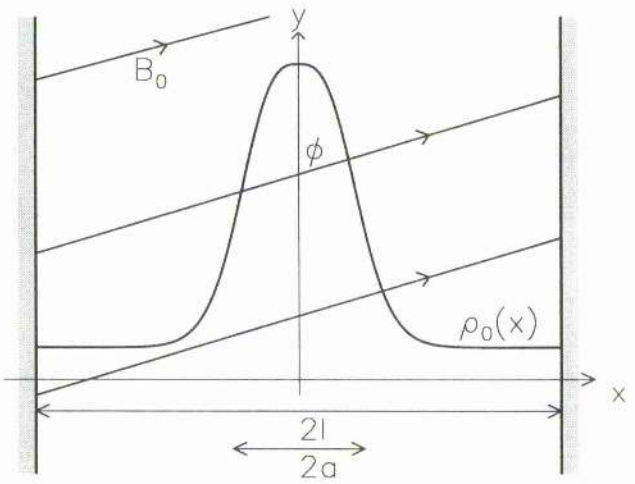

Figure 5.3: Sketch of the equilibrium configuration. Gravity is neglected and all parameters are assumed independent of y and z. We take constant plasma pressure p_0, and a uniform magnetic field B_0 in the xy-plane making an angle ϕ with the y-axis and line-tied at the photosphere, which we represent by rigid walls at $x = \pm l$. The prominence is defined by an enhancement in the density $\rho_0(x)$ of scalewidth $2a$, inversely proportional to the temperature $T_0(x)$. When $\phi = \pi/2$, the magnetic field is transverse to the prominence.

reducing the system (5.4)-(5.5) to a single governing equation (Roberts and Joarder 1994)

$$\frac{\partial^2 \mathbf{v}_1}{\partial t^2} = \left[c_s^2(x) + v_A^2(x)\right] \text{grad div } \mathbf{v}_1 - \frac{1}{\mu\rho_0(x)} (\mathbf{B}_0 \cdot \text{grad}) \{(\mathbf{B}_0 \times \text{curl } \mathbf{v}_1) + \mathbf{B}_0 \text{ div } \mathbf{v}_1\} . \tag{5.8}$$

In the above $c_s(x) = (\gamma p_0/\rho_0(x))^{1/2}$ and $v_A(x) = (B^2/\mu\rho_0(x))^{1/2}$ are the sound speed and Alfvén speed respectively, satisfying the equilibrium constraint

$$c^2(x)\rho_0(x) = \text{constant} = \mathcal{T} = \begin{cases} \gamma p_0, & c = c_s \\ B_0^2/\mu, & c = v_A \end{cases} \tag{5.9}$$

where γ is the adiabatic index.

Equation 5.8 is the basic vector wave equation, and is valid for arbitrary field angle ϕ, density profile $\rho_0(x)$ and propagation direction. Its complexity reflects the fact that the modes are strongly coupled, and this tends to obscure their basic physical nature. However, we are able to shed light on this through the use of certain limits, appropriate for conditions within and around prominences.

Simplifications

For low frequency modes, the periods are principally determined by variations in the direction with the shortest lengthscale. Since the medium is structured in the x-direction only, and the typical width $2a$ ($\approx$ 5000 km) of the prominence is very much less than both its height H ($\approx$ 50,000 km) and its length L ($\approx$ 200,000 km), we consider one-dimensional propagation, purely across the prominence; the general case of arbitrary propagation direction is discussed in Joarder and Roberts (1993a) and Joarder (1993). This gives infinitely long wavelengths in the y- and z- (i.e. longitudinal and vertical) directions.

Hence, setting $\partial/\partial y = \partial/\partial z = 0$ in equation (5.8), with $\mathbf{v}_1 = (v_x, v_y, v_z)$ we obtain (Roberts and Joarder 1994)

$$\frac{\partial^2 v_x}{\partial t^2} = \left[c_s^2(x) + v_A^2(x)\cos^2\phi\right] \frac{\partial^2 v_x}{\partial x^2} - v_A^2(x)\cos\phi\sin\phi\frac{\partial^2 v_y}{\partial x^2} \tag{5.10}$$

$$\frac{\partial^2 v_y}{\partial t^2} = v_A^2(x)\sin^2\phi\frac{\partial^2 v_y}{\partial x^2} - v_A^2(x)\cos\phi\sin\phi\frac{\partial^2 v_x}{\partial x^2} \tag{5.11}$$

$$\frac{\partial^2 v_z}{\partial t^2} = v_A^2(x)\sin^2\phi\frac{\partial^2 v_z}{\partial x^2} . \tag{5.12}$$

We note that for the case of a constant sound speed c_s and Alfvén speed v_A, and

Fourier form $v_x(x,t) = v_x\, e^{i(\omega t - kx)}$ (with similar forms for v_y and v_z), Equations (5.10)-(5.12) reduce to

$$\left[\omega^2 - k^2(c_s^2 + v_A^2\cos^2\phi)\right] v_x + k^2 v_A^2 \cos\phi \sin\phi\, v_y = 0 \tag{5.13}$$

$$k^2 v_A^2 \cos\phi \sin\phi\, v_x + \left[\omega^2 - k^2 v_A^2 \sin^2\phi\right] v_y = 0 \tag{5.14}$$

$$\left[\omega^2 - k^2 v_A^2 \sin^2\phi\right] v_z = 0, \tag{5.15}$$

which for a nontrivial solution yields

$$\left(\omega^2 - k_\parallel^2 v_A^2\right)\left[\omega^4 - \omega^2 k^2\left(c_s^2 + v_A^2\right) + k^2 k_\parallel^2 c_s^2 v_A^2\right] = 0. \tag{5.16}$$

Here $k_\parallel = k\sin\phi = k\cos\theta$ is the component of the wave vector in the direction of the magnetic field. Hence for an infinite uniform medium we recover the dispersion relations for the Alfvén mode (first factor) and the fast and slow magnetoacoustic modes (second factor), given that propagation is at an angle $\theta = \pi/2 - \phi$ to the equilibrium magnetic field $\mathbf{B_0}$, see Chapter 1.

We return now to the x-structured case of equations (5.10), (5.11) and (5.12). The z component is a simple 1D wave equation for vertical motions. This is the Alfvén mode, since it involves the Alfvén speed only and the motions are transverse to both the equilibrium magnetic field and the direction of propagation. For a uniform medium the propagation speed involved is that appropriate to the Alfvén mode for propagation at an angle $(\pi/2 - \phi)$ to the equilibrium magnetic field.

The Alfvén mode is decoupled from the fast and slow magnetoacoustic modes. For the general case of skewed field and non-uniform density these modes are represented by the coupled equations (5.10) and (5.11), which govern horizontal motions.

For the special case of a purely transverse magnetic field, corresponding to $\phi = \pi/2$, all three modes are decoupled and are represented by simple 1D wave equations (Roberts and Joarder 1994):

$$\frac{\partial^2 v_x}{\partial t^2} = c_s^2(x)\frac{\partial^2 v_x}{\partial x^2} \tag{5.17}$$

$$\frac{\partial^2 v_y}{\partial t^2} = v_A^2(x)\frac{\partial^2 v_y}{\partial x^2} \tag{5.18}$$

$$\frac{\partial^2 v_z}{\partial t^2} = v_A^2(x)\frac{\partial^2 v_z}{\partial x^2}\,. \tag{5.19}$$

These equations govern the slow, fast and Alfvén modes respectively, with propagation in the direction of the equilibrium magnetic field. For the remainder of this Chapter we restrict attention to the case $\mathbf{B} \parallel \hat{\mathbf{x}} \parallel \mathbf{k}$.

5.2.1 Basic model for a transverse magnetic field

Hence all three MHD modes may be expressed in terms of equations of the form

$$\frac{\partial^2 v}{\partial t^2} = c^2(x)\frac{\partial^2 v}{\partial x^2} \tag{5.20}$$

such that

$$c^2(x)\rho_0(x) = \mathcal{T} \tag{5.21}$$

with the constant $\mathcal{T}$ given by (5.9) as appropriate to the propagation speed $c(x)$ for the particular choice of $v \in \{v_x, v_y, v_z\}$.

We consider density profiles of the general form

$$\rho_0(x) = \rho_c\,[1 + rg(x)] \tag{5.22}$$

where $r \geq 0$ and

$$0 \leq g(x) \leq g(0) = 1 \qquad g(-x) = g(x). \tag{5.23}$$

Hence the prominence represents a density enhancement over the background (coronal) value ρ_c, with $\rho_0(x)$ peaking at $x = 0$ with the value

$$\rho_0(0) \;=\; \rho_c(1 + r) \;\equiv\; \rho_p. \tag{5.24}$$

We have therefore split the overall density distribution $\rho_0(x)$ into the constant contribution ρ_c due to the corona and the x dependent contribution $\rho_c r g(x)$ due to the prominence. The (dimensionless) symmetric function $g(x)$ determines the shape of this density enhancement, of scalewidth $2a$, with r as a scaling factor. See Figures 5.4 and 5.7 for the particular profiles used.

For the general profile (5.22), seeking solutions of the form $v(x,t) = v(x)e^{i\omega t}$ in (5.20) yields

$$\frac{d^2 v}{dx^2} + \frac{\omega^2}{{c_c}^2}\,[1 + rg(x)]\,v = 0 \tag{5.25}$$

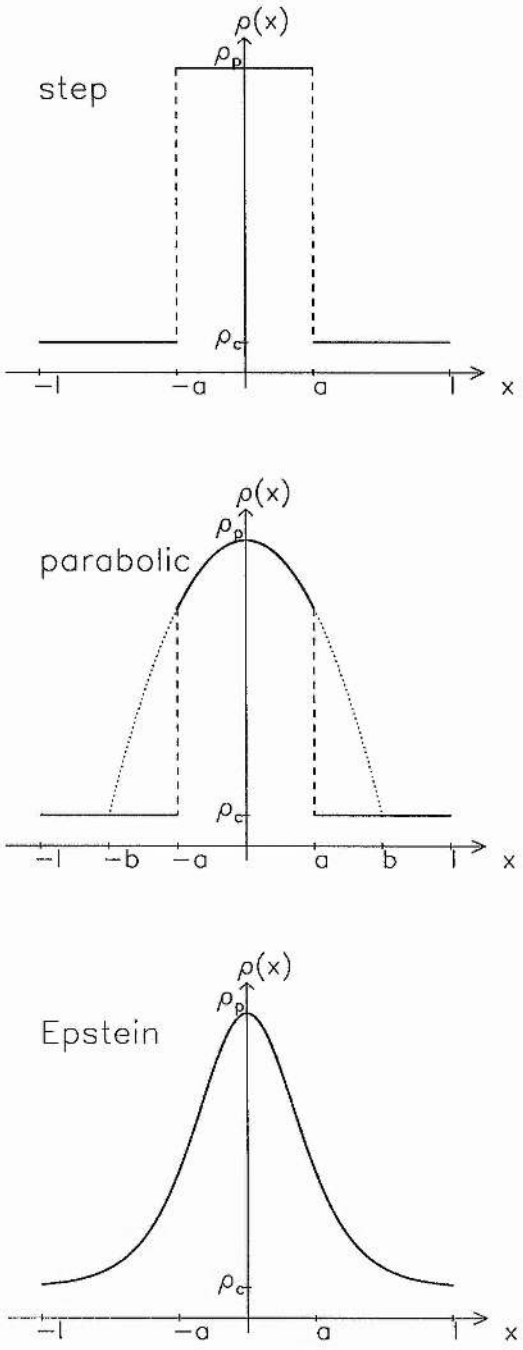

Figure 5.4: Sketches of the step function profile (see (5.58)), parabolic profile (see (5.67)) and Epstein profile (see(5.109)) of plasma density. These profiles are considered in detail in Sections 5.3.2, 5.3.3 and 5.4.1, respectively.

where c_c is the constant value of the characteristic propagation speed $c(x)$ when $\rho_0(x) = \rho_c$. We define $c_p = c(0)$ as the propagation speed at centre of the inhomogeneity. Then

$$c_c{}^2\rho_c \;=\; c^2(x)\rho_0(x) \;= c_p{}^2\rho_p. \tag{5.26}$$

We have thus reduced our problem to the study of a single second order ordinary differential equation (5.25), which we solve for different forms of the enhancement function $g(x)$ subject to appropriate boundary conditions, in order to determine the frequency ω and period $\tau = 2\pi/\omega$ of the mode.

To model the photospheric line-tying effect we impose (Raadu 1972, Hood and Priest 1979, Van der Linden, Hood and Goedbloed 1994)

$$v = 0 \quad \text{at } x = \pm l\,, \tag{5.27}$$

so that disturbances propagating through the medium bounce off the photosphere, which acts effectively as a rigid wall due to the vast increase in density.

We also impose the condition

$$\frac{dv}{dx} = 0 \quad \text{at } x = 0\,, \tag{5.28}$$

so that we restict attention to modes which disturb the prominence centre.

5.2.2 String analogy

Equation (5.20) and boundary condition (5.27) are of identical form to those governing the small amplitude transverse displacements $y(x,t)$ of a stretched elastic string under constant tension $\mathcal{T} = c^2/\rho$, where c is the elastic speed of the string and $\rho(x)$ is the mass per unit length of the string:

$$\frac{\partial^2 y}{\partial t^2} = c^2(x)\frac{\partial^2 y}{\partial x^2}, \qquad y(x = \pm l) = 0\,, \tag{5.29}$$

The string is aligned with the x-axis in equilibrium and has its ends tied at $x = \pm l$. Then the basic modes of oscillation of a prominence-coronal system are analogous to standing waves on a string of length $2l$ and non-uniform density.

For solutions of the form $y = u(x)e^{i\omega t}$ to (5.29), $u(x)$ satisfies

$$\frac{d^2u}{dx^2} + \frac{\omega^2}{c^2(x)}u = 0\,. \tag{5.30}$$

For c constant (5.30) has general solution

$$u(x) = C \sin\left(D - \frac{\omega}{c}x\right). \tag{5.31}$$

Then, for a uniform string, the conditions $y(x = \pm l) = 0$ yield the dispersion relation $\omega l/c = n\pi/2$ where $n = 1, 2, \ldots$. Hence the frequencies of oscillation take on discrete values, and depend on the length of the string and the elastic speed within the string.

For conditions typical of the prominence and surrounding corona, we consider $a \ll l$ and $\rho_p \gg \rho_c$ in our density enhancement model above. As a first approximation we concentrate the enhancement to a point, leading us to consider the oscillations of a uniform string loaded with a mass M at a point $x = x_0$.

Uniform string loaded with a point mass

Let us determine the effect a load mass M at $x = x_0$ has on the mode frequencies obtained for the uniform string without load. We may think of the point mass as dividing the string into two uniform sections, each of which may be treated separately. Then

$$u(x) = \begin{cases} u_1(x), & -l \leq x \leq x_0 \\ u_2(x), & x_0 \leq x \leq l \end{cases} \tag{5.32}$$

where $u_1(x)$, $u_2(x)$ are of the form (5.31). Continuity of the string requires that $u(x)$ be continuous across $x = x_0$. This, together with the requirement that $u_1(-l) = 0 = u_2(l)$, yields the solutions

$$u_1(x) = \frac{u(x_0)}{\sin\frac{\omega}{c}(l + x_0)} \sin\frac{\omega}{c}(l + x) \tag{5.33}$$

$$u_2(x) = \frac{u(x_0)}{\sin\frac{\omega}{c}(l - x_0)} \sin\frac{\omega}{c}(l - x). \tag{5.34}$$

Here we assume that the denominators in (5.33) and (5.34) are non-zero, hence excluding vibrations for which the load is situated at a node. Only modes which disturb the mass will be affected by the load.

The dispersion relation may be obtained on physical grounds from the equation of motion of the load mass M, whereby the force due to its acceleration must at all times be balanced by the net tension acting on M along the line of motion. The y-component of tension from the left-handside is $\mathcal{T} \sin\psi_1$, where ψ_1 is the angle that the tangent to the

string at M makes with the x-axis . For small displacements, ψ_1 is small and we may write $\sin\psi_1 = \tan\psi_1 = \partial y_1/\partial x$. Similarly for the y-component from the other side.

The equation of motion may then be written as

$$\mathcal{T}\left[\frac{\partial y_2}{\partial x} - \frac{\partial y_1}{\partial x}\right] = M\frac{\partial^2 y_2}{\partial t^2} \tag{5.35}$$

where the derivatives are evaluated at $x = x_0$. With $y_1 = u_1(x)e^{i\omega t}$, $y_2 = u_2(x)e^{i\omega t}$ we obtain, for $u(x_0) \neq 0$,

$$\cot\frac{\omega}{c}(l - x_0) + \cot\frac{\omega}{c}(l + x_0) = \frac{\omega c M}{\mathcal{T}}. \tag{5.36}$$

Now suppose that the load is situated at the centre of the string. Letting $x_0 = 0$ and setting $\mathcal{T} = c^2\rho$ yields

$$\frac{\omega l}{c}\tan\frac{\omega l}{c} = \frac{2\rho l}{M}. \tag{5.37}$$

Equation (5.37) is the dispersion relation for transverse vibrations of a uniform stretched elastic string of length $2l$, loaded with a mass M at its centre (Rayleigh 1877, Lamb 1910, Coulson 1941). It gives the frequencies ω of the *even* [3] modes only, for which the displacement $y(x,t)$ is symmetric about $x = 0$ and the mass is displaced in the vibration.

Introduce the dimensionless parameters

$$Z = \frac{\omega l}{c}, \qquad R = \frac{M}{2\rho l}\,. \tag{5.38}$$

Here Z is the dimensionless frequency and R is the ratio of the mass of the load to that of the uniform string. Then (5.37) may be written as

$$Z\tan Z = \frac{1}{R} \tag{5.39}$$

whose solutions for Z may be found graphically by considering the intersections of the line $y = RZ$ with the curve $y = \cot Z$. It is found by this approach that the solutions are given by $Z = n\pi + \epsilon$, where $\epsilon = \pi/2$ for $R = 0$ and $\epsilon \to 0$ as $R \to \infty$.

For large R, that is a heavy load, we have $\epsilon \ll 1$, and so

$$\tan Z = \tan\epsilon \approx \epsilon = Z - n\pi\,. \tag{5.40}$$

[3] Odd modes, for which the load is situated at a node (i.e. $u(0) = 0$) satisfy $\sin\omega l/c = 0$, i.e. $\omega l/c = n\pi$, $n = 1, 2, \ldots$, as for an unloaded string. Such modes are therefore unaffected by the load.

Thus dispersion relation (5.39) becomes approximated by the quadratic

$$Z(Z - n\pi) = \frac{1}{R}, \quad (R \gg 1), \tag{5.41}$$

with solutions (for $Z > 0$)

$$Z = \frac{n\pi}{2}\left(1 + \sqrt{1 + \frac{4}{Rn^2\pi^2}}\right), \qquad n = 1, 2, \ldots ; \tag{5.42}$$

for $n = 0$ we obtain

$$Z^2 = \frac{1}{R}. \tag{5.43}$$

For the purpose of applying this to global prominence oscillations in our simple model, we consider the fundamental mode, $n = 0$. Returning to the original parameters, we see that for a heavy mass, i.e. for $M \gg 2\rho l$, the frequency of the fundamental mode is given by

$$\left(\frac{\omega l}{c}\right)^2 \approx \frac{2\rho l}{M} \tag{5.44}$$

$$\text{i.e.} \quad \omega^2 \approx \frac{2\mathcal{T}}{Ml}. \tag{5.45}$$

Equation (5.45) gives a period $\tau (= 2\pi/\omega)$ of

$$\tau \approx \pi\left(\frac{2lM}{\mathcal{T}}\right)^{1/2}. \tag{5.46}$$

Hence the period of oscillation for this mode is determined by the mass M of the load, and the tension $\mathcal{T}$ within the string of length $2l$.

5.3 Slab models

In our basic prominence model, the density enhancement is spread over a scalewidth $2a$ rather than being concentrated at a point. The density distribution may be non-uniform. However, under appropriate conditions we may expect similar results to those obtained for the analogous situation of a uniform string loaded with a point mass. Since dispersion relation (5.37) also arises for linear longitudinal motions of a stretched uniform spring loaded with a point mass M at its centre, the results from this analogy ought to apply in our prominence model to motions that are either longitudinal (slow mode) or transverse (fast or Alfvén mode) to the equilibrium magnetic field $\mathbf{B_0}$.

We consider the case of the density enhancement of our prominence model being spread out over a *finite* width. The prominence is now represented, not by a point mass, but by a *slab* of width $2a$, so that the enhancement function $g(x)$ is piecewise continuous, with discontinuities at $x = \pm a$. The regions $|x| \leq a$ and $a < |x| < l$ correspond to the prominence and the surrounding corona respectively. Continuous profiles for $g(x)$ will be considered in Section 5.4.

5.3.1 General procedure

Since we are primarily interested in how the modes are influenced by the structure of the prominence, we consider a uniform corona and allow for the prominence to be transversely structured. Then

$$g(x) = 0, \quad a < |x| < l \tag{5.47}$$

with

$$\rho_0(x) = \begin{cases} \rho_p(x), & |x| \leq a \\ \rho_c, & |x| > a \end{cases} \tag{5.48}$$

and

$$c\,(x) = \begin{cases} c_p(x), & |x| \leq a \\ c_c, & |x| > a \end{cases} \tag{5.49}$$

such that

$$c_p^2(x)\rho_p(x) = \mathcal{T} = {c_c}^2\rho_c \tag{5.50}$$

and $\rho_p(x) > \rho_c$, with the constant $\mathcal{T}$ given by the appropriate form of (5.9) and analogous to the uniform tension in the loaded string (or the spring constant in the loaded spring, in the case of slow modes).

The string equation (5.25) is solved in each region, subject to the boundary conditions (5.27) and (5.28). The presence of discontinuities necessitates the application of additional boundary conditions at the interfaces. These are in general determined from the jump conditions at a plasma-plasma interface (Krall and Trivelpiece 1973, Goedbloed 1979), which for our equilibrium state imply

$$v \text{ and } \frac{dv}{dx} \text{ continuous across } x = a, \tag{5.51}$$

that is, continuity of the velocity and its first order derivative across the interface (Joarder and Roberts 1992b, Oliver, Ballester, Hood and Priest 1993). The first condition is apparent from physical considerations, while the second condition may also be obtained from integrating equation (5.25) from $x = a - \epsilon$ to $x = a + \epsilon$ and letting $\epsilon \to 0$. With $g(x)$ symmetric we need consider only $x > 0$.

Slab models are most useful where it is possible to obtain analytical solutions to (5.25) in each region, for then the application of these boundary conditions leads to a dispersion relation. This proves useful in investigating the basic physical nature of the modes.

Dispersion relations

Suppose equation (5.25) has analytical solution of the form

$$v(x) = \begin{cases} A_p v_p(x), & 0 \leq x \leq a \\ A_c v_c(x), & a \leq x \leq l \end{cases} \tag{5.52}$$

where A_p and A_c are arbitrary constants, and $v_p(x)$ and $v_c(x)$ are known functions of x. These solutions each contain only one arbitrary constant as a result of application of boundary conditions (5.27) and (5.28).

Requiring continuity of $v(x)$ and dv/dx across $x = a$ yields the matrix equation

$$\begin{pmatrix} v_p(a) & -v_c(a) \\ v_p'(a) & -v_c'(a) \end{pmatrix} \begin{pmatrix} A_p \\ A_c \end{pmatrix} = 0 \tag{5.53}$$

where a prime ($'$) denotes the derivative. For a non-trivial solution, the matrix determinant must be zero. This yields the dispersion relation

$$v_p'(a) v_c(a) = v_p(a) v_c'(a) \,. \tag{5.54}$$

With a uniform coronal plasma the appropriate solution in $x > a$ satisfying the boundary condition (5.27) is

$$v_c(x) = \sin \frac{\omega}{c_c} (l - x) \,. \tag{5.55}$$

Then, provided $v_p(a) \neq 0$, the dispersion relation (5.54) may be written as

$$\cot \frac{\omega}{c_c} (l - a) = -\frac{c_c}{\omega} \frac{v_p'(a)}{v_p(a)} \,. \tag{5.56}$$

The exact form of the expression on the right-handside will depend on the density structure of the prominence, which is characterised by the enhancement function $g(x)$ in $|x| \leq a$ determining the form of the solution $v_p(x)$ subject to (5.28).

5.3.2 Uniform prominence: step function profile

The simplest case to treat is that of a uniform prominence. Then with

$$g(x) = \begin{cases} 1, & 0 \leq |x| \leq a \\ 0, & a < |x| \leq l \end{cases} \tag{5.57}$$

the density within the prominence-coronal medium takes the step function profile (see Figure 5.4):

$$\rho_0(x) = \begin{cases} \rho_p, & 0 \leq |x| \leq a \\ \rho_c, & a < |x| \leq l \end{cases} \tag{5.58}$$

with $\rho_p = \rho_c(1 + r)$ and $r \geq 0$. Hence the situation is analogous to even modes of a two-density string.

Dispersion relation

For a uniform prominence region the appropriate solution satisfying the boundary condition (5.28) is

$$v_p(x) = \cos\frac{\omega x}{c_p} . \tag{5.59}$$

The dispersion relation for the step function density profile is then easily found, from (5.56), to be (Joarder and Roberts 1992b, Joarder and Roberts 1993b, Oliver et al. 1993, Roberts and Joarder 1994)

$$\cot\frac{\omega}{c_c}(l - a) = \left(\frac{\rho_p}{\rho_c}\right)^{1/2} \tan\frac{\omega a}{c_p} . \tag{5.60}$$

Analytical limits

We may consider analytical limits of the dispersion relation (5.60), applicable to the global modes of a thin, dense prominence.

Take the limit $\omega a/c_p \ll 1$, corresponding to a long wavelength, low frequency vibration with respect to the width of the prominence. The dispersion relation given by equation

(5.60) then reduces to

$$\cot\frac{\omega}{c_c}(l-a) = \frac{\omega a}{c_c}\frac{\rho_p}{\rho_c}. \tag{5.61}$$

For a thin prominence $a \ll l$ the fundamental mode is approximated (Roberts 1991b, Roberts and Joarder 1994) by the solution to

$$\frac{\omega l}{c_c}\tan\frac{\omega l}{c_c} = \frac{2\rho_c l}{M} \tag{5.62}$$

where $M = 2\rho_p a$.

Hence, in these limits we may draw the analogy of a uniform string loaded with an equivalent point mass at the centre. Then for a heavy mass, i.e. provided $\rho_c l/\rho_p a \ll 1$, the frequency ω and period τ of the fundamental mode (for which $\omega l/c_c \ll 1$) satisfy (Roberts 1991b, Joarder and Roberts 1992b, Joarder and Roberts 1993b, Oliver et al. 1993, Roberts and Joarder 1994, Joarder et al. 1997a)

$$\left(\frac{\omega l}{c_c}\right)^2 \approx \frac{\rho_c l}{\rho_p a} \tag{5.63}$$

$$\tau \approx \pi\left(\frac{2lM}{\mathcal{T}}\right)^{1/2} = 2\pi\frac{(al)^{1/2}}{c_p}. \tag{5.64}$$

Therefore, in terms of prominence parameters, the period of this mode depends on the characteristic speed within the prominence and the geometric mean of the prominence width and the line-tying distance. The conditions under which the approximation (5.63) has been derived collectively yield the constraints

$$\left(\frac{\rho_c}{\rho_p}\right)^{1/2} \ll \left(\frac{a}{l}\right)^{1/2} \ll 1 \tag{5.65}$$

so that the prominence must be sufficiently thin and dense relative to the surrounding coronal medium.

In Figure 5.5 we show the exact fundamental solutions to the step function dispersion relation (5.60), plotting the dimensionless frequency $\omega l/c_c$ as a function of the density ratio parameter r, for $a/l = 0.1$, 0.05 and 0.01. For $r = 0$ (no enhancement) we recover the uniform string fundamental solution $\omega l/c_c = \pi/2$ for any given a/l; this solution is similarly recovered for all r when $a/l = 0$. As r increases the frequency decreases, and for r sufficiently large (with larger r required for smaller a/l) the exact solutions are well approximated by the the formula (5.63) obtained from the point mass analogy, which are also shown (dotted curves) in Figure 5.5.

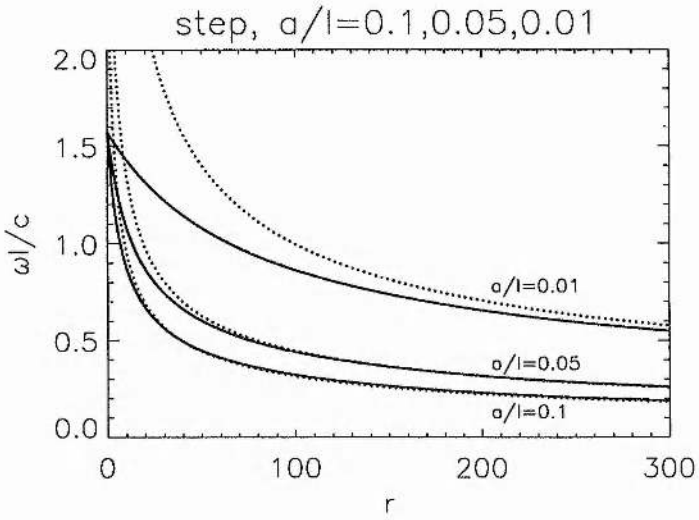

Figure 5.5: Solutions (solid curves) to the dispersion relation (5.60) for the step function profile (5.58), showing the dimensionless frequency $\omega l/c_c$ as a function of the density ratio parameter r, and taking $a/l = 0.1, 0.05, 0.01$ as indicated. We also show (dotted curves) the approximations (5.63) given by the point mass analogy, which in each case applies for r sufficiently large.

For conditions typical of a prominence, $\rho_p > 200\rho_c$ and $l \approx 10a$ so that (5.65) is satisfied and the approximation applies. Hence we may expect the loaded string analogy to apply to the global oscillations of the prominence and surrounding line-tied coronal arcade, these oscillations having period τ approximated by (5.64).

5.3.3 Non-uniform prominence: parabolic profile

In reality a prominence is not uniform, and there is no sharp discontinuity between the prominence and the corona. We wish to investigate whether a similar approximation will hold for more "realistic" density profiles. Observations show that there is a transition region surrounding the prominence made up of low emission, i.e. lower density, material.

We can model this transition region (and still obtain analytical results) by using a parabolic profile for the density, as follows. Let

$$g(x) = \begin{cases} 1 - \frac{x^2}{b^2}, & 0 \leq |x| \leq a \\ 0, & a < |x| \leq l \end{cases} \tag{5.66}$$

so that

$$\rho_0(x) = \begin{cases} \rho_c \left[1 + r\left(1 - \frac{x^2}{b^2}\right)\right], & 0 \leq |x| \leq a \\ \rho_c, & a < |x| \leq l \end{cases} \tag{5.67}$$

where $b > a$ and $\rho_0(x) \leq \rho_0(0) = \rho_c(1+r) = \rho_p$, see Figure 5.4. We may define a profile parameter q,

$$q \equiv \frac{b}{a} \geq 1, \tag{5.68}$$

which allows for variation between a continuous profile for $q = 1$ and the step function profile (of Section 5.3.2), which is recovered for $q \to \infty$. The continuous profile given by $b = a$ has been used in an examination of the effects of different density profiles on the properties of ducted magnetic Love and Pekeris waves in dense coronal loops (Edwin and Roberts 1988).

Solution to the governing equation

For the parabolic profile (5.67) the form of the string equation (5.25) applicable to the prominence region $|x| \leq a$ may be written as

$$\frac{d^2v}{dx^2} + \frac{\omega^2}{c_c^2}\left[1 + r\left(1 - \frac{x^2}{b^2}\right)\right] v = 0. \tag{5.69}$$

Equation (5.69) may be solved analytically as follows. First let

$$\sigma^2 = \frac{\omega^2}{c_c^2} r = \frac{\omega^2}{c_p^2} - \frac{\omega^2}{c_c^2}\,. \tag{5.70}$$

Then equation (5.69) may be written as

$$\frac{d^2v}{dx^2} + \left(A - Bx^2\right) v = 0 \tag{5.71}$$

where

$$A = \frac{\omega^2}{c_c^2}(1+r), \qquad B = \frac{\sigma^2}{b^2}. \tag{5.72}$$

Change variables by setting $s = px^2$, where $p(>0)$ is to be determined. Then

$$\frac{ds}{dx} = 2px; \quad \frac{dv}{dx} = 2p^{1/2}s^{1/2}\frac{dv}{ds}; \quad \frac{d^2v}{dx^2} = 4ps\frac{d^2v}{ds^2} + 2p\frac{dv}{ds}\,. \tag{5.73}$$

Dividing by $4p$, equation (5.71) becomes,

$$s\frac{d^2v}{ds^2} + \frac{1}{2}\frac{dv}{ds} + \left(\frac{A}{4p} - \frac{B}{4p^2}s\right) v = 0\,. \tag{5.74}$$

Seek a solution of (5.74) of the form

$$v(s) = e^{-\alpha s} u(s), \tag{5.75}$$

where α is to be determined. Then

$$\frac{dv}{ds} = e^{-\alpha s}\left\{\frac{du}{ds} - \alpha u\right\}, \quad \frac{d^2v}{ds^2} = e^{-\alpha s}\left\{\frac{d^2u}{ds^2} - 2\alpha\frac{du}{ds} + \alpha^2 u\right\}, \tag{5.76}$$

and equation (5.74) yields

$$s\frac{d^2u}{ds^2} + \left(\frac{1}{2} - 2\alpha s\right)\frac{du}{ds} - \left\{\frac{\alpha}{2} - \frac{A}{4p} + \left(\frac{B}{4p^2} - \alpha^2\right)s\right\}u = 0\,. \tag{5.77}$$

Compare equation (5.77) with Kummer's equation (Abramowitz and Stegun 1965)

$$z\frac{d^2w}{dz^2} + (f - z)\frac{dw}{dz} - ew = 0 \tag{5.78}$$

for which two linearly independent solutions are

$$w_1(z) = M(e, f, z) \tag{5.79}$$

$$w_2(z) = z^{1-f}M(e + 1 - f, 2 - f, z). \tag{5.80}$$

Here $M(e, f, z)$ is the confluent hypergeometric function, given by

$$M(e, f, z) = 1 + \frac{e}{f}z + \frac{(e)_2}{(f)_2}\frac{z^2}{2} + \cdots + \frac{(e)_n}{(f)_n}\frac{z^n}{n!} + \cdots \tag{5.81}$$

where

$$(e)_n = e(e + 1)(e + 2)\ldots(e + n - 1), \quad (e)_0 = 1. \tag{5.82}$$

Equation (5.77) is in the form of Kummer's equation if

$$2\alpha = 1, \qquad \frac{B}{4p^2} - \alpha^2 = 0 \tag{5.83}$$

which yields

$$\alpha = \frac{1}{2}, \qquad p = \sqrt{B} = \frac{\sigma}{b}\,. \tag{5.84}$$

Then

$$e = \frac{1}{4}\left(1 - \sigma b\left(\frac{1 + r}{r}\right)\right), \qquad f = \frac{1}{2}\,. \tag{5.85}$$

Hence our two linearly independent solutions to (5.69) are

$$v_1(x) = e^{-\frac{\sigma x^2}{2b}} M\left(\frac{1}{4}\left\{1 - \sigma b\left(\frac{1 + r}{r}\right)\right\}, \frac{1}{2}, \frac{\sigma x^2}{b}\right) \tag{5.86}$$

$$v_2(x) = \left(\frac{\sigma}{b}\right)^{1/2} x e^{-\frac{\sigma x^2}{2b}} M\left(\frac{1}{4}\left\{3 - \sigma b\left(\frac{1 + r}{r}\right)\right\}, \frac{3}{2}, \frac{\sigma x^2}{b}\right). \tag{5.87}$$

Dispersion relation

Now (Abramowitz and Stegun 1965)

$$\frac{d}{dz}M(e,f,z) = \frac{e}{f}M(e+1,f+1,z) \tag{5.88}$$

so clearly $v_1(0) \neq 0$, $v_1'(0) = 0$ while $v_2(0) = 0$, $v_2'(0) \neq 0$. Hence, for the prominence region $|x| \leq a$ the appropriate choice of solution to (5.69) satisying the boundary condition (5.28) is

$$v_p(s(x)) = e^{-s/2}M(e,f,s) \tag{5.89}$$

where $s = \sigma x^2/b$ and e, f are given by (5.85).

By use of (5.88) and the chain rule, we obtain

$$v_p{}'(x) = \frac{\sigma x}{b}e^{-s/2}\left\{4eM(e+1,f+1,s) - M(e,f,s)\right\} . \tag{5.90}$$

Write $M_1 = M(e,f,\sigma a^2/b)$ and $M_2 = M(e+1,f+1,\sigma a^2/b)$. Then we may write

$$-\frac{c}{\omega}\frac{v_p{}'(a)}{v_p(a)} = \frac{\sigma a}{b}\left\{1 - 4e\frac{M_2}{M_1}\right\} \tag{5.91}$$

with

$$M_1 = M\left(\frac{1}{4}\left\{1 - \sigma b\left(\frac{1+r}{r}\right)\right\}, \frac{1}{2}, \frac{\sigma a^2}{b}\right) \tag{5.92}$$

$$M_2 = M\left(\frac{1}{4}\left\{5 - \sigma b\left(\frac{1+r}{r}\right)\right\}, \frac{3}{2}, \frac{\sigma a^2}{b}\right) . \tag{5.93}$$

Thus our generalised slab dispersion relation (5.56) may be written as

$$\cot\frac{\omega}{c_c}(l-a) = \frac{c_c\sigma}{\omega}\frac{a}{b}\left\{1 + \left[\sigma b\left(\frac{1+r}{r}\right) - 1\right]\frac{M_2}{M_1}\right\} . \tag{5.94}$$

Equation (5.94) is the dispersion relation for the parabolic density profile (5.67).

Expansion of the dispersion relation

Dispersion relation (5.94) is considerably more complicated than that for the step function density profile, making it difficult to say anything directly about the physical properties of the modes. However, we can make further analytical progress in this respect through the use of limits similar to those applied to the step function case.

It is first necessary to expand the right-handside of the dispersion relation (5.94). Write

$$M_2 = M(e+1, f+1, S) = 1 + a_1 S + a_2 S^2 + \ldots \tag{5.95}$$

$$M_1 = M(e, f, S) = 1 + b_1 S + b_2 S^2 + \ldots \tag{5.96}$$

where $S = \sigma a^2/b$ and

$$a_n = \frac{(e+1)_n}{(f+1)_n}\frac{1}{n!}, \qquad b_n = \frac{(e)_n}{(f)_n}\frac{1}{n!}. \tag{5.97}$$

Then

$$\frac{M_2}{M_1} = 1 + c_1 S + c_2 S^2 + \ldots \tag{5.98}$$

where

$$c_1 = a_1 - b_1 = \frac{f-e}{f(f+1)} \tag{5.99}$$

$$c_2 = (a_2 - b_2) - b_1 c_1 = \frac{(f-2e)}{f(f+2)} c_1 \,. \tag{5.100}$$

Then manipulation yields

$$\frac{a}{b}\left\{1 + \left[\sigma b\left(\frac{1+r}{r}\right) - 1\right]\frac{M_2}{M_1}\right\} =$$
$$\sigma a\left[\left\{\left(\frac{r+1}{r}\right) - \frac{a^2}{3b^2}\right\} + \frac{(\sigma a)^2}{15}\left(\frac{r+1}{r}\right)\left\{5\left(\frac{r+1}{r}\right) - \frac{2a^2}{b^2}\right\} + O\left[(\sigma a)^4\right]\right]. \tag{5.101}$$

Analytical limits

Now take the limit $\sigma a \ll 1$, corresponding to long wavelengths with respect to the prominence. Then, using (5.101) the dispersion relation (5.94) reduces to

$$\cot\frac{\omega}{c_c}(l-a) = \frac{\omega a}{c_c} r\left\{\frac{r+1}{r} - \frac{a^2}{3b^2}\right\}. \tag{5.102}$$

The significance of this result is revealed if we express it in terms of the average density within the prominence. Introduce

$$\overline{\rho}_p = \frac{1}{a}\int_0^a \rho_p(x)dx \tag{5.103}$$

$$= \rho_c\left[(1+r) - \frac{ra^2}{3b^2}\right]; \tag{5.104}$$

$\overline{\rho}_p$ is the mean density within the prominence region $|x| \leq a$. Then (5.102) becomes

$$\cot\frac{\omega}{c_c}(l-a) = \frac{\omega a}{c_c}\frac{\overline{\rho}_p}{\rho_c}\,. \tag{5.105}$$

Hence in the long wavelength limit, given here by $\sigma a \ll 1$, the dispersion relation (5.94) for the parabolic profile of peak density ρ_p reduces to the same equation (5.105) as is obtained in the long wavelength limit of the step function profile for which $\overline{\rho}_p = \rho_p$ (cf. (5.61), obtained from (5.60) when $\omega a/c_p \ll 1$, with ρ_p replaced by $\overline{\rho}_p$).

Thus, for a long wavelength ($\sigma a \ll 1$, $\omega l/c_c \ll 1$) oscillation of a thin ($a \ll l$), dense ($\overline{\rho}_p \gg \rho_c$) prominence with parabolic density profile (5.67), we may similarly draw the analogy of uniform string loaded with a point mass $M = 2\overline{\rho}_p a$ at its centre, so that the solution satisies

$$\left(\frac{\omega l}{c_c}\right)^2 \approx \frac{\rho_c l}{\overline{\rho}_p a}. \tag{5.106}$$

We therefore obtain the approximation

$$\tau \approx 2\pi\frac{(al)^{1/2}}{\overline{c}_p} \tag{5.107}$$

to the period τ of the fundamental mode, where the characteristic speed $\overline{c}_p$ satisfies

$$\overline{c}_p{}^2\overline{\rho}_p = c_c^2\rho_c = \mathcal{T}, \tag{5.108}$$

with $\mathcal{T}$ given by (5.9).

For the exact dispersion relation (5.94) for the parabolic profile (5.67), solving for the dimensionless frequency $\omega l/c_c$ as a function of r for fixed a/l yields curves similar to the those given in Figure 5.5 for the step function profile (5.58).

In Figure 5.6 we show the exact fundamental solutions (solid curves) to the parabolic dispersion relation (5.94), plotting the dimensionless frequency $\omega l/c_c$ as a function of the profile parameter q, for $a/l = 0.1$ and $r = 50, 250$. In each case we also show the exact solutions (dashed curves) for the equivalent uniform slab case, given by the step function dispersion relation (5.60) with ρ_p replaced by $\overline{\rho}_p$, which is given by (5.103). There is good agreement between the solutions for the two profiles, for all values of the profile parameter q, and these are in turn well approximated by the formula (5.106) obtained from the point mass analogy, which are also shown (dotted curves) in Figure 5.6.

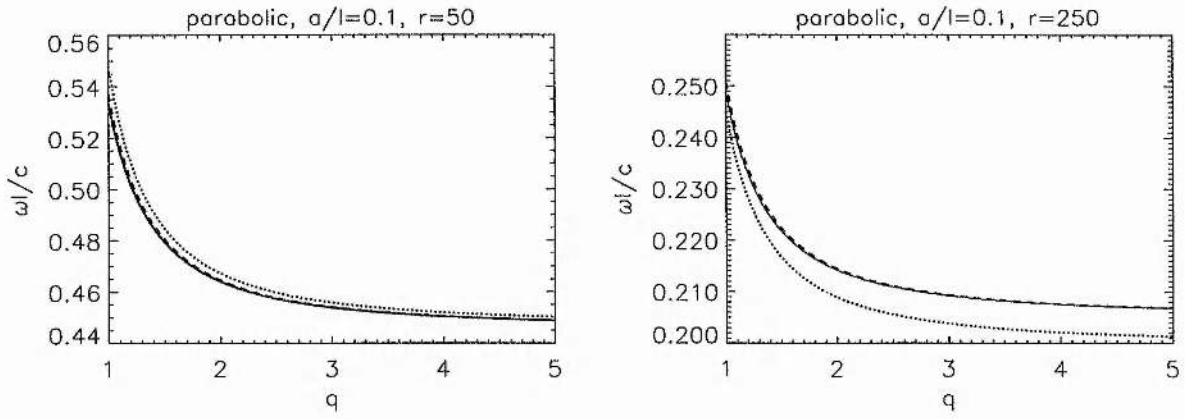

Figure 5.6: Solutions (solid curves) for the parabolic profile (5.67) as a function of the profile parameter q. We also show the solutions (dashed curves) for the equivalent uniform slab case with density $\overline{\rho}_p$ defined by (5.103), and the approximation (5.106) (dotted curves) yielded by the point mass analogy. We show separate plots for the cases $r = 50$ and $r = 250$, with $a/l = 0.1$.

5.4 Continuous profiles

We are interested in the effects of transverse structuring on the low order, long wavelength oscillations of the prominence and corona. It has been found that slab models which give analytical results are useful in gaining an insight into the physical nature of the modes through the application of certain limits as appropriate to prominences, for which we may draw the analogy of a string loaded with a point mass. In these cases the system behaves as though the mass represented by the prominence were concentrated in an infinitely thin sheet, of mass density per unit area $M = 2\overline{\rho}_p a$, thereby rendering the mode independent of the details of structuring in the transverse direction (expressed in terms of the enhancement function $g(x)$).

However, we have considered only two profiles for $g(x)$, both of which involve simple, algebraic functions. Also, while the parabolic case goes some way towards modelling the prominence-corona transition region, it is not entirely satisfactory for this purpose due to the discontinuities involved. We can avoid discontinuites by using a single smooth function $g(x)$ in our general profile (5.22) which defines the density structuring within both the prominence and the surrounding corona.

5.4.1 Epstein profile

Consider the Epstein profile for density (Epstein 1930), given by

$$\rho_0(x) = \rho_c \left[1 + r \operatorname{sech}^2\left(\frac{x}{a}\right)\right], \tag{5.109}$$

as shown in Figure 5.4. Here

$$g(x) = \operatorname{sech}^2\left(\frac{x}{a}\right), \quad 0 \leq |x| \leq l, \tag{5.110}$$

and equation (5.25) may be written as

$$\frac{d^2v}{dx^2} + \frac{\omega^2}{c_c^2}\left[1 + r \operatorname{sech}^2\left(\frac{x}{a}\right)\right] v = 0. \tag{5.111}$$

The Epstein profile has been used in examinations of the effects of different density profiles on the properties of ducted magnetic Love and Pekeris waves in dense coronal loops (Edwin and Roberts 1988, Nakariakov and Roberts 1995b).

For the transcendental profile (5.109), an analytical solution to the string equation (5.111) proves elusive, and no dispersion relation has been found. However we can determine ω by numerical solution of the governing differential equation (5.111). We write (5.111) as a system of first order differential equations in dimensionless form, which we solve subject to the boundary conditions (5.27) and (5.28), through the application of a shooting method using NAG routine D02HAF.

As for the preceeding models, we may solve for the dimensionless frequency $\omega l/c_c$ as a function of the density ratio r, concentrating on the fundamental solution. This yields exact solution curves similar to the those given in Figure 5.5 for the step function profile (5.58). We may compare these results more easily through the introduction of a modified Epstein profile, which we now consider.

5.4.2 Modified Epstein profile

Consider the modified Epstein profile (see Nakariakov and Roberts (1995b))

$$\rho_0(x) = \rho_c \left[1 + r \operatorname{sech}^2\left(\frac{x}{a}\right)^p\right]. \tag{5.112}$$

Here

$$g(x) = \operatorname{sech}^2\left(\frac{x}{a}\right)^p, \quad 0 \leq |x| \leq l, \tag{5.113}$$

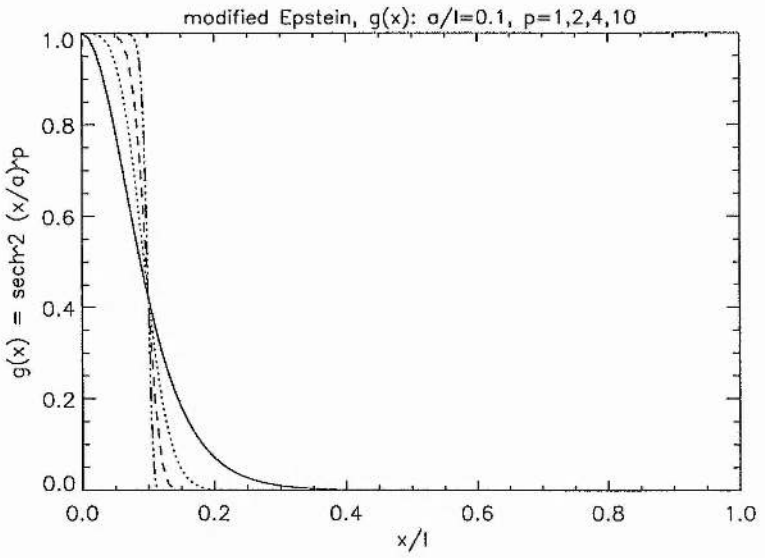

Figure 5.7: Form of $g(x) = \mathrm{sech}^2(x/a)^p$ for the modified Epstein profile (5.112), shown for $0 < x < l$, with $a/l = 0.1$ and taking $p = 1$ (solid), $p = 2$ (dotted), $p = 4$ (dot-dashed) and $p = 10$ (dot-dot-dot-dashed).

and equation (5.25) may be written as

$$\frac{d^2v}{dx^2} + \frac{\omega^2}{c_c^2}\left[1 + r\ \mathrm{sech}^2\left(\frac{x}{a}\right)^p\right] v = 0. \tag{5.114}$$

The profile parameter $p \geq 1$ allows us to vary between the basic Epstein profile $p = 1$ and the step function profile of Section 5.3.2, which is recovered for $p \to \infty$; see Figure 5.7. This modified Epstein profile has been used by Nakariakov and Roberts (1995b) in an examination of the effects of different density profiles on the properties of ducted magnetic Love and Pekeris waves in dense coronal loops.

The string equation (5.114) has been solved numerically using the same method as described above for the basic Epstein profile. For any given p, the exact solution curves for the dimensionlesss frequency $\omega l/c_c$ as a function of the density ratio parameter r, are similar to those given in Figure 5.5 for the step function profile (5.58).

5.4.3 Equivalent uniform slab case

We pointed out earlier that the results for the parabolic profile may be discussed in terms of an equivalent uniform slab, namely that whose uniform density within $|x| \leq a$ is equal to the mean density ρ_p of the parabolic profile within $|x| \leq a$. We find that we may similarly define an equivalent uniform slab case for the Epstein and modified Epstein profiles, and that this definition generalises the result for the parabolic profile.

For continuous profiles of the enhancement function $g(x)$, the prominence width is not defined precisely, unlike the slab models which have $g(x) = 0$ in $|x| \geq a$. We may instead consider the problem in terms of the overall density enhancement *in excess* of the background coronal value ρ_c, examining

$$\int_0^l \rho_c r g(x) dx.$$

Now redistribute this "excess" within a uniform slab within $|x| \leq a$ surrounded by a uniform background of density ρ_c within $a \leq |x| \leq l$. This equivalent slab has peak density $\overline{\rho}_p$, where

$$\overline{\rho}_p = \rho_c (1 + rI) \tag{5.115}$$

with the factor I given by

$$I = \frac{1}{a} \int_0^l g(x) dx. \tag{5.116}$$

The definition (5.115) of the density $\overline{\rho}_p$ of the equivalent slab is more general than that given for the parabolic profile above: definition (5.115) allows for $g(x) > 0$ in $|x| \geq a$ and gives results in agreement to the earlier definition (5.103) when $g(x) = 0$ in $|x| \geq a$. The factor I is a function of the profile parameter, p for the modified Epstein profile and q for the parabolic profile. Figure 5.8 displays its form for the modified Epstein profile and the parabolic profile; note that in each case $I \to 1$ for large values of the profile parameter. Then, subject to the criterion (5.65) with ρ_p replaced by $\overline{\rho}_p$, we expect the solution to be well approximated by (5.106) as is given from the analogy of a uniform string loaded with a point mass $M = 2\overline{\rho}_p a$ at its centre.

In Figure 5.9 we show the numerically computed fundamental solutions for the modified Epstein profile (5.112), plotting the dimensionless frequency $\omega l / c_c$ as a function of the profile parameter p, for $a/l = 0.1$ and cases $r = 150$ and 250. In each case we also

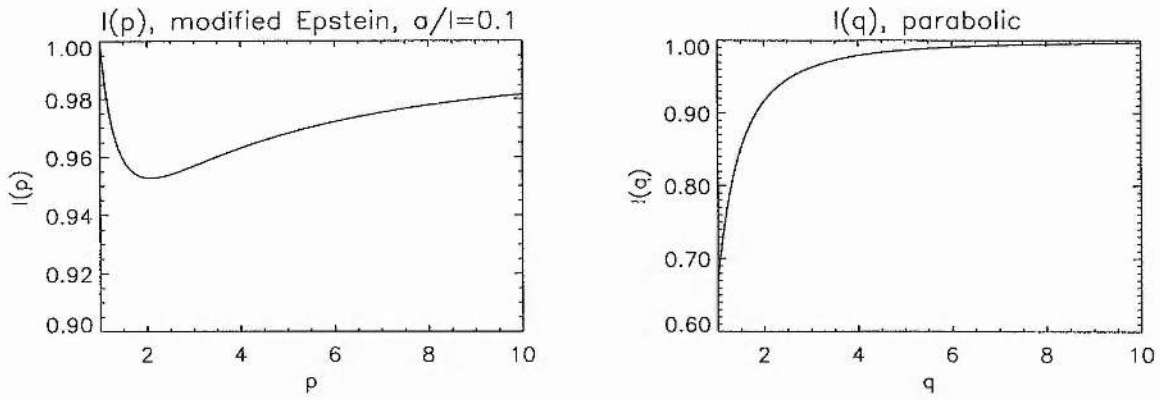

Figure 5.8: Plot of the factor I (see (5.116) as a function of the profile parameter for the modified Epstein and parabolic profiles. For the modified Epstein profile (5.112), $I = I(p)$, shown on the left-hand plot for the case $a/l = 0.1$. For the parabolic profile (5.67), $I = I(q)$ where $q = b/a$, shown on the right-hand plot. In both cases, $I \to 1$ for large values of the profile parameter, so that the result $I = 1$ for the step function profile (5.58) is recovered.

show the exact solutions (dashed curves) for the equivalent uniform slab, given by the step function dispersion relation (5.60) with ρ_p replaced by $\overline{\rho}_p$ (given by the generalised form (5.115)). There is good agreement between the solutions for the two profiles, for all values of p, although this agreement improves with increasing p. The exact solutions for both profiles are well approximated by the formula (5.106) obtained from the point mass analogy, shown with dotted curves. For comparison, we also show the exact solutions (dot-dashed curves) for the uniform slab dispersion relation (5.60) with ρ_p replaced by $\overline{\rho}_p$ with $\overline{\rho}_p$ given by the earlier form (5.103); clearly, this case does not given as good agreement as found using the general definition (5.115) of $\overline{\rho}_p$.

The qualitative similarity of the solutions as functions of p for the modified Epstein profile is in agreement with the results above for the parabolic profile, where solutions were compared as functions of the parabolic profile parameter q.

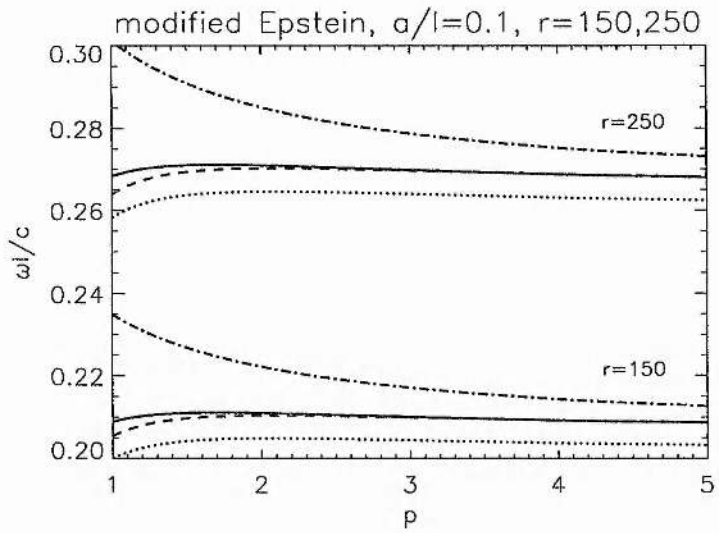

Figure 5.9: Solutions (solid curves) for the modified Epstein profile (5.112) as a function of the profile parameter p. We also show the solutions for the equivalent uniform slab case, with density $\overline{\rho}_p$ defined by both the slab form (5.103) (dot-dashed curves) and generalised form (5.115) (dashed curves). Clearly the generalised form is the appropriate equivalent uniform slab case, for which we also show the approximation (5.106) (dotted curves) yielded by the point mass analogy. We show separate sets of curves for the cases $r = 150$ and $r = 250$, as indicated, with $a/l = 0.1$.

5.5 Summary and conclusions

We have extended the uniform slab model of Joarder and Roberts (1992b, 1993b) by considering the effects of different density profiles $\rho_0(x)$ (each characterised by an enhancement function $g(x)$ and scaling parameter r; see (5.22) and Figures 5.4 and 5.7) on the properties of the string mode, and in particular the formula (5.64) approximating its period, obtained from the point mass analogy (see Section 5.2.2).

All "realistic" density profiles have an equivalent uniform slab profile (see Section 5.4.3), yielding a period very close to that obtained for the original profile. Our results indicate that for the fundamental mode of our model, the results for the uniform slab are of more general validity, and are applicable to other profiles with enhancement function $g(x)$ typical of the prominence-coronal inhomogeneity.

For flatter density profiles (such as the modified Epstein profile with $p > 4$) the density $\overline{\rho}_p$ (see (5.115)) of this equivalent uniform slab is close to the profile's peak density ρ_p and to the average density (see (5.103)) within the prominence scale width. Such a profile is likely to well represent the averaged density structuring within and around a real prominence, so that the formula obtained from the point mass analogy may be applied using the value of prominence density obtained from observations.

This implies that for parameter values typical of the prominence and surrounding corona the oscillation period of the string mode is principally determined by the average conditions within the prominence as a whole. Accordingly, one may usefully employ the uniform slab model developed by Joarder and Roberts (1992b, 1993b). Hence, as was found for the case of fast body modes in coronal loops (Edwin and Roberts 1988, Nakariakov and Roberts 1995b), the essence of the problem studied here is contained within the uniform slab model. This result provides continued support for the use of simple models to describe the basic physics of MHD wave propagation in structured plasmas.

Chapter 6

Conclusions

6.1 Summary

In this thesis we have considered ideal MHD wave propagation in structured media, using models relevant to structures in the solar atmosphere. Let us discuss the main results of each chapter in turn.

Chapter 2

In Chapter 2 we consider stationary state configurations which are *discretely* structured in a direction *transverse* to the magnetic field, namely the single interface, uniform slab and uniform cylinder, which are of relevance to a variety of solar structures such as coronal loops, sunspots and coronal streamers. We derive and discuss the dispersion relations governing ideal linear MHD modes in each case, where in the stationary state we allow for structuring in the velocity (taken to be aligned with the magnetic field), in addition to the other plasma variables. In the absence of flow, stable surface waves (associated with the interface) are obtained for all three geometries, while the slab and cylinder additionally support stable body waves (internal to the structure).

As a valuable preliminary to the examination of the ways in which these well known solutions for the static case are modified by the presence of field-aligned flows, we consider the effects of field-aligned flows on the propagation of MHD waves in an unstructured medium, from a stationary frame of reference. Such a study is an important building

block for work on MHD waves of discretely structured media, showing how the basic wave speeds within each medium (the propagation speeds of surface modes represent a "mean" of these speeds) are modified by field-aligned flows relative to adjacent media and/or the reference frame. This modification due to the flow leads to distortions in the usual polar phase diagrams, with modes becoming "backward" (in the given reference frame) for sufficiently large flow speeds. The resulting asymmetry makes it important to consider *both* solutions for a given mode type in the presence of flows, whereas in the static case the two solutions are essentially equivalent, each having the same phase speed, but oppositely directed.

Chapter 3

In Chapter 3 our focus is on *surface modes*, which arise as a result of the structuring rather than being merely modified by inhomogeneities. In the treatment of surface modes, the analysis simplifies greatly if we consider the incompressible approximation, given by $\gamma \to \infty$ and $c_s \to \infty$. We carry out a detailed investigation for this case, and gain insight into the nature of incompressible surface modes in the presence of relative flows by means of a generalised treatment applicable to the single interface, uniform slab and uniform cylinder, in which we trace the evolution of stable solutions and their propagation windows, as the relative flow is increased within a fixed reference frame for given Alfvén speeds v_{A0} and v_{Ae}.

This novel approach reveals the combined effect of dispersion and the ratio of densities in the two media, which we discuss in terms of an *effective* density ratio $f\rho_0/\rho_e$, where $f = f(|k|a)$ is defined for each mode type. We find the new result that for given Alfvén speeds the stability threshold attains its minimum value of $v_{A0} + v_{Ae}$ when $f = f^*$, where $f^* \equiv (\rho_e v_{Ae})/(\rho_0 v_{A0})$. This minimum threshold may also be predicted from our analysis of the evolution of the propagation windows, which proves particularly invaluable in our discussion of the critical relative flows for the qualitative properties of the modes. We show how knowledge of the evolution of the propagation windows combined with the critical case $f = f^*$ and the form of $f(|k|a)$ together yields information about the dispersive and stability properties of a given mode and configuration of plasmas, without requiring solution of the dispersion relation itself.

Chapter 4

In Chapter 4 we continue to focus on surface waves, this time considering the relevance of the incompressible approximation to compressible surface modes, in the light of its usefulness in Chapter 3. Here we draw on the particular example of a static compressible single interface, one side of which is field-free. This case is found to be amenable to detailed analytical treatment for several special cases, for which the properties of the solutions are compared with those for the incompressible case. The aim of this investigation is to develop and employ means of assessing the applicability of the incompressible case, and to identify the situations in which the incompressible approximation is valid. This is done by not only comparing the obtained solution c_p with the solution c_k for the "equivalent" incompressible case, but also considering the variation of m_0/k, m_e/k and m_e/m_0, all of which are equal to unity in the incompressible case.

We found that for the static compressible magnetic-nonmagnetic interface, the incompressible approximation is valid for the slow mode when the ratio c_{s0}/v_{A0} is only moderately large, and that it is not necessary that c_{se}/v_{A0} be large also; here c_{s0} and v_{A0} are the sound and Alfvén speed respectively of the magnetic medium, while c_{se} is the sound speed of the nonmagnetic medium. Hence the incompressible case may yield good results for the slow mode not only for the case of high β plasmas ($c_s > v_A$) to which is generally applies, and indeed it is found that in certain cases it may also find applicability to the fast mode. We also note that for a low β magnetic medium ($c_{s0} \ll v_{A0}$) one may apply the "cold" plasma ($c_{s0} = 0$) approximation to the fast surface mode.

Chapter 5

In Chapter 5 we consider global oscillations of quiescent prominences. In a uniform slab model of the prominence-coronal inhomogeneity threaded by a line-tied magnetic field, it is found that there exist modes which are analogous to the oscillation modes of a stretched elastic string of non-uniform density with its ends tied. These modes are called *string modes* and have periods τ given approximately by the formula $\tau = 2\pi(al)^{1/2}/c_p$, where c_p is the propagation speed characterising the mode, $2a$ is the width of the prominence sheet threaded by a magnetic field anchored in the photosphere at a distance l to either side

of the prominence sheet. The given formula is not only consistent the most commonly observed period range of prominence oscillations, but also agrees well with the numerical results of models based on more complex equilibrium configurations.

This leads us to investigate the applicability of the results from the uniform slab calculation to more realistic profiles of the prominence-coronal inhomogeneity, considering the robustness of the given formula as a description of the period of the string mode, for various density profiles. It is found that the uniform slab case does indeed have relevance to other density profiles, and the global oscillation periods are principally determined by the average conditions within the prominence.

6.2 Suggestions for further work

Effects of steady flows on MHD waves in structured plasmas

The approaches used in our investigation of the incompressible case could be usefully applied to other parameter regimes, and a useful starting point could be the cold plasma ($c_s = 0$) extreme typical of the corona. Our analysis could also be extended to include the case of non-parallel magnetic field, flow and propagation direction.

In any given case, consideration of the evolution of the solutions and their propagation windows as the relative flow increases provides a means of not only understanding the likely modes for a given solar situation, but also of gaining insight into the conditions leading to the onset of instability, which is of general interest. The propagation window evolution ought to be useful not only in determining the possible locations of stable solutions but also in discussing their qualitative evolution with increasing flow. A complete treatment must consider in full the effects of dispersion and density inhomogeneity.

Applicability of the incompressible case to compressible surface modes

For surface modes, the analysis simplifies dramatically for the incompressible case, hence it is sensible to use the incompressible approximations in situations in which it may be applied. Results from Chapter 4 suggest that the applicability of the incompressible case is not restricted to the case of both sound speeds c_{s0} and c_{se} greatly exceeding both Alfvén

speeds v_{A0} and v_{Ae}; further, in situations in which both the fast and the slow modes exist, the incompressible approximation may yield reasonable results for the fast mode.

This work could be extended to the dispersive modes of the isolated slab or tube ($v_{Ae} = 0$), or current sheet or tube ($v_{A0} = 0$), where it would be of interest to determine if the applicability of the incompressible case depends on the wavelength of the mode. Further studies such as these may help shed additional light on the issue of the relevance of the incompressible case to compressible surface modes.

Prominence oscillations

We analysed only certain density profiles; an obvious next stage is to consider an arbitrary function $g(x)$ in the density profile (5.22), for which we suggest the Rayleigh-Ritz method (Scarborough 1955, for example) be employed.

Another possibility to consider is the case of a skewed magnetic field with nonuniform density profiles. While this case is more complicated due to the coupling between the magnetoacoustic modes, we expect similar results to those found in Chapter 5 with appropriate expressions for c_p given for each mode type in Section 5.1.2. That is, the results of the uniform slab model with skewed magnetic field (Joarder and Roberts 1993b), may similarly have relevance to the global oscillations of more complicated configurations with non-transverse magnetic field.

We expect the results presented here to be of use when considering more sophisticated models for wave propagation in various solar and coronal structures. Such models can be tested against the exciting new data obtained from satellites such as SOHO, YOHKOH and TRACE, in observations of not only the oscillation periods of a given prominence, but also its physical properties.

6.3 Concluding remarks

We have investigated MHD wave propagation in a variety of simple models relevant to solar atmospheric structures. Despite their simplicity, these models (particularly the case of incompressible surface modes with flow) have yielded solutions rich in structure, which we have been able to extract by means of generalised approaches applicable to a range of cases under consideration. Such approaches have also provided a framework on which to base future studies, and our results give further support for the use of simple models to describe the basic physics of MHD wave propagation in structured plasmas.

Appendix: Derivations of linearised ideal MHD equations

A.1 Introduction

In this Appendix we give the linearisation of the ideal MHD equations in the general perturbed state, together with reductions for a stationary state with uniform flow and for a static equilibrium. The linearised MHD equations may be combined into a single governing vector partial differential equation, and this process is carried out for specific configurations relevant to the models in this thesis.

In our study of the effects of field-aligned steady flows, we take discretely structured media, with the structuring transverse to both the magnetic field and the steady flow in the unperturbed state. We use both cartesian and cylindrical geometry, with the magnetic field in the z-direction, and use the equations for a uniform stationary state. The linearised MHD equations for this case are combined into a single vector partial differential equation applicable to both geometries. Then, for cartesian and cylindrical geometries separately, we Fourier analyse perturbations in all directions except the direction of structuring. The variation in the direction of structuring gives the wave amplitude. The components of the partial differential equation are then combined into a single ordinary differential equation in the amplitude of the total pressure perturbation, with the other perturbation amplitudes expressed in terms of this quantity. The ordinary differential equation is used in the text to derive the dispersion relations.

A.2 Linearisation of ideal MHD equations for general case

For convenience, we here restate the ideal MHD equations (1.14)–(1.18) used:

$$\frac{D\rho}{Dt} = -\rho\nabla\cdot\mathbf{v} \tag{A.1}$$

$$\frac{Dp}{Dt} = -\frac{\gamma p}{\rho}(\rho\nabla\cdot\mathbf{v}) \tag{A.2}$$

$$\frac{D\mathbf{B}}{Dt} = -\mathbf{B}(\nabla\cdot\mathbf{v}) + (\mathbf{B}\cdot\nabla)\mathbf{v} \tag{A.3}$$

$$\rho\frac{D\mathbf{v}}{Dt} = -\nabla\left(p+\frac{B^2}{2\mu}\right) + (\mathbf{B}\cdot\nabla)\frac{\mathbf{B}}{\mu} + \rho\mathbf{g} \tag{A.4}$$

together with

$$\nabla\cdot\mathbf{B} = 0. \tag{A.5}$$

A.2.1 Ideal MHD equations describing general stationary state

First consider the ideal MHD equations as applied to describing a plasma in its unperturbed state. We will consider the most general case so that more specific cases may derived from it. In particular we will consider the case of a static equilibrium (no flow) and a stationary state with uniform flow.

General case

The stationary ($\partial/\partial t = 0$) state is given by

$$\rho = \rho_0(\mathbf{r}), \quad p = p_0(\mathbf{r}), \quad T = T_0(\mathbf{r}), \quad \mathbf{B} = \mathbf{B}_0(\mathbf{r}), \quad \mathbf{v} = \mathbf{v}_0(\mathbf{r}). \tag{A.6}$$

Then with all time derivatives zero the ideal MHD equations (A.1)–(A.4) become

$$(\mathbf{v}_0\cdot\nabla)\rho_0 = -\rho_0\nabla\cdot\mathbf{v}_0 \tag{A.7}$$

$$(\mathbf{v}_0\cdot\nabla)p_0 = -c_s^2\rho_0\nabla\cdot\mathbf{v}_0 \tag{A.8}$$

$$(\mathbf{v}_0\cdot\nabla)\mathbf{B}_0 = -\mathbf{B}_0(\nabla\cdot\mathbf{v}_0) + (\mathbf{B}_0\cdot\nabla)\mathbf{v}_0 \tag{A.9}$$

$$\rho_0(\mathbf{v}_0\cdot\nabla)\mathbf{v}_0 = -\nabla\left(p_0+\frac{B_0^2}{2\mu}\right) + (\mathbf{B}_0\cdot\nabla)\frac{\mathbf{B}_0}{\mu} + \rho_0\mathbf{g} \tag{A.10}$$

where $c_s = (\gamma p_0/\rho_0)^{1/2}$ is the speed of sound in the unperturbed state. These equations, together with (A.5) may be used to describe an arbitrary stationary state (A.6), in any orthogonal coordinate system.

Reductions for uniform flow and for static equilibirum

For the case of a uniform flow $\mathbf{v}_0$ (of arbitrary direction) equations (A.7)–(A.9) reduce to

$$(\mathbf{v}_0 \cdot \nabla)\,\rho_0 = (\mathbf{v}_0 \cdot \nabla)\,p_0 = (\mathbf{v}_0 \cdot \nabla)\,\mathbf{B}_0 = 0. \tag{A.11}$$

Then ρ_0, p_0 and $\mathbf{B}_0$ must be either invariant in the direction of the flow, or uniform. Equation (A.10) yields

$$0 = -\nabla\left(p_0 + \frac{B_0^2}{2\mu}\right) + (\mathbf{B}_0 \cdot \nabla)\,\frac{\mathbf{B}_0}{\mu} + \rho_0 \mathbf{g} \tag{A.12}$$

and corresponds to force balance. Equation (A.5) must also be satisfied.

For the static ($\mathbf{v}_0 = 0$) case, (A.7)–(A.9) are trivially satisfied.

A.2.2 Linearised ideal MHD equations describing general perturbed state

Now consider small perturbations about the general stationary state (A.6). The general perturbed state is

$$\left.\begin{aligned} \rho = \rho_0(\mathbf{r}) + \rho_1(\mathbf{r},t), \qquad p = p_0(\mathbf{r}) + p_1(\mathbf{r},t), \qquad T = T_0(\mathbf{r}) + T_1(\mathbf{r},t), \\ \mathbf{B} = \mathbf{B}_0(\mathbf{r}) + \mathbf{B}_1(\mathbf{r},t), \qquad \mathbf{v} = \mathbf{v}_0(\mathbf{r}) + \mathbf{v}_1(\mathbf{r},t) \end{aligned}\right\} \tag{A.13}$$

where the subscript 1 denotes the arbitrary perturbations about the state (A.6).

General case

We substitute the perturbed state (A.13) into the ideal MHD equations (A.1)–(A.4). Then, on linearising the equations by neglecting products of perturbation quantities, and on setting time derivatives of unperturbed quantities equal to zero, we obtain

$$\frac{\partial \rho_1}{\partial t} = -(\rho_0 + \rho_1)\,(\nabla\cdot\mathbf{v}_0) - \rho_0\,(\nabla\cdot\mathbf{v}_1) - (\mathbf{v}_0 \cdot \nabla)\,(\rho_0 + \rho_1) - (\mathbf{v}_1 \cdot \nabla)\,\rho_0 \tag{A.14}$$

$$\frac{\partial p_1}{\partial t} = -c_s^2\,(\rho_0 + \rho_1)\,\nabla\cdot\mathbf{v}_0 - c_s^2\rho_0\nabla\cdot\mathbf{v}_1 - (\mathbf{v}_0 \cdot \nabla)\,(p_0 + p_1) - (\mathbf{v}_1 \cdot \nabla)\,p_0 \tag{A.15}$$

$$\begin{aligned} \frac{\partial \mathbf{B}_1}{\partial t} = {} & -(\mathbf{B}_0 + \mathbf{B}_1)\,(\nabla\cdot\mathbf{v}_0) - \mathbf{B}_0\,(\nabla\cdot\mathbf{v}_1) - (\mathbf{v}_0 \cdot \nabla)\,(\mathbf{B}_0 + \mathbf{B}_1) - (\mathbf{v}_1 \cdot \nabla)\,\mathbf{B}_0 \\ & + (\mathbf{B}_0 \cdot \nabla)\,(\mathbf{v}_0 + \mathbf{v}_1) + (\mathbf{B}_1 \cdot \nabla)\,\mathbf{v}_0 \end{aligned} \tag{A.16}$$

$$\begin{aligned} \rho_0\frac{\partial \mathbf{v}_1}{\partial t} = {} & -\nabla\,(p_0 + p_1) - \nabla\left(\frac{B_0^2}{2\mu} + \frac{\mathbf{B}_0 \cdot \mathbf{B}_1}{\mu}\right) + (\mathbf{B}_0 \cdot \nabla)\,\frac{(\mathbf{B}_0 + \mathbf{B}_1)}{\mu} + (\mathbf{B}_1 \cdot \nabla)\,\frac{\mathbf{B}_0}{\mu} \\ & + (\rho_0 + \rho_1)\,\mathbf{g} - \rho_0\,(\mathbf{v}_0 \cdot \nabla)\,(\mathbf{v}_0 + \mathbf{v}_1) - \rho_0\,(\mathbf{v}_1 \cdot \nabla)\,\mathbf{v}_0 - \rho_1\,(\mathbf{v}_0 \cdot \nabla)\,\mathbf{v}_0. \end{aligned} \tag{A.17}$$

On using the general stationary state conditions (A.7)–(A.10), the linearised equations (A.14)–(A.17) reduce to

$$\frac{\partial \rho_1}{\partial t} = -\rho_1 (\nabla \cdot \mathbf{v}_0) - \rho_0 (\nabla \cdot \mathbf{v}_1) - (\mathbf{v}_0 \cdot \nabla) \rho_1 - (\mathbf{v}_1 \cdot \nabla) \rho_0 \tag{A.18}$$

$$\frac{\partial p_1}{\partial t} = -c_s^2 \rho_1 (\nabla \cdot \mathbf{v}_0) - c_s^2 \rho_0 (\nabla \cdot \mathbf{v}_1) - (\mathbf{v}_0 \cdot \nabla) p_1 - (\mathbf{v}_1 \cdot \nabla) p_0 \tag{A.19}$$

$$\frac{\partial \mathbf{B}_1}{\partial t} = -\mathbf{B}_1 (\nabla \cdot \mathbf{v}_0) - \mathbf{B}_0 (\nabla \cdot \mathbf{v}_1) - (\mathbf{v}_0 \cdot \nabla) \mathbf{B}_1 - (\mathbf{v}_1 \cdot \nabla) \mathbf{B}_0 + (\mathbf{B}_1 \cdot \nabla) \mathbf{v}_0 + (\mathbf{B}_0 \cdot \nabla) \mathbf{v}_1 \tag{A.20}$$

$$\rho_0 \frac{\partial \mathbf{v}_1}{\partial t} = -\nabla p_T + (\mathbf{B}_0 \cdot \nabla) \frac{\mathbf{B}_1}{\mu} + (\mathbf{B}_1 \cdot \nabla) \frac{\mathbf{B}_0}{\mu} + \rho_1 \mathbf{g} - \rho_0 (\mathbf{v}_0 \cdot \nabla) \mathbf{v}_1 - \rho_0 (\mathbf{v}_1 \cdot \nabla) \mathbf{v}_0 - \rho_1 (\mathbf{v}_0 \cdot \nabla) \mathbf{v}_0 \tag{A.21}$$

where we have introduced the total pressure perturbation p_T given by

$$p_T = p_1 + \frac{\mathbf{B}_0 \cdot \mathbf{B}_1}{\mu}. \tag{A.22}$$

Equations (A.18)–(A.21) are the *linearised ideal MHD equations in their most general form*, and apply, together with (1.18), to the most general case (1.23) of small perturbations about a stationary state, in any orthogonal coordinate system.

The set of linearised MHD equations appropriate to all cases considered in the text are obtained from (A.18)–(A.21), with (A.5).

Reductions for uniform flow and for static equilibrium

For the case of uniform flow we may also set to zero all spatial derivatives of $\mathbf{v}_0$. Then the general linearised MHD equations (A.18)–(A.21) further reduce to give

$$\frac{\partial \rho_1}{\partial t} = -\rho_0 (\nabla \cdot \mathbf{v}_1) - (\mathbf{v}_0 \cdot \nabla) \rho_1 - (\mathbf{v}_1 \cdot \nabla) \rho_0 \tag{A.23}$$

$$\frac{\partial p_1}{\partial t} = -c_s^2 \rho_0 (\nabla \cdot \mathbf{v}_1) - (\mathbf{v}_0 \cdot \nabla) p_1 - (\mathbf{v}_1 \cdot \nabla) p_0 \tag{A.24}$$

$$\frac{\partial \mathbf{B}_1}{\partial t} = -\mathbf{B}_0 (\nabla \cdot \mathbf{v}_1) - (\mathbf{v}_0 \cdot \nabla) \mathbf{B}_1 - (\mathbf{v}_1 \cdot \nabla) \mathbf{B}_0 + (\mathbf{B}_0 \cdot \nabla) \mathbf{v}_1 \tag{A.25}$$

$$\rho_0 \frac{\partial \mathbf{v}_1}{\partial t} = -\nabla p_T + (\mathbf{B}_0 \cdot \nabla) \frac{\mathbf{B}_1}{\mu} + (\mathbf{B}_1 \cdot \nabla) \frac{\mathbf{B}_0}{\mu} + \rho_1 \mathbf{g} - \rho_0 (\mathbf{v}_0 \cdot \nabla) \mathbf{v}_1. \tag{A.26}$$

For the static case set $\mathbf{v}_0 = 0$ in equations (A.23)–(A.26).

A.3 Treatment for uniform stationary state

We now consider the linearised ideal MHD equations in more detail for the case of a uniform stationary state, with a view to applying them to media which are discretely structured in a direction transverse to the magnetic field, with field-aligned steady flow.

A.3.1 Equations for arbitrary coordinate system

Consider a uniform equilibrium state given by

$$\rho_0 = const, \quad p_0 = const, \quad \mathbf{B}_0 = const, \quad \mathbf{v}_0 = const \tag{A.27}$$

with gravity ignored ($\mathbf{g} = 0$). Then the equilibrium equations (A.7)–(A.10) are trivially satisfied.

Now consider the perturbed state

$$\rho = \rho_0 + \rho_1(\mathbf{r}, t) \tag{A.28}$$

$$p = p_0 + p_1(\mathbf{r}, t) \tag{A.29}$$

$$\mathbf{B} = \mathbf{B}_0 + \mathbf{B}_1(\mathbf{r}, t) \tag{A.30}$$

$$\mathbf{v} = \mathbf{v}_0 + \mathbf{v}_1(\mathbf{r}, t). \tag{A.31}$$

Using the equations for the case of uniform flow, the linearised MHD equations (A.23)-(A.26) reduce for a uniform equilibrium to

$$\left(\frac{\partial}{\partial t} + \mathbf{v}_0 \cdot \nabla\right) \rho_1 = -\rho_0 \left(\nabla \cdot \mathbf{v}_1\right) \tag{A.32}$$

$$\left(\frac{\partial}{\partial t} + \mathbf{v}_0 \cdot \nabla\right) p_1 = -c_s^2 \rho_0 \left(\nabla \cdot \mathbf{v}_1\right) \tag{A.33}$$

$$\left(\frac{\partial}{\partial t} + \mathbf{v}_0 \cdot \nabla\right) \mathbf{B}_1 = -\mathbf{B}_0 \left(\nabla \cdot \mathbf{v}_1\right) + \left(\mathbf{B}_0 \cdot \nabla\right) \mathbf{v}_1 \tag{A.34}$$

$$\rho_0 \left(\frac{\partial}{\partial t} + \mathbf{v}_0 \cdot \nabla\right) \mathbf{v}_1 = -\nabla p_T + \left(\mathbf{B}_0 \cdot \nabla\right) \frac{\mathbf{B}_1}{\mu} \tag{A.35}$$

where we again note

$$p_T = p_1 + \frac{\mathbf{B}_0 \cdot \mathbf{B}_1}{\mu}. \tag{A.36}$$

A.3.2 Equations for cartesian and cylindrical coordinate systems with $\mathbf{v}_0$ and $\mathbf{B}_0$ in z-direction

The linearised MHD equations in the form (A.32)–(A.36) apply to any coordinate system, and the unperturbed velocity $\mathbf{v}_0$ and magnetic field $\mathbf{B}_0$ may have up to 3 components, all of which are constants.

We now restrict attention to cartesian and cylindrical geometry, and consider the case

$$\mathbf{v}_0 = v_0\hat{\mathbf{z}}, \qquad \mathbf{B}_0 = B_0\hat{\mathbf{z}}. \tag{A.37}$$

Then, for both cartesian and cylindrical geometries,

$$(\mathbf{v}_0 \cdot \nabla)(\alpha\mathbf{A}) = \alpha v_0 \frac{\partial \mathbf{A}}{\partial z} \tag{A.38}$$

$$(\mathbf{v}_0 \cdot \nabla)(\nabla\alpha) = \nabla\left((\mathbf{v}_0 \cdot \nabla)\,\alpha\right) \tag{A.39}$$

$$(\mathbf{v}_0 \cdot \nabla)\left[(\mathbf{B}_0 \cdot \nabla)\mathbf{A}\right] = (\mathbf{B}_0 \cdot \nabla)\left[(\mathbf{v}_0 \cdot \nabla)\mathbf{A}\right] \tag{A.40}$$

for any scalar α and vector $\mathbf{A}$. Then taking $(\partial/\partial t + \mathbf{v}_0 \cdot \nabla)$ of Equation (A.35) we obtain

$$\rho_0\left(\frac{\partial}{\partial t} + \mathbf{v}_0 \cdot \nabla\right)^2 \mathbf{v}_1 = -\nabla\left(\frac{\partial}{\partial t} + \mathbf{v}_0 \cdot \nabla\right) p_T + \frac{B_0}{\mu}\frac{\partial}{\partial z}\left(\frac{\partial}{\partial t} + \mathbf{v}_0 \cdot \nabla\right)\mathbf{B}_1, \tag{A.41}$$

which reduces, on using the linearised MHD equations in the form (A.32)–(A.35), to

$$\rho_0\left[\left(\frac{\partial}{\partial t} + \mathbf{v}_0 \cdot \nabla\right)^2 - {v_A}^2\frac{\partial^2}{\partial t^2}\right]\mathbf{v}_1 = -\nabla\left(\frac{\partial}{\partial t} + \mathbf{v}_0 \cdot \nabla\right) p_T - \rho_0 {v_A}^2 \frac{\partial \Delta}{\partial z}\hat{\mathbf{z}} \tag{A.42}$$

where

$$\left(\frac{\partial}{\partial t} + \mathbf{v}_0 \cdot \nabla\right) p_T = -\rho_0\left[({c_s}^2 + {v_A}^2)\Delta - {v_A}^2\Gamma\right]. \tag{A.43}$$

Note that

$$\mathbf{v}_0 \cdot \nabla \equiv v_0\frac{\partial}{\partial z}, \tag{A.44}$$

and we have have introduced (Lighthill 1960)

$$\Delta = \nabla\cdot\mathbf{v}_1, \qquad \Gamma = \frac{\partial v_z}{\partial z}; \tag{A.45}$$

v_z is the z-component of the perturbed velocity $\mathbf{v}_1$, and ${v_A}^2 = {B_0}^2/\mu\rho_0$ is the square of the Alfvén speed v_A.

A.3.3 Ordinary differential equation for cartesian geometry

In cartesian coordinates (x, y, z) we have

$$\mathbf{v}_1 = v_x\hat{\mathbf{x}} + v_y\hat{\mathbf{y}} + v_z\hat{\mathbf{z}} \tag{A.46}$$

$$\mathbf{B}_1 = B_x\hat{\mathbf{x}} + B_y\hat{\mathbf{y}} + B_z\hat{\mathbf{z}} \tag{A.47}$$

and the components of (A.42) are (using (A.43) for the z-component)

$$\rho_0\left[\left(\frac{\partial}{\partial t} + v_0\frac{\partial}{\partial z}\right)^2 - v_A^2\frac{\partial^2}{\partial z^2}\right]v_x = -\left(\frac{\partial}{\partial t} + v_0\frac{\partial}{\partial z}\right)\frac{\partial p_T}{\partial x} \tag{A.48}$$

$$\rho_0\left[\left(\frac{\partial}{\partial t} + v_0\frac{\partial}{\partial z}\right)^2 - v_A^2\frac{\partial^2}{\partial z^2}\right]v_y = -\left(\frac{\partial}{\partial t} + v_0\frac{\partial}{\partial z}\right)\frac{\partial p_T}{\partial x} \tag{A.49}$$

$$\rho_0\left(\frac{\partial}{\partial t} + v_0\frac{\partial}{\partial z}\right)^2 v_z = c_s^2\frac{\partial\Delta}{\partial z}. \tag{A.50}$$

These equations are applied in Chapter 2 to media which are discretely structured in the x-direction (that is, transverse to the unperturbed magnetic field). We Fourier analyze perturbations ψ in all variables except x, writing

$$\psi = \hat{\psi}(x)e^{i(\omega t - ly - kz)}. \tag{A.51}$$

Then equations (A.48)–(A.50) yield

$$\rho_0\left(k^2v_A^2 - \Omega^2\right)\hat{v}_x = -i\Omega\frac{d\hat{p}_T}{dx} \tag{A.52}$$

$$\rho_0\left(k^2v_A^2 - \Omega^2\right)\hat{v}_y = -\Omega l\hat{p}_T \tag{A.53}$$

$$\hat{v}_z = \frac{ikc_s^2}{\Omega^2}\hat{\Delta} \tag{A.54}$$

where

$$i\Omega\hat{p}_T = -\rho_0\left[({c_s}^2 + {v_A}^2)\hat{\Delta} - {v_A}^2\hat{\Gamma}\right] \tag{A.55}$$

$$\hat{\Delta} = \frac{d\hat{v}_x}{dx} - il\hat{v}_y + \hat{\Gamma} \tag{A.56}$$

$$\hat{\Gamma} = -ik\hat{v}_z \tag{A.57}$$

and we have defined

$$\Omega = \omega - v_0k \tag{A.58}$$

as the Doppler shifted frequency.

From (A.56), (A.57) and (A.54) we may write

$$\frac{d\hat{v}_x}{dx} - il\hat{v}_y = \hat{\Delta} - \hat{\Gamma} = \frac{(\Omega^2 - k^2 {c_s}^2)}{\Omega^2}\hat{\Delta} \tag{A.59}$$

while from (A.55) $\hat{p}_T$ may be written in terms of $\hat{\Delta}$ as

$$i\Omega\hat{p}_T = -\frac{\rho_0}{\Omega^2}({c_s}^2 + {v_A}^2)(\Omega^2 - k^2 {c_T}^2)\hat{\Delta} \tag{A.60}$$

where ${c_T}^2 = {c_s}^2{v_A}^2/({c_s}^2 + {v_A}^2)$ is the square of the tube speed c_T.

We may combine equations (A.48), (A.49), (A.59) and (A.60) to yield a single ordinary differential equation in $\hat{p}_T$ as follows. From (A.48), (A.49) we have

$$\frac{\rho_0(k^2{v_A}^2 - \Omega^2)}{-i\Omega}\left(\frac{d\hat{v}_x}{dx} - il\hat{v}_y\right) = \frac{d^2\hat{p}_T}{dx^2} - l^2\hat{p}_T. \tag{A.61}$$

Using (A.59) followed by (A.60) the left-handside of (A.61) may be written in terms of $\hat{p}_T$ as

$$\frac{\rho_0(k^2{v_A}^2 - \Omega^2)}{-i\Omega}\left(\frac{d\hat{v}_x}{dx} - il\hat{v}_y\right) = \frac{(k^2{v_A}^2 - \Omega^2)(\Omega^2 - k^2{c_s}^2)}{({c_s}^2 + {v_A}^2)(\Omega^2 - k^2{c_T}^2)}\hat{p}_T. \tag{A.62}$$

Then (A.61) and (A.62) combine to yield

$$\frac{d^2\hat{p}_T}{dx^2} - (m^2 + l^2)\hat{p}_T = 0 \tag{A.63}$$

where

$$m^2 = \frac{(k^2{v_A}^2 - \Omega^2)(\Omega^2 - k^2{c_s}^2)}{({c_s}^2 + {v_A}^2)(\Omega^2 - k^2{c_T}^2)}. \tag{A.64}$$

Equation (A.63) is our required ordinary differential equation in $\hat{p}_T$. It is used in Section 2.2.3 in the determination of the dispersion relations for the single interface and uniform slab.

We note that equations (A.48), (A.49), (A.59) and (A.60) can alternatively be used, by a similar prcedure, to show that equation (A.63) is also satisfied by $\hat{\Delta}$.

Expression of the other perturbation amplitudes in terms of $\hat{p}_T$

With the other perturbation quantities expressed in the Fourier form (A.51), their amplitudes $\hat{\psi}$ may be written in terms of $\hat{p}_T$ as follows.

Using equations (A.52)-(A.54) and (A.60) we may obtain

$$\hat{\Delta} = \frac{-i\Omega^3}{\rho_0({c_s}^2+{v_A}^2)(\Omega^2-k^2{c_T}^2)}\hat{p}_T \tag{A.65}$$

$$\hat{v}_x = \frac{-i\Omega}{\rho_0(k^2{v_A}^2-\Omega^2)}\frac{d\hat{p}_T}{dx} \tag{A.66}$$

$$\hat{v}_y = \frac{-\Omega l}{\rho_0(k^2{v_A}^2-\Omega^2)}\hat{p}_T \tag{A.67}$$

$$\hat{v}_z = \frac{-ik{c_s}^2}{\Omega^2}\hat{\Delta} = \frac{-k\Omega{c_s}^2}{\rho_0({c_s}^2+{v_A}^2)(\Omega^2-k^2{c_T}^2)}\hat{p}_T. \tag{A.68}$$

Meanwhile, the Fourier forms of the linearised MHD equations (A.32)-(A.34) yield

$$\hat{p}_1 = \frac{i\rho_0}{\Omega}\hat{\Delta} = \frac{\Omega^2}{({c_s}^2+{v_A}^2)(\Omega^2-k^2{c_T}^2)}\hat{p}_T \tag{A.69}$$

$$\hat{p}_1 = {c_s}^2\rho_1 = \frac{{c_s}^2\Omega^2}{({c_s}^2+{v_A}^2)(\Omega^2-k^2{c_T}^2)}\hat{p}_T \tag{A.70}$$

$$\hat{B}_x = \frac{-kB_0}{\Omega}\hat{v}_x = \frac{-ikB_0}{\rho_0(k^2{v_A}^2-\Omega^2)}\frac{d\hat{p}_T}{dx} \tag{A.71}$$

$$\hat{B}_y = \frac{-kB_0}{\Omega}\hat{v}_y = \frac{klB_0}{\rho_0(k^2{v_A}^2-\Omega^2)}\hat{p}_T \tag{A.72}$$

$$\hat{B}_z = \frac{iB_0}{\Omega}(\hat{\Delta}-\hat{\Gamma}) = \frac{(\Omega^2-k^2{c_s}^2)B_0}{\rho_0({c_s}^2+{v_A}^2)(\Omega^2-k^2{c_T}^2)}\hat{p}_T. \tag{A.73}$$

A.3.4 Ordinary differential equation for cylindrical geometry

In cylindrical coordinates (r,θ,z) we have

$$\mathbf{v_1} = v_r\hat{\mathbf{r}} + v_\theta\hat{\theta} + v_z\hat{\mathbf{z}} \tag{A.74}$$

$$\mathbf{B_1} = B_r\hat{\mathbf{r}} + B_\theta\hat{\theta} + B_z\hat{\mathbf{z}} \tag{A.75}$$

and the components of (A.42) are (using (A.43) for the z-component)

$$\rho_0\left[\left(\frac{\partial}{\partial t}+v_0\frac{\partial}{\partial z}\right)^2 - v_A^2\frac{\partial^2}{\partial z^2}\right]v_r = -\left(\frac{\partial}{\partial t}+v_0\frac{\partial}{\partial z}\right)\frac{\partial p_T}{\partial r} \tag{A.76}$$

$$\rho_0\left[\left(\frac{\partial}{\partial t}+v_0\frac{\partial}{\partial z}\right)^2 - v_A^2\frac{\partial^2}{\partial z^2}\right]v_\theta = -\frac{1}{r}\left(\frac{\partial}{\partial t}+v_0\frac{\partial}{\partial z}\right)\frac{\partial p_T}{\partial \theta} \tag{A.77}$$

$$\rho_0\left(\frac{\partial}{\partial t}+v_0\frac{\partial}{\partial z}\right)^2 v_z = c_s^2\frac{\partial\Delta}{\partial z}. \tag{A.78}$$

These equations are applied in Chapter 2 to media which are discretely structured in the r-direction (that is, transverse to the unperturbed magnetic field). We Fourier analyze

perturbations ψ in all variables except r, writing

$$\psi = \hat{\psi}(r)e^{i(\omega t - n\theta - kz)}. \tag{A.79}$$

Then equations (A.76)–(A.78) yield

$$\rho_0 \left(k^2 v_A^2 - \Omega^2\right) \hat{v}_r = -i\Omega \frac{d\hat{p}_T}{dr} \tag{A.80}$$

$$\rho_0 \left(k^2 v_A^2 - \Omega^2\right) \hat{v}_\theta = -\frac{\Omega n}{r} \hat{p}_T \tag{A.81}$$

$$\hat{v}_z = \frac{ikc_s^2}{\Omega^2} \hat{\Delta} \tag{A.82}$$

where

$$\hat{\Delta} = \frac{1}{r}\frac{d}{dr}(r\hat{v}_r) - \frac{in}{r}\hat{v}_\theta + \hat{\Gamma} \tag{A.83}$$

and $\hat{p}_T$, $\hat{\Gamma}$ and Ω are defined as for the cartesian case (by (A.55), (A.57) and (A.58) respectively).

We see that the cylindrical case is essentially similar to the cartesian case (for the configuration studied here), the difference being due to the θ-dependence and manifesting itself in the θ-component (A.81) and in the expression (A.83) for $\hat{\Delta}$. We therefore apply a similar approach to combining the components into a single ordinary differential equation in $\hat{p}_T$, to obtain

$$\frac{1}{r}\frac{d}{dr}\left(r\frac{d\hat{p}_T}{dr}\right) - \left(m^2 + \frac{n^2}{r^2}\right)\hat{p}_T = 0 \tag{A.84}$$

where again

$$m^2 = \frac{(k^2 {v_A}^2 - \Omega^2)(\Omega^2 - k^2 {c_s}^2)}{({c_s}^2 + {v_A}^2)(\Omega^2 - k^2 {c_T}^2)}. \tag{A.85}$$

Equation (A.84) may be rewritten as the Bessel equation

$$\frac{d^2\hat{p}_T}{dr^2} + \frac{1}{r}\frac{d\hat{p}_T}{dr} - \left(m^2 + \frac{n^2}{r^2}\right)\hat{p}_T = 0. \tag{A.86}$$

Equation (A.86) is our required ordinary differential equation in $\hat{p}_T$, and is used in Section 2.2.4 in the determination of the dispersion relations for the uniform cylinder. We can also show that equation (A.86) is satisfied by $\hat{\Delta}$.

Expression of the other perturbation amplitudes in terms of $\hat{p}_T$

With the other perturbation quantities expressed in the Fourier form (A.79), their amplitudes $\hat{\psi}$ may be written in terms of $\hat{p}_T$ by applying a similar approach to that used for the static case.

We find that the expressions for $\hat{\Delta}$, $\hat{v}_z$, $\hat{\rho}_1$, $\hat{p}_1$ and $\hat{B}_z$ in terms of $\hat{p}_T$ are the same as for the cartesian case, although the form of $\hat{p}_T$ will be different for each geometry. Meanwhile, the other perturbation amplitudes are given by

$$\hat{v}_r = \frac{-i\Omega}{\rho_0(k^2 {v_A}^2 - \Omega^2)} \frac{d\hat{p}_T}{dr} \tag{A.87}$$

$$\hat{v}_\theta = \frac{-\Omega n}{\rho_0(k^2 {v_A}^2 - \Omega^2)} \frac{\hat{p}_T}{r} \tag{A.88}$$

$$\hat{B}_r = \frac{-kB_0}{\Omega}\hat{v}_r = \frac{-ikB_0}{\rho_0(k^2 {v_A}^2 - \Omega^2)} \frac{d\hat{p}_T}{dr} \tag{A.89}$$

$$\hat{B}_\theta = \frac{-kB_0}{\Omega}\hat{v}_\theta = \frac{knB_0}{\rho_0(k^2 {v_A}^2 - \Omega^2)} \frac{\hat{p}_T}{r}. \tag{A.90}$$

The forms for $\hat{v}_r$ and $\hat{B}_r$ are identical to those for $\hat{v}_x$ and $\hat{B}_x$ for the cartesian case, and therefore the nature of the perturbations in the structured direction are essentially the same for each geometry. This is not the case for the perturbations in the other transverse direction, namely the y direction for the cartesian system and the θ direction for the cylindrical system.

Here we note that when $n = 0$ we have $\hat{v}_\theta = \hat{B}_\theta = 0$, giving no torsional fields. This may be compared with the cartesian case where for $l = 0$ we similarly obtain $\hat{v}_y = \hat{B}_y = 0$. There are similarities between the geometries for such cases. Meanwhile, for $n \geq 1$ both $\hat{v}_\theta$ and $\hat{B}_\theta$ have a $1/r$ dependence, leading to differences between the geometries.

Bibliography

Abdelatif, T. E.: 1988, *Astrophys. J.* **333**, 395.

Abramowitz, M. and Stegun, I. A.: 1965, *Handbook of Mathematical Functions*, Dover.

Antia, H. M. and Chitre, S. M. (eds): 1996, *Proceedings of the International Conference on "Windows on the Sun's Interior", October 19-21, 1995*, Vol. 24 of *Bull. Astr. Soc. India.*

Aschwanden, M. J.: 1987, *Solar Phys.* **111**, 113.

Axford, W. I.: 1960, *Quart. Journ. Mech. and Applied Math.* **13**, 314.

Ballester, J. L. and Priest, E. R. (eds): 1987, *Dynamics and Structure of Solar Prominences*, Universitat de les Illes Balears, Palma.

Balthasar, H., Knölker, M., Stellmacher, G. and Wiehr, E.: 1986, *Astron. Astrophys.* **163**, 343.

Balthasar, H., Stellmacher, G. and Wiehr, E.: 1988, *Astron. Astrophys.* **204**, 286.

Balthasar, H. and Wiehr, E.: 1994, *Astron. Astrophys.* **286**, 639.

Balthasar, H., Wiehr, E., Schleicher, H. and Wöhl, H.: 1993, *Astron. Astrophys.* **277**, 635.

Balthasar, H., Wiehr, E. and Stellmacher, G.: 1988, *in* J. L. Ballester and E. R. Priest (eds), *Dynamics and Structure of Solar Prominences*, Universitat de les Illes Balears, p. 63.

Bashkirtsev, V. S., Kobanov, N. I. and Mashnich, G. P.: 1983, *Solar Phys.* **82**, 443.

Bashkirtsev, V. S. and Mashnich, G. P.: 1984, *Solar Phys.* **91**, 93.

Bashkirtsev, V. S. and Mashnich, G. P.: 1993, *Astron. Astrophys.* **279**, 610.

Birkinshaw, M.: 1991, Chapter 6, *in* P. A. Hughes (ed.), *Beams and Jets in Astrophysics*, Cambridge University Press.

Blanco, S., Bocchialini, K., Costa, A., Domenech, G., Rovira, M. and Vial, J.-C.: 1998, *Solar Phys.* . Preprint.

Bodo, G., Massaglia, S., Ferrari, A. and Trussoni, E.: 1994, *Astron. Astrophys.* **283**, 655.

Bodo, G., Massaglia, S., Rossi, P., Rosner, R., Malagoli, A. and Ferrari, A.: 1995, *Astron. Astrophys.* **303**, 281.

Bodo, G., Rosner, R., Ferrari, A. and Knobloch, E.: 1989, *Astrophys. J.* **341**, 631.

Bodo, G., Rosner, R., Ferrari, A. and Knobloch, E.: 1996, *Astrophys. J.* **470**, 797.

Boyd, T. J. M. and Sanderson, J. J.: 1969, *Plasma Dynamics*, Nelson, London.

Cairns, R. A.: 1979, *J. Fluid Mech.* **92**, 1.

Campos, L. M. B. C.: 1987, *Rev. Mod. Phys.* **59**, 363.

Chakraborty, B. B.: 1968, *Prog. Theor. Phys.* **40**, 210.

Chandrasekhar, S.: 1961, *Hydrodynamic and Hydromagnetic Stability*, Clarendon Press, Oxford.

Christensen-Dalsgaard, J., Gough, D. O. and Toomre, J.: 1985, **229**, 923.

Coulson, C. A.: 1941, *Waves*, Oliver and Boyd, Edinburgh.

Cowling, T. G.: 1957, *Magnetohydrodynamics*, Interscience, New York.

Cowling, T. G.: 1976, *Magnetohydrodynamics*, 2nd edn, Adam Hilger, Bristol.

Craik, A. D. D. and Adam, J. A.: 1979, *J. Fluid Mech.* **92**, 15.

Cram, L. E. and Wilson, P. R.: 1975, *Solar Phys.* **41**, 313.

Cramer, N. F.: 1995, *Physica Scripta* **T60**, 185.

Csik, A., Erdélyi, R. and Cadez, V. M.: 1997, *Solar Phys.* **172**, 61.

Démoulin, P.: 1991, Solar prominences, Chapter 13, *in* E. R. Priest and A. W. Hood (eds), *Advances in Solar System Magnetohydrodynamics*, Cambridge University Press.

Deubner, F. L. and Gough, D. O.: 1984, *Ann. Rev. Astr. Astrophys.* **22**, 593.

Edwin, P. M.: 1984, PhD thesis, University of St Andrews.

Edwin, P. M.: 1991, *Ann. Geophysicae* **9**, 188.

Edwin, P. M.: 1992, *Ann. Geophysicae* **10**, 631.

Edwin, P. M. and Roberts, B.: 1982, *Solar Phys.* **76**, 239.

Edwin, P. M. and Roberts, B.: 1983, *Solar Phys.* **88**, 179.

Edwin, P. M. and Roberts, B.: 1988, *Astron. Astrophys.* **192**, 343.

Engvold, O.: 1981, *Solar Phys.* **70**, 315.

Epstein, P. S.: 1930, *Porc. Nat. Acad. Sci.* **16**, 627.

Erdélyi, R. and Goossens, M.: 1996, *Astron. Astrophys.* **313**, 664.

Evans, D. J. and Roberts, B.: 1990, *Astrophys. J.* **348**, 346.

Fejer, J. A.: 1963, *Phys. Fluids* **6**, 508.

Fejer, J. A.: 1964, *Phys. Fluids* **7**, 499.

Feldman, W. C., Philips, J. L., Barraclough, B. L. and Hammond, C. M.: 1996, ULYSSES observations of the solar wind out of the ecliptic plane, *in* K. C. Tsinganos (ed.), *Solar and Astrophysical Magnetohydrodynamic Flows.*

Ferrari, A., Trussoni, E. and Zaninetti, L.: 1980, *Mon. Not. R. Astr. Soc* **193**, 469.

Ferrari, A., Trussoni, E. and Zaninetti, L.: 1981, *Mon. Not. R. Astr. Soc* **196**, 1051.

Fleck, B.: 1997, *Rev. Mod. Astron.* **10**, 273.

Geronicolas, E. A.: 1977, *Astrophys. J.* **214**, 607.

Gerwin, R. A.: 1968, *Rev. Mod. Phys.* **40**, 652.

Gheonjian, L. A., Klepikov, V. Y. and Stepanov, A. I.: 1990, *Academy of Sciences of the USSR* . Preprint No 4.

Gill, A. E.: 1965, *Phys. Fluids* **8**, 1428.

Goedbloed, J. P.: 1979, *Lecture Notes on Ideal Magnetohydrodynamics*, Rijnhuizen Report 83-145.

Goossens, M.: 1991, MHD waves and heating, Chapter 7, *in* E. R. Priest and A. W. Hood (eds), *Advances in Solar System Magnetohydrodynamics*, Cambridge University Press.

Goossens, M., Hollweg, J. V. and Sakurai, T.: 1992, *Solar Phys.* **138**, 233.

Goossens, M. and Ruderman, M.: 1996, MHD waves in magnetic flux tubes, *in* K. C. Tsinganos (ed.), *Solar and Astrophysical Magnetohydrodynamic Flows.*

Hardee, P. E.: 1995, *in* J. H. Hunter and R. E. Wilson (eds), *Waves in Astrophysics*, Vol. 773 of *Annals of the New York Academy of Sciences*, p. 14.

Hardee, P. E., Clarke, D. A. and Rosen, A.: 1997, *Astrophys. J.* **485**, 533.

Hardee, P. E., Cooper, M. A., Norman, M. L. and Stone, J. M.: 1992, *Astrophys. J.* **399**, 478.

Heyvaerts, J. and Priest, E. R.: 1983, Coronal heating by phase-mixed shear Alfvén waves, *Astron. Astrophys.* **117**, 220.

Hollweg, J. V.: 1987, *Astrophys. J.* **317**, 918.

Hollweg, J. V.: 1990, *Comp. Phys. Rep.* **12**, 205.

Hollweg, J. V., Yang, G., Cadez, V. M. and Gakovic, B.: 1990, *Astrophys. J.* **349**, 335.

Hood, A. W. and Anzer, U.: 1990, *Solar Phys.* **126**, 117.

Hood, A. W. and Priest, E. R.: 1979, *Solar Phys.* **77**, 233.

Hyder, C. L.: 1966, *Z. Astrophys.* **63**, 78.

Jain, R. and Roberts, B.: 1991, *Solar Phys.* **133**, 263.

Jensen, E., Yi Zhang and Engvold, O.: 1994, *Solar Phys.* **149**, 209.

Joarder, P. S.: 1993, PhD thesis, University of St Andrews.

Joarder, P. S., Nakariakov, V. M. and Roberts, B.: 1997a, *Solar Phys.* **173**, 81.

Joarder, P. S., Nakariakov, V. M. and Roberts, B.: 1997b, *Solar Phys.* **176**, 285.

Joarder, P. S. and Roberts, B.: 1992a, *Astron. Astrophys.* **256**, 264.

Joarder, P. S. and Roberts, B.: 1992b, *Astron. Astrophys.* **261**, 625.

Joarder, P. S. and Roberts, B.: 1993a, *Astron. Astrophys.* **273**, 642.

Joarder, P. S. and Roberts, B.: 1993b, *Astron. Astrophys.* **277**, 225.

Kent, A.: 1968, *J. Plasma Phys.* **2**, 543.

Kippenhahn, R. and Schlüter, A.: 1957, *Z. Astrophys.* **43**, 36.

Kirtskhalia, V. G.: 1994, *Planet. Space Sci.* **42**, 513.

Kleczek, J. and Kuperus, M.: 1969, *Solar Phys.* **6**, 72.

Krall, N. A. and Trivelpiece, A. W.: 1973, *Principles of Plasma Physics*, McGraw-Hill, New York.

Kruskal, M. and Schwarzschild, M.: 1954, *Proc. Roy. Soc. (London)* **A223**, 348.

Kuperus, M. and Raadu, M. A.: 1974, *Astron. Astrophys.* **31**, 189.

Lamb, H.: 1910, *The dynamical theory of sound*, Arnold, London.

Landau, L. D. and Lifshitz, E. M.: 1960, *Electrodynamics of Continuous Media*, Vol. 8 of *Course of Theoretical Physics*, Pergamon Press. p. 227.

Lau, Y. Y. and Liu, C. S.: 1980, *Phys. Fluids* **23**, 939.

Lee, L. C., Wang, S., Wei, C. Q. and Tsurutani, B. T.: 1988, *J. Geophys. Res.* **93**, 7354.

Leibacher, J. W., Noyes, R. W., Toomre, J. and Ulrich, R. K.: 1985, *Scient. Amer.* **253**, 48.

Lighthill, M. J.: 1960, *Phil. Trans. Roy. Soc* **A252**, 397.

Low, B. C. and Wu, S. T.: 1981, *Astrophys. J.* **248**, 335.

Malherbe, J. M., Schmieder, B. and Mein, B.: 1981, *Astron. Astrophys.* **102**, 124.

Malherbe, J. M., Schmieder, B., Mein, B. and Tandberg-Hanssen, E.: 1987, *Astron. Astrophys.* **172**, 316.

Mann, G., Marsch, E. and Roberts, B.: 1992, *in* E. Marsch and R. Schwein (eds), *Solar Wind VII*, COSPAR, Pergamon Press, p. 495.

Mashnich, G. P. and Bashkirtsev, V. S.: 1990, *Astron. Astrophys.* **235**, 428.

Mashnich, G. P., Druzhinin, S. A., Pevtsov, A. A. and Levkovsky, V. I.: 1993, *Astron. Astrophys.* **269**, 503.

Menzel, D.: 1951, *in* P. L. Bhatnagar, M. Krook and D. Menzel (eds), *Proceedings Conference on Dynamics of Ionised Media*, London.

Miles, A. J. and Roberts, B.: 1989, *Solar Phys.* **119**, 257.

Miles, J. W.: 1958, *J. Fluid Mech.* **4**, 537.

Molowny-Horas, R., Oliver, R., Ballester, J. L. and Baudin, F.: 1997, *Solar Phys.* **171**, 181.

Mundie, C. and Roberts, B.: 1998. In preparation.

Nakariakov, V. M. and Roberts, B.: 1995a, *Solar Phys.* **159**, 213.

Nakariakov, V. M. and Roberts, B.: 1995b, *Solar Phys.* **159**, 399.

Nakariakov, V. M., Roberts, B. and Mann, G.: 1996, *Astron. Astrophys.* **311**, 311.

Nakariakov, V. M., Roberts, B. and Murawski, K.: 1998, *Astron. Astrophys.* **332**, 795.

Narain, U. and Ulmschneider, P.: 1990, Chromospheric and coronal heating mechansims, *Space Sci. Rev.* **54**, 377.

Oliver, R. and Ballester, J. L.: 1995, *Astrophys. J.* **448**, 444.

Oliver, R. and Ballester, J. L.: 1996, *Astrophys. J.* **456**, 393.

Oliver, R., Ballester, J. L., Hood, A. W. and Priest, E. R.: 1992, *Astrophys. J.* **400**, 369.

Oliver, R., Ballester, J. L., Hood, A. W. and Priest, E. R.: 1993, *Astrophys. J.* **409**, 809.

Parhi, S.: 1992, *Phys. Fluids B* **4**, 1589.

Parker, E. N.: 1964, *Astrophys. J.* **139**, 690.

Parker, E. N.: 1979a, *Astrophys. J.* **233**, 1005.

Parker, E. N.: 1979b, *Cosmical Magnetic Fields*, Oxford.

Poland, A. I.: 1986, Coronal and prominence plasmas, *NASA Conf. Publ.* **2442**.

Poland, A. I. and Anzer, U.: 1971, *Solar Phys.* **104**, 303.

Prialnik, D., Eviatar, A. and Ershkovich, A. I.: 1986, *J. Plamsa Physics* **35**, 209.

Priest, E. R.: 1982, *Solar Magnetohydrodynamics*, Vol. 21 of *Geophysics and Astrophysics Monographs*, Reidel, Dordrecht.

Priest, E. R.: 1995, The sun and its magnetohydrodynamics, *in* M. Kivelson and C. Russell (eds), *An Introduction to Space Physics*, Cambridge University Press.

Priest, E. R. (ed.): 1988, *Dynamics and Structure of Quiescent Solar Prominences*, Kluwer, Dordrecht.

Priest, E. R., Hood, A. W. and Anzer, U.: 1989, *Astrophys. J.* **344**, 1010.

Pu, Z.-Y. and Kivelson, M. G.: 1983, *J. Geophys. Res.* **88**, 841.

Raadu, M. A.: 1972, *Solar Phys.* **22**, 425.

Rae, I. C.: 1983, *Astron. Astrophys.* **126**, 209.

Rae, I. C. and Roberts, B.: 1981, *Geophys. Astrophys. Fluid Dyn.* **18**, 197.

Ramsey, H. E. and Smith, S. F.: 1966, *Astron. J.* **71**, 197.

Ray, T. P.: 1981, *Mon. Not. R. Astr. Soc* **196**, 195.

Ray, T. P. and Ershkovich, A. I.: 1983, *Mon. Not. R. Astr. Soc* **204**, 821.

Rayleigh, Lord: 1877, *The Theory of Sound*, Vol. 1, 1945 edn, Dover, New York. p. 205.

Roberts, B.: 1981a, *Solar Phys.* **69**, 27.

Roberts, B.: 1981b, *Solar Phys.* **69**, 39.

Roberts, B.: 1985, Magnetohydrodynamic waves, Chapter 3, *in* E. R. Priest (ed.), *Solar System Magnetic Fields*, Reidel, Dordrecht, p. 37.

Roberts, B.: 1987, *Astrophys. J.* **318**, 590.

Roberts, B.: 1988, Magnetohydrodynamic waves in stratified atmospheres, *in* L. Tanovic, N. Konjevic and N. Tanovic (eds), *The Physics of Ionized Gases*, Nova Science Publishers, New York.

Roberts, B.: 1990, Properties and models of photospheric flux tubes, *in* C. T. Russell, E. R. Priest and L. C. Lee (eds), *Physics of Magnetic Flux Ropes*, Vol. 58 of *Geophysical Monograph*, p. 113.

Roberts, B.: 1991a, *Geophys. Astrophys. Fluid Dyn.* **62**, 83.

Roberts, B.: 1991b, Magnetohydrodynamic waves on the sun, Chapter 6, *in* E. R. Priest and A. W. Hood (eds), *Advances in Solar System Magnetohydrodynamics*, Cambridge University Press.

Roberts, B.: 1992, Magnetohydrodynamic waves in structured magnetic fields, *in* J. H. Thomas and N. O. Weiss (eds), *Sunspots: Theory and Observations*, Kluwer, Netherlands, p. 303.

Roberts, B., Edwin, P. M. and Benz, A. O.: 1984, *Astrophys. J.* **279**, 857.

Roberts, B. and Joarder, P. S.: 1994, Oscillations in quiescent prominences, *Advances in Solar Physics.*

Roberts, B. and Ulmschneider, P.: 1997, Dynamics of flux tubes in the solar atmosphere: Theory, *in* G. M. Simnett, C. E. Alissandrakis and L. Vlahos (eds), *Solar and Heliospheric Physics*, Lecture Notes in Physics, Springer-Verlag, Berlin, p. 75.

Roberts, B. and Webb, A. R.: 1978, *Solar Phys.* **56**, 5.

Roberts, B. and Webb, A. R.: 1979, *Solar Phys.* **64**, 77.

Ropchan, C. B. and Swaters, G. E.: 1993, *Q. Jl. Mech. Appl. Math* **46**, 657.

Ruderman, M. S. and Goossens, M.: 1995, *J. Plasma Phys.* **54**, 149.

Ruzdjak, V. and Tandberg-Hanssen, E. (eds): 1989, *Dynamics of quiescent prominences*, I. A. U. Colloq. No 117, Hvar Obs. Bull. 13.

Ryutov, D. D. and Ryutova, M. P.: 1976, *Sov. Phys. J. E. T. P.* **43**, 491.

Ryutova, M. P.: 1988, *Sov. Phys. J. E. T. P.* **67**, 1594.

Satya Narayanan, A.: 1991, *Plasma Phys. Contr. Fusion* **33**, 333.

Satya Narayanan, A. and Somasundaram, K.: 1985, *Astrophys. Space Sci.* **109**, 357.

Scarborough, J. B.: 1955, *Numerical Mathematical Analysis*, 3rd edn, Oxford University Press. p. 341.

Schmieder, B.: 1988, *in* J. L. Ballester and E. R. Priest (eds), *Dynamics and Structure of Solar Prominences*, Universitat de les Illes Balears, p. 10.

Schmieder, B.: 1989, *in* E. R. Priest (ed.), *Dynamics of Quiescent Solar Prominences*, Kluwer, p. 37.

Schmieder, B.: 1997, Flows through the magnetically structured solar atmosphere, *Solar and Heliospheric Physics*, Lecture Notes in Physics, Springer-Verlag, Berlin, p. 139.

Sen, A. K.: 1963, *Phys. Fluids* **6**, 1154.

Sen, A. K.: 1964, *Phys. Fluids* **7**, 1293.

Singh, A. P. and Talwar, S. P.: 1993, *Solar Phys.* **148**, 27.

Singh, A. P. and Talwar, S. P.: 1994, *Solar Phys.* **149**, 331.

Solanki, S. K.: 1997, Dynamics of flux tubes in the solar atmosphere: Observations, *in* G. M. Simnett, C. E. Alissandrakis and L. Vlahos (eds), *Solar and Heliospheric Physics*, Lecture Notes in Physics, Springer-Verlag, Berlin, p. 49.

Somasundaram, K. and Satya Narayanan, A.: 1987, *Plasma Phys. Contr. Fusion* **29**, 497.

Somasundaram, K. and Uberoi, C.: 1982, *Solar Phys.* **81**, 19.

Spruit, H. C.: 1982, *Solar Phys.* **75**, 3.

Spruit, H. C. and Roberts, B.: 1983, *Nature* **304**, 401.

Suematsu, Y., Yoshinaga, R., Terao, N. and Tsubaki, T.: 1990, *Publ. Astron. Soc. Japan* **42**, 187.

Tandberg-Hanssen, E.: 1974, *Solar Prominences*, Reidel, Dordrecht.

Thompson, W. T. and Schmieder, B.: 1991, *Astron. Astrophys.* **243**, 501.

Todd, L.: 1966, *Phys. Fluids* **9**, 814.

Trehan, S. K. and Singh, M.: 1978, *Astrophys. Space Sci.* **53**, 165.

Tsubaki, T.: 1988, *in* R. C. Altrock (ed.), *Solar and Stellar Coronal Structure and Dynamics*, p. 140. Sac. Peak. workshop 1988.

Tsubaki, T., Ohnishi, Y. and Suematsu, Y.: 1987, *Publ. Astron. Soc. Japan* **39**, 179.

Tsubaki, T. and Takeuchi, A.: 1986, *Solar Phys.* **104**, 313.

Tsubaki, T., Toyoda, M. and Suematsu, Y.: 1988, *Publ. Astron. Soc. Japan* **40**, 121.

Uberoi, C. and Somasundaram, K.: 1980, *Plasma Phys.* **22**, 747.

Van der Linden, R., Hood, A. W. and Goedbloed, J. P.: 1994, *Solar Phys.* **154**, 69.

Vrsnak, B.: 1993, *Hvar Obs. Bull.* **17**, 23.

Wentzel, D. G.: 1979, *Astrophys. J.* **227**, 319.

Wiehr, E., Stellmacher, G. and Balthasar, H.: 1984, *Solar Phys.* **94**, 285.

Wilson, P. R.: 1980, *Astron. Astrophys.* **87**, 121.

Yi Zhang and Engvold, O.: 1991, *Solar Phys.* **134**, 275.

Yi Zhang, Engvold, O. and Keil, S. L.: 1991, *Solar Phys.* **132**, 63.